Nonlinear Wind Design of Steel Reinforced Concrete (SRC) Coupling Beams: Final Report

Alexander Hill

Jacob Forbes

Christopher J. Motter

Washington State University

RGA #06-19

CHARLES PANKOW FOUNDATION

Building Innovation through Research

Acknowledgements

This research was supported by funding from the Charles Pankow Foundation, with co-funding from the American Concrete Institute (ACI) Foundation and the Magnusson Klemencic Associates (MKA) Foundation. The authors express their gratitude to the Charles Pankow Foundation, ACI Foundation, and MKA Foundation. Any opinions, findings, and conclusions expressed in this material are those of the authors and do not necessarily reflect those of the Charles Pankow Foundation, ACI Foundation, or MKA Foundation. Thanks are extended to the members of the industry advisory panel, comprised of Viral Patel, Rafael Sabelli, Gregory Deierlein, Mark Denavit, Brad Malmsten, John Peronto, Roberto Leon, Amit Varma, Ron Klemencic, David Fields, John Hooper, Kevin Aswegan, Sean Clifton, Juliana Rochester, Russell Larsen, Jordan Jarrett, and Bahram Shahrooz. Thanks are extended to Scott Lewis, Joshah Jennings, Jesse Black, Levi Arnold, Britnie Casillas, Isaac Nisbet, Parker Likes, Kyle Doering, Nicholas Bonnington, Walker Smith, and Riley Haug for assistance with laboratory testing. This study on steel reinforced concrete (SRC) coupling beams was conducted in parallel with a companion study on steel coupling beams conducted at the University of Cincinnati. Sushil Kunwar, Bahram Shahrooz, and Patrick Fortney are thanked for collaborative discussions. This research is dedicated to the memory of Patrick J. Fortney.

Abstract

Structures are typically designed to yield and sustain damage in a controlled manner during design-level earthquakes. While a similar approach has traditionally not been used for design-level windstorms, the recently-published ASCE/SEI Prestandard for Performance Based Wind Design (ASEC/SEI, 2019) describes design for modest nonlinear response of select structural members such as coupling beams. In this study, four steel reinforced concrete (SRC) coupling beams, with steel sections that embedded into a reinforced concrete wall, were tested quasi-statically under fully reversed cyclic wind demands with peak beam deformation of three times the yield rotation. The beams and walls were designed in accordance with seismic provisions in AISC 341-22 Section H5, and the walls were compliant with ACI 318-19 Section 18.10.6.5. The exception was the wall reinforcement for two of the four tests, in order to examine potential reductions to that prescribed. For one of these tests, the ratio of the strength of wall longitudinal reinforcement crossing the embedment length to that prescribed was 0.53. For the other of these tests, this value was 0.22 and the wall boundary transverse reinforcement at the embedment zone was also less than that prescribed. During each test, the wall was subjected to constant axial gravity load and fully reversed-cyclic lateral loading that was linearly proportional to the load in the test beam. The ratio of wall shear to beam shear was constant for the four tests, while the wall moment at the height of the coupling beam produced by the applied wall demands was the same for three tests and was larger by a factor of 2.0 for one of the tests with wall reinforcement compliant with AISC 341-22 Section H5.

For the test with the least wall reinforcement, significant damage was observed in the wall at the embedded connection. The load developed in the beam was limited by yielding in the wall. Significant pinching, characteristic of gapping, was observed in the load-deformation response. Significant stiffness degradation occurred for repeated loading cycles at 40% of the computed peak strength, and the beam was unable to develop 75% of the computed beam strength, despite being loaded to 6.0% chord rotation. The quantity of wall reinforcement was inadequate to promote favorable performance. Performance was more favorable for the other three tests, which were observed to have similarities in damage patterns and load-deformation responses. Damage concentrated at the beam-wall interface, with the majority of the coupling beam deformation at this location. Although the stiffness degradation for these three tests was much less than the test with wall yielding, stiffness degradation for repeated loading cycles at a given load level was found to be significant in these three tests, particularly for larger loading levels prior to yielding. However, significant strength degradation of initial cycles at new peak deformation demands was not observed in any tests, and significant pinching in the load-deformation response was not observed for the three tests with more favorable performance. Peak load resistance was reached at peak deformation demand, which was 5.70% chord rotation for the test with the largest wall demands, 4.80% chord rotation for two tests, and 6.0% for the test with wall yielding. The primary difference in load-deformation responses for the wind tests conducted in this study and previous seismic tests was the stiffness degradation with repeated loading cycles, noting that the number of cycles used in the wind tests was substantially higher than that used in typical seismic tests.

Stiffness for the first loading cycle at 75% of the expected strength was examined using the results from the three test beams from this study that reached this level and three SRC coupling beams

from other studies. The difference between stiffness in the positive and negative direction was more significant for larger cyclic wall demands, with higher stiffness in the positive direction due to wall demands producing compression at the embedment region. The average of the positive and negative stiffness was larger for walls with higher compression force in the wall on the positive excursion. If cyclic stiffness degradation for repeated cycles at a given increment is not explicitly modeled, it is recommended to use a backbone model based on average values of all cycles at each increment, as this would lead to equal area under the curve for the backbone model and test data. Parameters for a bilinear backbone model for nonlinear wind design are suggested, with effective stiffness of 75% of that prescribed in AISC 341-22 for seismic design, a yield force computed using moment-curvature analysis at full yielding of the tension flange using expected material properties, a computed expected strength from AISC 341-22, and a post-yield slope based on 4.0% chord rotation from yield to expected strength. It is recommended that the hysteretic model be determined by modeling the test beams and calibrating to dissipated energy test data for the three tests with favorable performance. Each of the four backbone parameters were determined based on fit to test data.

This study did not include testing on SRC coupling beams that were designed using provisions in AISC 341-22 Section H4 and tested to peak deformation demands more consistent with ordinary walls. It is recommended that nonlinear wind design of steel reinforced concrete (SRC) coupling beams follow the seismic provisions in AISC 341-22 Section H5. It is recommended that the quantity of wall longitudinal reinforcement crossing the embedment length prescribed by AISC 341-22 Section H5 be reduced by 50% for cases in which wall demands do not exceed that applied for the test that supported this recommendation. These wall demands were $0.49M_y$ and 0.00047

tensile strain in outermost reinforcement at the coupling beam mid-height and an average of $0.24M_y$ and 0.00008 tensile strain in outermost reinforcement over one story height, taken as half a story above and below the coupling beam mid-height. These demands were determined from moment-curvature analysis for the moment and axial load in the wall determined by assuming transfer of coupling beam shear and moment to the wall at coupling beam mid-height. This recommendation applies for both seismic and wind design, due to favorable performance for this test under wind demands to a peak deformation of 4.65% chord rotation.

Table of Contents

Acknowledgements ii

Abstract iii

Table of Contents vii

List of Figures ix

List of Tables xiv

1. Introduction 1

2. Background 4

2.1. Previous Research on Steel and SRC Coupling Beams 4

2.2. Summary of Building Code Design Provisions for SRC Coupling Beams 6

3. Experimental Program 10

3.1. Specimen Design 10

3.2. Construction 17

3.3. Material Properties 22

3.4. Test Set-Up 24

3.5. Instrumentation 30

3.6. Loading Protocol 33

4. Test Results 46

4.1. Observed Damage 46

4.2. Load-Deformation 76
4.3. Dissipated Energy 83
4.4. Moment-Rotation 85
4.5. Axial Elongation and Axial Load 87
4.6. Components of Beam Deformation 90
4.7. Wall Load-Deformation 93
4.8. Wall Strain Profiles 95
4.9. Wall Reinforcement Strain 121
5. Modeling Recommendations 130
5.1. Effective Stiffness 130
5.2. Backbone Models 138
6. Summary and Conclusions 143
References 149

List of Figures

Figure 3.1. Elevation View of Test Specimen with SRC-W1 and SRC-W2 11

Figure 3.2. Elevation View of Test Specimen with SRC-W3 and SRC-W4 12

Figure 3.3. Coupling Beam Cross-Section 12

Figure 3.4. Wall Cross-Sections 13

Figure 3.5. Embedment Detail 17

Figure 3.6. U-Bars Spliced to Web Horizontal Reinforcement at Embedded Steel Section 17

Figure 3.7. Photo of Reinforcement in Wall and Coupling Beams for SRC-W1 and SRC-W2 .. 19

Figure 3.8. Photo of Reinforcement in Wall and Coupling Beams for SRC-W3 (right) and SRC-W4 (left) 20

Figure 3.9. Photo of Coupling Beam Cross-Sections for a) SRC-W1, b) SRC-W2, c) SRC-W3, and d) SRC-W4 20

Figure 3.10. Photos Prior to Casting Concrete from Base of Wall to Top of Coupling Beams ... 21

Figure 3.11. Photos of Test Specimens after Completion of Construction 22

Figure 3.12. Measured Stress-Strain from Tensile Testing of Reinforcement 24

Figure 3.13. Test Set-Up a) Plan View and b) Elevation View 26

Figure 3.14. Photo of Test Set-Up 27

Figure 3.15. Photos of Out-of-Plane Test Beam Bracing 30

Figure 3.16. LVDT Layout 32

Figure 3.17. Strain Gage Layout for SRC-W1 and SRC-W2 33

Figure 3.18. Loading Protocol 34

Figure 3.19. Applied Loads 36

Figure 3.20. Wall Demands at $V@M_{pbe}$ for SRC-W1 in the Positive Loading Direction, with Strain Demands Determined from Moment-Curvature Analysis 37
Figure 3.21. Wall Demands at $V@M_{pbe}$ for SRC-W1 in the Negative Loading Direction, with Strain Demands Determined from Moment-Curvature Analysis 38
Figure 3.22. Wall Demands at $V@M_{pbe}$ for SRC-W2 in the Positive Loading Direction, with Strain Demands Determined from Moment-Curvature Analysis 39
Figure 3.23. Wall Demands at $V@M_{pbe}$ for SRC-W2 in the Negative Loading Direction, with Strain Demands Determined from Moment-Curvature Analysis 40
Figure 3.24. Wall Demands at $V@M_{pbe}$ for SRC-W3 in the Positive Loading Direction, with Strain Demands Determined from Moment-Curvature Analysis 41
Figure 3.25. Wall Demands at $V@M_{pbe}$ for SRC-W3 in the Negative Loading Direction, with Strain Demands Determined from Moment-Curvature Analysis 42
Figure 3.26. Wall Demands at $V@M_{pbe}$ for SRC-W4 in the Positive Loading Direction, with Strain Demands Determined from Moment-Curvature Analysis 43
Figure 3.27. Wall Demands at $V@M_{pbe}$ for SRC-W4 in the Negative Loading Direction, with Strain Demands Determined from Moment-Curvature Analysis 44
Figure 3.28. Wall Demands, Excluding Coupling Beam Demands, at Location of Coupling Beam, Determined from Moment-Curvature Analysis 45
Figure 4.1. Damage Photos for SRC-W1 49
Figure 4.2. Damage Photos for SRC-W2 52
Figure 4.3. Damage Photos for SRC-W3 55
Figure 4.4. Damage Photos for SRC-W4 58
Figure 4.5. Wall Damage Photos for SRC-W1 60

Figure 4.6. Wall Damage Photos for SRC-W2 62
Figure 4.7. Wall Damage Photos for SRC-W3 64
Figure 4.8. Wall Damage Photos for SRC-W4 66
Figure 4.9. Location of Cracks 0.2 Millimeters or Larger for SRC-W1 67
Figure 4.10. Location of Cracks 0.2 Millimeters or Larger for SRC-W2 67
Figure 4.11. Location of Cracks 0.2 Millimeters or Larger for SRC-W3 68
Figure 4.12. Location of Cracks 0.2 Millimeters or Larger for SRC-W4 through the 30th Cycle at 0.4M_{pbe} 69
Figure 4.13. Location of Cracks 0.2 Millimeters or Larger for SRC-W4 following the 30th Cycle at 0.4M_{pbe} 70
Figure 4.14. Load-Deformation for a) SRC-W1, b) SRC-W2, c) SRC-W3, and d) SRC-W4 78
Figure 4.15. Effective Stiffness for a) All Cycles and b) Cycles at 0.75M_{pbe} 78
Figure 4.16. Measured Torsion in SRC-W1 at the Point of Shear Load Application Relative to a) Cycle Number, and b) Beam Rotation 81
Figure 4.17. Measured Torsion in SRC-W2 at the Point of Shear Load Application Relative to a) Cycle Number, and b) Beam Rotation 82
Figure 4.18. Measured Torsion in SRC-W3 at the Point of Shear Load Application Relative to a) Cycle Number, and b) Beam Rotation 82
Figure 4.19. Measured Torsion in SRC-W4 at the Point of Shear Load Application Relative to a) Cycle Number, and b) Beam Rotation 83
Figure 4.20. a) Cumulative Dissipated Energy, and b) Dissipated Energy per Cycle 84
Figure 4.21. Moment-Rotation at Beam-Wall Interface for a) SRC-W1, b) SRC-W2, c) SRC-W3, and d) SRC-W4 86

Figure 4.22. Moment-Rotation at First Sensor Location in Beam for a) SRC-W1, b) SRC-W2, c) SRC-W3, and d) SRC-W4 87

Figure 4.23. Axial Load versus Rotation for a) SRC-W1, b) SRC-W2, c) SRC-W3, and d) SRC-W4 89

Figure 4.24. Axial Elongation versus Rotation for a) SRC-W1, b) SRC-W2, c) SRC-W3, and d) SRC-W4 90

Figure 4.25. Components of Deformation for a) SRC-W1, b) SRC-W2, c) SRC-W3 92

Figure 4.26. Wall Rotation for a) SRC-W1, b) SRC-W2, c) SRC-W3, and d) SRC-W4 94

Figure 4.27. Stiffness Degradation during First Group of 75 Cycles at $0.75M_{pbe}$ 95

Figure 4.28. Wall Strain along Cross-Sections for SRC-W1 97

Figure 4.29. Wall Strain along Cross-Sections for SRC-W2 100

Figure 4.30. Wall Strain along Cross-Sections for SRC-W3 103

Figure 4.31. Wall Strain along Cross-Sections for SRC-W4 106

Figure 4.32. Wall Strain over Height for SRC-W1 109

Figure 4.33. Wall Strain over Height for SRC-W2 112

Figure 4.34. Wall Strain over Height for SRC-W3 115

Figure 4.35. Wall Strain over Height for SRC-W4 118

Figure 4.36. Wall Longitudinal Reinforcement Strain along Cross-Sections for SRC-W1 122

Figure 4.37. Wall Longitudinal Reinforcement Strain along Cross-Sections for SRC-W2 124

Figure 4.38. Wall Longitudinal Reinforcement Strain over Height for SRC-W1 126

Figure 4.39. Wall Longitudinal Reinforcement Strain over Height for SRC-W2 128

Figure 5.1. Wall Demands at $0.75M_{pbe}$, Excluding Coupling Beam Demands, at Location of Coupling Beam (Coupling Beam on Right), Determined from Moment-Curvature Analysis ... 135

Figure 5.2. Backbone Models Fit to Test Data for a) SRC-W1, b) SRC-W2, and c) SRC-W3 . 140

Figure 5.3. Backbone Models using a) Data at Cycle Peaks, b) Bilinear Fit..... 142

List of Tables

Table 3.1. Tested Compressive Strength of Concrete 23

Table 3.2. Measured Strength and Elongation from Tensile Testing of Reinforcement 24

Table 4.1. Measured Crack Widths (Millimeters) for SRC-W1 71

Table 4.2. Measured Crack Widths (Millimeters) for SRC-W2 72

Table 4.3. Measured Crack Widths (Millimeters) for SRC-W3 73

Table 4.4. Measured Crack Widths (Millimeters) for SRC-W4 through the 30th Cycle at 0.4M_{pbe} 74

Table 4.5. Measured Crack Widths (Millimeters) for SRC-W4 through the 30th Cycle at 0.4M_{pbe} 75

Table 4.6. Average Dissipated Energy per Cycle at Each Loading Increment 85

Table 5.1. Measured and Predicted Chord Rotation for Test Beams at 0.75M_{pbe} 131

Table 5.2. Load-Rotation Coordinates of Test Data Backbones 141

Table 5.3. Load-Rotation Coordinates of Bilinear Backbone Models 141

Table 5.4. Strength and Plastic Deformation of Bilinear Backbone Models 142

1. Introduction

Reinforced concrete coupled walls are often used in buildings to provide lateral resistance to seismic and wind demands. Coupling beams are located at the top of story levels and connect to adjacent coplanar walls, creating openings beneath the coupling beams. Shear and moment demand from the coupling beams are transferred into the wall to provide coupling. The shear demands create axial load in the walls. Coupled walls are stiffer and stronger than uncoupled walls due to the moment resistance provided by beams and by the axial tension-compression force couple. During large earthquakes, plasticity is expected to concentrate at the ends of the coupling beams and at the base of the walls. Coupling beams are typically designed to yield prior to walls and provide ductility, energy dissipation, and redundancy. Rotational demands on coupling beams from lateral loads acting on coupled walls are typically higher than other structural components.

Seismic design provisions for diagonally and conventionally reinforced concrete coupling beams are provided in ACI 318-19. The use of diagonal reinforcement rather than conventional reinforcement is often necessary to satisfy shear demands. The use of diagonal reinforcement provides improved resistance to shear sliding relative to longitudinal reinforcement (Paulay and Binney, 1974). However, the need to develop the diagonal reinforcement into the wall leads to congestion of reinforcement at the wall boundaries that complicates construction. Steel and steel reinforced concrete (SRC) coupling beams are an alternative to rebar-reinforced concrete coupling beams that reduce reinforcement congestion in the wall to simplify construction. Relative to steel coupling beams, the concrete encasement used in SRC coupling beams provides fire protection

and stability against flange and web buckling. From past studies on steel coupling beams (Shahrooz et al, 1993; Harries et al, 1993; Harries et al, 1997) and SRC coupling beams (Gong and Shahrooz, 2001a,b; Motter et al, 2017a,b), it is evident that the deformation capacity can meet or exceed that of rebar-reinforced concrete coupling beams. This previous research focused on seismic behavior in special coupled walls, which are designed for ductile post-yield response in earthquakes. This led to development of performance-based seismic design guidelines (Motter et al, 2013) and updates to the AISC Seismic Provisions (AISC 341-22) for prescriptive seismic design.

Research and resulting development of design provisions on coupling beams subjected to nonlinear demand from wind loading is lacking. This is largely due to the difference in design approach reflected in building codes for seismic and wind. Existing seismic design guidelines (e.g., PEER TBI, 2017) recommend an essentially elastic structural response for a service-level earthquake with 43-year return period, with significant nonlinearity permitted for the maximum considered earthquake with a 2475-year return period. Seismic design provisions in ASCE 7-16 similarly allow for significant nonlinearity in the design-level earthquake, which reflects a roughly 475-year return period. Wind design provisions in ASCE 7-16 are based on linear behavior for an approximately 1700-year design wind speed. Due to the inconsistency in design philosophy for wind and seismic, the design of buildings in U.S. regions with significant seismicity may be controlled by wind. Efforts to provide more consistency between wind and seismic design are reflected by the recently-published ASCE/SEI Prestandard for Performance Based Wind Design (ASEC/SEI, 2019), which describes design for modest nonlinear response of select structural members such as coupling beams. Previous research on the behavior of coupling beams subjected

to many loading cycles at modest peak ductility demands is limited. There is a need to address this research gap in order to design for modest coupling beam nonlinearity using the ASCE/SEI Prestandard for Performance Based Wind Design (ASCE/SEI, 2019). This study focuses on characterization of the nonlinear response of SRC coupling beams under wind demands. Recent research was conducted on the nonlinear response of reinforced concrete coupling beams to wind demand (Abdullah et al, 2020). Abdullah et al (2020) tested one SRC coupling beam, with the steel section embedded into concrete blocks that were post-tensioned. To provide additional data on the behavior of SRC coupling beams under nonlinear wind demands, cyclic tests on SRC coupling beams embedded into structural walls were conducted in this study. Four tests were conducted, and the testing and data analysis are summarized in this report. Design recommendations were formulated and are also provided in this report.

2. Background

2.1. Previous Research on Steel and SRC Coupling Beams

For steel and SRC coupling beams, the steel section is embedded into the structural wall to make a connection through a bearing mechanism. Marcakis and Mitchell (1980) and Mattock and Gaafar (1982) studied embedment behavior of steel sections embedded into concrete columns and provided recommended equations to compute the embedment strength that were adopted into AISC 341-22 for steel and SRC coupling beams embedded into walls. The equations adopted into AISC 341-22 included modification of the embedment strength for spalling of wall cover concrete, as recommended by Harries et al (1993).

The vertical stresses in the structural wall at the embedded connection may vary considerably. Shahrooz et al (1993) conducted seismic testing on steel coupling beams embedded into cyclically loaded reinforced concrete structural walls, such that the wall stresses at the embedded connection could vary from compression to tension. Shahrooz et al (1993) observed asymmetric response in the coupling beams, with reduced fixity of the embedded steel section under wall tension demands compared to compression demands. This reduced the fixity of the embedded coupling beam to increase the effective beam length, and Shahrooz et al (1993) recommended that the effective length be increased by one third of the embedment length.

Gong and Shahrooz (2001a,b) conducted seismic tests on SRC coupling beams. Gong and Shahrooz (2001a) reported unfavorable performance when embedment length is based on capacity design for the beam excluding the reinforced concrete encasement. Conversely, Gong and Shahrooz (2001b) reported favorable performance when embedment length was based on capacity design for the beam including the reinforced concrete encasement. Gong and Shahrooz (2001b) provided a recommended equation for determining the peak shear strength of an SRC coupling beam and recommended that this peak strength be used for capacity design of the embedment for shear-controlled coupling beams.

Harries et al (1993, 1997) conducted seismic tests on steel coupling beams embedded into concrete wall segments. Harries et al (1993, 1997) recommended use of longitudinal reinforcement with strength exceeding the beam shear strength to control the crack opening along the flanges of the embedded steel section. This recommendation was adopted into AISC 341. The embedment creates local tensile demands in the wall at the connection region, due to the bearing forces in the embedded connection. The localized tensile demands can cause or exacerbate yielding in the wall in the connection region. Wall yielding was observed in tests in which it was not computed when modeling the transfer of beam shear and moment to the wall at a discrete point, potentially leading to significant damage if not accounted for in design (Motter et al, 2017a). Recognizing that this modeling approach is not uncommon, additional longitudinal reinforcement in the wall may be required to mitigate the effect of the additional demands at the embedment region (Harries et al, 1993, 1997; Motter et al, 2017b). Motter et al (2017b) recommended that the wall longitudinal reinforcement crossing the embedment length provide nominal strength that also meets or exceeds

the resultant back bearing force in the coupling beam, and this provision was introduced into AISC 341-22.

2.2. Summary of Building Code Design Provisions for SRC Coupling Beams

Seismic design provisions for SRC coupling beams are provided in AISC 341-22. H4 applies to composite ordinary shear walls, and H5 applies to composite special shear walls. H4 and H5 provisions are summarized in this section.

For composite ordinary shear walls, provisions in H4.5b.2 specify that the beam shear demand determined from analysis not exceed the connection shear strength, $\phi_v V_{n,connection}$, with ϕ_v=0.9 and $V_{n,connection}$ determined from:

$$V_{n,connection} = 1.54\sqrt{f_c'}\left(\frac{b_w}{b_f}\right)^{0.66}\beta_1 b_f L_e\left(\frac{0.58-0.22\beta_1}{0.88+\frac{g}{2L_e}}\right) \quad (2\text{-}1)$$

where L_e is the embedment length of the coupling beam measured from the face of the wall, g is the clear span of the coupling beam, b_w is the thickness of the wall, b_f is the width of the steel section flange, f'_c is the specified compressive strength of concrete in ksi, and β_1 is a factor relating the depth of the equivalent rectangular compressive stress block to neutral axis depth, as defined in ACI 318-19. This provision may be used to determine the minimum L_e for satisfactory design. Provisions in H4.5b.2 also specify that the beam shear demand determined from analysis not exceed the design shear strength, $\phi_v V_{nc}$, with ϕ_v=0.9 and V_{nc} determined from:

$$V_{nc} = V_p + 0.0632\sqrt{f_c'}\,b_{wc}d_c + \frac{A_{sr}F_{ysr}d_c}{s} \quad (2\text{-}2)$$

where A_{sr} is the area of transverse reinforcement within s, F_{ysr} is the specified minimum yield stress of transverse reinforcement, b_{wc} is the width of concrete encasement, d_c is the effective depth of concrete encasement, s is the spacing of transverse reinforcement, and $V_p = 0.6F_yA_w$, where F_y is the specified yield strength of steel for the steel section, and A_w is the web area of the steel section. It is specified that the peak moment demand, M_u, in the coupling beam determined from analysis, which occurs at the beam-wall interface, be multiplied by $1+[(2L_e)/(3g)]$ to account for fixity at $L_e/3$ into the wall from the beam-wall interface, where L_e is the minimum embedment length computed from Eq. (2-1) to provide sufficient connection shear strength. The flexural strength of the beam is $\phi_b M_n$, as defined in ANSI/AISC 360-22 Chapter I. Wall longitudinal reinforcement is required over the embedment length of the beam with nominal axial strength not less than:

$$\left(\frac{\frac{g}{2L_e}+0.33\beta_1}{0.88-0.33\beta_1}\right)V_u \geq V_u \quad (2\text{-}3)$$

where V_u is the maximum shear demand in the beam. This wall longitudinal reinforcement is prescribed to extend at least one tension development length above and below the flanges of the embedded steel section. Beam longitudinal and transverse reinforcement is prescribed to be distributed around the perimeter with total area in each direction of at least $0.002b_{wc}$ and spacing not exceeding 12". The beam longitudinal reinforcement is prescribed not to extend into the wall and not to be included in the computation of flexural strength.

For composite special shear walls, provisions in H5.5d specify that the embedment length of the steel section into the wall be determined from:

$$V_{be} = 1.54\sqrt{f_c'}\left(\frac{b_w}{b_f}\right)^{0.66}\beta_1 b_f L_e\left(\frac{0.58-0.22\beta_1}{0.88+\frac{g}{2L_e}}\right) \quad (2\text{-}4)$$

where L_e is the embedment length of the coupling beam considered to begin inside the first layer of confining reinforcement, nearest to the edge of the wall, in the wall boundary member, V_{be} is the expected shear strength of the coupling beam, and g is the clear span of the coupling beam plus the wall concrete clear cover at each end of the beam. V_{be} is specified to be the lesser of the expected flexural and shear strength, computed as:

$$V_{be} = \frac{2(1.1)M_{pbe}}{g} \leq V_{ce} \quad (2\text{-}5)$$

where M_{pbe} is the expected flexural strength calculated using the plastic stress distribution or the strain compatibility method, with applicable R_y and R_c factors used for different elements of the cross-section, and V_{ce} is computed as:

$$V_{ce} = 1.1R_y V_p + 0.08\sqrt{R_c f_c'}b_{wc}d_c + \frac{1.33R_{yr}A_{sr}F_{ysr}d_c}{s} \quad (2\text{-}6)$$

where R_c = 1.3 is a factor to account for the expected strength of concrete, R_y is the ratio of the expected yield stress to the specified yield stress for the structural steel section, and R_{yr} is the ratio

of the expected yield stress to the specified yield stress for the transverse reinforcement, with values for R_y and R_{yr} taken from Table A3.2 in AISC 341-22 (2022). Wall longitudinal reinforcement is required over the embedment length of the beam with nominal axial strength not less than:

$$\left(\frac{\frac{g}{2L_e}+0.33\beta_1}{0.88-0.33\beta_1}\right)V_{be} \geq V_{be} \tag{2-7}$$

This wall longitudinal reinforcement is prescribed to extend at least one tension development length above and below the flanges of the embedded steel section. This wall reinforcement is prescribed to be confined by transverse reinforcement that meets ACI 318 Section 18.10.6. For cases in which the longitudinal reinforcement ratio is less than $400/f_y$, transverse reinforcement satisfying ACI 318-19 Section 18.10.6.5(b) through (e) over the distance calculated in accordance with ACI 318-19 Section 18.10.6.4(a) is required between a height of L_e below the bottom flange and L_e above the top flange of an embedded steel section. The vertical spacing of this transverse reinforcement is prescribed not to exceed the lesser of 8" and eight times the diameter of the smallest longitudinal reinforcement confined by this transverse reinforcement. Beam longitudinal and transverse reinforcement is prescribed to be distributed around the perimeter with total area in each direction of at least $0.002b_{wc}$ and spacing not exceeding 12". The beam longitudinal reinforcement is prescribed not to extend into the wall and not to be included in the computation of flexural strength.

3. Experimental Program

3.1. Specimen Design

Four SRC coupling beams embedded into reinforced concrete walls were designed, constructed, and tested. Each of two test specimens, shown in Figure 3.1 and Figure 3.2, was comprised of two coupling beams, a wall, a footing, and a top block. For each test specimen, the coupling beams were tested separately with load simultaneously applied to the wall. The coupling beams were tested as cantilevers, with the point of load application representing mid-length of a full-length coupling beam. The coupling beams were nominally identical. The test variables were the wall longitudinal reinforcement and the level of wall demands applied. For the four tests, SRC-W1, SRC-W2, SRC-W3, and SRC-W4, the wall longitudinal reinforcement ratio at the boundary was 0.026, 0.026, 0.012, and 0.0031, respectively, noting that the value for SRC-W4 is the web reinforcement ratio due to the lack of boundary element. The ratio of applied wall demands to applied coupling beam shear were the same for SRC-W2, SRC-W3, and SRC-W4 and half that of SRC-W1. More details on the wall demands are provided in Section 3.6. Each coupling beam, shown in Figure 3.3, had 12” by 18” cross-section and a W12x96 A992 structural steel section with the flanges trimmed to 5.5” width. The flanges were trimmed to achieve improved scaling, as the test beams represented a ½-scale 24” by 36” rectangular cross section reinforced with a W24x250 A992 steel section. The beams were tested as 30” cantilevers. Each wall had 12” by 96” cross-section, shown in Figure 3.4, with 90” clear height. The footings were 33” wide by 18” tall by 120” long, and the top blocks were 27” wide by 18” tall by 120” long.

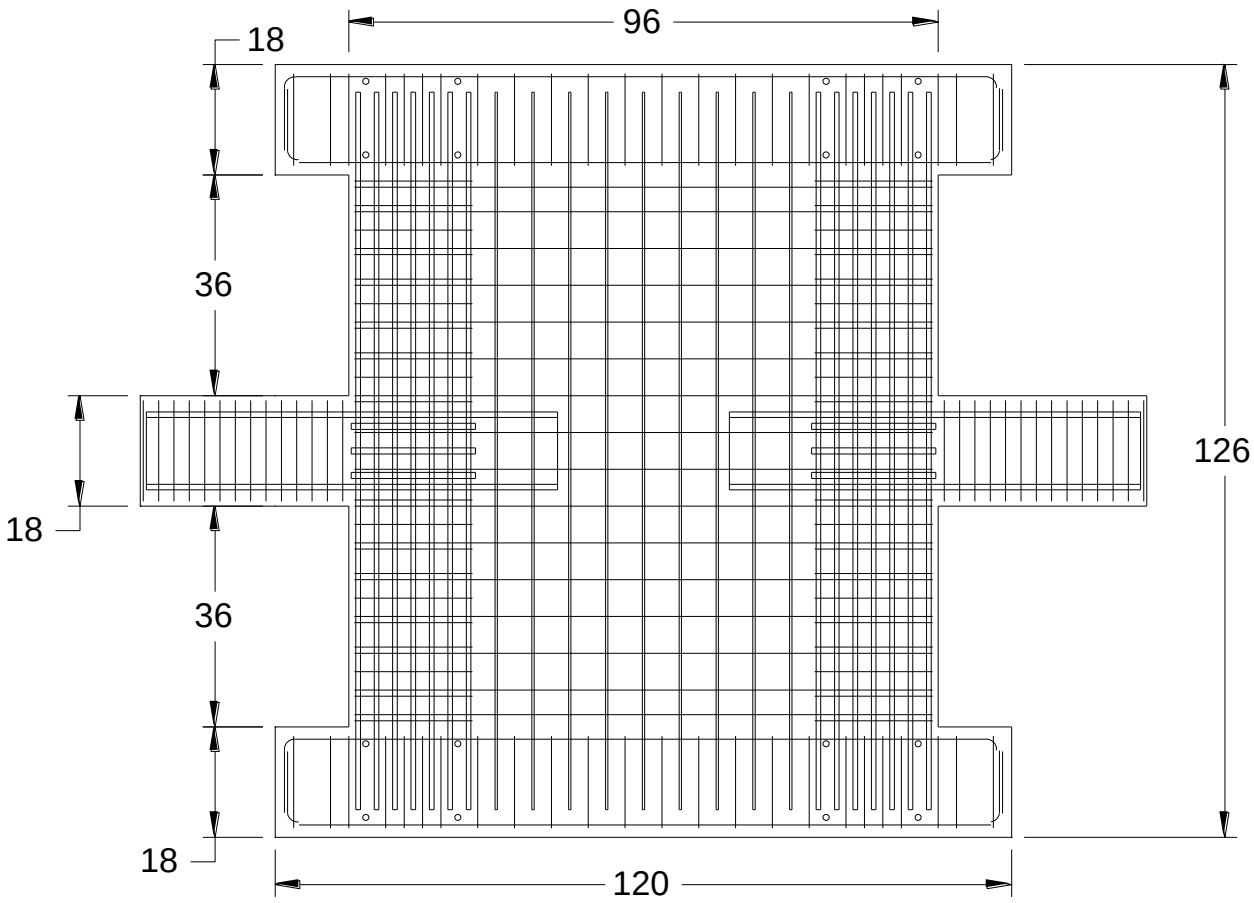

Figure 3.1. Elevation View of Test Specimen with SRC-W1 and SRC-W2

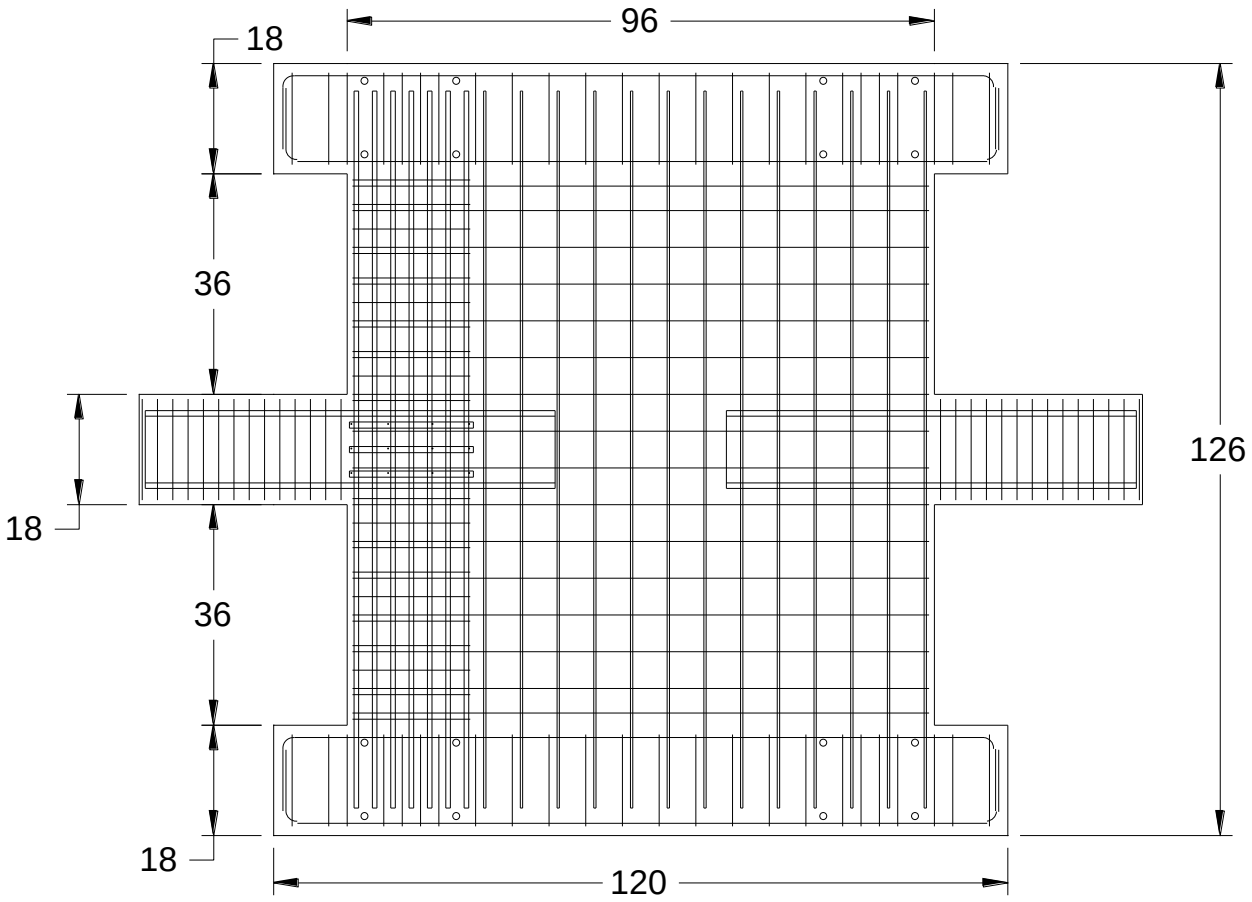

Figure 3.2. Elevation View of Test Specimen with SRC-W3 and SRC-W4

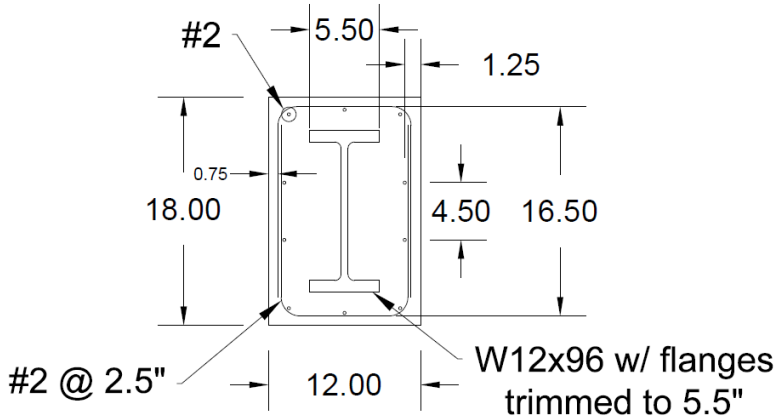

Figure 3.3. Coupling Beam Cross-Section

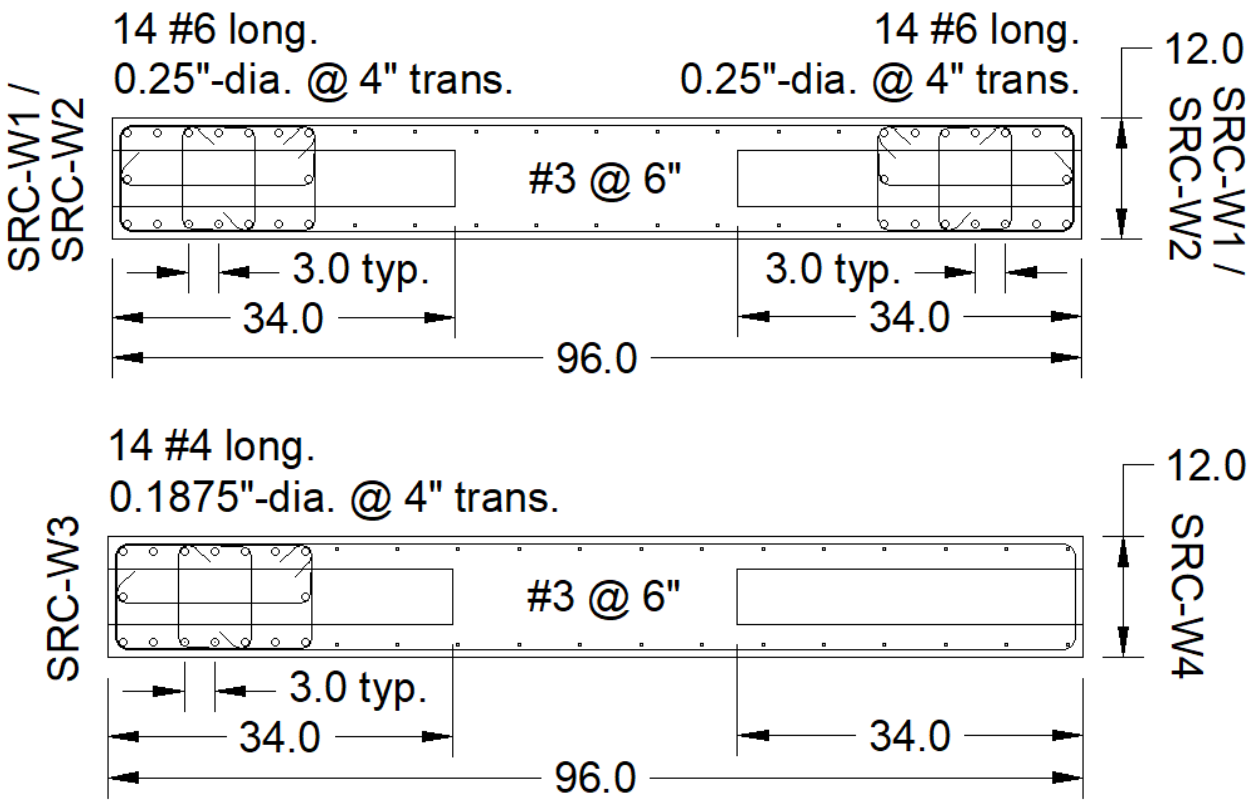

Figure 3.4. Wall Cross-Sections

There is a lack of previous research on the nonlinear wind behavior of SRC coupling beams, such that there is lack of design guidance. However, seismic design guidelines are provided in AISC 341-22 and were summarized in the previous chapter. In AISC 341-22, Section H5 applies to composite special shear walls, while Section H4 applies to composite ordinary shear walls. AISC 341-22 Section H4 provisions are expected to provide limited inelastic deformation capacity through yielding, as specified in AISC 341-22 Section H4.2. AISC 341-22 Section H5 provisions are expected to provide significant inelastic deformation capacity through yielding, such that the walls are specified to be designed including Chapter 18 of ACI 318, as specified in AISC 341-22 Section H5.2. ACI 318-19 Section 18.10.1.1 specifies that Section 18.10 applies to special

structural walls. In this study, the coupling beams were tested to peak deformation demands of three times the yield rotation, with more details on loading protocol provided in Section 3.6. This level of demand is comparable to peak coupling beam demands under MCE-level earthquake for the 42-story reinforced concrete core wall building analyzed in Moehle et al (2011). The peak demands on the test beams were deemed to be more consistent with AISC 341-22 Section H5 design than AISC 341-22 Section H4 design. Therefore, the beams and walls were designed to satisfy AISC 341-22 Section H5.5 and ACI 318-19 Section 18.10.

0.25”-diameter A36 undeformed bar was used as reinforcement in the beam. This included ten longitudinal bars around the perimeter of the section and transverse reinforcement comprised of hoops spaced at 2.5” on center. Each hoop used as transverse reinforcement consisted of U-bars with long legs overlapping. The concrete clear cover to the beam transverse reinforcement was 0.75”. At full-scale, this reinforcement in the half-scale beam satisfied AISC 341-22 Section H4.5b.2(c) for a total area in each direction of at least $0.002b_{wc}$ and spacing not exceeding 12”. The longitudinal reinforcement was not embedded into the wall, as recommended by Barbachyn et al (2012) and prescribed by AISC 341-22, rather than embedded a short distance as shown in ACI 318-19 Fig. R18.10.7.b.

The specified compression strength of concrete, f'_c, used in the beams and wall was 5.5 ksi. Using R_y = 1.1 for A992, R_{yr} = 1.5 for A36, and R_c = 1.3 from AISC 341-22, M_{pbe} was computed to be 448 k-ft, and V_{ce} was computed to be 344 k for the beam. The clear cover at the end of the wall was 0.75” to 0.25”-diameter wall boundary transverse reinforcement and 0.625” to #3 U-bars spliced to wall shear reinforcement. Using the larger clear cover to determine g, V_{be} was computed

to be 192 k for the flexure-controlled beam. L_e was computed to be 33.0” using Eq. (2-4). L_e begins from the inside of the wall boundary transverse reinforcement, which was located 1.0” from the beam-wall interface. Thus, the required embedment length from the beam-wall interface was 34.0”, which was the length provided. Auxiliary transfer bars and end bearing plates were not provided in the embedment region. Web stiffeners were not provided in the steel section.

The minimum required strength of wall longitudinal reinforcement crossing the embedment length was determined to be 366 kips in accordance with Eq. (2-7). SRC-W1 and SRC-W2 had 14#6 and 4#3 Grade 60 longitudinal bars crossing the embedment length, as shown in Figure 3.4 and Figure 3.2, for a provided nominal strength of 396 kips, which was 1.08 times that required. This ratio was less than 1.0 for SRC-W3 and SRC-W4 to assess whether the quantity of reinforcement prescribed by AISC 341-22 could be reduced if wall demands are sufficiently low. SRC-W3 had 14#4 and 4#3 Grade 60 longitudinal bars crossing the embedment length for a provided nominal strength of 194.4 kips, which was 0.53 times that required. SRC-W4 had 12#3 Grade 60 longitudinal bars crossing the embedment length for a provided nominal strength of 79.2 kips, which was 0.22 times that required.

It was assumed that the test beams were not located in a wall location with a special boundary element. The corresponding boundary longitudinal reinforcement ratio of 0.026 for SRC-W1 and SRC-W2 and 0.012 for SRC-W3 exceeded $400/f_y$ = 0.0067, such that an intermediate level of boundary transverse reinforcement was required by ACI 318-19 Section 18.10.6.5(b). The boundary element transverse reinforcement was configured as hoops and cross-ties with 0.75” clear cover that were spaced longitudinally at 4” on center with every other longitudinal bar

restrained along the length of the wall. This satisfied the requirements of ACI 318-19 Section 18.10.6.5(b) at half-scale. The boundary element transverse reinforcement was 0.25”-diameter A36 undeformed bar for SRC-W1 and SRC-W2 and 0.1875”-diameter A36 undeformed bar for SRC-W3. This satisfied the requirements of ACI 318-19 Section 25.7.2.2, which specifies #3 or larger transverse reinforcement for #10 or smaller longitudinal reinforcement and #4 or larger transverse reinforcement for #11 or larger longitudinal reinforcement, at half-scale. The two longitudinal bars in each boundary located at the wall centerline were discontinuous at the embedment of the steel section. Wall boundary element transverse reinforcement was provided in the embedment zone using threaded rods and plates, as shown in Figure 3.5. The threaded rods and plates, which were spaced longitudinally at 4”, were sized to provide stiffness and strength not less than that of the boundary element transverse reinforcement above and below the embedded steel section. The threaded rods passed through holes pre-drilled into the web of the steel section prior to assembly. This detailing is consistent with that used by Motter et al (2017a). For SRC-W4, the longitudinal reinforcement ratio of 0.0031 was less than $400/f_y$ = 0.0067, such that an intermediate level of boundary transverse reinforcement was not required by ACI 318-19 Section 18.10.6.5(b). The wall boundary transverse reinforcement required by AISC 341-22 Section H5.5b between a height L_e below the bottom flange and L_e above the top flange was not provided for SRC-W4.

Wall web horizontal and vertical reinforcement was #3 spaced at 6”, and the resulting reinforcement ratio of 0.0031 exceeded the minimum of 0.0025 required by ACI 318-19 Section 18.10.2.1. The vertical web reinforcement extended to the end of the wall for SRC-W4. U-bars at the ends of the wall were spliced to the wall web horizontal reinforcement to satisfy ACI 318-19

Section 18.10.6.5(a). At the location of the embedded steel section, the U-bars did not pass through the web of the steel section, and a double U-bar detail was used, as shown in Figure 3.6.

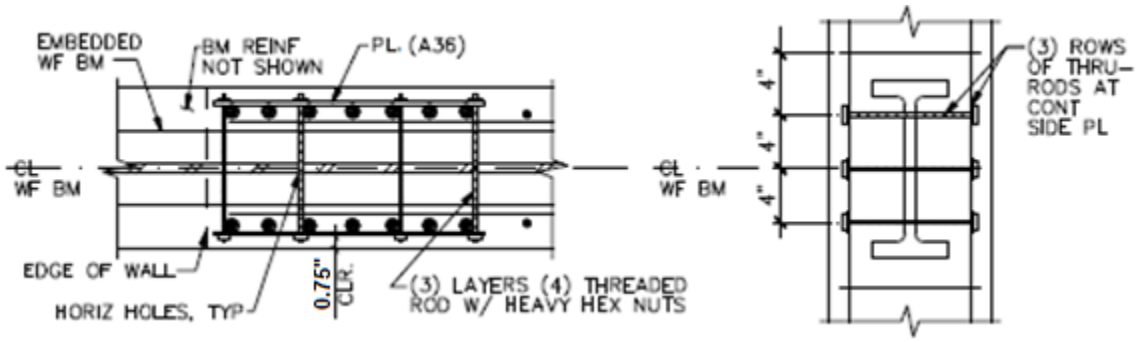

Figure 3.5. Embedment Detail

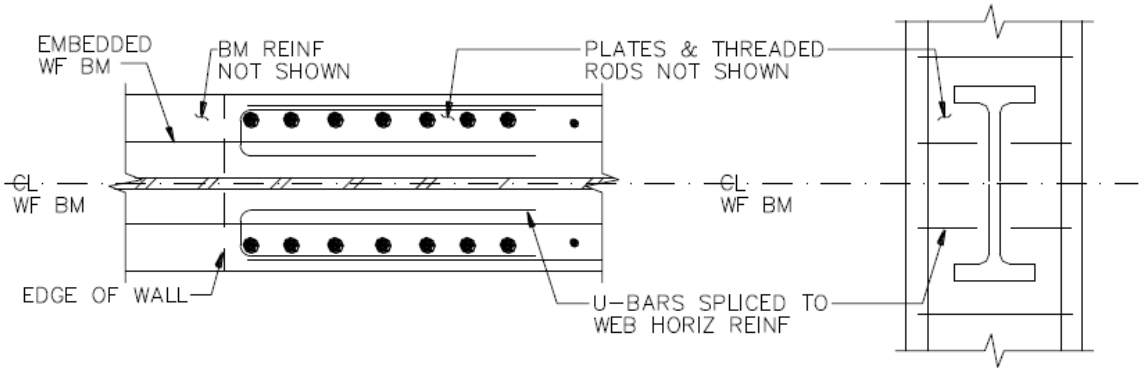

Figure 3.6. U-Bars Spliced to Web Horizontal Reinforcement at Embedded Steel Section

3.2. Construction

The test specimens were built indoors on a level surface. The first specimen, with SRC-W1 and SRC-W2, was constructed and tests were completed prior to construction of the second specimen, with SRC-W3 and SRC-W4. For each specimen, construction began with building of footing

formwork and tying of the footing reinforcement cage, followed by placement of the reinforcement cage in the footing with spacers used to maintain clear cover. Formwork for one side of the wall and coupling beams was built, positioned, and braced to the floor. The wall boundary element reinforcement cages were assembled and placed, with the formwork used for positioning. For the specimen with SRC-W1 and SRC-W2, some reinforcement in the footing was removed and replaced to accommodate placement of the wall boundary element reinforcement, which had #6 hooked longitudinal reinforcement. Wall web horizontal and vertical reinforcement were then tied into position individually. PVC was installed in the footing formwork to create voids that were later used for post-tensioning rods. The footing was poured, and the footing surface within the plan of the wall was roughened, as this was a construction joint. After several days, the footing formwork was removed.

Formwork for the coupling beams was built, positioned, and braced to the floor. Reinforcement cages for the coupling beams were tied. The steel sections and rebar cages were moved into position with spacers used to set cover, with photos provided in Figure 3.7 through Figure 3.9. The remaining face of formwork from the base of the wall to the top of the coupling beams was built, installed, and braced to the floor. Threaded rods for instrumentation were installed through the thickness of the wall and coupling beams, with holes drilled in the formwork to accommodate the threaded rods. Photos prior to subsequent concrete placement are provided in Figure 3.10. Concrete was pumped from the bottom of the wall to the height of the top of the coupling beams, including the coupling beams. The concrete surface in the wall at the height of the coupling beams was roughened, as this was a construction joint.

Formwork for the remaining face of the upper wall and for the top block was built, installed, and braced to the floor. The top block reinforcement cage was tied and placed into the formwork with spacers used to maintain clear cover. PVC was installed in the top block formwork. Threaded rods for instrumentation were installed in the wall. Concrete in the wall and top block was pumped from the top of the coupling beams to the top of the specimen. Photos of the test specimens after completion of construction and removal of formwork are provided in Figure 3.11. The construction process resulted in construction joints at the footing-wall interface and at the top of the coupling beams. A construction joint at the top of the coupling beams is consistent with standard practice in which construction joints are present between story levels.

Figure 3.7. Photo of Reinforcement in Wall and Coupling Beams for SRC-W1 and SRC-W2

Figure 3.8. Photo of Reinforcement in Wall and Coupling Beams for SRC-W3 (right) and SRC-W4 (left)

a)  b)  c)  d) 

Figure 3.9. Photo of Coupling Beam Cross-Sections for a) SRC-W1, b) SRC-W2, c) SRC-W3, and d) SRC-W4

Figure 3.10. Photos Prior to Casting Concrete from Base of Wall to Top of Coupling Beams

(Left Photo: SRC-W1 and SRC-W2. Right Photo: SRC-W3 and SRC-W4.)

Figure 3.11. Photos of Test Specimens after Completion of Construction

(Left Photo: SRC-W1 and SRC-W2. Right Photo: SRC-W3 and SRC-W4.)

3.3. Material Properties

The specified compressive strength of concrete, f'_c, was 5.5 ksi. Concrete was provided by a local supplier. Each specimen was constructed in three separate lifts, as described in Section 3.2. For each concrete lift, 6”x12” concrete cylinders were prepared in accordance with ASTM C31 (2022). Compressive tests were conducted at 28 days as well as before and after each coupling beam test. Values of the tested compressive strength of concrete, $f'_{c,test}$, are provided in Table 3.1.

Table 3.1. Tested Compressive Strength of Concrete

Test Name	Location	Age (days)	$f'_{c,test}$ (ksi)				
			Test #1	Test #2	Test #3	Test #4	Average
SRC-W1	Lower Wall	220	7.43	7.06	7.04	6.95	7.12
		240	7.05	7.65	7.18	7.41	7.33
	Upper Wall	198	5.50	5.03	5.28	5.49	5.32
		218	5.53	5.52	5.73	5.52	5.58
SRC-W2	Lower Wall	342	7.39	7.67	7.57	7.57	7.55
		356	7.33	6.76	7.63	7.62	7.33
	Upper Wall	320	5.47	5.48	5.41	5.23	5.40
		334	5.43	5.61	5.49	4.98	5.37
SRC-W3	Lower Wall	98	4.74	4.59	3.95	5.02	4.57
		105	4.21	4.93	4.74	5.16	4.76
	Upper Wall	84	5.42	6.04	5.41	5.40	5.57
		91	5.86	5.17	4.89	4.99	5.25
SRC-W4	Lower Wall	154	5.30	4.93	4.98	5.47	5.17
		160	4.73	5.20	5.11	4.52	4.89
	Upper Wall	133	5.57	4.37	5.18	-	5.04
		139	5.86	6.08	5.60	-	5.47

The wall contained #6, #4, and #3 Grade 60 reinforcement compliant with either ASTM A615 or ASTM A706. The reinforcement was cut and bent by a local supplier, with test samples provided. 0.25”-diameter and 0.1875”-diameter A36 undeformed reinforcement was used in the beams and walls. This reinforcement was cut and bent in-house. Tensile testing was conducted on #6, #4, and #3 reinforcement samples, with results provided in Table 3.2 and Figure 3.12.

Table 3.2. Measured Strength and Elongation from Tensile Testing of Reinforcement

Reinforcement Size	Test No.	F_y (ksi)	F_u (ksi)	% Elong.
#6	Test #1	66.5	107.5	17.5
	Test #2	67.2	107.6	17.3
	Test #3	66.0	107.6	17.5
	Test #4	66.2	107.6	17.5
	Average	66.5	107.6	17.5
#4	Test #1	67.0	108.2	15.1
	Test #2	66.0	107.7	15.5
	Test #3	66.0	107.6	14.9
	Test #4	66.0	107.4	15.2
	Average	66.25	107.9	15.4
#3	Test #1	68.5	110.0	12.8
	Test #2	69.0	110.7	12.2
	Test #3	68.0	108.9	12.4
	Test #4	66.6	107.1	13.0
	Average	68.0	109.2	12.6

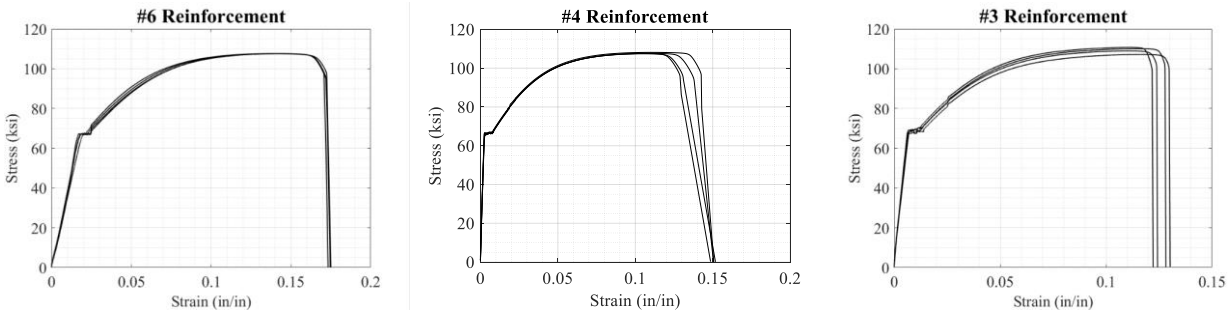

Figure 3.12. Measured Stress-Strain from Tensile Testing of Reinforcement

3.4. Test Set-Up

The test set-up is shown in Figure 3.13 and Figure 3.14 and is similar to that used by Motter et al (2017a) in previous seismic tests on SRC coupling beams. The test specimen was positioned atop

a 20” wide by 39” tall by 120” long concrete spacer block to achieve sufficient clearance between the coupling beams and the floor for the actuator used to load the coupling beam. To level the test specimen and provide contact between concrete surfaces, grout was used between the spacer block and strong floor and between the spacer block and specimen footing. Using high-strength threaded rods, the footing was post-tensioned to the laboratory strong floor and was also post-tensioned in the transverse direction. A steel loading beam with welded base plate was installed at the top of the specimen, with grout used between the surfaces for contact and leveling. The steel loading beam was post-tensioned to the top block. The top block was post-tensioned in the transverse direction.

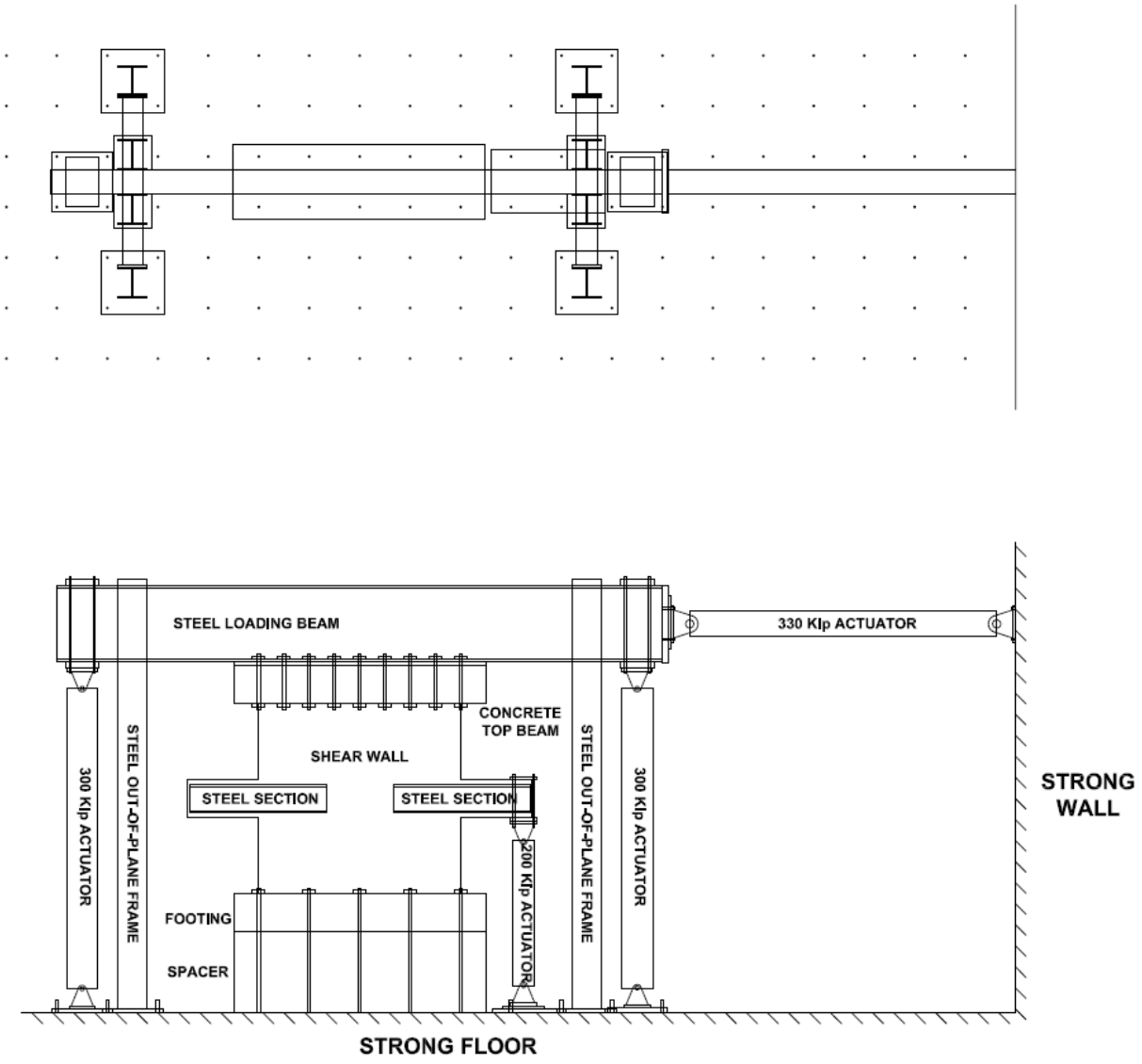

Figure 3.13. Test Set-Up a) Plan View and b) Elevation View

Figure 3.14. Photo of Test Set-Up

Four actuators were used in the test. An actuator with 200-kip capacity and ±10” stroke was connected from the strong floor to the coupling beam. This actuator was oriented vertically and located 30” from the face of the wall. This actuator was attached to the strong floor using an adaptor plate and attached to the coupling beam using a top and bottom plate post-tensioned to the coupling beam. 6” wide by ½” thick by 12” long bearing plates were used between the plates and the beam concrete to apply the load over the full beam thickness and a 6” width. Three actuators were connected to the steel loading beam. One of these was a 330-kip capacity actuator with ±20” stroke that was oriented horizontally and spanned from the strong wall to the loading beam. This actuator was attached to an adaptor plate that was post-tensioned to the strong wall and to a welded end plate on the loading beam. The other two actuators that were connected to the loading beam were oriented vertically and spanned from the loading beam to the strong floor. These were 268-kip

capacity actuators with ±30” stroke. These two actuators were located 22’ feet apart at opposite ends of the loading beam. Spacers, consisting of short length steel I-beams, were used under each of these two actuators. These actuators had adaptor plates that were post-tensioned to the strong floor and post-tensioned to the loading beam.

Passive axial restraint was applied to the test beam. The axial restraint was comprised of 3/8” threaded rod running horizontally on each side of the wall and spanning from the end of the coupling beam being tested to the end of the coupling beam not being tested. Steel sections were used to spread load from the coupling beam to the threaded rods. This passive restraint was such that the axial compressive load on the coupling beam increased with increasing axial elongation, and the load was measured during testing using a load cell between the end of the coupling beam not being tested and the steel spreader beam. This axial restraint was expected to apply a low level of force with the intent of mitigating outward ratcheting of the test beam over repeated loading cycles. The approach was consistent with that used by Motter et al (2017a) in two of the four tests. Motter et al (2017a) had observed significant outward ratcheting in two of the tests and applied this type of axial restraint to mitigate outward ratcheting in the next two tests. The measured axial load was reported by Motter et al (2017a) to be sufficiently small to have minimal effect on the beam behavior through P-M interaction. This level of restraint is expected to be less than that provided by floor slabs and adjacent walls in actual coupling beams.

Out-of-plane restraint was installed near each end of the steel loading beam to mitigate out-of-plane deformation during testing. The out-of-plane restraint at each end consisted of a structural steel frame, comprised of two columns, a beam, and two short-length columns attached to the

beam. These short-length columns were positioned in contact with the top and bottom flanges of the loading beam and had welded end plates that were then post-tensioned to the beam of the out-of-plane restraint frame. In addition to providing out-of-plane translational restraint, these columns were intended to resist torsion of the loading beam associated with out-of-plane rotation at the top of the wall. Grease was applied to the flanges of the loading beam and faces of the columns to mitigate frictional resistance to in-plane translation.

During testing of SRC-W2, bracing was installed to mitigate torsion and out-of-plane translation at the end of the test beam. This bracing, shown in Figure 3.15, was used for the entire test for SRC-W3 and SRC-W4. Two braces were used, and each brace consisted of a steel section with angled end plates that spanned from the column of the out-of-plane restraint frame to the lower base plate that was post-tensioned to the test beam. This bracing was oriented on an angle in a horizontal plane. The end plate at one end of each brace was bolted to the columns of the out-of-plane restraint frame. Grease was applied between the end plate at the other end of the brace and the edge of the lower base plate that was post-tensioned to the test beam.

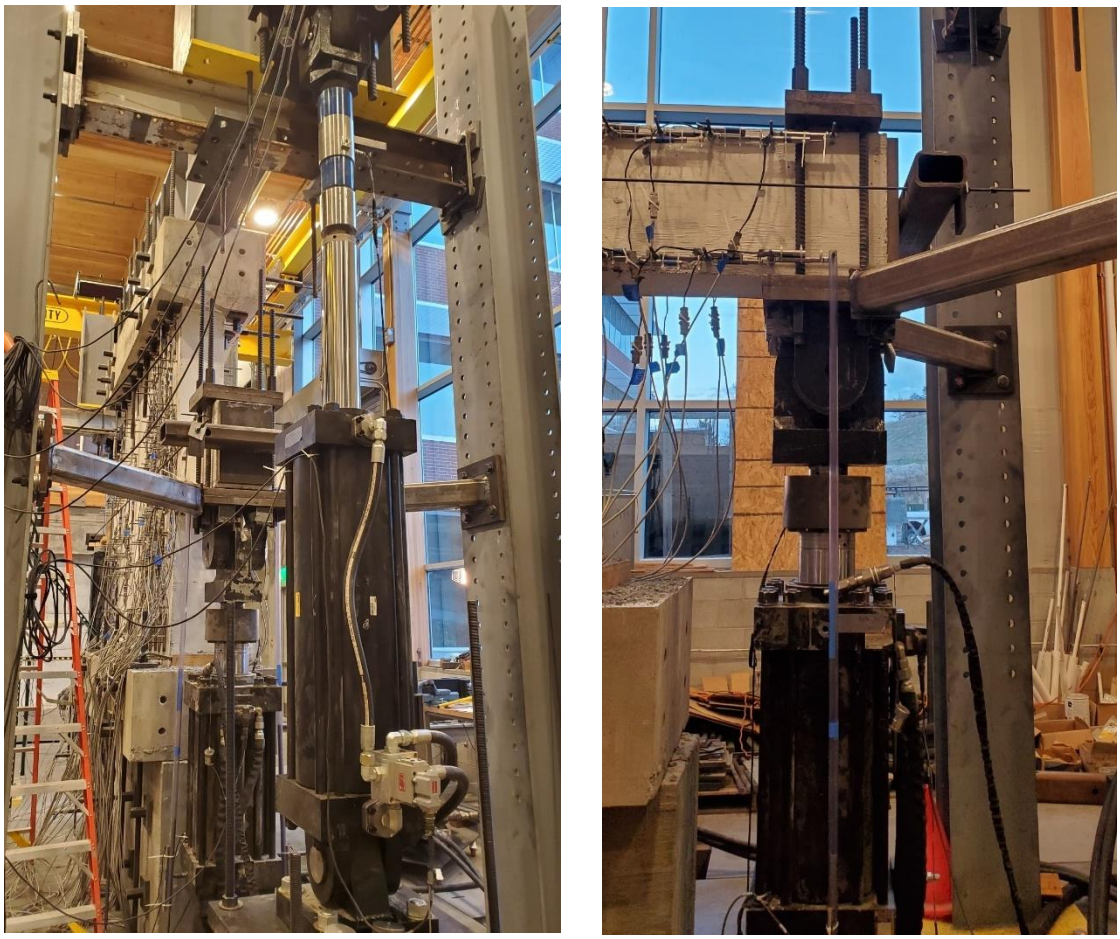

Figure 3.15. Photos of Out-of-Plane Test Beam Bracing

3.5. Instrumentation

Instrumentation was comprised of 95 linear variable differential transformers (LVDTs), one load cell on each of the four actuators, and one load cell to measure axial force in the test beam. Additionally, for the first specimen, with SRC-W1 and SRC-W2, there were 36 strain gauges on wall longitudinal reinforcement. The layout of LVDTs, shown in Figure 3.16, was selected to enable determination of the components of deformation from axial-flexure, shear, and interface axial-flexure and shear in the test beam and to determine the strain field and assess plane section

behavior in the wall. The embedment model for the steel section reflected in AISC 341-22 is based on the assumption of plane section behavior over the embedment length, while a wall in bending is typically analyzed based on plane section behavior. The layout in instrumentation was selected to enable assessment of the extent to which plane section behavior in the wall is disturbed by embedment of the beam. The layout of strain gages used for the first specimen, with SRC-W1 and SRC-W2, is provided in Figure 3.17, with 18 strain gages provided on the longitudinal reinforcement in each of the two wall boundary elements. This layout of strain gages was selected to aid in the assessment of the local tensile increase or compressive reduction in strain in wall longitudinal reinforcement due to the effect of the embedment demands, which create local tension.

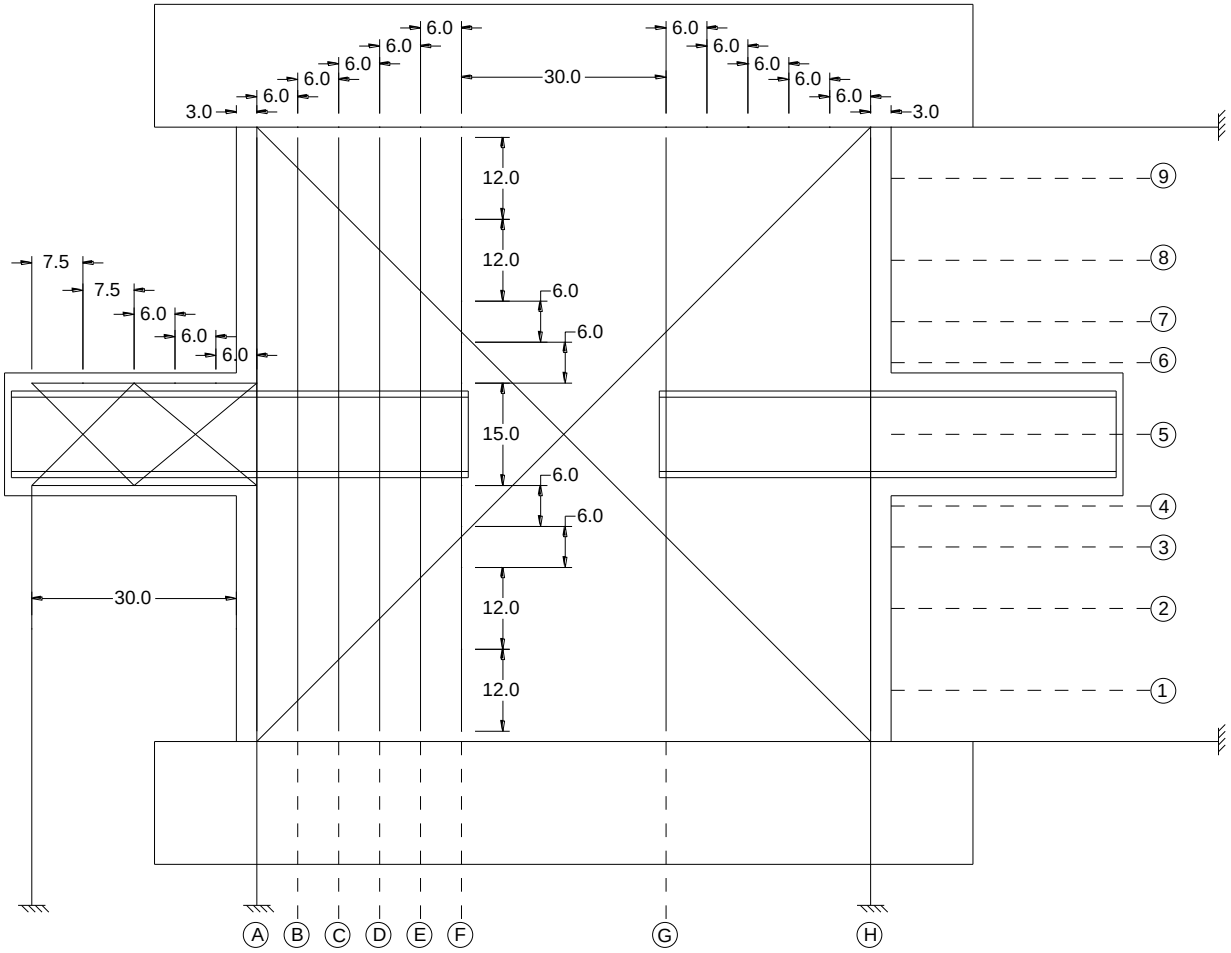

Figure 3.16. LVDT Layout

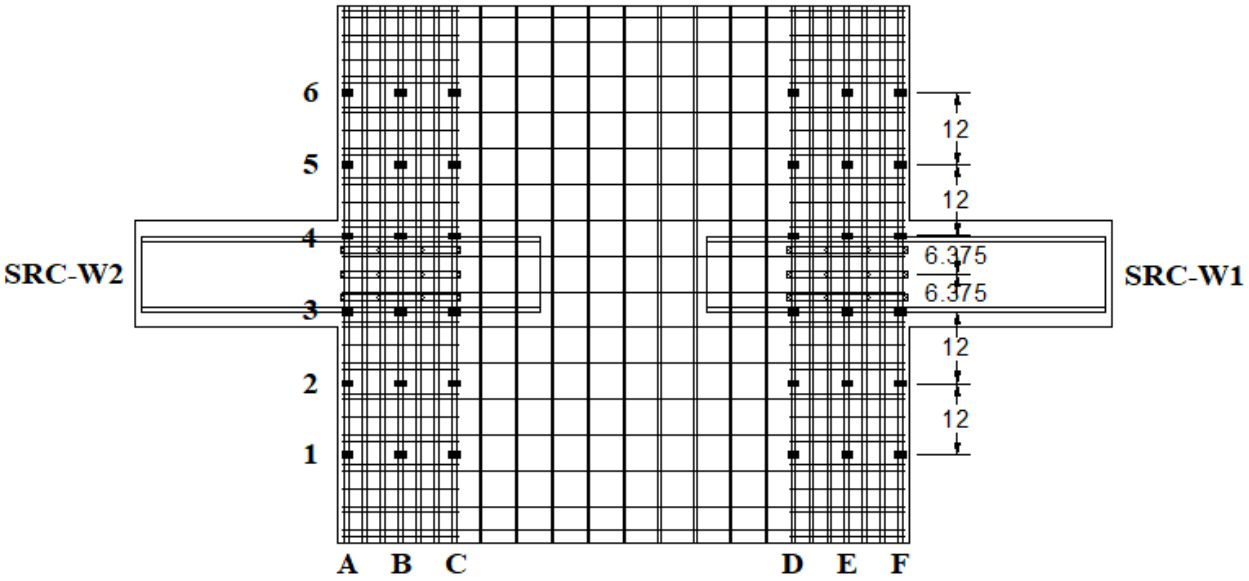

Figure 3.17. Strain Gage Layout for SRC-W1 and SRC-W2

3.6. Loading Protocol

During testing, reversed cyclic load was applied to the test beam, with reversed cyclic load and constant axial load applied to the wall. The loading protocol used for the test beam, shown in Figure 3.18, was comprised of 250 cycles at $0.15M_{pbe}$, 500 cycles at $0.40M_{pbe}$, 75 cycles at $0.75M_{pbe}$, five cycles at $1.2\theta_y$, three cycles at $1.5\theta_y$, two cycles at $2.0\theta_y$, two cycles at $2.5\theta_y$, and one cycle at $3.0\theta_y$, followed by the same sequence in reverse, where θ_y is the yield rotation. For SRC-W4, the loading protocol consisted of 250 cycles at $0.15M_{pbe}$, 500 cycles at $0.40M_{pbe}$, and two cycles at 6.0% chord rotation, as $0.75M_{pbe}$ was not reached prior to reaching 6.0% chord rotation during the first excursion after 500 cycles at $0.40M_{pbe}$. M_{pbe} was computed as 447.8 k-ft for SRC-W1, 450.7 k-ft for SRC-W2, 426.7 k-ft for SRC-W3, and 432.7 k-ft for SRC-W4 using 55 ksi expected yield strength for A992 steel and the average tested concrete compressive strength before the start of the test of 7.12 ksi for SRC-W1, 7.55 ksi for SRC-W2, 4.57 ksi for SRC-W3,

and 5.17 ksi for SRC-W4. The corresponding $V@M_{pbe}$ was computed for a 2.5' cantilever as 179.1 kips for SRC-W1, 180.3 kips for SRC-W2, 170.7 kips for SRC-W3, and 173.1 kips for SRC-W4. These values for $V@M_{pbe}$ were used to control the tests. θ_y was determined during testing. During the first positive excursion to $1.2\theta_y$, the measured chord rotation at $0.75M_{pbe}$ was multiplied by $M_y/(0.75M_{pbe})$ to determine θ_y, where M_y was the moment at which the tension flange fully yields (i.e., the strain on the inner face of the tension flange is equal to the yield strain), computed from moment-curvature analysis using the same material properties used for calculating M_{pbe}. This loading protocol was a modification of that used by Abdullah et al (2020). The protocol used by Abdullah et al (2020) had a peak rotation of $1.5\theta_y$, while the protocol used in this study had a peak rotation of $3.0\theta_y$.

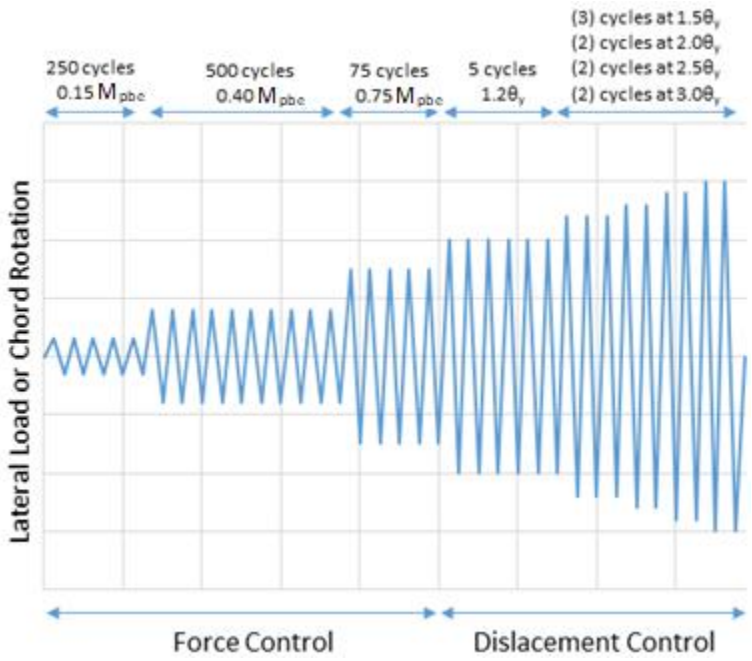

Figure 3.18. Loading Protocol

For the displacement-controlled cycles in the loading protocol, the chord rotation was computed as the beam displacement divided by the 30” cantilever length, with a correction for footing and wall deformation. The correction for footing deformation was made using the two vertical LVDTs on the footing to estimate rotation and vertical translation of the top plane of the footing. The correction for wall rotation was taken in a similar manner using the two sensors that spanned over the clear height of the wall, but the value was halved due to the coupling beam being located at mid-height of the wall.

The loads applied during testing are shown in Figure 3.19, with the resulting wall demands shown in Figure 3.20 through Figure 3.28 for the four tests. A constant axial gravity load of 328 kips was applied to the wall during all beam tests. This was determined as $0.04A_g f'_{c,test}$ = 328 kips using $f'_{c,test}$ = 7.12 ksi obtained from the lower wall concrete prior to the first beam test. Reversed cyclic lateral load was applied to the wall through force proportionality among actuators. The gravity load was applied using the two vertical actuators prior to the force proportionality, such that the gravity load was maintained during loading cycles. The wall shear demand was determined so that the change in moment from wall shear over a story height was equal to the moment created by the coupling beam in the wall. Assuming a 12’ story height, which would be 6’ at half-scale, the wall shear demand was programmed to be 6.5’/6’ = 1.083 times the beam shear demand. At the largest $V@M_{pbe}$ for the four test beams of 180.3 kips, the peak wall shear is 195.3 kips, which is roughly equal to $2\sqrt{R_c f'_c} A_{cv}$ = 194.8 kips. Additional moment was applied to the wall using equal and opposite forces in the two vertical actuators. Each of these forces was programmed to be 0.275 times the beam shear demand for SRC-W1 and -0.034 times the beam shear demand for SRC-W2, SRC-W3, and SRC-W4, and these two actuators were located 22’ apart. The value -0.034 was

selected to produce a wall mid-height moment (i.e., at location of coupling beam) for SRC-W2, SRC-W3, and SRC-W4 that was half of that for SRC-W1 at a given beam shear, while maintaining the same wall shear, as shown in Figure 3.20 through Figure 3.27. The wall demands for SRC-W1 were intended to be larger than typical demands at most locations in coupled walls but not so large as to produce wall yielding. At the expected beam strength of 179.1 kips for SCR-W1, the wall demands, excluding coupling beam demand, at mid-height were computed to produce a peak tensile strain of 0.55e_y and peak compressive strain of 0.00047, based on moment-curvature analysis, where e_y is the yield strain of the wall longitudinal reinforcement based on the tested strength provided in Table 3.2. For SRC-W2 at 180.3 kips, these strains were 0.12e_y in tension and 0.00020 in compression. For SRC-W3 at 170.7 kips, these strains were 0.21e_y in tension in the negative loading direction and 0.00039 in compression in the positive loading direction. For SRC-W4 at 173.1 kips, these strains were 0.32e_y in tension in the negative loading direction and 0.00031 in compression in the positive loading direction. The local demands are larger due to the influence of the coupling beam connection (Motter et al, 2017a,b).

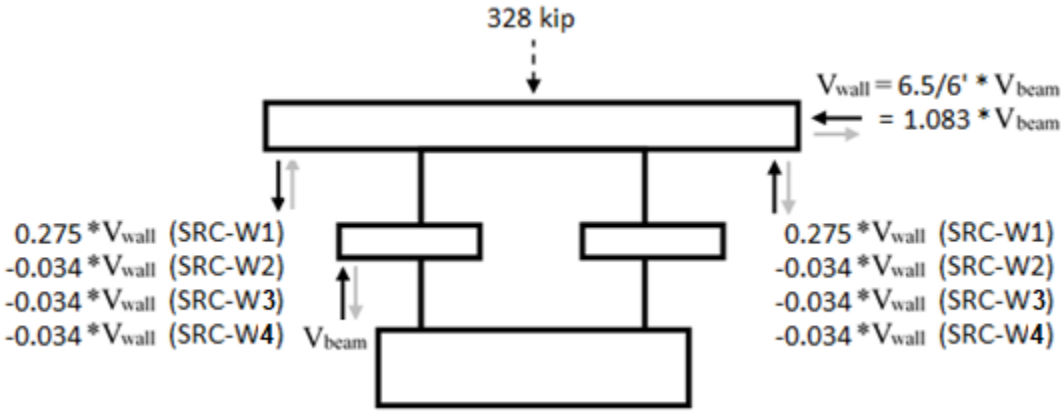

Figure 3.19. Applied Loads

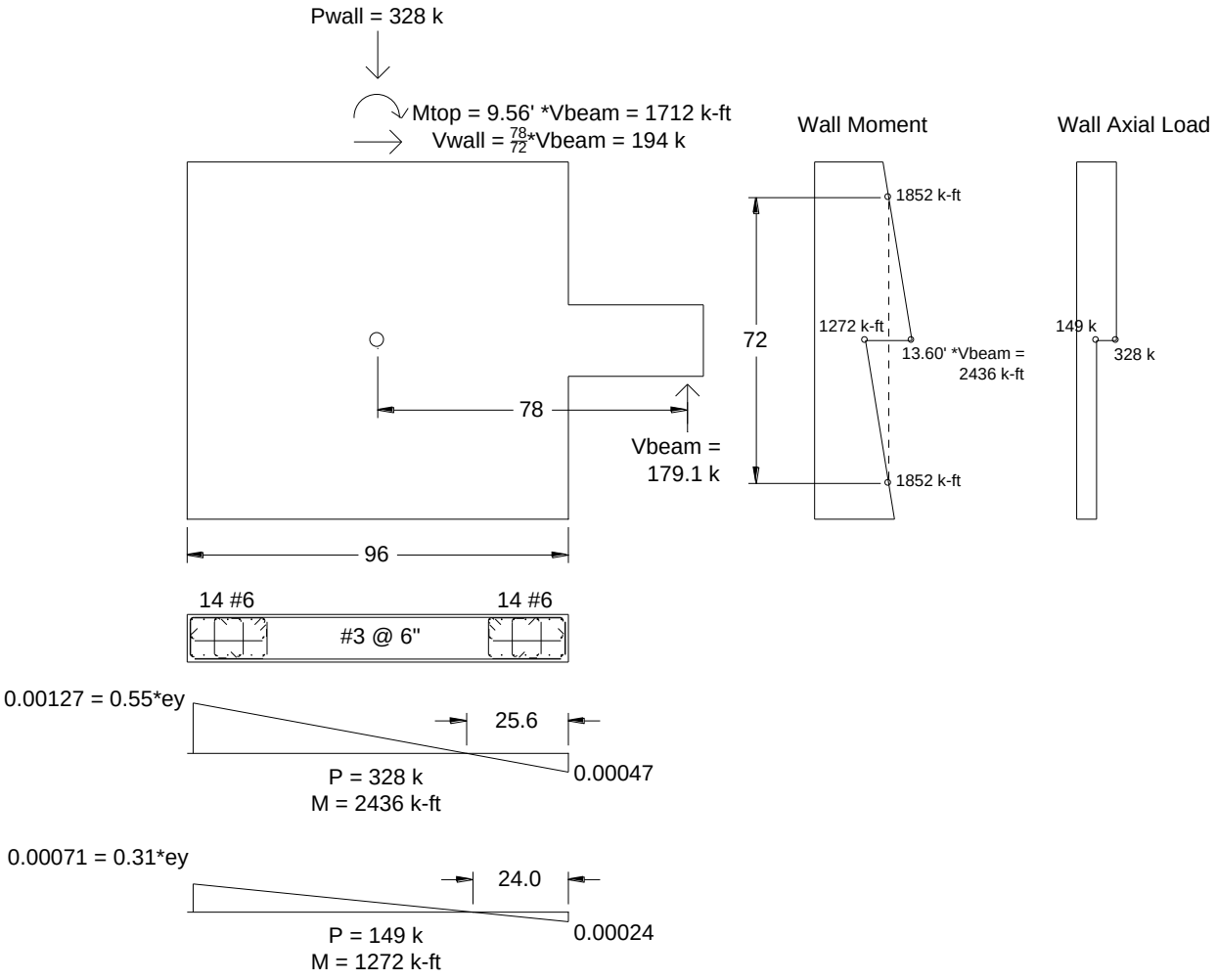

Figure 3.20. Wall Demands at $V@M_{pbe}$ for SRC-W1 in the Positive Loading Direction, with Strain Demands Determined from Moment-Curvature Analysis

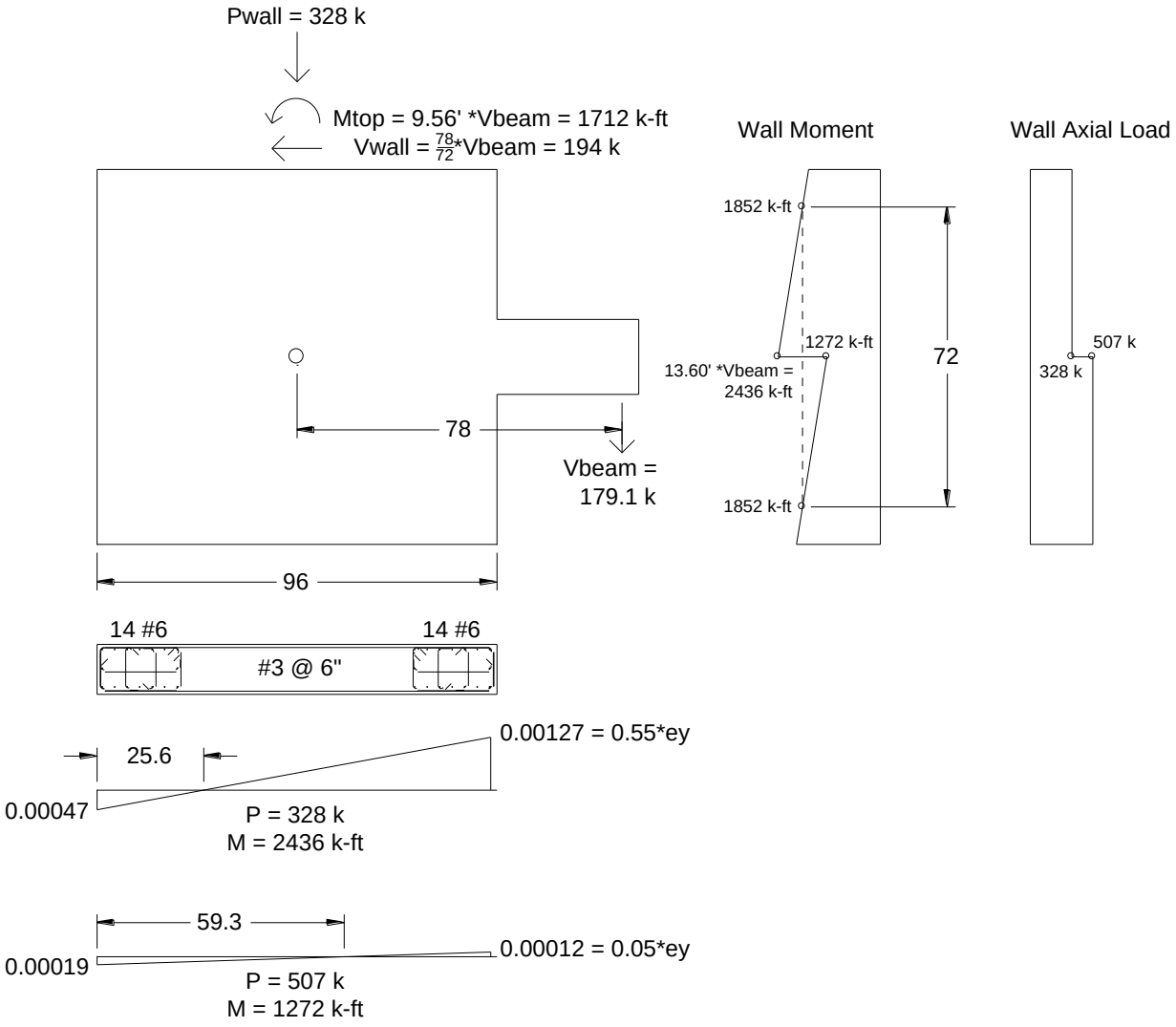

Figure 3.21. Wall Demands at $V@M_{pbe}$ for SRC-W1 in the Negative Loading Direction, with Strain Demands Determined from Moment-Curvature Analysis

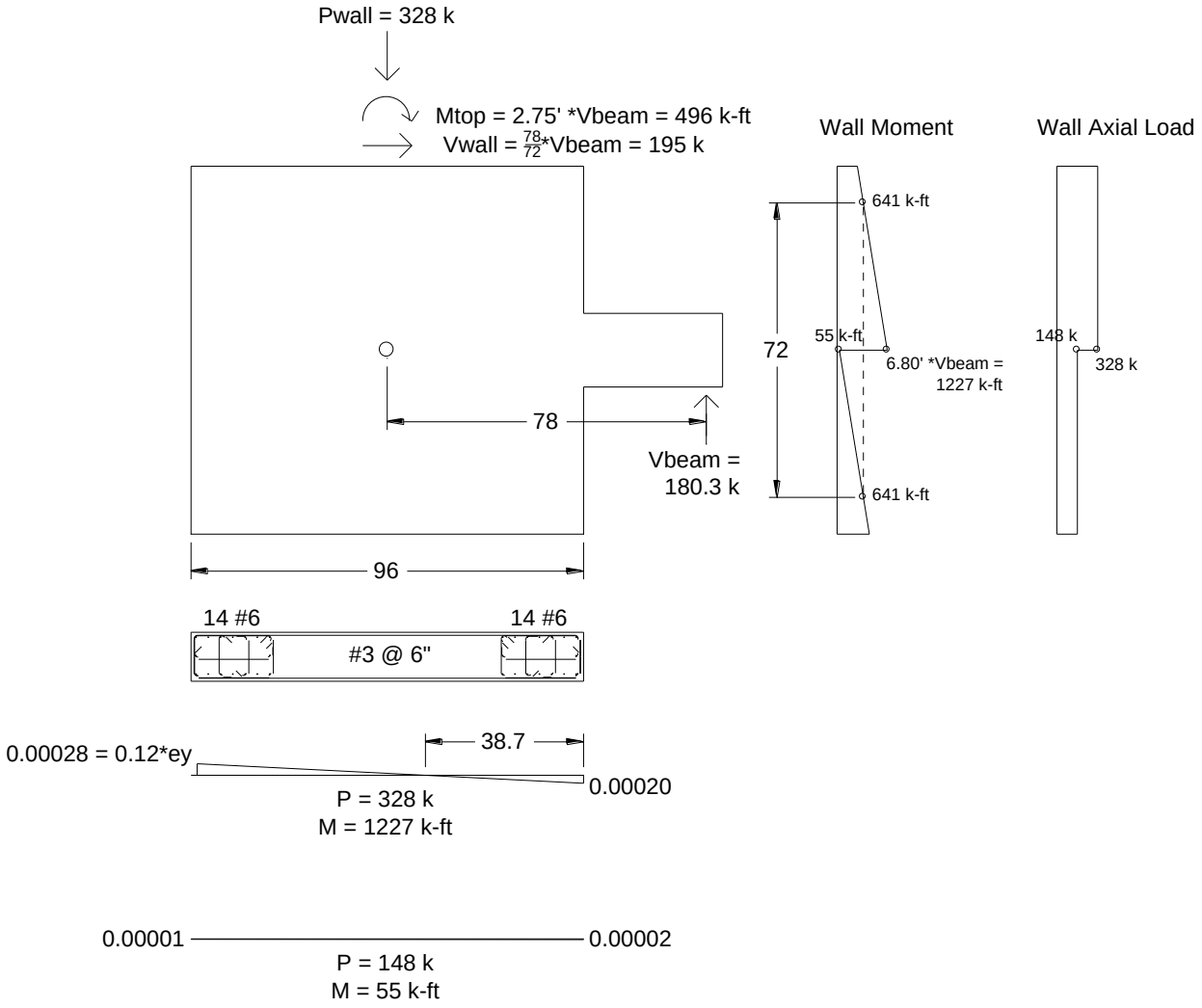

Figure 3.22. Wall Demands at $V@M_{pbe}$ for SRC-W2 in the Positive Loading Direction, with Strain Demands Determined from Moment-Curvature Analysis

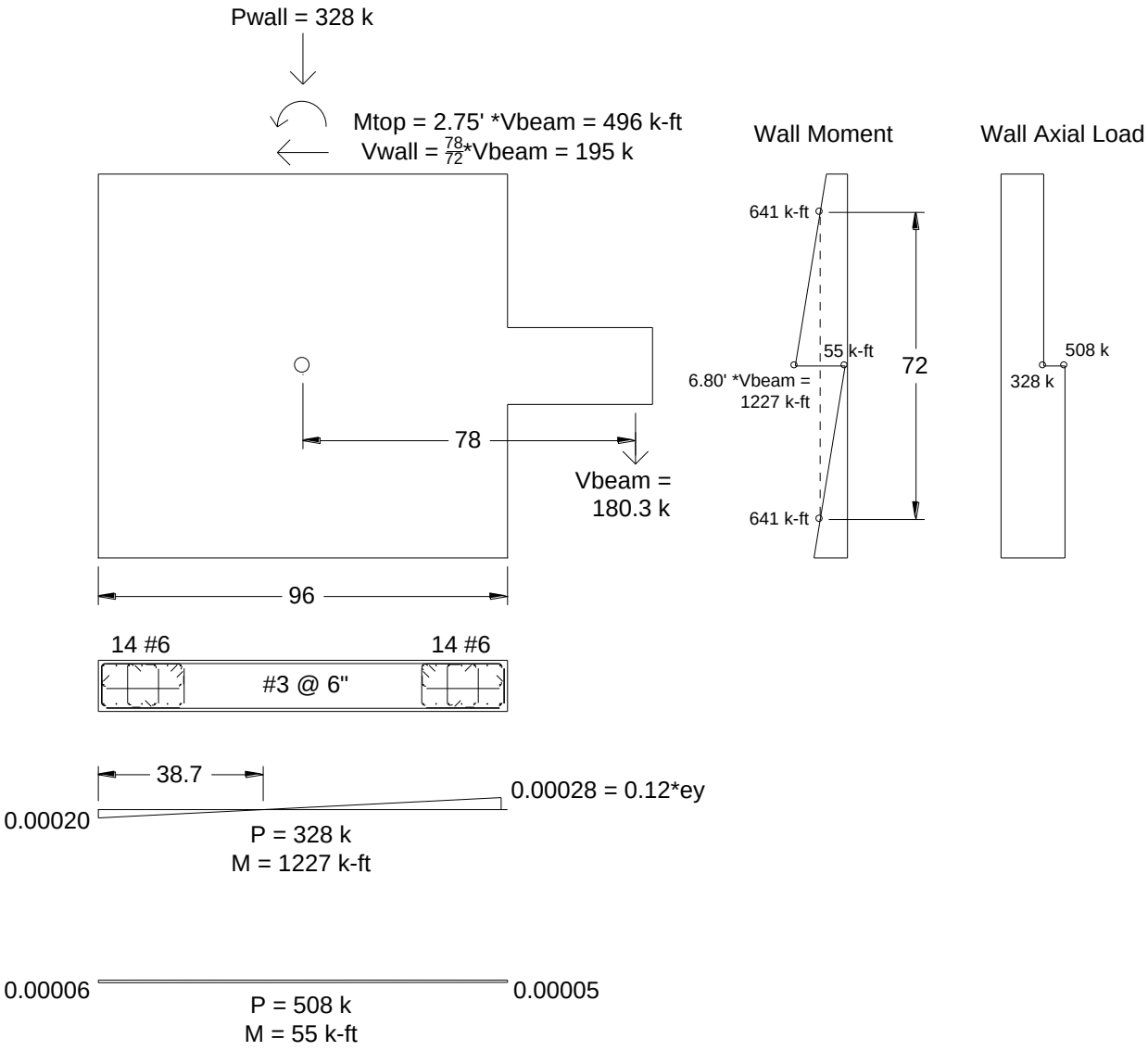

Figure 3.23. Wall Demands at $V@M_{pbe}$ for SRC-W2 in the Negative Loading Direction, with Strain Demands Determined from Moment-Curvature Analysis

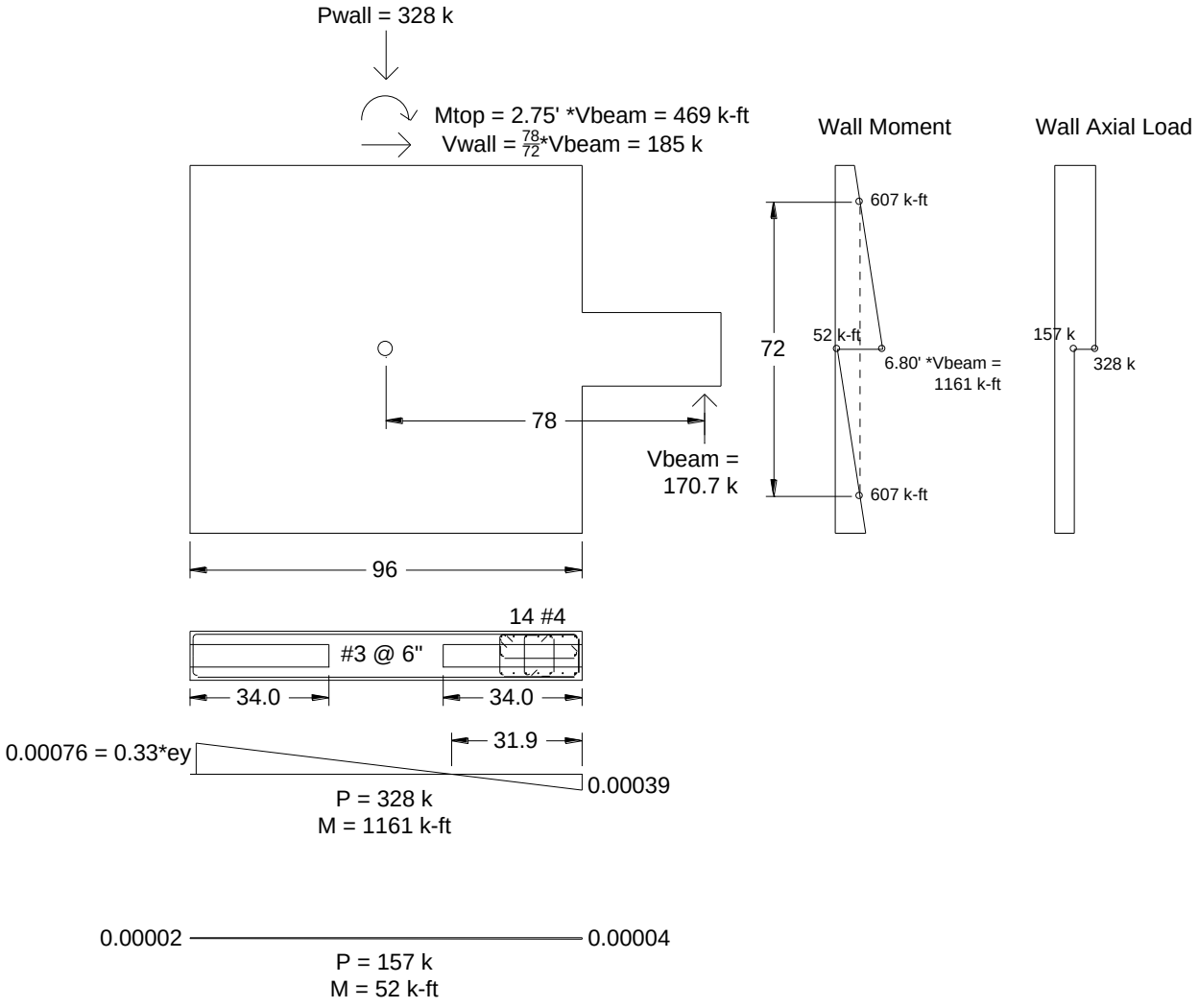

Figure 3.24. Wall Demands at $V@M_{pbe}$ for SRC-W3 in the Positive Loading Direction, with Strain Demands Determined from Moment-Curvature Analysis

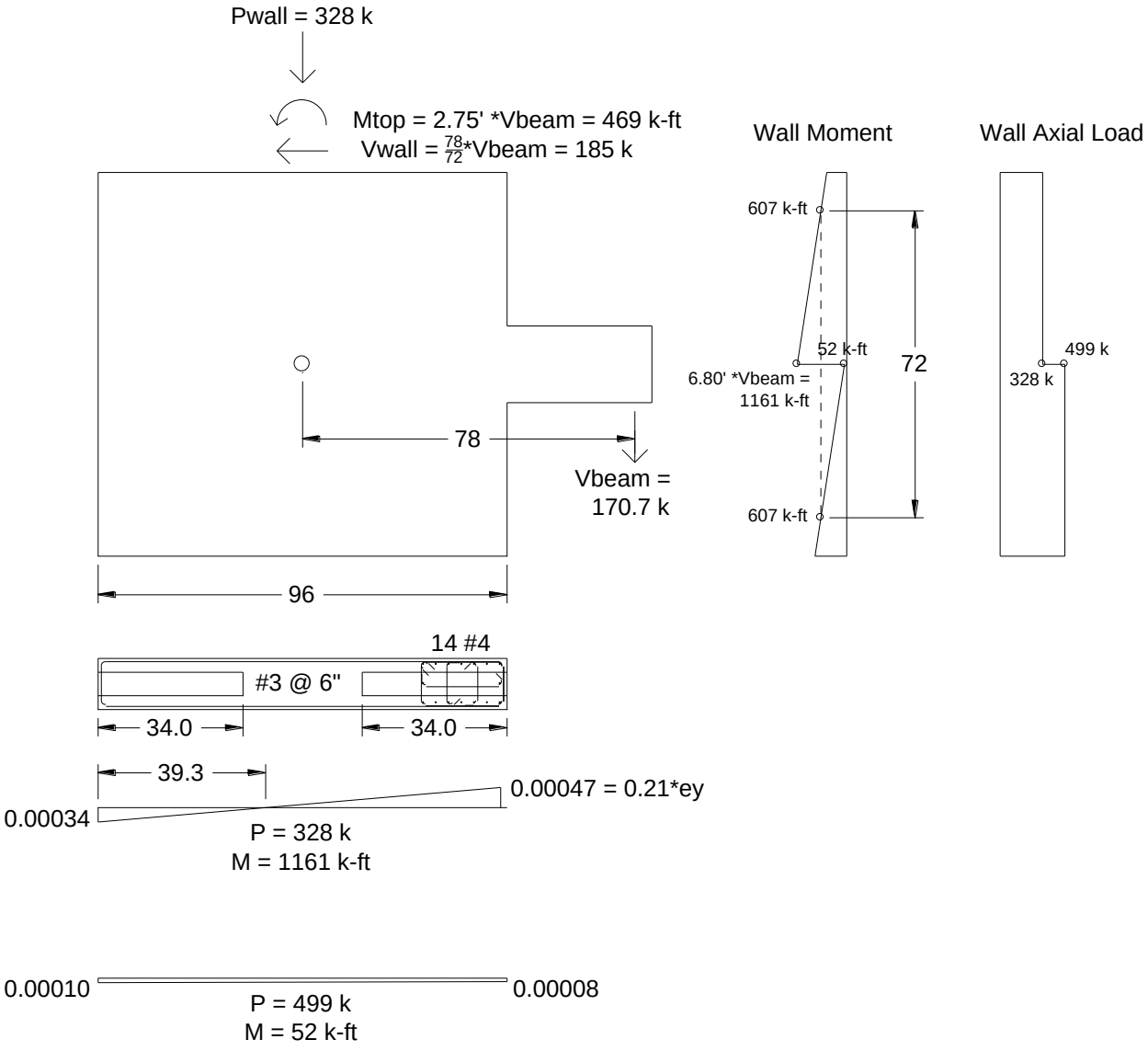

Figure 3.25. Wall Demands at $V@M_{pbe}$ for SRC-W3 in the Negative Loading Direction, with Strain Demands Determined from Moment-Curvature Analysis

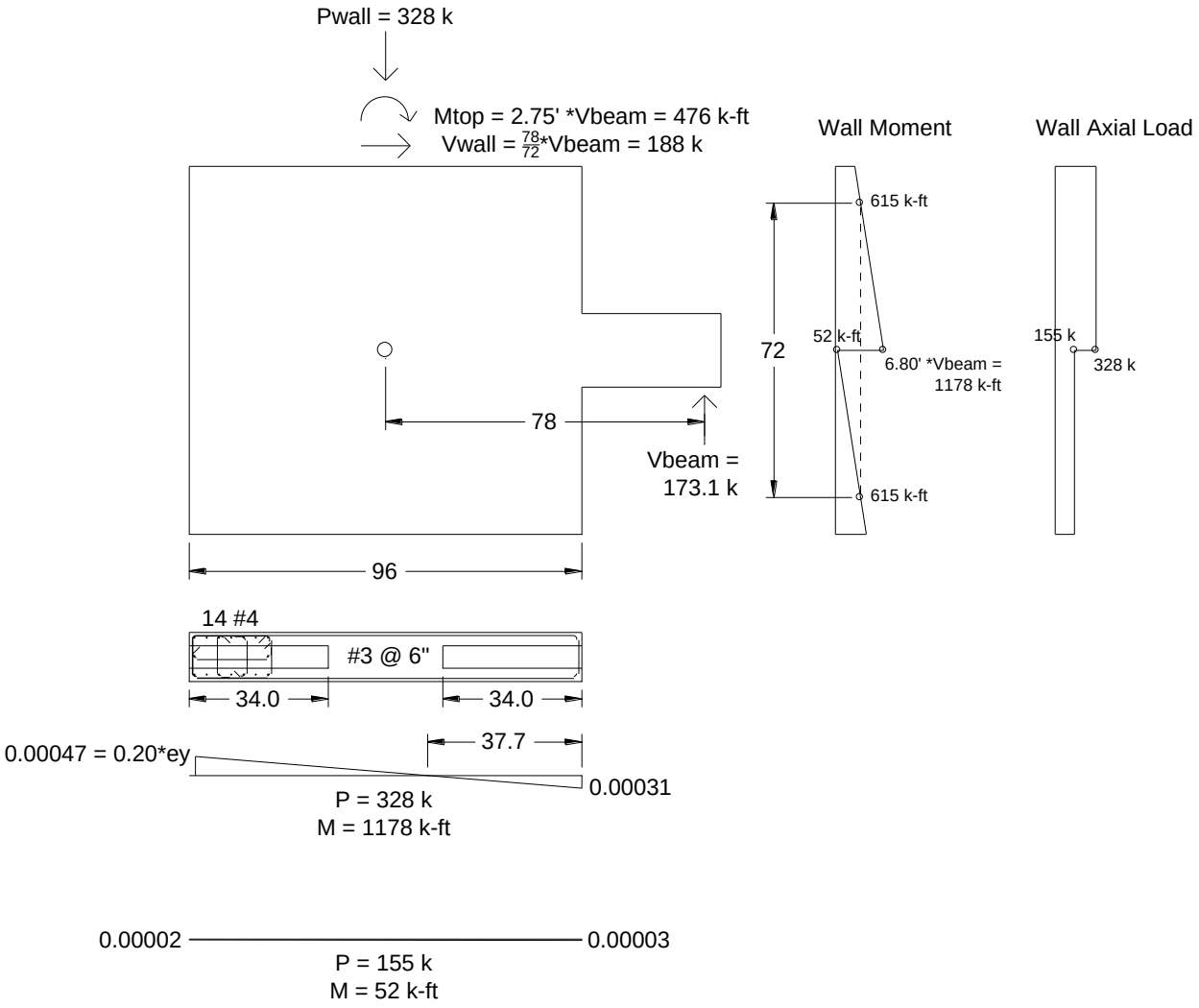

Figure 3.26. Wall Demands at $V@M_{pbe}$ for SRC-W4 in the Positive Loading Direction, with Strain Demands Determined from Moment-Curvature Analysis

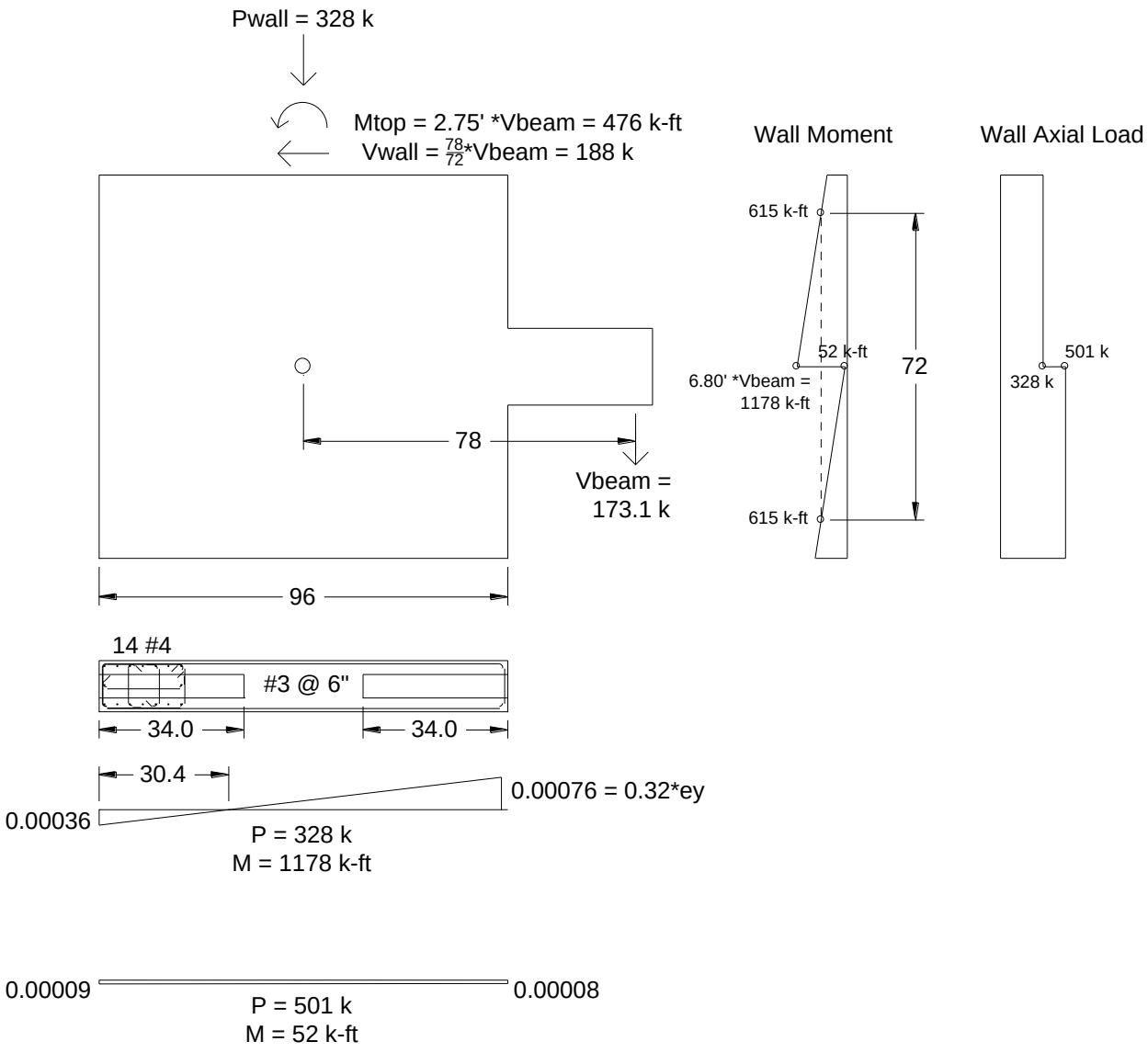

Figure 3.27. Wall Demands at $V@M_{pbe}$ for SRC-W4 in the Negative Loading Direction, with Strain Demands Determined from Moment-Curvature Analysis

SRC-W1:

At 0.15Mpbe:

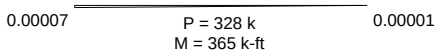

At 0.40Mpbe:

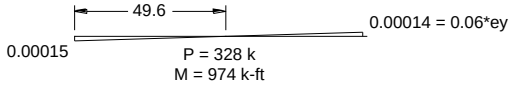

At 0.75Mpbe:

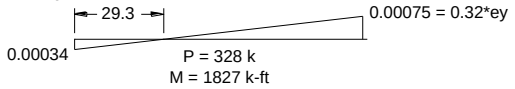

At Mpbe:

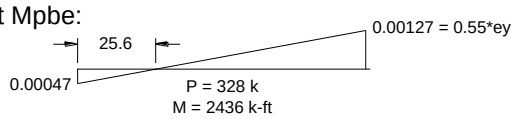

SRC-W2:

At 0.15Mpbe:

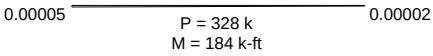

At 0.40Mpbe:

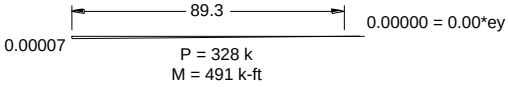

At 0.75Mpbe:

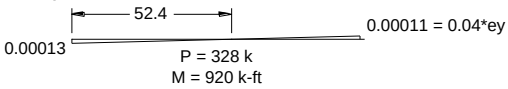

At Mpbe:

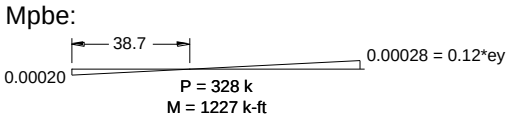

SRC-W3:

At 0.15Mpbe:

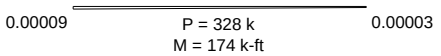

At 0.40Mpbe:

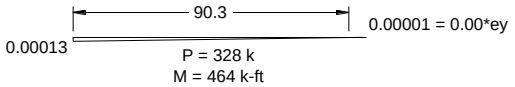

At 0.75Mpbe:

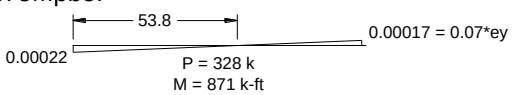

At Mpbe:

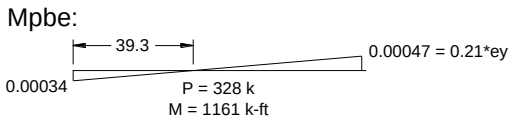

SRC-W4:

At 0.15Mpbe:

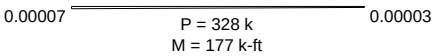

At 0.40Mpbe:

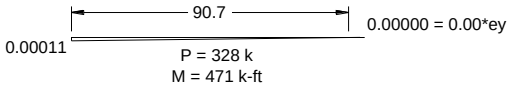

At 0.75Mpbe:

At Mpbe:

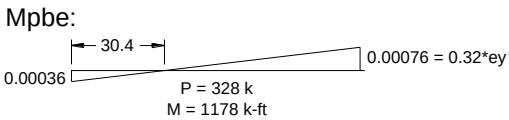

Figure 3.28. Wall Demands, Excluding Coupling Beam Demands, at Location of Coupling Beam, Determined from Moment-Curvature Analysis

4. Test Results

4.1. Observed Damage

Damage photos are provided in Figure 4.1 through Figure 4.4 for the beams and Figure 4.5 through Figure 4.8 for the wall. These photos were taken at zero rotation following completion of the cycle indicated on the figures. First and last cycles in each cycle group are shown for the beams, and the first cycle in each group is shown for the walls. Additional increments are shown for SRC-W4, which did not reach $0.75M_{pbe}$. After the cycles at $1.5\theta_y$ for SRC-W2, a brace to mitigate torsion and out-of-plane translation in the test beam was installed, as described in Section 3.5, and this changed the vantage point of the provided photos for subsequent cycles. Between loading cycles during testing, cracks were marked, and those 0.2 millimeters or larger were measured. For SRC-W1 and SRC-W3, cracks in the positive loading direction were marked in black, and cracks in the negative loading direction were marked in red. For SRC-W2 and SRC-W4, cracks in the positive loading direction were marked in blue, and cracks in the negative loading direction were marked in green. Locations and measured widths of cracks that were 0.2 millimeters or larger are provided in Figure 4.9 through Figure 4.13 and Table 4.1 through Table 4.5, respectively. Beam crack widths were reported as the largest values measured at the top and bottom beam surfaces, reported as “End”, and at the face, reported as “Face”. Wall crack widths were reported as the largest values measured at the end surface of the wall, reported as “End”, and at the face, reported as “Face”.

For SRC-W1, SRC-W2, and SRC-W3, damage concentrated at the beam-wall interface. This was the only location with concrete spalling, with minimal damage in the beam span. For SRC-W1, the crack across the beam-wall interface was the only crack to exceed 2.0 millimeters and was measured as 19 millimeters for cycles at $3.0\theta_y$. For SRC-W3, this was the only crack to exceed 1.0 millimeter and reached a maximum of 25 millimeters in the positive loading direction and 27 millimeters in the negative loading direction for cycles at $3.0\theta_y$. For SRC-W1 and SRC-W2, the next largest cracks formed horizontally along the flanges of the steel section. For SRC-W1, the lower crack reached 0.35 millimeters and the top crack reached 1.0 millimeter for cycles at $3.0\theta_y$. For SRC-W2, these cracks were measured as nearly 2.0 millimeters at upper flange locations. For SRC-W3, vertical cracks formed along the beam flanges during the first group of cycles at $0.75M_{pbe}$ and remained less than 0.3 millimeters throughout the test. For SRC-W1, wall cracks differed for positive and negative loading. Positive loading resulted in extensive cracks on the side of the wall opposite the test beam. Negative loading resulted in diagonal shear cracks extending to the top of the wall on the side of the wall with the test beam, while there were limited cracks at the base. SRC-W2 was tested after SRC-W1 with lower wall loads, and new wall cracks did not appear until the displacement-controlled cycles. However, several existing wall cracks opened earlier than observed during testing of SRC-W1. For SRC-W3, significantly more wall cracks developed in the positive loading direction than the negative loading direction. Horizontal cracks opened on the side of the wall opposite the test beam, similar to SRC-W1 but not to the same extent. As the test progressed, new cracks in the wall formed above the beam, while increases in cracks widths below the beam were more limited. Unlike SRC-W1, diagonal shear cracks were not observed in the wall during negative loading. Horizontal cracks in the embedment region near the centerline of the steel section formed during the second group of 75 cycles at $0.75M_{pbe}$. Relative to SRC1 and SRC2

tested by Motter et al (2017a), extensive ratcheting of the beams was not observed, indicating the effectiveness of the axial restraint.

Observed damage for SRC-W4 differed significantly from the other three tests, as significant wall damage was observed. For cycles at $0.15M_{pbe}$, the crack pattern for SRC-W4 was similar to the other tests, with the largest cracks forming at the beam-wall interface and smaller cracks along the flanges of the steel section forming as horizontal cracks with some vertical cracks branching from them. For cycles at $0.4M_{pbe}$, concrete spalled at the beam-wall interface and within the embedment region. The level of spalling was such that the cracks used for crack measurements were changed after the 30th cycle at $0.4M_{pbe}$, reflected by Figure 4.12 and Figure 4.13 and Table 4.4 and Table 4.5. The largest cracks formed at the beam-wall interface, with the crack width reaching more than 50 millimeters in the negative loading direction and 25 millimeters in the positive loading direction. As shown in Figure 4.4, spalling of cover concrete in the embedment region initiated and progressed significantly during the 500 cycles at $0.4M_{pbe}$, with the wall reinforcement and steel section visible. Horizontal cracks in the wall were observed above the embedment region, indicated as 3+W and 4+W in Figure 4.13 and Table 4.5. These cracks reached a maximum width of 1.5 millimeters, which occurred during the first cycle at 6.0% rotation. The damage in the wall was such that the beam did not reach $0.75M_{pbe}$. Despite the significant damage in the embedment region, buckling of wall longitudinal reinforcement was not observed.

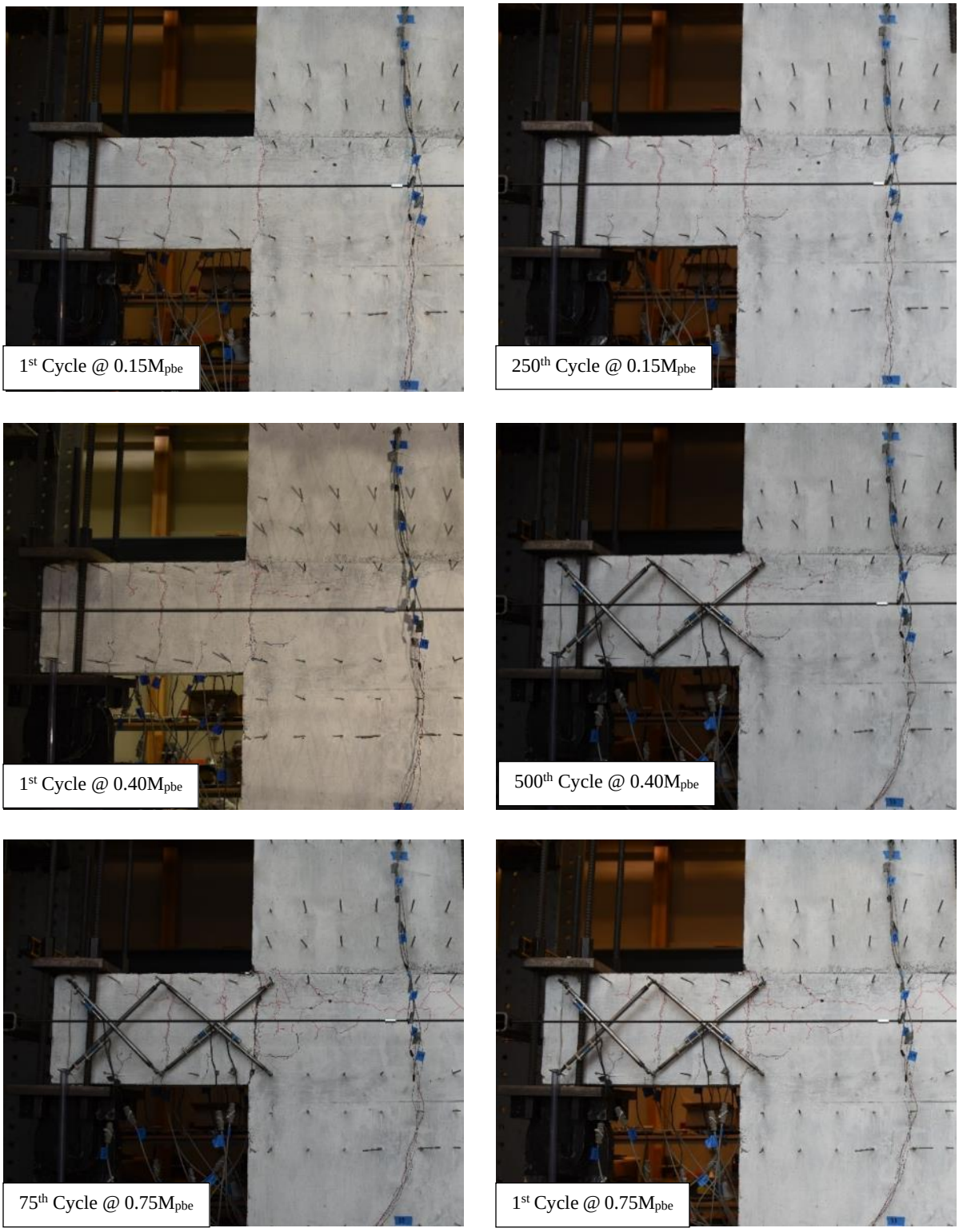

Figure 4.1. Damage Photos for SRC-W1

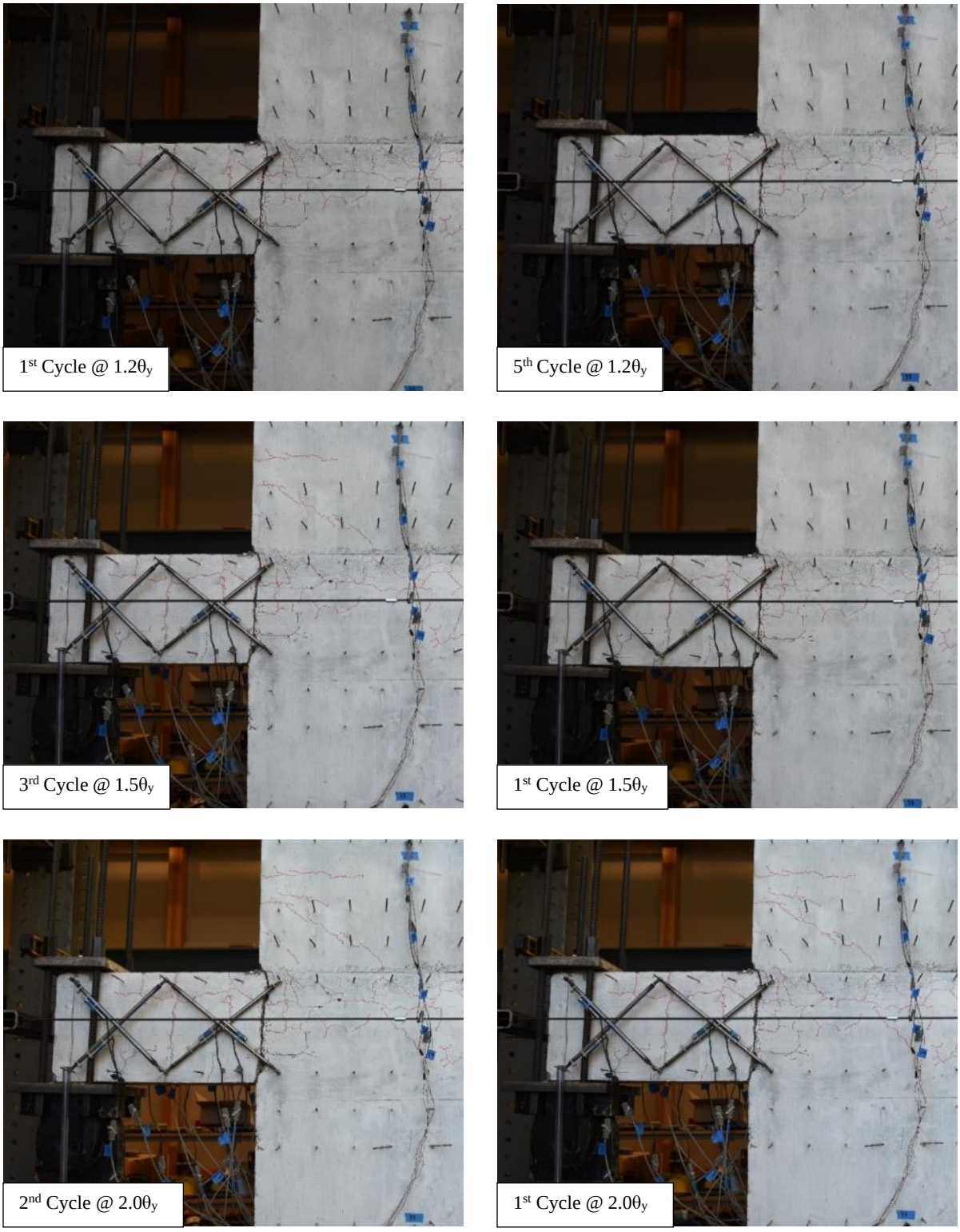

Figure 4.1. Damage Photos for SRC-W1 (continued)

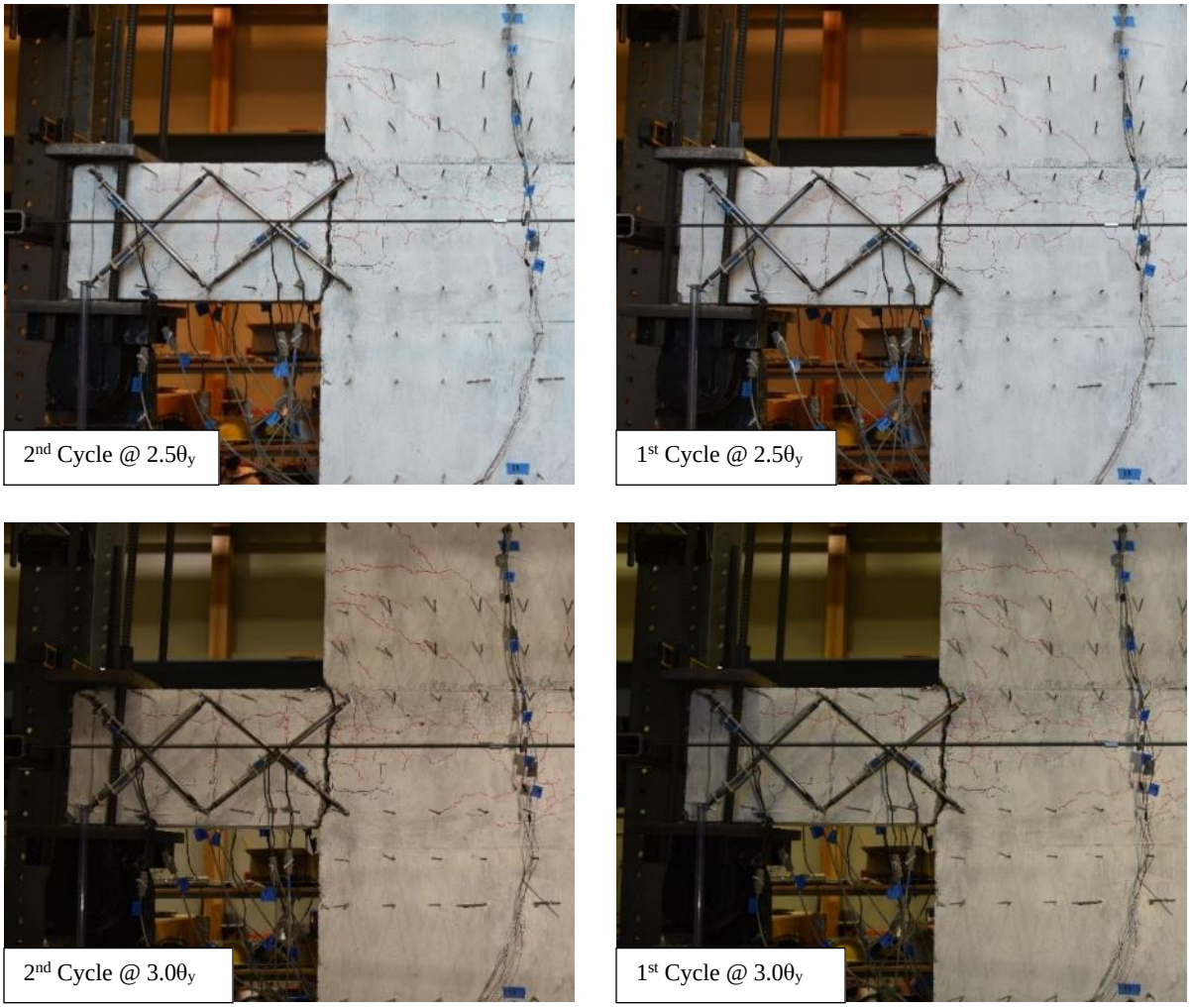

Figure 4.1. Damage Photos for SRC-W1 (continued)

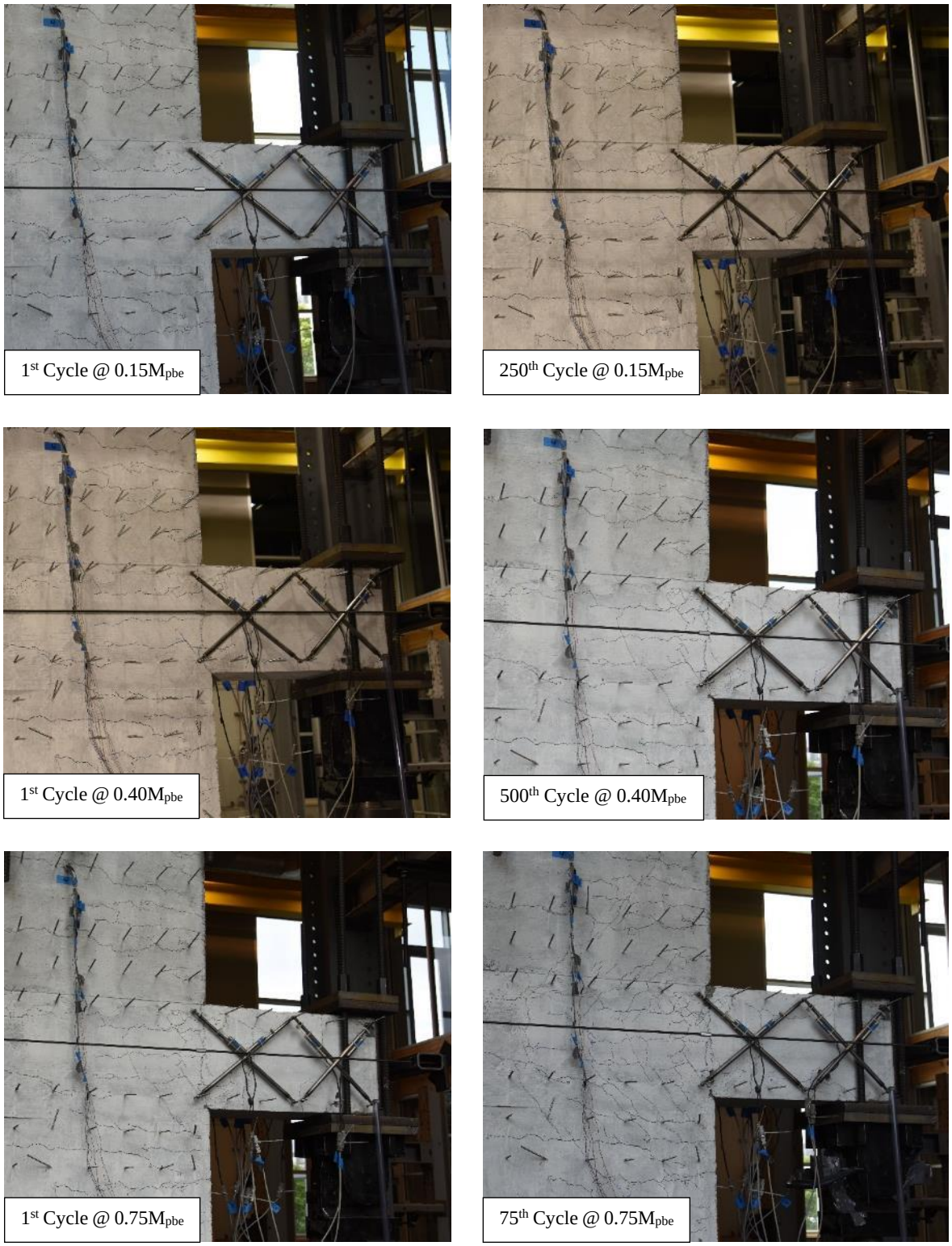

Figure 4.2. Damage Photos for SRC-W2

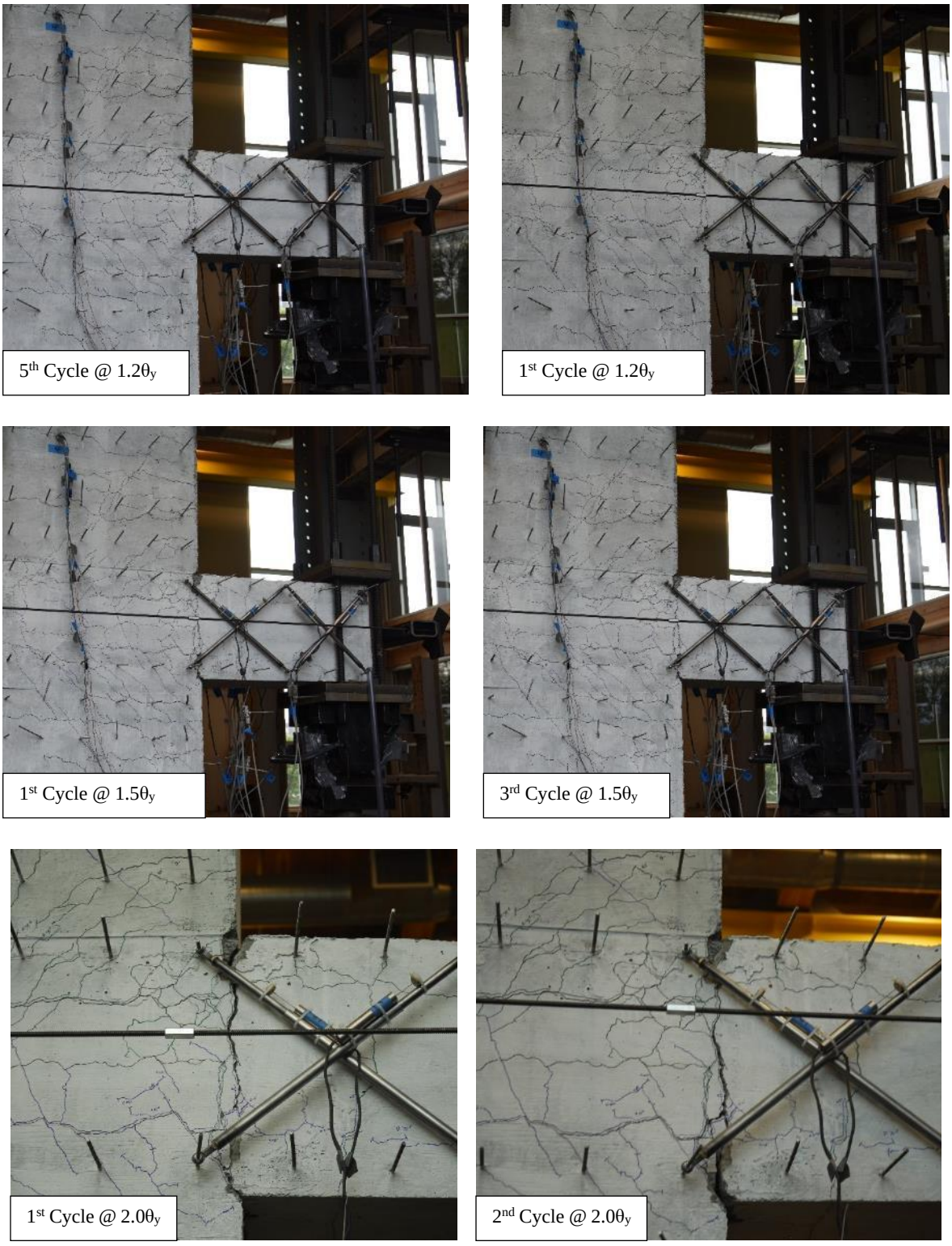

Figure 4.2. Damage Photos for SRC-W2 (continued)

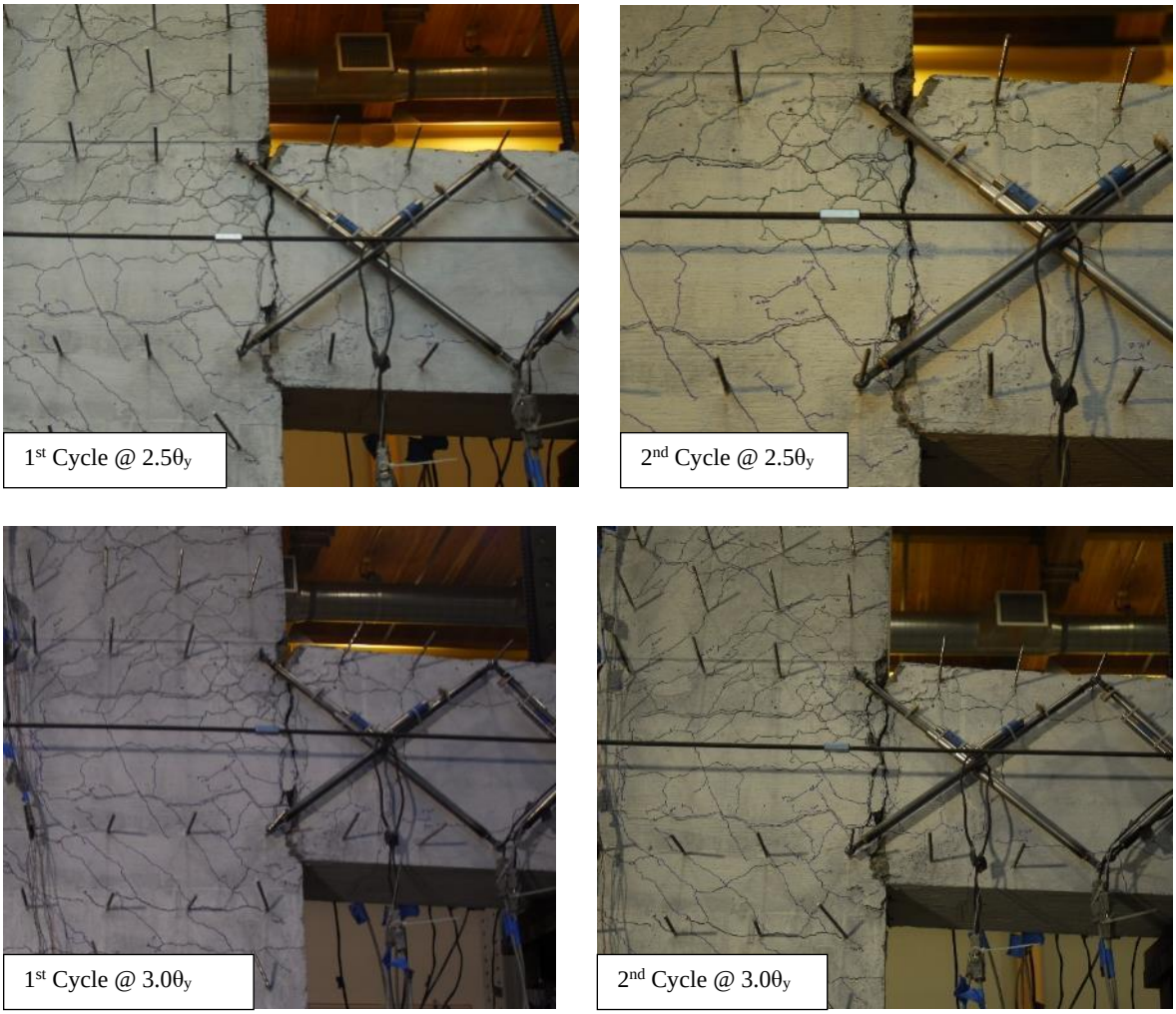

Figure 4.2. Damage Photos for SRC-W2 (continued)

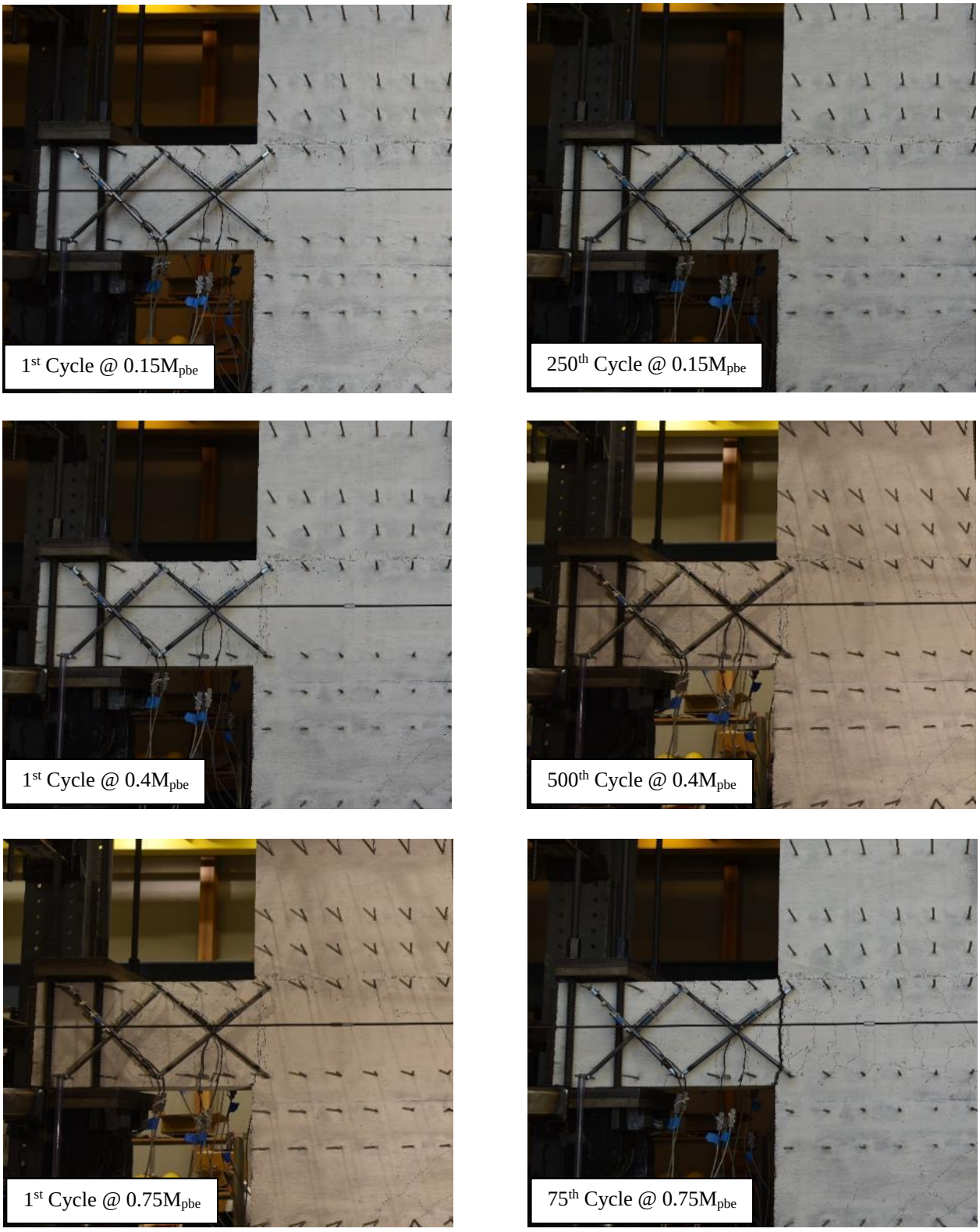

Figure 4.3. Damage Photos for SRC-W3

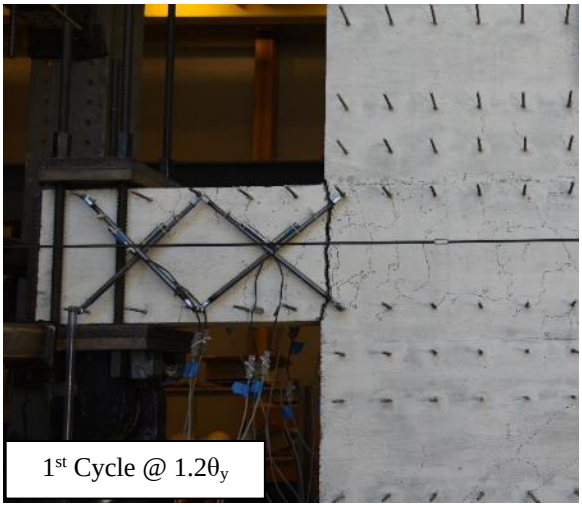

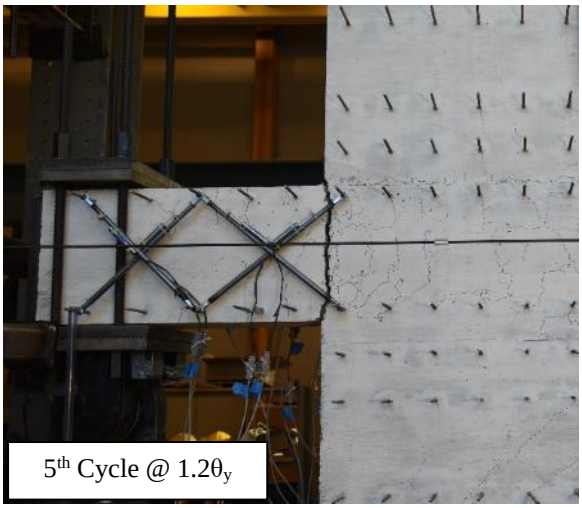

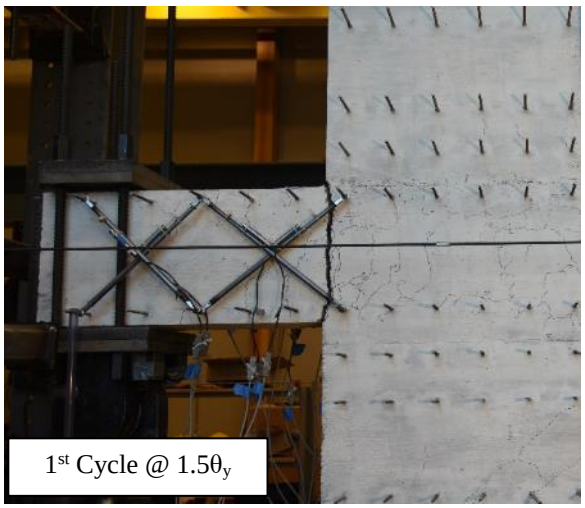

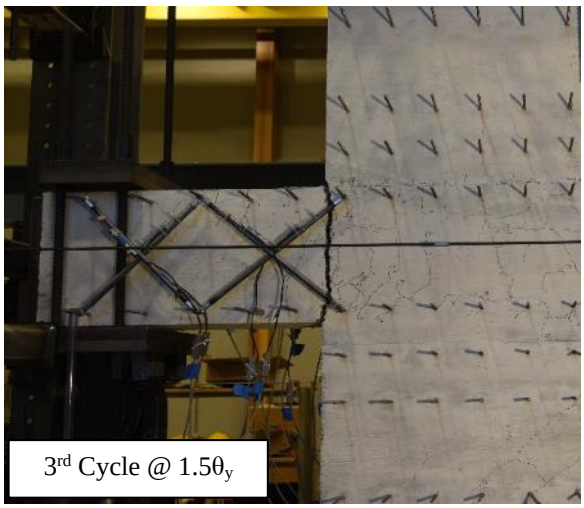

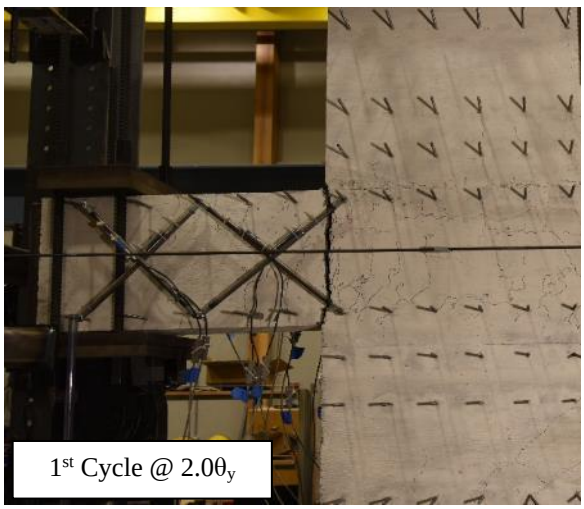

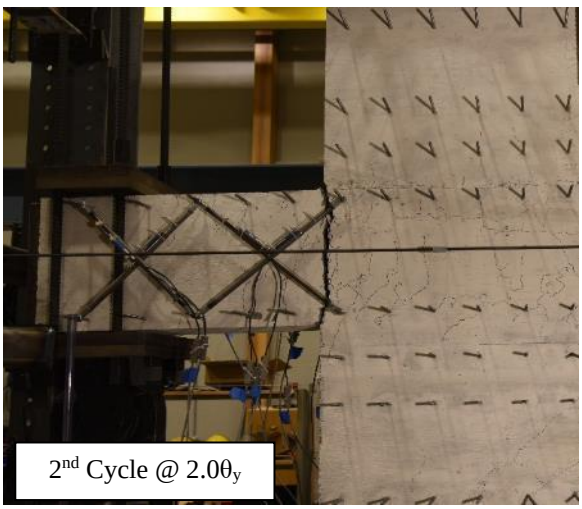

Figure 4.3. Damage Photos for SRC-W3 (continued)

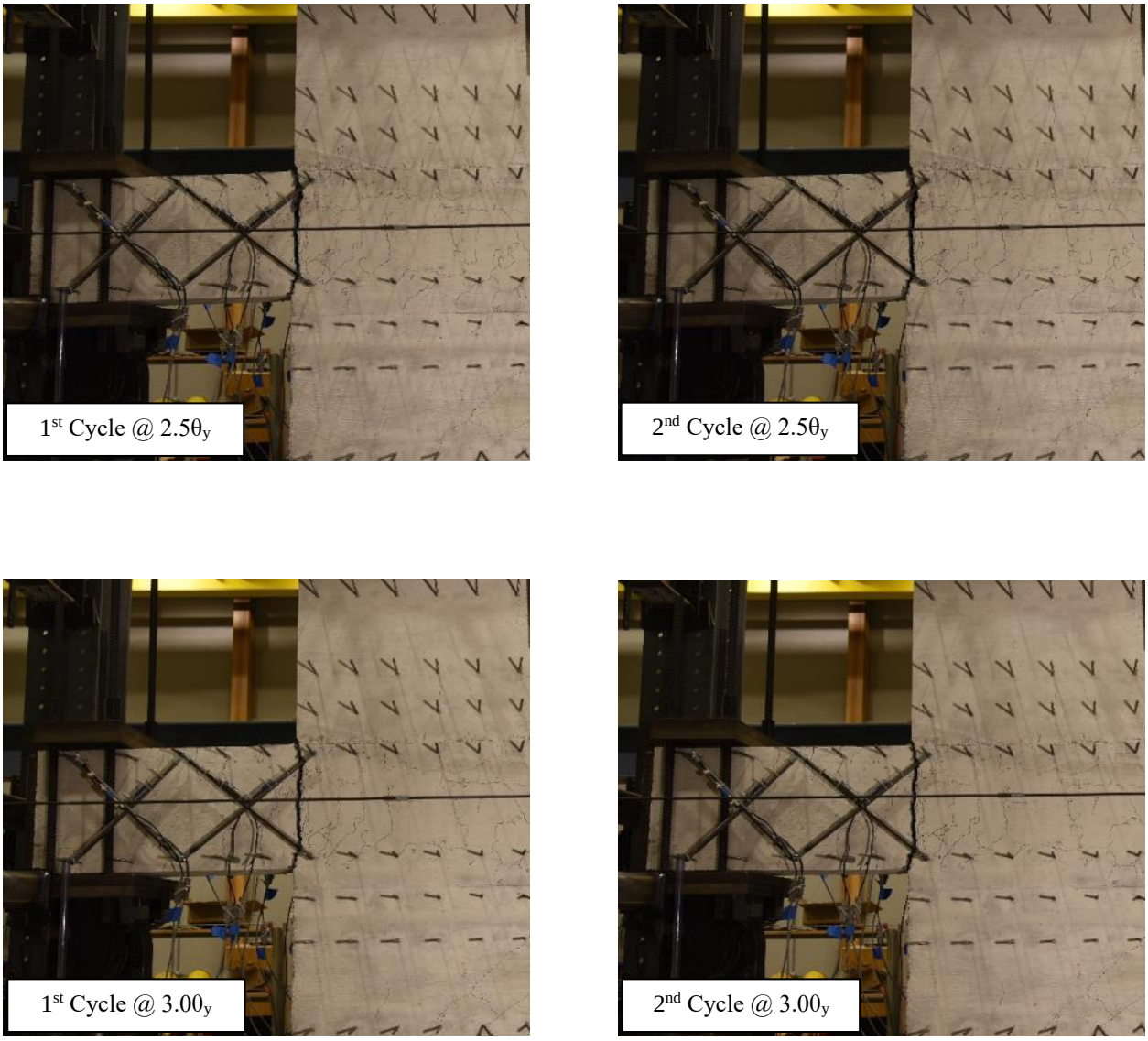

Figure 4.3. Damage Photos for SRC-W3 (continued)

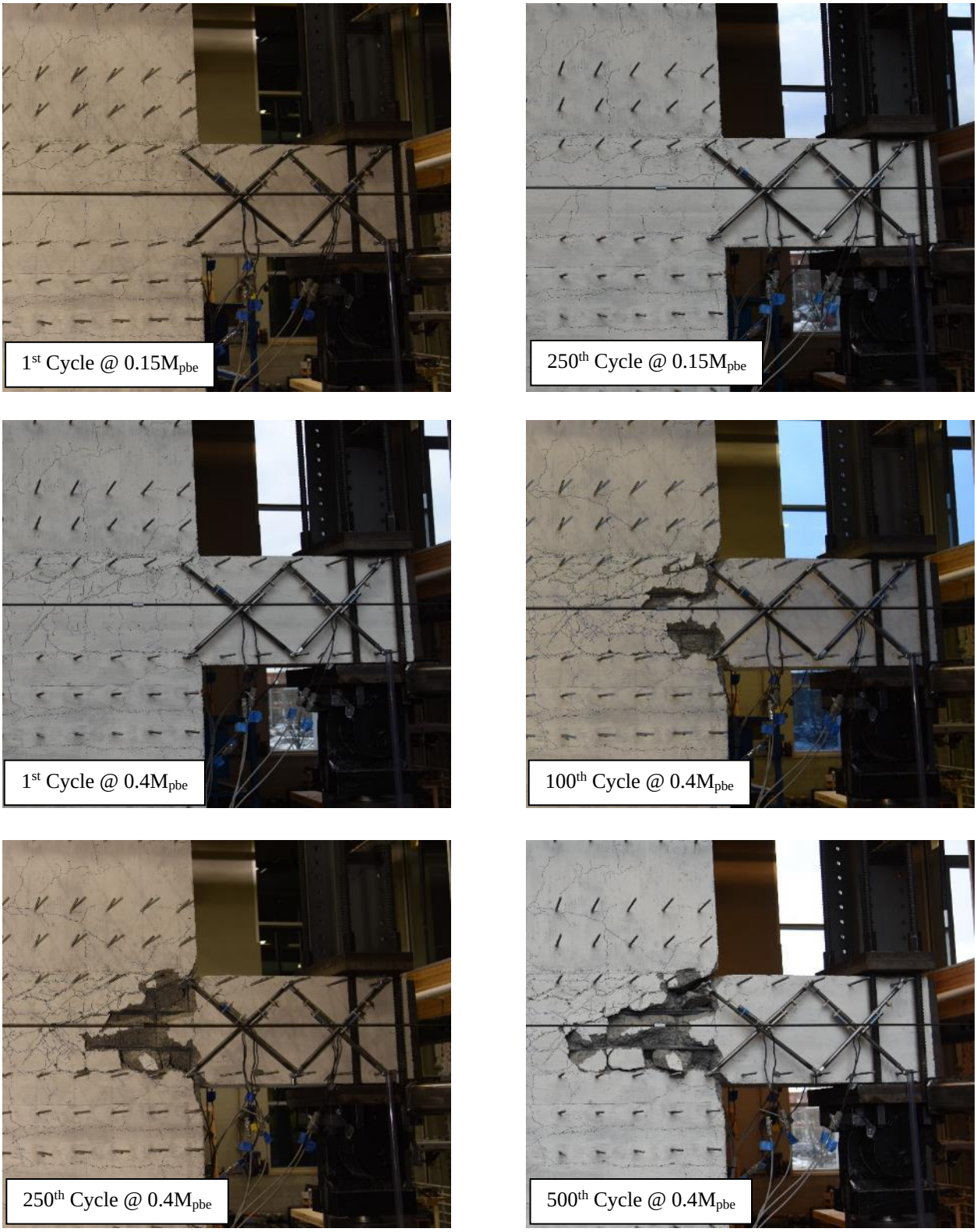

Figure 4.4. Damage Photos for SRC-W4

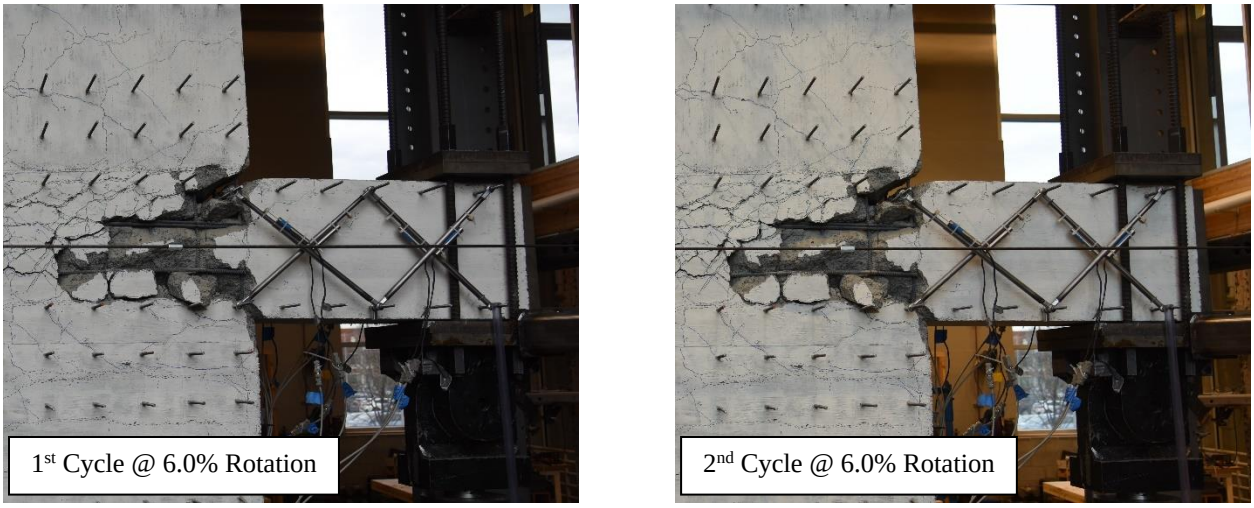

Figure 4.4. Damage Photos for SRC-W4 (continued)

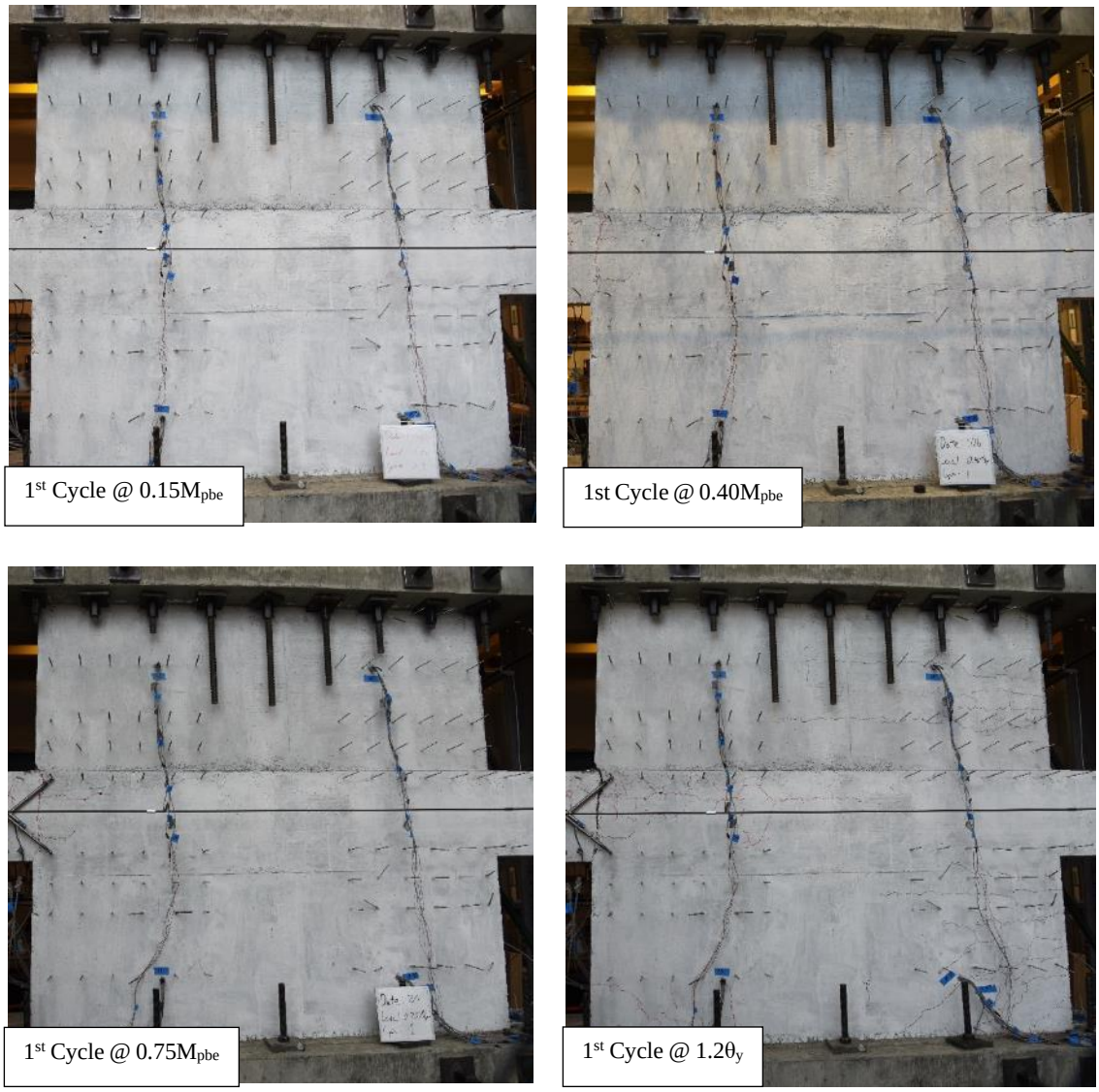

Figure 4.5. Wall Damage Photos for SRC-W1

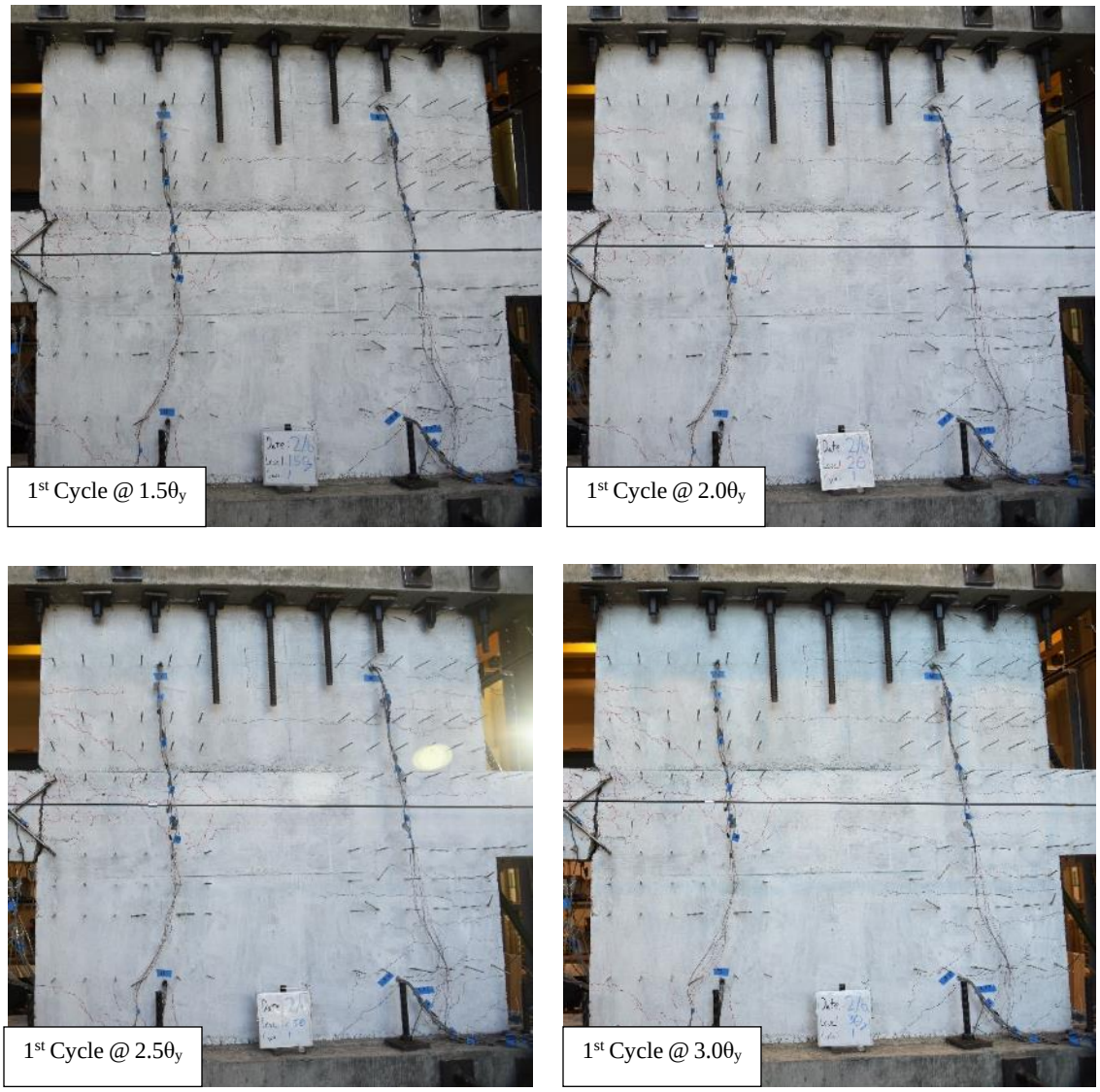

Figure 4.5. Wall Damage Photos for SRC-W1 (continued)

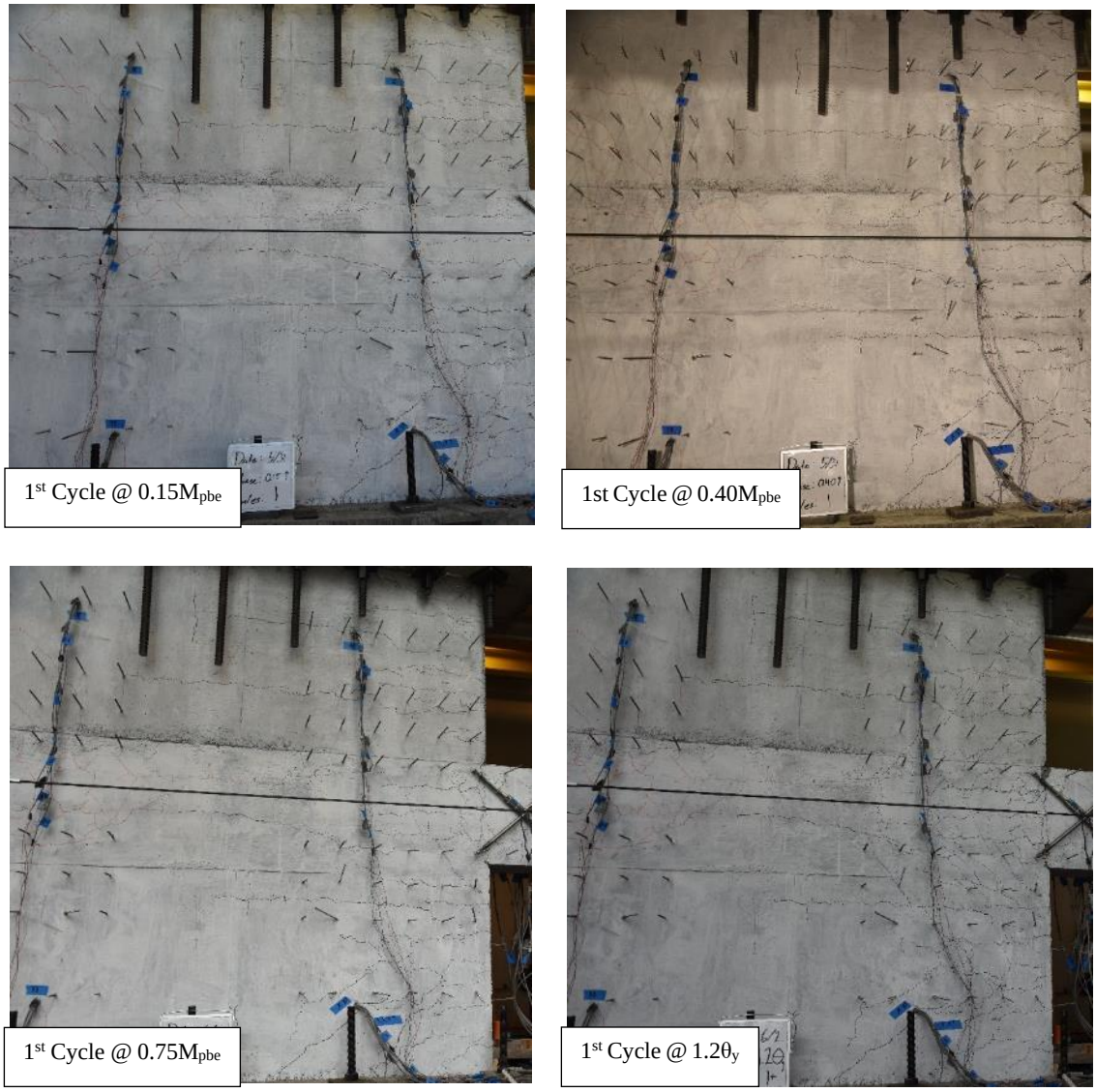

Figure 4.6. Wall Damage Photos for SRC-W2

Figure 4.6. Wall Damage Photos for SRC-W2 (continued)

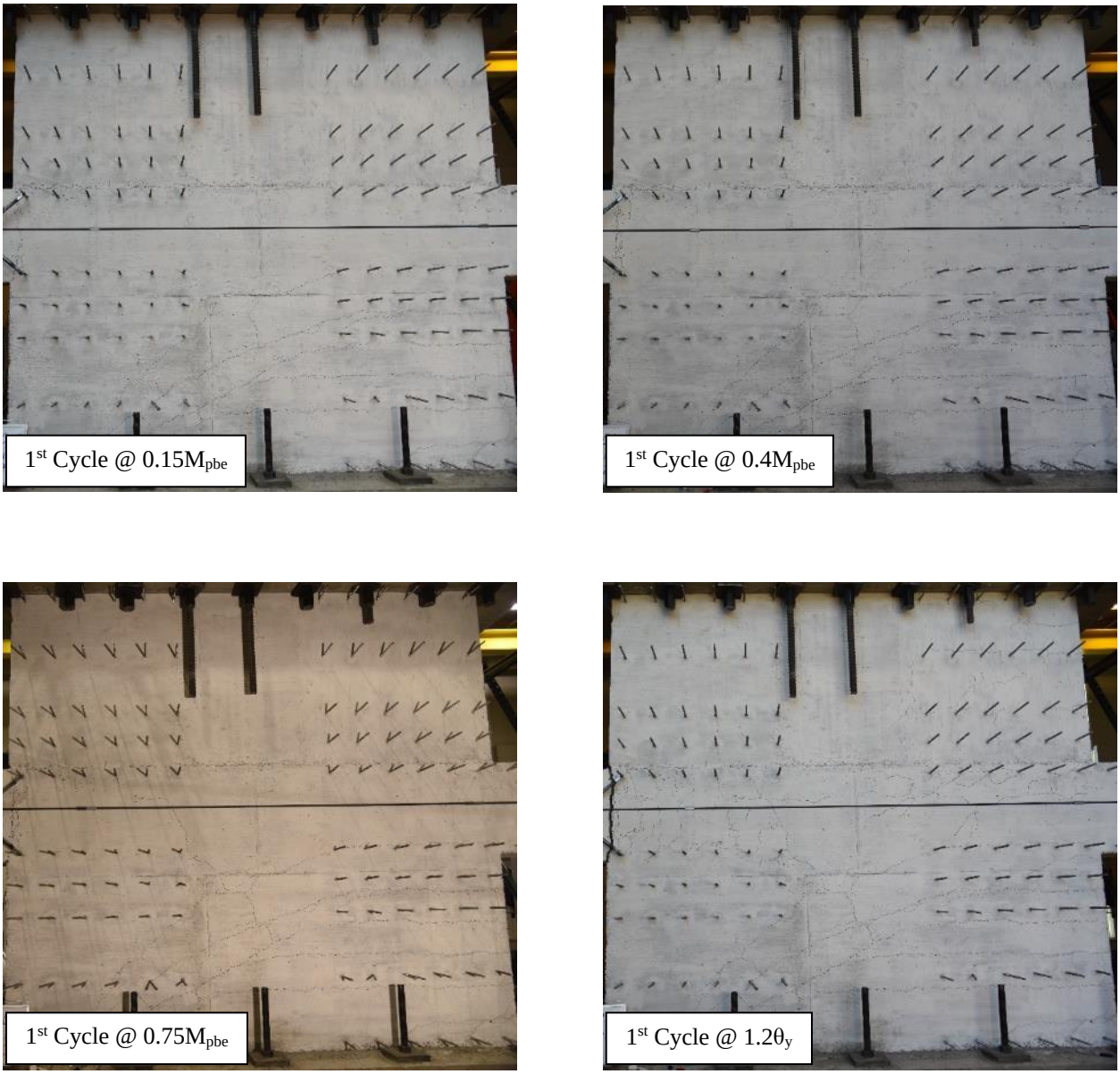

Figure 4.7. Wall Damage Photos for SRC-W3

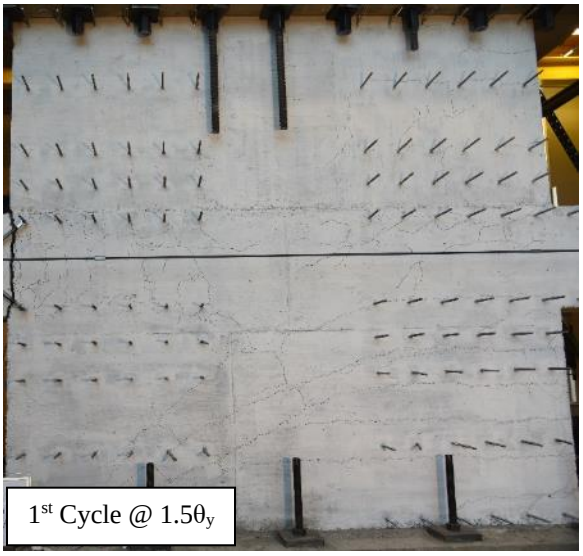

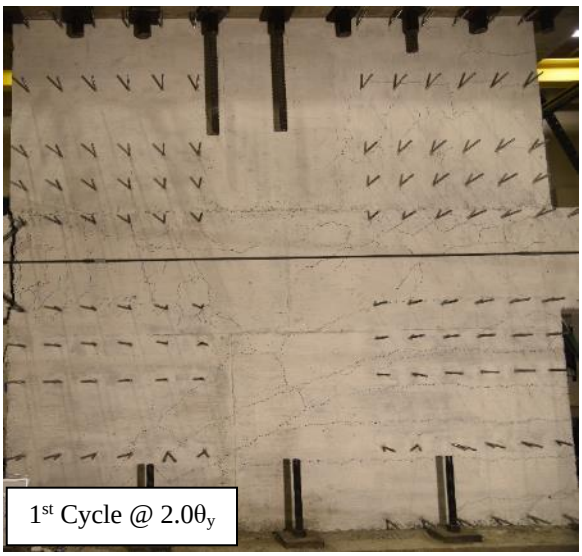

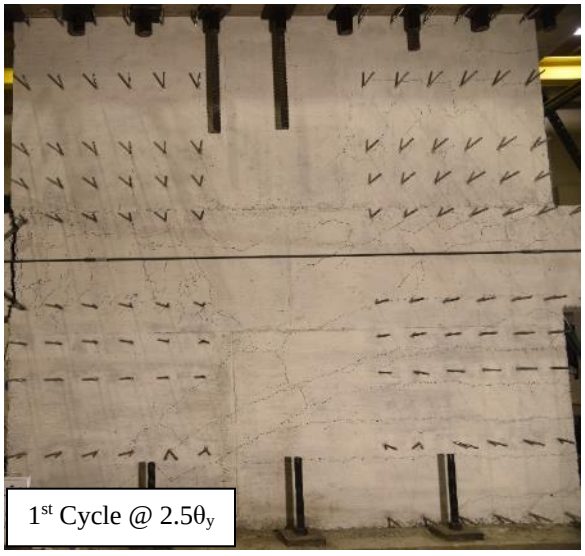

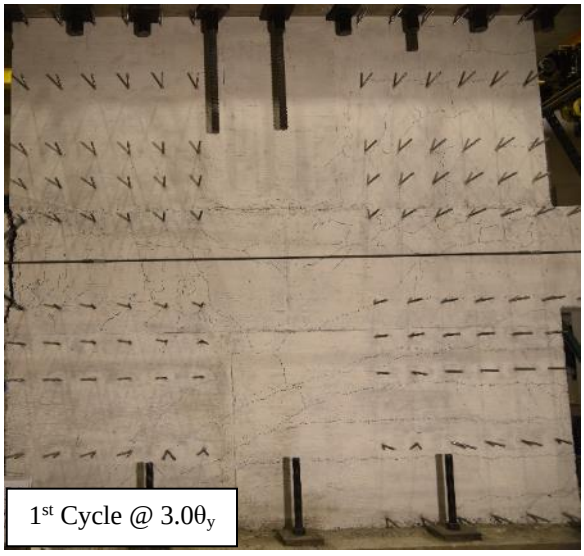

Figure 4.7. Wall Damage Photos for SRC-W3 (continued)

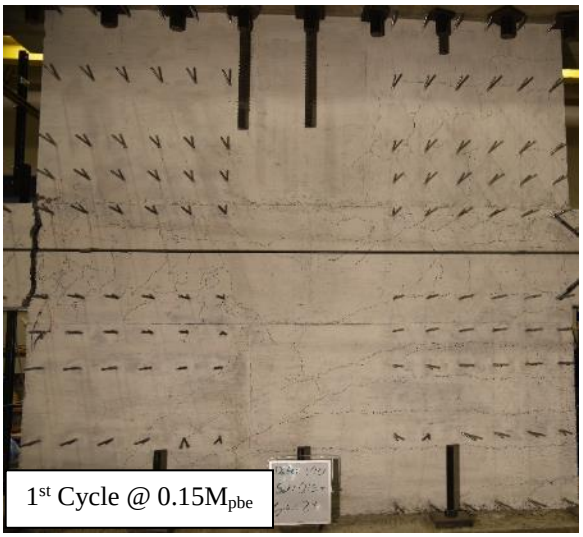

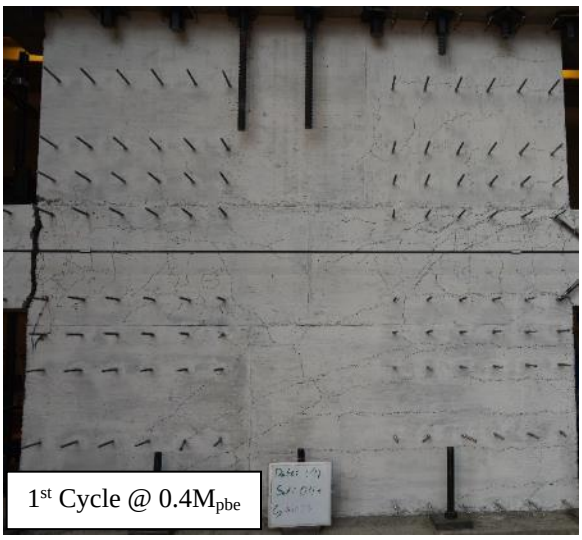

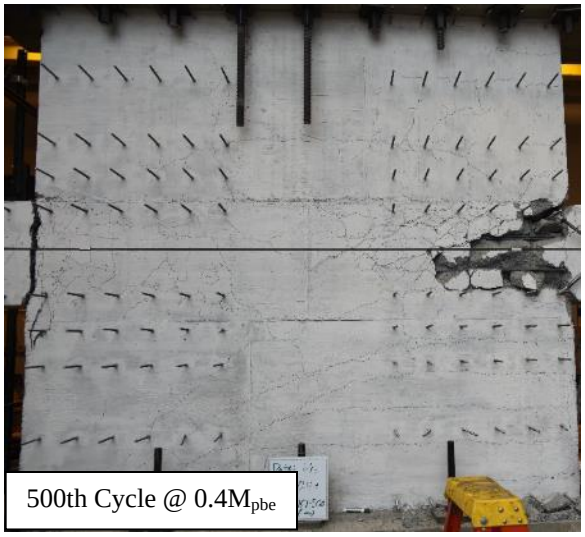

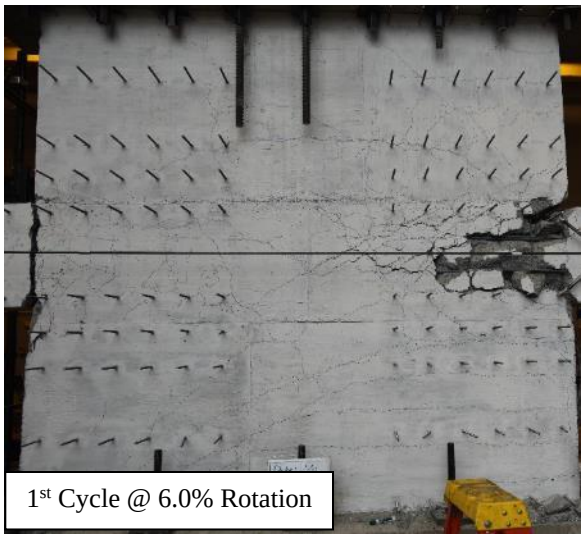

Figure 4.8. Wall Damage Photos for SRC-W4

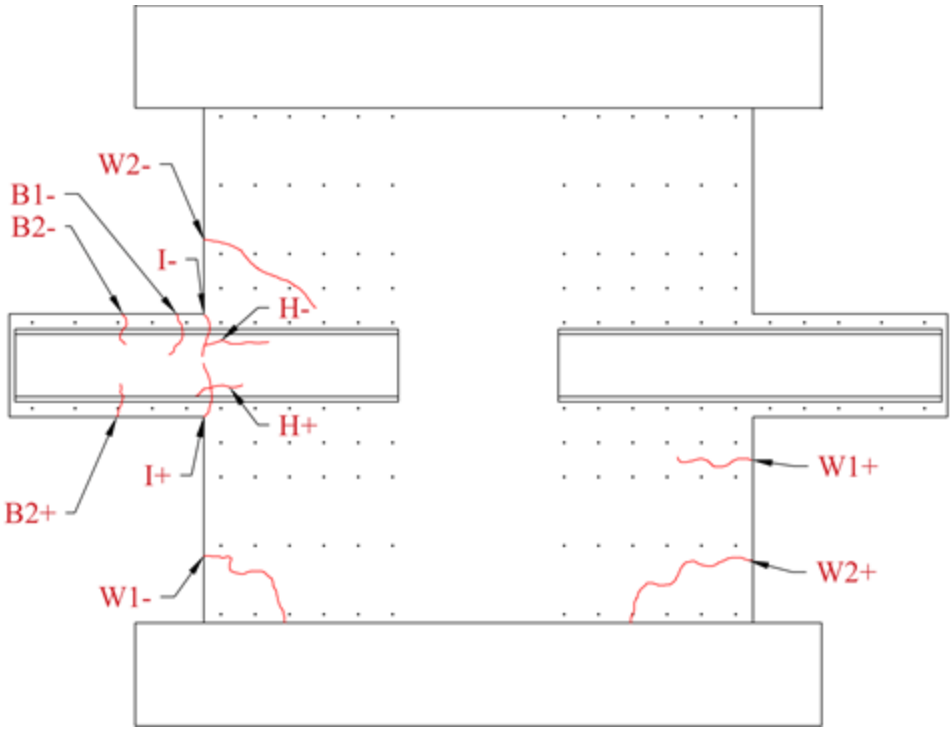

Figure 4.9. Location of Cracks 0.2 Millimeters or Larger for SRC-W1

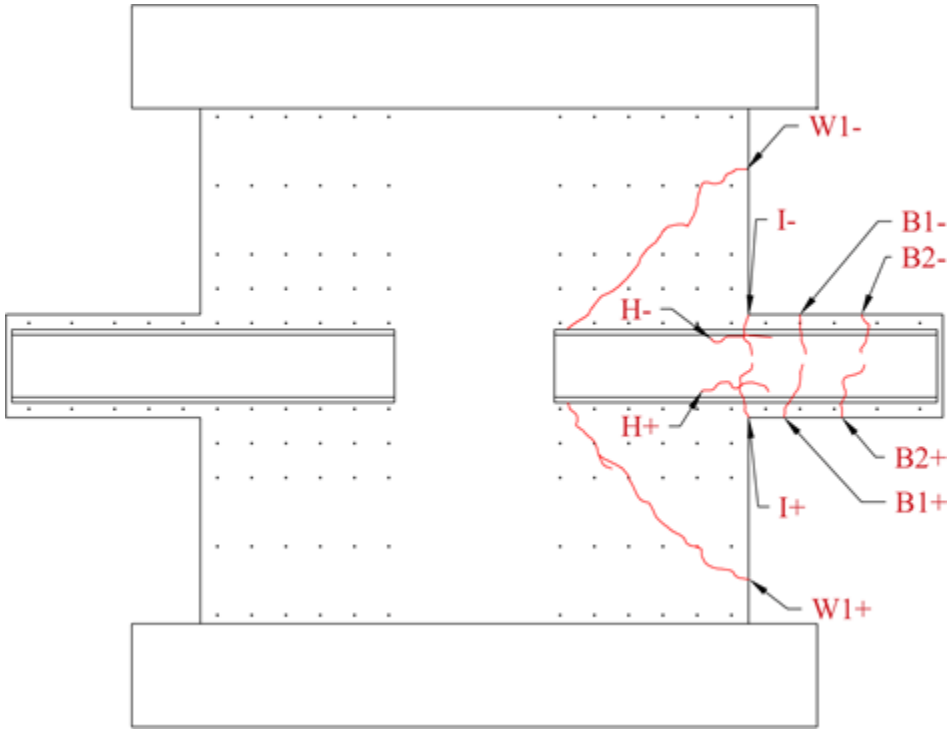

Figure 4.10. Location of Cracks 0.2 Millimeters or Larger for SRC-W2

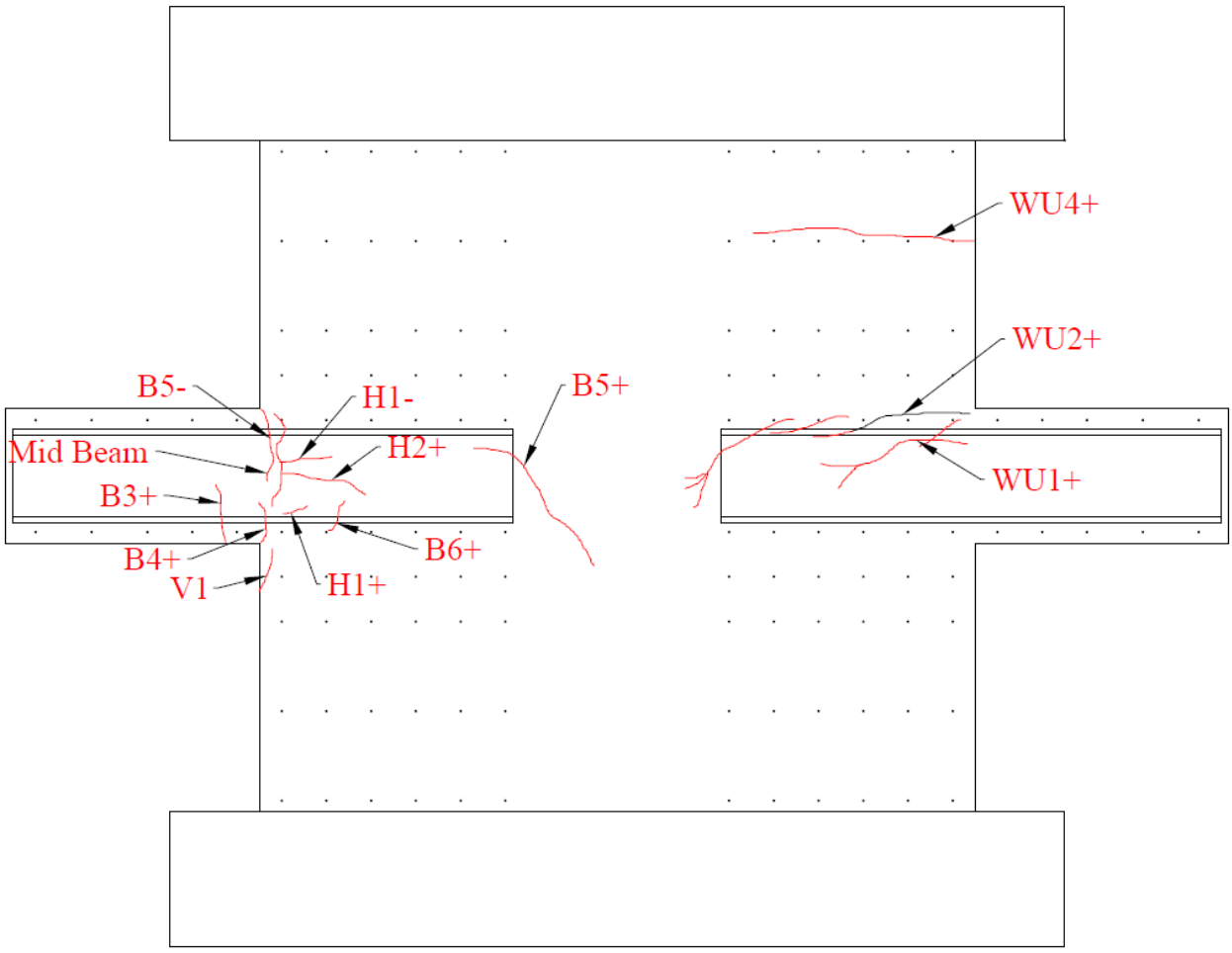

Figure 4.11. Location of Cracks 0.2 Millimeters or Larger for SRC-W3

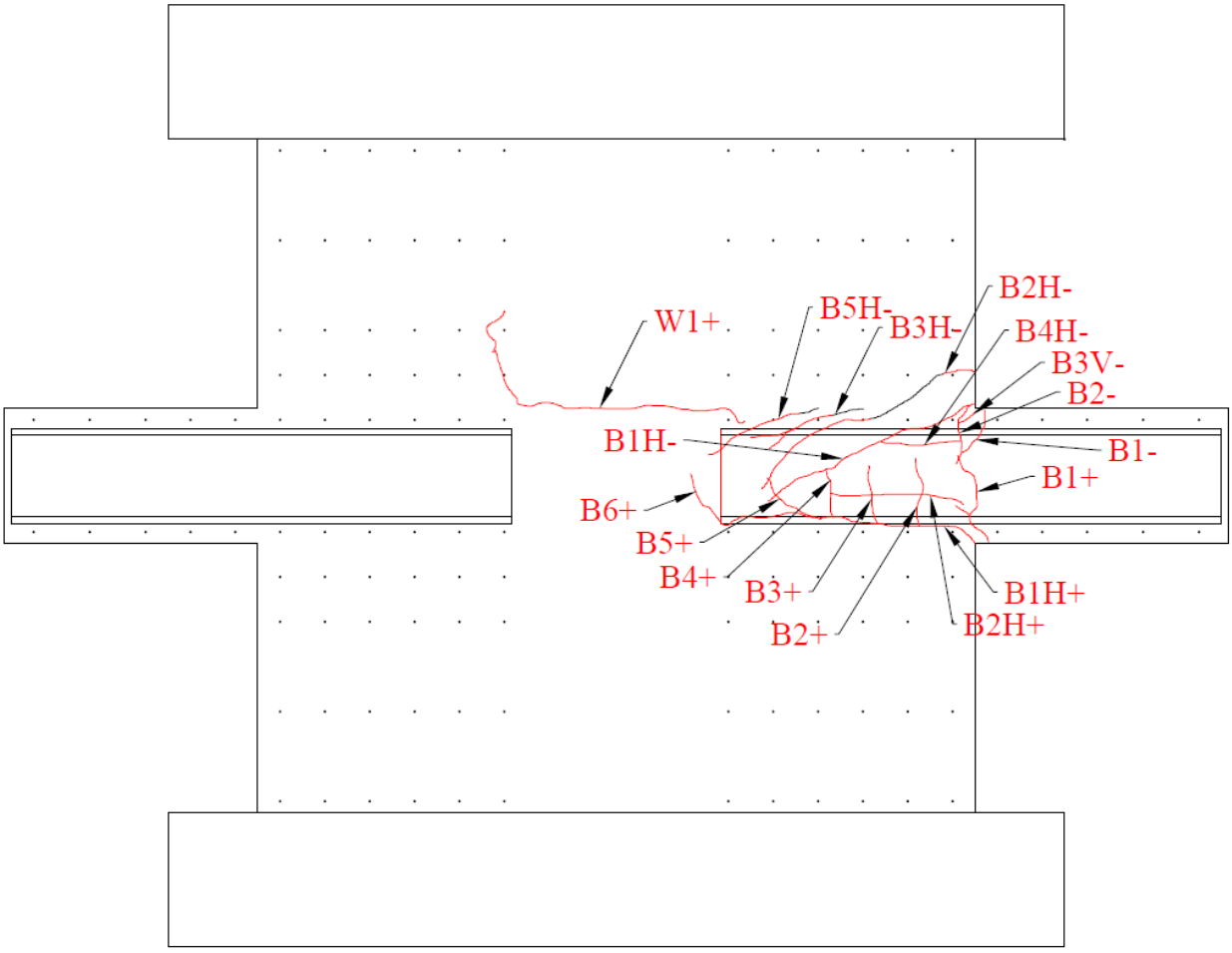

Figure 4.12. Location of Cracks 0.2 Millimeters or Larger for SRC-W4 through the 30th Cycle at $0.4M_{pbe}$

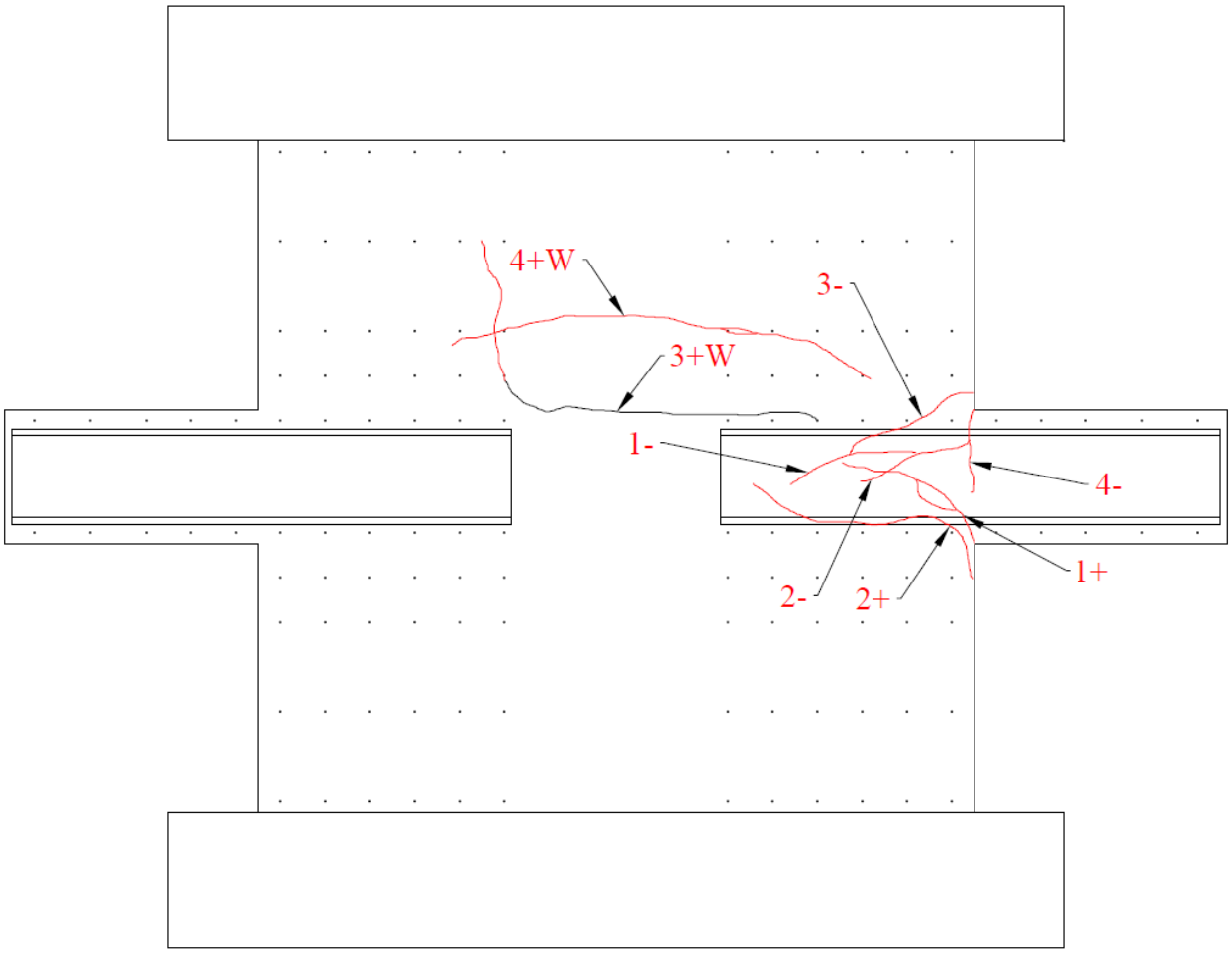

Figure 4.13. Location of Cracks 0.2 Millimeters or Larger for SRC-W4 following the 30th Cycle at 0.4M_{pbe}

Table 4.1. Measured Crack Widths (Millimeters) for SRC-W1

Crack:	I1+		I1-		B2+		B2-		H+		H-		W1+		W2+	
Group/Cycle	End	Face	End	Face	End	Face	End	Face	End	Face	End	Face	Face	End	Face	End
0.15Mp First	0.4	0.2	0.2	0.3	H	H	H	0.2	-	-	-	-	-	-	-	-
0.15Mp Last	0.6	0.4	0.5	0.35	H	0.25	H	0.2	H	H	H	H	-	-	-	-
0.4Mp First	1	0.5	1.5	0.6	0.2	0.25	H	0.2	H	H	H	H	-	-	-	-
0.4Mp Last	1.5	0.8	1.5	0.8	0.25	0.2	0.2	0.2	0.2	H	H	H	-	-	-	-
0.75Mp First	2.5	1.5	2.5+	1.5	0.3	0.25	0.25	0.2	0.25	H	0.3	H	-	-	-	-
0.75Mp Last	7	4	7	4	0.35	0.25	0.3	0.25	0.25	H	0.4	H	H	0.25	H	0.2
1.2θy First	9	5	10	4	0.35	0.25	0.3	0.25	0.25	H	0.5	H	H	0.25	H	0.2
1.2θy Last	9	6	10	5.5	0.35	0.25	0.3	0.25	0.35	H	0.6	H	H	0.25	H	0.25
1.5θy First	11	7	12	6	0.3	0.25	0.3	0.25	0.3	H	0.7	H	H	0.2	H	0.25
1.5θy Last	12	8	13	7	0.3	0.25	0.3	0.25	0.3	H	0.7	H	H	0.2	H	0.25
2.0θy First	15	12	17	9	0.3	0.25	0.3	0.25	0.3	H	0.8	H	H	0.2	H	0.2
2.0θy Last	16	12	17	10	0.3	0.25	0.3	0.25	0.3	H	0.8	H	H	0.2	H	0.2
2.5θy First	19	14	21	11	0.3	0.25	H	H	0.35	H	0.8	H	H	0.2	H	0.2
2.5θy Last	20	15	21	15	0.35	0.25	H	H	0.35	H	0.8	H	H	0.2	H	0.25
3.0θy First	23	17	24	17	0.35	0.25	H	H	0.35	H	0.8	H	H	0.2	H	0.25
3.0θy Last	23	17	24	17	0.35	0.25	H	H	0.3	H	1	H	H	0.2	H	0.25
2.5θy First	21	14	21	17	0.4	0.3	H	H	0.35	H	1	H	H	0.2	H	0.2
2.5θy Last	20	14	21	14	0.4	0.3	H	H	0.35	H	0.6	H	H	0.2	H	0.2
2.0θy First	17	15	18	12	0.4	0.25	H	H	0.4	H	0.6	H	H	0.2	H	0.2
2.0θy Last	17	11	17	12	0.5	0.2	H	H	0.35	H	0.6	H	H	0.2	H	0.2
1.5θy First	14	11	15	13	0.5	0.2	H	H	0.35	H	0.6	H	H	0.2	H	0.2
1.5θy Last	13	11	13	11	0.35	0.2	H	H	0.35	H	0.5	H	H	0.2	H	0.2
1.2θy First	12	10	13	11	0.4	0.25	H	H	0.35	H	0.6	H	H	0.2	H	0.2
1.2θy Last	11	11	12	10	0.4	0.2	H	H	0.6	H	0.35	H	H	0.2	H	2
0.75Mp First	13	10	13	11	0.4	0.2	H	H	0.4	H	0.8	H	H	0.2	H	0.2
0.75Mp Last	12	10	13	9	0.5	0.2	H	H	0.35	H	0.6	H	H	0.2	H	0.2
0.4Mp First	6	7	9	10	0.4	0.2	H	H	H	H	0.3	H	H	0.2	H	0.2
0.4Mp LAst	5	8	8	8	0.4	0.2	H	H	H	H	0.3	H	H	0.2	H	0.2
0.15Mp First	4	8	8	8	0.35	H	H	H	H	H	H	H	H	0.2	H	0.2
0.15Mp Last	4	5	7	6	0.35	H	H	H	H	H	H	H	H	0.2	H	0.2

Table 4.2. Measured Crack Widths (Millimeters) for SRC-W2

Crack	I1+		I1-		B1+		B2+		B1-		B2-		W1+		W1-		H+		H-	
Group/Cycle	End	Face	End	Face	End	Face	End	Face	End	Face	End	Face	End	Face	End	Face	Face	End	Face	End
0.15Mp First	-	-	0.6	0.3	-	-	-	-	-	-	-	-	-	-	-	-	-	-	-	-
0.15Mp Last	0.8	0.4	0.7	0.35	-	-	-	-	-	-	-	-	-	-	-	-	-	-	-	-
0.4Mp First	1.5	0.4	1.5	0.5	H	H	H	H	H	0.25	H	H	-	-	-	-	-	-	-	-
0.4Mp Last	1.5	0.5	2	0.6	H	H	H	H	H	0.3	H	H	-	-	-	-	-	-	-	-
0.75Mp First	3	0.8	3.5	1.5	0.3	0.2	0.2	H	0.35	0.2	0.2	0.2	-	-	-	-	-	-	-	-
0.75Mp Last	4.5	1.4	4.5	1.5	0.35	0.25	0.2	H	0.35	0.2	0.2	0.2	0.25	0.4	0.25	0.4	0.2	0.4	0.2	0.5
1.2θy First	9	2	8	2	H	H	H	H	0.2	0.25	0.2	H	0.2	0.4	0.25	0.4	0.2	0.8	H	0.6
1.2θy Last	9	2	8	2	H	H	H	H	0.2	0.2	0.2	H	0.2	0.4	0.25	0.4	0.2	0.8	H	0.6
1.5θy First	11	2.5	11	3	H	H	H	H	0.2	0.25	0.25	0.2	0.2	0.6	0.2	0.4	0.2	1	0.2	1
1.5θy Last	11	2.5	11	3	H	H	H	H	0.2	0.25	0.25	0.2	0.2	0.6	0.2	0.4	0.2	0.9	0.2	1.5
2.0θy First	13	5	14	5	H	H	H	H	0.2	0.25	0.25	0.2	0.25	0.6	0.3	0.5	0.25	1	0.25	0.8
2.0θy Last	13	5	13	6	H	H	H	H	0.2	0.25	0.25	0.2	0.25	0.5	0.2	0.4	0.25	1.5	0.25	1.25
2.5θy First	14	7.5	16	6	H	H	H	H	0.25	0.25	0.2	0.25	0.25	0.6	0.25	0.5	0.25	1.25	0.25	1
2.5θy Last	14	6	18	7	H	H	H	H	0.25	0.25	0.2	0.25	0.25	0.6	0.25	0.4	0.25	1.5	0.25	1.25
3.0θy First	20	9	22	6	H	H	H	H	0.2	0.25	0.25	0.2	0.25	0.6	0.25	0.5	0.25	2	0.25	3
3.0θy Last	21	9	22	6	H	H	H	H	0.2	0.25	0.25	0.2	0.25	0.6	0.25	0.4	0.25	1.5	0.25	3
2.5θy First	17	7	17	6	H	H	H	H	0.25	0.25	0.2	0.25	0.25	0.6	0.25	0.4	0.25	1.75	0.6	3
2.5θy Last	19	8	18	6	H	H	H	H	0.25	0.25	0.2	0.25	0.25	0.6	0.25	0.4	0.25	1.5	0.6	3.5
2.0θy First	15	7	17	9	H	H	H	H	0.2	0.25	0.25	0.2	0.25	0.6	0.25	0.35	0.25	1.5	0.25	3.5
2.0θy Last	15	7	18	10	H	H	H	H	0.2	0.25	0.25	0.2	0.25	0.5	0.25	0.35	0.25	1.5	0.25	3.5
1.5θy First	10	6	12	7	H	H	H	H	0.2	0.25	0.25	0.2	0.25	0.5	0.25	0.4	0.25	1	0.25	3
1.5θy Last	11	5	12	7	H	H	H	H	0.2	0.25	0.25	0.2	0.2	0.4	0.25	0.4	0.25	1.5	0.25	3
1.2θy First	11	8	9	8	H	H	H	H	0.2	0.25	0.25	0.2	0.2	0.4	0.2	0.35	0.25	1	0.2	1
1.2θy Last	10	8	10	8	H	H	H	H	0.2	0.25	0.25	0.2	0.2	0.35	0.2	0.3	0.2	0.9	0.25	1
0.75Mp First	15	7	16	8	H	H	H	H	0.2	0.25	0.25	0.2	0.25	0.45	0.2	0.35	0.2	1.25	0.2	1.5
0.75Mp Last	14	12	14	8	H	H	H	H	0.2	0.25	0.25	0.2	0.2	0.6	0.25	0.5	0.25	1.75	0.2	1.5
0.4Mp First	8	7	9	6	H	H	H	H	0.2	0.25	0.25	0.2	0.25	0.4	0.2	0.4	0.25	1.5	0.2	1.5
0.4Mp LAst	9	6	10	6	H	H	H	H	0.2	0.25	0.25	0.2	0.25	0.4	0.2	0.35	0.25	1.25	0.2	1.5
0.15Mp First	6	6	6	5	H	H	H	H	0.2	0.25	0.25	0.2	0.2	0.35	0.2	0.3	H	1	0.2	1
0.15Mp Last	6	5	6	5	H	H	H	H	0.2	0.25	0.25	0.2	0.2	0.3	0.2	0.3	H	0.8	0.2	1

Table 4.3. Measured Crack Widths (Millimeters) for SRC-W3

Crack:	B3+		B4+		B5+		B6+	B5-		Mid Beam	WU1+		WU2+		WU4+		V1	H1-		H1+		H2+	
Group/Cycle	End	Face	End	Face	End	Face	Face	End	Face	Face	End	Face	End	Face	End	Face	Face	End	Face	End	Face	End	Face
0.15Mp First	H	H	H	H	-	-	-	H	H	-	-	-	-	-	-	-	-	-	-	-	-	-	-
0.15Mp First	0.15	H	0.15	0.2	-	-	-	0.2	0.25	-	-	-	-	-	-	-	-	-	-	-	-	-	-
0.4Mp First	0.15	H	0.5	0.3	-	-	-	0.8	0.6	-	-	-	-	-	-	-	-	-	-	-	-	-	-
0.4Mp First	0.15	H	0.8	0.5	0.2	0.2		1	0.8	0.35	-	-	-	-	-	-	-	-	-	-	-	-	-
0.75Mp First	0.15	H	2	1	0.2	0.25	H	2.5	1.8	0.6	-	-	-	-	-	-	-	-	-	-	-	-	-
0.75Mp First	0.4	0.3	14	13	0.25	0.3	H	15	14	12	0.2	0.2	-	-	-	-	-	-	-	-	-	-	-
1.2θMp First	0.4	0.3	16	14	0.25	0.3	0.2	16	15	13	0.2	0.2	0.3	-	-	-	-	-	-	-	-	-	-
1.2θMp Last	0.4	0.3	16	14	0.25	0.3	0.2	17	15	13	0.2	0.2	0.35	0.2	-	-	-	-	-	-	-	-	-
1.5θMp First	0.4	0.3	17	15	0.25	0.3	0.2	18	17	14	0.2	0.2	0.35	0.2	-	-	-	-	-	-	-	-	-
1.5θMp Last	0.4	0.3	18	16	0.25	0.35	0.25	19	17	14	0.2	0.2	0.35	0.2	0.15	H	-	-	-	-	-	-	-
2.0θMp First	0.4	0.3	19	17	0.25	0.35	0.25	21	19	15	0.2	0.2	0.35	0.2	0.15	H	-	-	-	-	-	-	-
2.0θMp Last	0.4	0.3	20	18	0.25	0.35	0.25	21	19	15	0.2	0.2	0.35	0.2	0.15	H	-	-	-	-	-	-	-
2.5θMp First	0.4	0.3	22	18	0.25	0.35	0.25	24	21	16	0.2	0.2	0.35	0.2	0.15	H	-	-	-	-	-	-	-
2.5θMp Last	0.4	0.3	22	18	0.25	0.35	0.25	24	23	16	0.2	0.2	0.35	0.2	0.15	H	-	-	-	-	-	-	-
3.0θMp First	0.4	0.3	27	20	0.25	0.35	0.25	27	23	18	0.2	0.2	0.35	0.2	0.15	H	-	-	-	-	-	-	-
3.0θMp Last	0.4	0.3	27	20	0.25	0.35	0.25	27	25	18	0.2	0.2	0.35	0.2	0.15	H	-	-	-	-	-	-	-
2.5θMp First	0.4	0.3	22	20	0.25	0.35	0.25	25	25	19	0.2	0.2	0.35	0.2	0.15	H	2	-	-	-	-	-	-
2.5θMp Last	0.4	0.3	23	20	0.25	0.35	0.25	25	23	18	0.2	0.2	0.35	0.2	0.15	H	2	-	-	-	-	-	-
2.0θMp First	0.4	0.3	22	20	0.25	0.3	0.2	23	22	17	0.2	0.2	0.35	0.2	0.15	H	2.5	-	-	-	-	-	-
2.0θMp Last	0.4	0.3	23	20	0.25	0.3	0.2	23	20	18	0.2	0.2	0.35	0.2	0.15	H	2.5	-	-	-	-	-	-
1.5θMp First	0.4	0.3	21	19	0.3	0.25	0.2	21	20	19	0.2	0.2	0.35	0.2	0.15	H	2.5	-	-	-	-	-	-
1.5θMp Last	0.4	0.3	21	19	0.3	0.25	0.2	21	20	19	0.2	0.2	0.35	0.2	0.15	H	2.5	-	-	-	-	-	-
1.2θMp First	0.4	0.3	20	19	0.3	0.25	0.2	21	20	18	0.2	0.2	0.35	0.2	0.15	H	2.5	-	-	-	-	-	-
1.2θMp Last	0.4	0.3	20	19	0.3	0.25	0.2	21	20	18	0.2	0.2	0.35	0.2	0.15	H	2.5	-	-	-	-	-	-
0.75Mp First	0.4	0.3	21	20	0.3	0.25	0.2	21	20	18	0.2	0.2	0.35	0.2	0.15	H	2.5	0.5	0.25	0.2	H	0.5	0.25
0.75Mp First	0.4	0.3	26	24	0.3	0.25	0.2	27	25	23	0.2	0.2	0.35	0.2	0.15	H	2.5	0.5	0.25	0.2	0.2	0.5	0.25
0.4Mp First	0.4	0.3	24	22	0.3	0.25	H	24	23	21	0.2	0.2	0.35	0.2	0.15	H	3	0.3	0.2	0.2	H	H	H
0.4Mp First	0.4	0.3	24	23	0.3	0.25	H	25	23	23	0.2	0.2	0.35	0.2	0.15	H	3	0.3	0.2	0.2	H	H	H
0.15Mp First	0.2	H	23	23	0.2	0.2	H	23	23	23	0.2	0.2	0.35	0.2	H	H	-	0.25	H	0.2	H	H	H
0.15Mp First	0.2	H	23	23	0.2	0.2	H	23	23	23	0.2	0.2	0.35	0.2	H	H	-	0.25	H	0.2	H	H	H

Table 4.4. Measured Crack Widths (Millimeters) for SRC-W4 through the 30th Cycle at 0.4M_{pbe}

Crack:	Group/Cycle	0.15Mp First	0.15Mp First	0.4Mp First	0.4Mp (30)
B1+	End	0.4	0.8	2.5	8
	Face 1	0.2	0.25	0.4	0.1
	Face 2	-	-	-	1
B2+	End	0.3	0.4	0.25	0.3
	Face	0.15	0.2	0.1	0.1
B3+	End	H	0.15	0.2	0.2
	Face	H	0.1	0.1	H
B4+	Face	H	H	0.3	0.25
	End	H	H	0.2	0.15
B5+	End	-	-	0.25	1
	Face	-	-	0.15	0.6
B6+	Face	-	-	0.2	0.35
	End	-	-	H	H
B1H+	1*	-	-	-	8
	2	-	-	1.5	1.5
	3	-	-	1.25	2.5
	4	-	-	0.5	1.5
	5	-	-	0.25	0.3
B2H+	1	-	-	-	0.6
	2	-	-	-	0.6
	3	-	-	-	0.3
W1+	1	-	-	-	0.6
	2	-	-	-	1
	3	-	-	-	0.6
B1V-	End	0.5	0.8	4	10
	Face	0.2	0.3	0.6	3
B2V-	End	0.15	0.15	0.15	H
	Face	0.4	0.4	0.5	0.3
B3V-	End	-	-	-	10
B1H-	1	1	1.25	2.5	0.4
	2	0.35	0.4	1.5	1
	3	-	-	0.4	1.5
	4	-	-	0.25	0.4
B2H-	1	-	-	-	0.35
	2	-	-	0.4	0.6
	3	-	-	0.5	0.2
	4	-	-	0.25	0.35
B3H-	1	-	-	0.15	0.35
	2	-	-	0.4	0.8
	3	-	-	0.15	0.4
B4H-	1	-	-	-	5
	2	-	-	-	1.5
B5H-	1	-	-	-	0.4
	2	-	-	-	0.8
	3	-	-	-	0.3

Table 4.5. Measured Crack Widths (Millimeters) for SRC-W4 through the 30th Cycle at $0.4M_{pbe}$

Crack:	Group/Cycle	0.4Mp (40)	0.4Mp (100)	0.4Mp (250)	0.4Mp (500)	0.75Mp (1)	0.75Mp (2)
1+	1*	8	8	10	10	22	25
	2	0.6	1				
	3	1	6				
	4	1	0.4				
2+	1	2.5					
	2	3	3.5				
	3	1.5	1.5	1.5			
	4	1	0.5	0.3			
3+W	1	0.6	0.5	0.6	0.4	1.5	0.6
	2	1	1	0.6	0.6	1.5	0.35
	3	0.6	0.6	0.8	0.8	1.5	0.8
4+W	1	0.25	0.3	0.3	0.3	0.6	0.35
	2	0.5	0.6	0.5	0.5	1.5	1.5
	3	0.4	0.5	0.5	0.5	0.8	0.6
1-	1	10	10	10	10	50	50
	2	3	2				
	3	2.5					
	4	1.5	2				
	5	1.5	2	2.5			
2-	1	2.5					
	2	1.5	2				
3-	1	1	3.5				
	2	1	1.5	1.5			
	3	0.35	0.5	0.4			
4-	1	0.6	0.5	0.5			

4.2. Load-Deformation

Load-deformation responses for the tested beams are provided in Figure 4.14. Cyclic stiffness degradation occurred during repeated loading cycles at a given increment, particularly during the groups of 75 cycles at $0.75M_{pbe}$, as shown in Figure 4.15. θ_y, determined as described in Section 3.6, was 1.90% chord rotation for SRC-W1, 1.55% chord rotation for SRC-W2 and SRC-W3, and indeterminate for SRC-W4, as $0.75M_{pbe}$ was not reached. For the three tests in which θ_y was determined, peak deformation demand was $3\theta_y$, as discussed in Section 3.6, resulting in peak deformation of 5.70% for SRC-W1 and 4.65% for SRC-W2 and SRC-W3. For these three tests, the demands during displacement-controlled cycles led to a reduction in stiffness for the second batches of load-controlled cycles relative to the initial batches of load-controlled cycles at a given increment. The hysteretic loops for SRC-W2 had slightly more pinching than SRC-W1 and SRC-W3, although the level of pinching in both tests was small, as was the level of strength degradation. The shape of the hysteretic loops is generally consistent with SRC1 tested by Motter et al (2017a), which is reflective of favorable embedment behavior and sufficient wall longitudinal reinforcement relative to the wall demands. The peak strength reached in these three tests was 173.5 kips in the positive direction and 179.8 kips in the negative direction for SRC-W1, 178.0 kips in the positive direction and 180.4 kips in the negative direction for SRC-W2, and 160.5 kips in the positive direction and 171.0 kips in the negative direction for SRC-W3. The stock beam used for steel sections in SRC-W1 and SRC-W2 differed from the stock beam used for steel sections in SRC-W3 and SRC-W4, which may have impacted the difference in strength for SRC-W3 relative to SRC-W1 and SRC-W2. As mentioned in Section 3.1, V_{be} for the test beams was computed to be 192 kips. This computed value is intended to be an upper bound for beam strength

and is used for capacity design of the embedment length and wall longitudinal reinforcement. The post-yield strength increase was larger for these three test beams than for SRC1 tested by Motter et al (2017a). This was likely due to improved concrete contact in compression at the beam-wall interface for the case of reduced axial elongation, as axial restraint reduced axial elongation for these three test beams relative to SRC1, which was tested without axial restraint. More information on axial elongation is provided in Section 4.5.

This study did not include testing on SRC coupling beams that were designed using provisions in AISC 341-22 H4 and tested to peak deformation demands more consistent with ordinary walls. As mentioned in Section 3.1, the maximum deformation demands of $3\theta_y$ were deemed to be more consistent with the seismic design provisions in AISC 341-22 Section H5 for special walls than AISC 341-22 Section H4 for ordinary walls, such that the provisions in H5 were used for design of the test specimens. It is recommended that nonlinear wind design of steel reinforced concrete (SRC) coupling beams follow the seismic provisions in AISC 341-22 Section H5. Advanced levels of deformation demand under wind demands were reached for SRC-W1, SRC-W2, and SRC-W3 without significant strength degradation of initial cycles at new peak deformation demands or significant pinching in the load-deformation response. Similar to seismic design, a specified deformation capacity limit on the coupling beam is likely unnecessary for nonlinear wind design. However, based on the available data, the use of a deformation capacity limit of 6.0% chord rotation could be considered, based on modest extrapolation of data for SRC-W1.

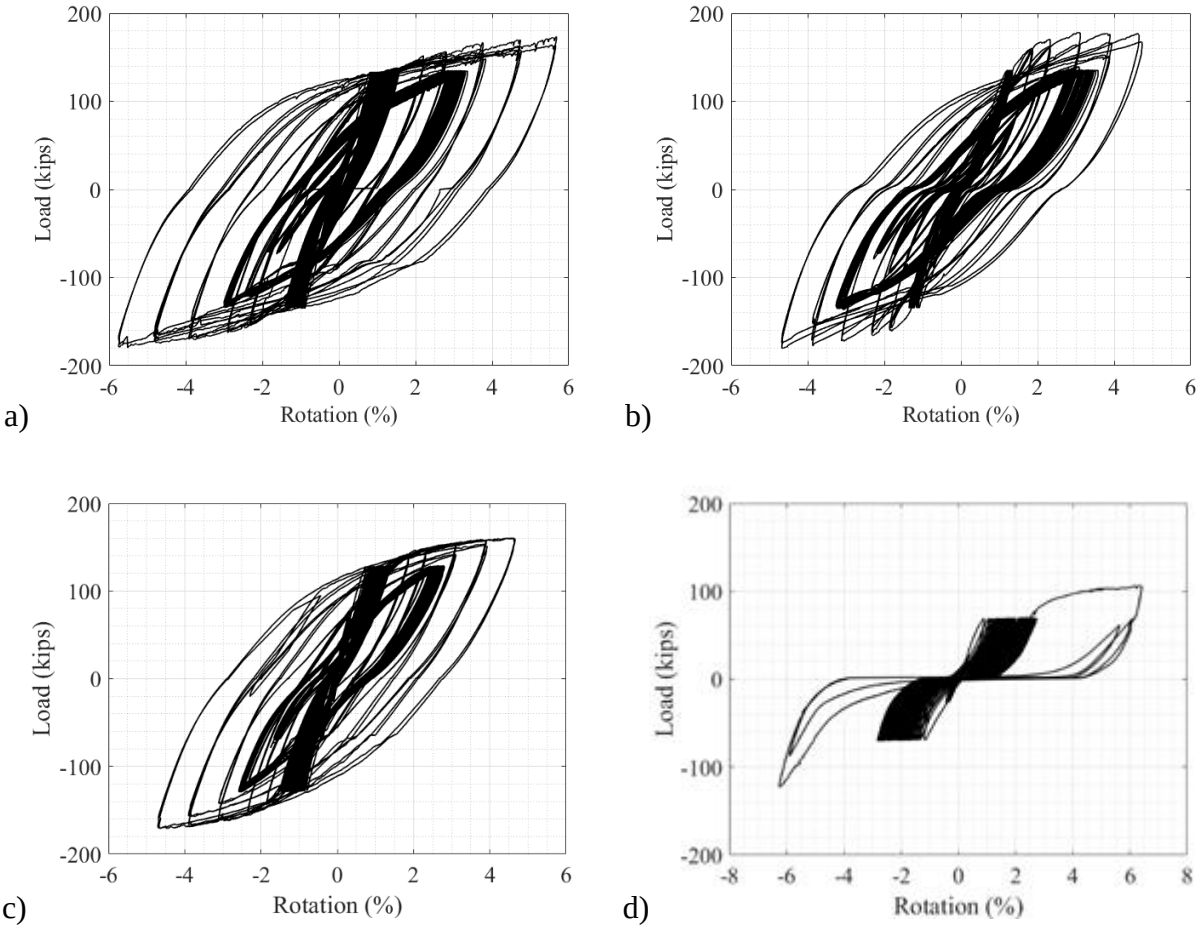

Figure 4.14. Load-Deformation for a) SRC-W1, b) SRC-W2, c) SRC-W3, and d) SRC-W4

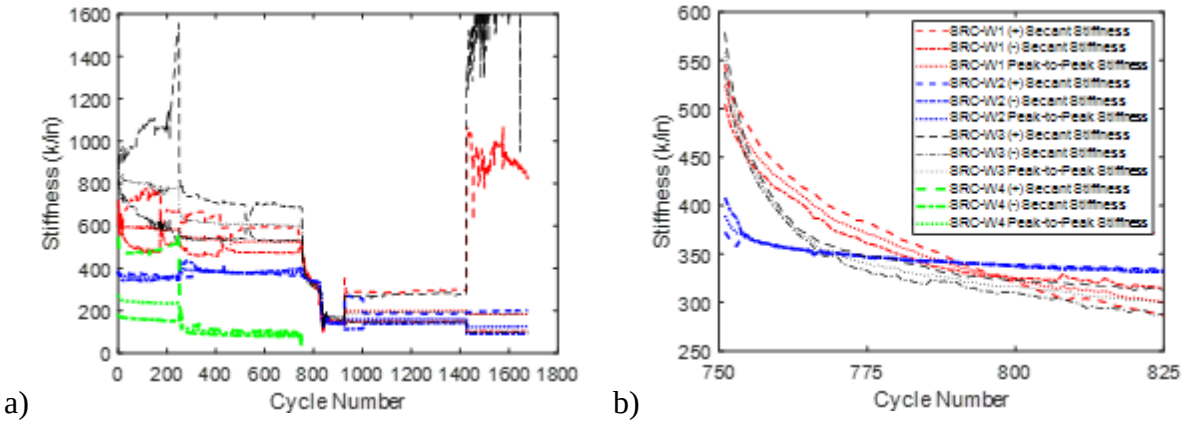

Figure 4.15. Effective Stiffness for a) All Cycles and b) Cycles at 0.75M_{pbe}

The behavior of SRC-W4 differed significantly from the other three tests. SRC-W4 and SRC-W3 were nominally identical tests, with the exception of the quantity of wall longitudinal reinforcement crossing the embedment length and the quantity of wall boundary transverse reinforcement. For SRC-W4, the wall longitudinal reinforcement was insufficient to prevent yielding at the connection, with the embedded steel section prying the wall open. Measured yielding occurred in the wall, with more details provided in Section 4.7. The significant stiffness degradation in the beam during the 500 cycles at $0.4M_{pbe}$ was consistent with that for the wall, as described in Section 4.7. For the 500 cycles at $0.4M_{pbe}$, the largest chord rotation reached by the beam was 2.57% in the positive loading direction and 2.98% in the negative loading direction. During the next positive excursion following the 500 cycles at $0.4M_{pbe}$, the beam reached 6.0% chord rotation prior to reaching $0.75M_{pbe}$. Two loading cycles were conducted at 6.0% chord rotation prior to stopping the test. Significant pinching was observed in the load-displacement hysteresis, with minimal load resistance for the second cycle at 6.0% until approaching the extents of the previous cycle at 6.0% rotation. This type of hysteresis is characteristic of gapping behavior. In this case, the beam pried the wall apart on the initial cyclic excursion to 6.0% with a gap remaining. The peak strength developed in the beam, 106.3 kips in the positive loading direction and 122.8 kips in the negative loading direction, was limited by the yielding in the wall and was significantly less than the other three tests. The combination of wall demands and wall reinforcement for SRC-W3 and SRC-W4 was adequate and inadequate, respectively, to produce favorable performance in the coupled wall.

It is recommended that the quantity of wall longitudinal reinforcement crossing the embedment length prescribed by AISC 341-22 Section H5 be reduced by 50% for cases in which wall demands

do not exceed that applied for SRC-W3. This recommendation applies for both seismic and wind design, as favorable performance of SRC-W3 under wind demands to a peak deformation of 4.65% chord rotation was observed. The poor performance of SRC-W4 did not support further reduction to the quantity of wall reinforcement crossing the embedment length or reduction to the quantity of wall boundary transverse reinforcement required by AISC 341-22 Section H5. The peak wall demands for SRC-W3 were $0.49M_y$ and 0.00047 tensile strain in outermost reinforcement at the coupling beam mid-height and an average of $0.24M_y$ and 0.00008 tensile strain in outermost reinforcement over one story height, taken as half a story above and below the coupling beam mid-height. These demands were determined from moment-curvature analysis for the moment and axial load, with moment and axial load diagrams determined based on transfer of coupling beam moment and shear to the wall at mid-height of the coupling beam. The moment-curvature analysis used the Hognestad (1951) concrete model, with the compressive strength of concrete taken as the average tested value for SRC-W3, which was 4.67 ksi. The M_y indicated here was based on reaching 70 ksi, the expected yield strength of A615 Grade 60 reinforcement (PEER TBI, 2017), in the outermost longitudinal reinforcement. The tested yield strength of the reinforcement was not used here, since the demands were less than yielding.

Measured torsional rotation at the point of load application in the test beams is provided in Figure 4.16 through Figure 4.19. This torsional rotation was determined from two LVDTs located at opposite beam faces and both located at the point of load application. Torsional rotation was smaller for SRC-W1 than the other three tests. For SRC-W2 and SRC-W3, the torsional rotation remained relatively small through the pre-yielding load-controlled cycles but grew larger during the displacement-controlled cycles. After the cycles at $1.5\theta_y$ for SRC-W2, a brace was installed on

the beam to mitigate additional torsion. The brace was used for SRC-W3 and SRC-W4 for the duration of the test, and the torsion was less for SRC-W3 than SRC-W2. The peak measured torsional rotation was 1.8% for SRC-W2 and 0.94% for SRC-W3. The peak measured torsional rotation for SRC-W4 reached 1.1% during the $0.4M_{pbe}$ cycles and 1.8% overall. The larger torsional rotation for SRC-W4 than SRC-W3 was potentially due to wall damage.

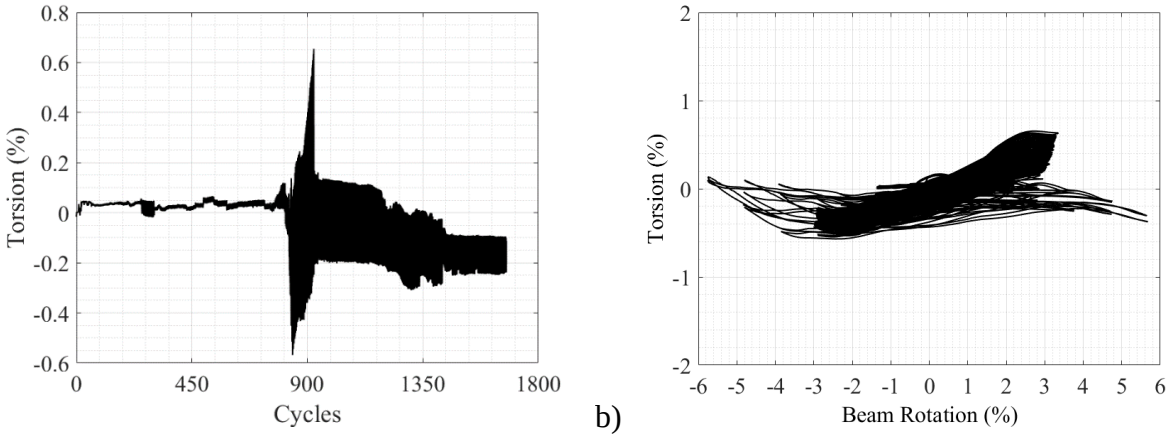

a) b)

Figure 4.16. Measured Torsion in SRC-W1 at the Point of Shear Load Application Relative to a) Cycle Number, and b) Beam Rotation

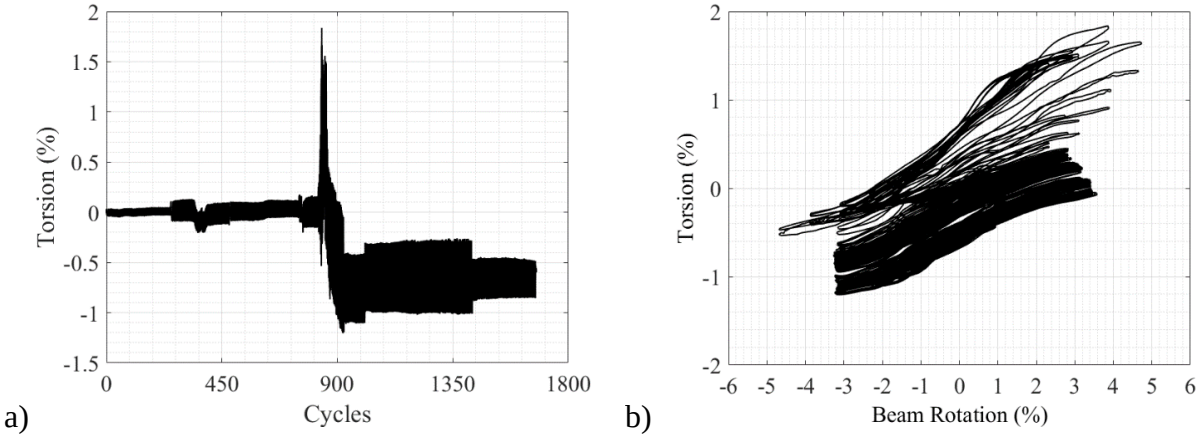

Figure 4.17. Measured Torsion in SRC-W2 at the Point of Shear Load Application Relative to a) Cycle Number, and b) Beam Rotation

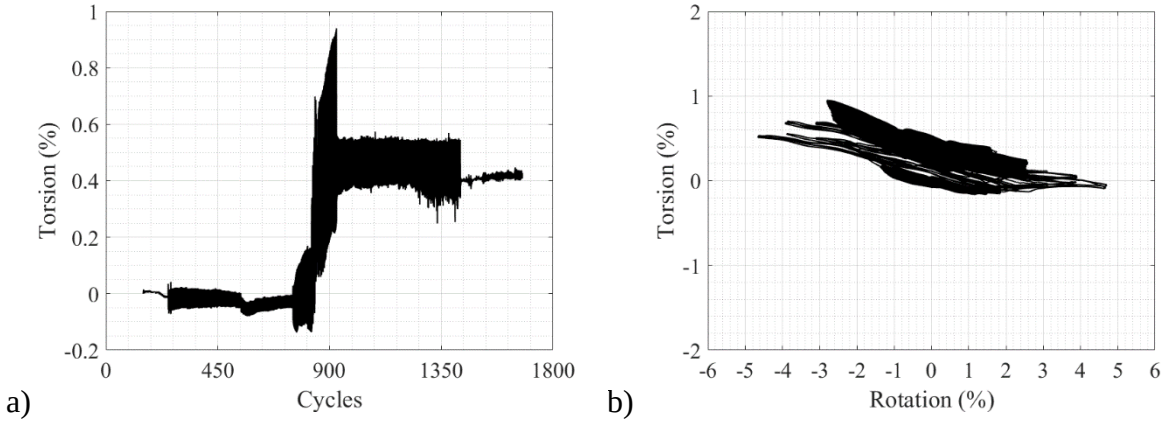

Figure 4.18. Measured Torsion in SRC-W3 at the Point of Shear Load Application Relative to a) Cycle Number, and b) Beam Rotation

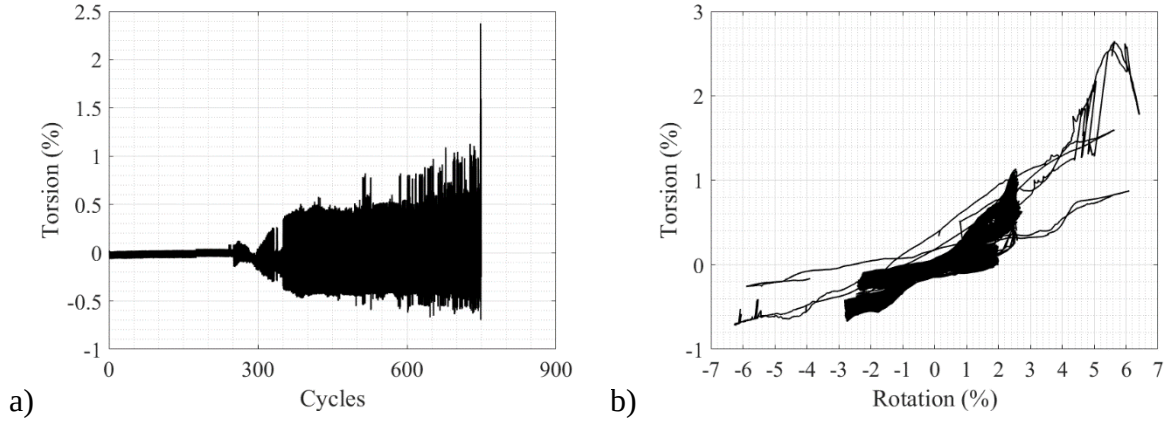

Figure 4.19. Measured Torsion in SRC-W4 at the Point of Shear Load Application Relative to a) Cycle Number, and b) Beam Rotation

4.3. Dissipated Energy

Plots of the cumulative dissipated energy and dissipated energy per cycle are provided in Figure 4.20 for the four tests, with the average dissipated energy per cycle at each loading increment provided in Table 4.6. Dissipated energy was computed as the area enclosed by the load-deformation hysteretic loops in Figure 4.14, with the chord rotation converted to beam displacement at the point of loading application. The dissipated energy per cycle was reasonably consistent for SRC-W1, SRC-W2, and SRC-W3 during the load-controlled cycles. During the displacement-controlled cycles, the energy dissipation was largest for SRC-W1 due to the larger yield displacement and resulting larger chord rotations in the testing protocol. The energy dissipation for SRC-W2 was smaller than SRC-W3 during the displacement-controlled cycles but significantly larger during the subsequent 75 cycles at $0.75M_{pbe}$. The total energy dissipated for SRC-W2 at the completion of testing was larger despite the slightly increased level of pinching

evident in the hysteric plots in Figure 4.14. The dissipated energy per cycle was highest for SRC-W4 likely due to energy being dissipated in the connection, as beam chord rotation and damage at the connection increased during repeated loading cycles significantly more than in the other three tests. The increase in cumulative dissipated energy for the two cycles to 6.0% rotation was relatively minor relative to the increase in dissipated energy over repeated cycles at $0.4M_{pbe}$. The total cumulative dissipated energy was significantly less for SRC-W4 than the other three tests at the completion of testing, despite SRC-W4 being the only test that reached 6.0% chord rotation. The poor energy dissipation for SRC-W4 was a result of the damage at the connection.

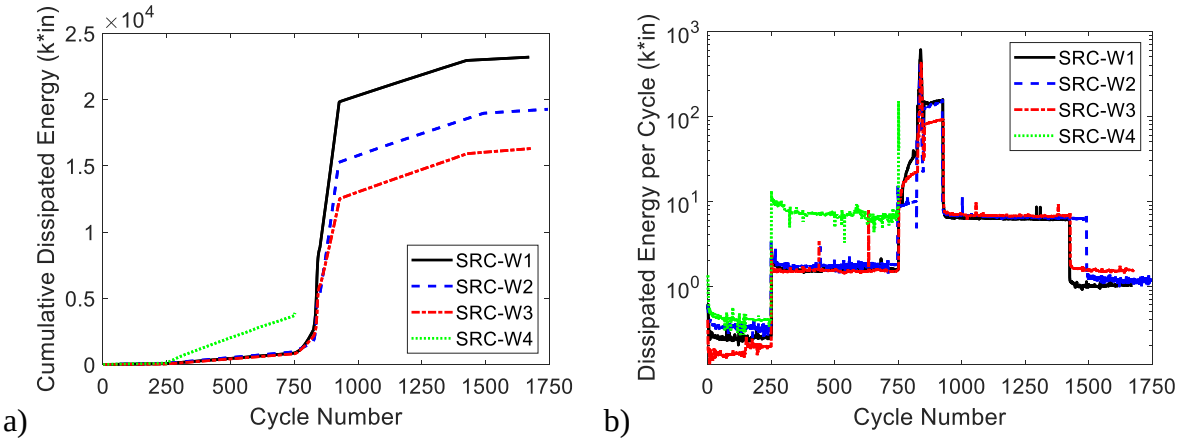

Figure 4.20. a) Cumulative Dissipated Energy, and b) Dissipated Energy per Cycle

Table 4.6. Average Dissipated Energy per Cycle at Each Loading Increment

Loading Increment	Average Dissipated Energy per Cycle (k*in^2)			
	SRC-W1	SRC-W2	SRC-W3	SRC-W4
0.15M_{pbe}	0.25	0.33	0.17	0.41
0.40M_{pbe}	1.60	1.74	1.53	7.16
0.75M_{pbe}	23.7	9.5	17.9	NA
1.2θ_y	113.2	48.8	59.9	NA
1.5θ_y	197.3	99.4	111.3	NA
2.0θ_y	329.2	195.5	209.6	NA
2.5θ_y	463.6	297.4	319.6	NA
3.0θ_y	600.1	401.1	430.0	NA
2.5θ_y	450.3	270.8	302.7	NA
2.0θ_y	288.7	150.9	170.8	NA
1.5θ_y	147.0	59.7	74.5	NA
1.2θ_y	79.3	25.9	32.5	NA
0.75M_{pbe}	145.8	134.6	86.2	NA
0.40M_{pbe}	6.30	6.59	6.83	NA
0.15M_{pbe}	1.02	1.19	1.55	NA

4.4. Moment-Rotation

Moment-rotation at the beam-wall interface is provided in Figure 4.21. The characteristics of the hysteretic plots are similar to those of the load-deformation plots in Figure 4.14. The majority of the beam deformation was from interface rotation. More information on sources of deformation is provided in Section 4.6. Much of the rotation at the beam-wall interface comes from slip of the embedded steel section. Rotation measured at the first location entirely within the beam span is provided in Figure 4.22 and provides a better indication of the bending in the beam. This location was centered at 9” from the beam-wall interface, as shown in Figure 3.16. Minimal rotation was

measured at this location, suggesting that the majority of the measured rotation at the beam-wall interface was due to slip.

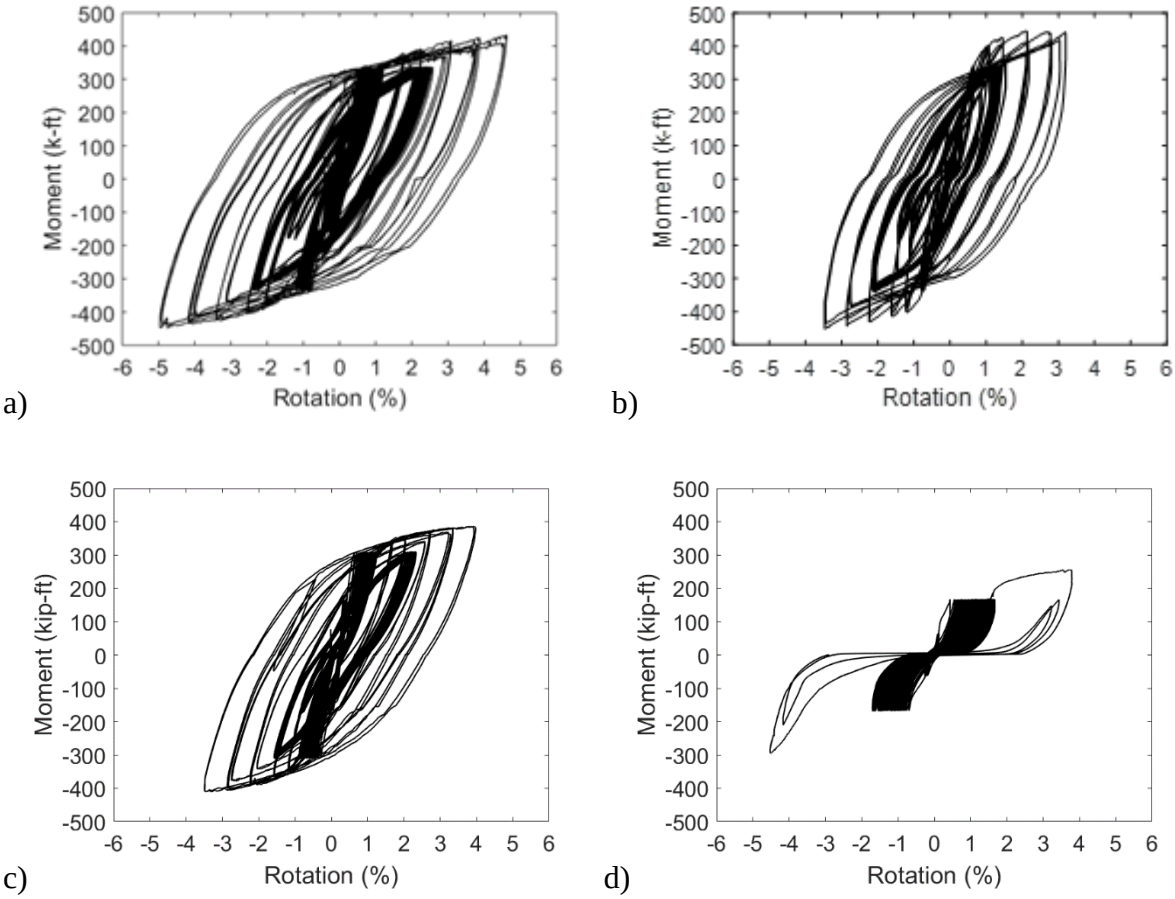

Figure 4.21. Moment-Rotation at Beam-Wall Interface for a) SRC-W1, b) SRC-W2, c) SRC-W3, and d) SRC-W4

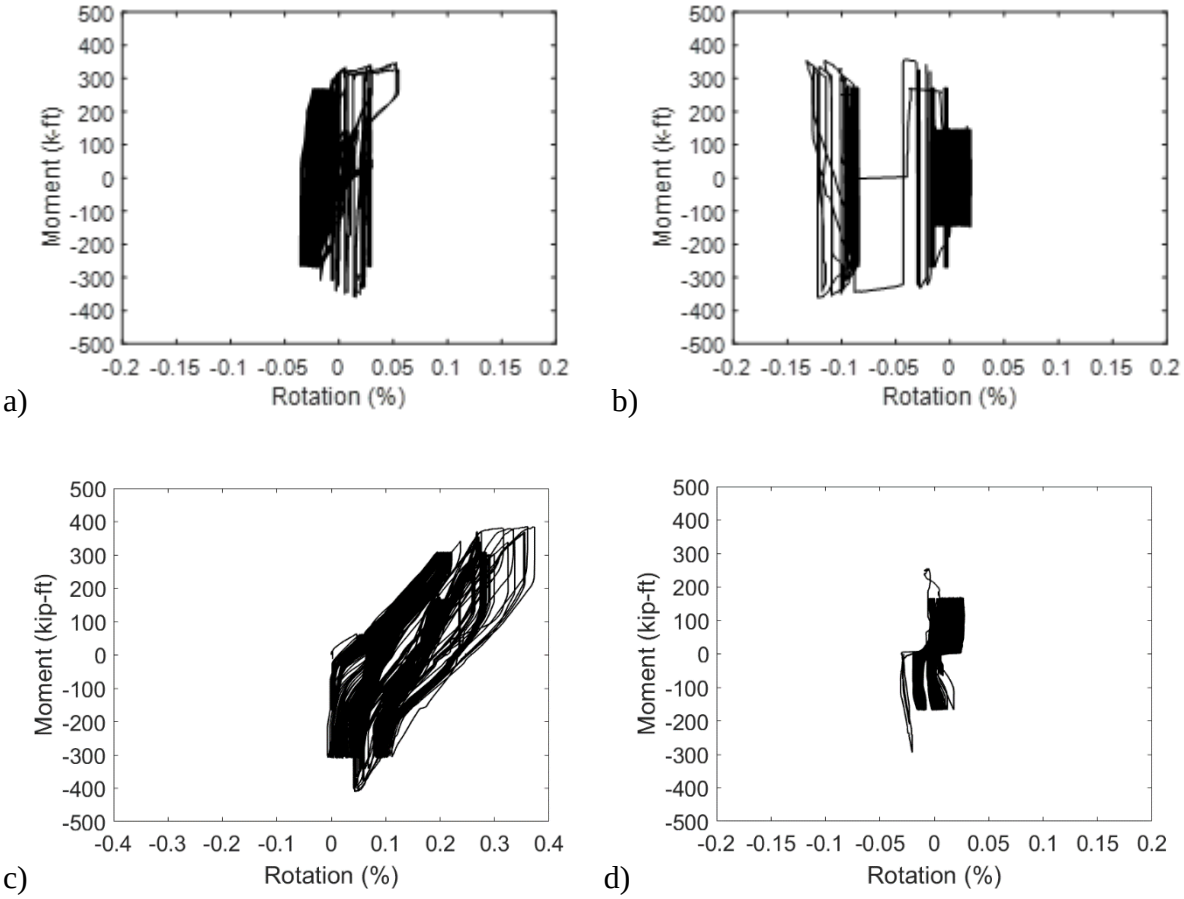

Figure 4.22. Moment-Rotation at First Sensor Location in Beam for a) SRC-W1, b) SRC-W2, c) SRC-W3, and d) SRC-W4

4.5. Axial Elongation and Axial Load

Plots of axial load versus coupling beam rotation are provided in Figure 4.23. The initial axial load was roughly 2.0 kips, as this was needed to hold the axial restraint system in place prior to the start of testing. For the first half of the testing protocol, the increase in axial load with beam deformation was roughly linear for SRC-W1 and SRC-W2 but not SRC-W3. Increase in axial load for repeated loading cycles at a given increment was more significant for SRC-W3 than SRC-W1 and more

significant for SRC-W1 than SRC-W2. The axial load did not exceed 15 kips and was less than $0.015A_g f'_{c,test}$ for all four tests, where A_g is the gross area of the beam cross-section. Plots of axial elongation versus coupling beam rotation are provided in Figure 4.24. The axial elongation did not exceed 1.0” in any test. This was less than that measured for SRC1 and SRC2, without axial restraint, tested by Motter et al (2017a), although these two beams were tested to higher levels of chord rotation. The increase in axial elongation with repeated loading cycles at a given increment was less for SRC-W1, SRC-W2, SRC-W3, and SRC-W4 with axial restraint than for SRC1 and SRC2 without axial restraint.

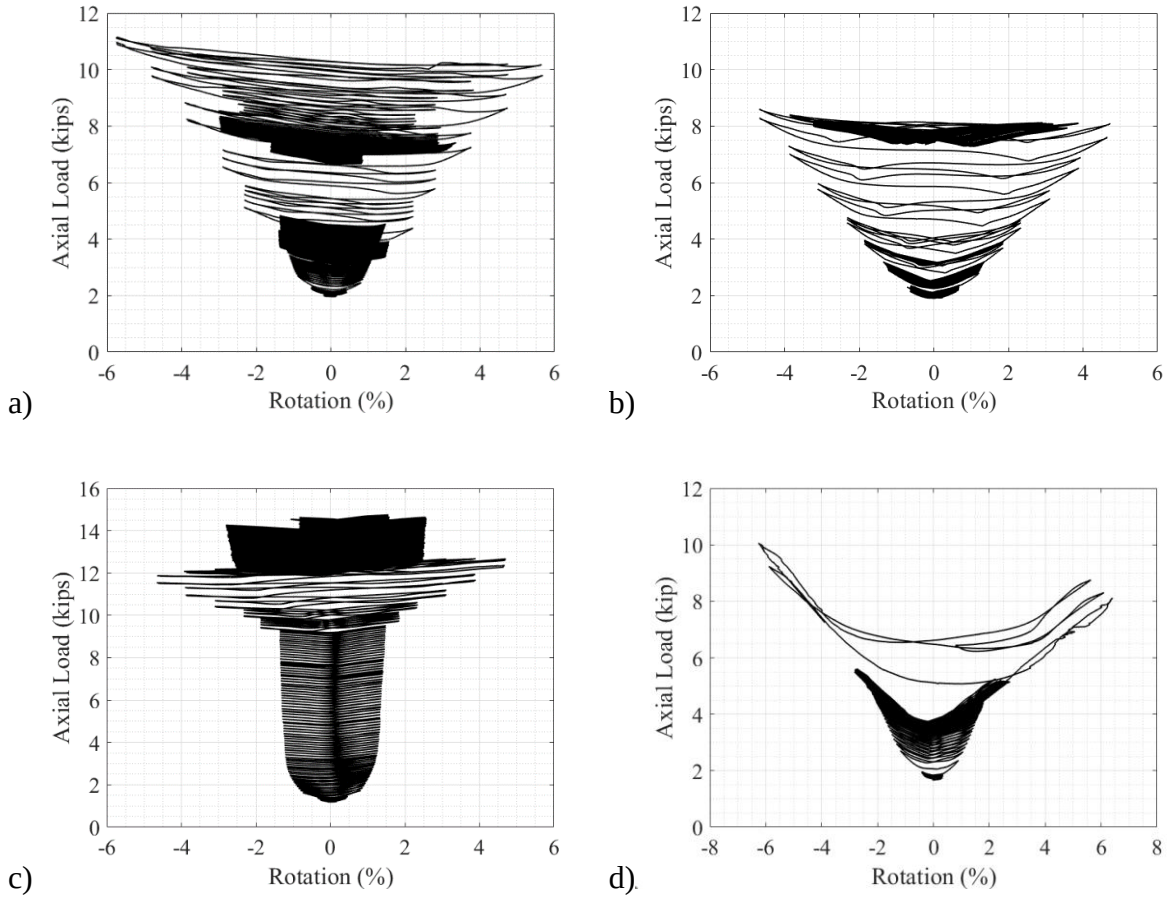

Figure 4.23. Axial Load versus Rotation for a) SRC-W1, b) SRC-W2, c) SRC-W3, and d) SRC-W4

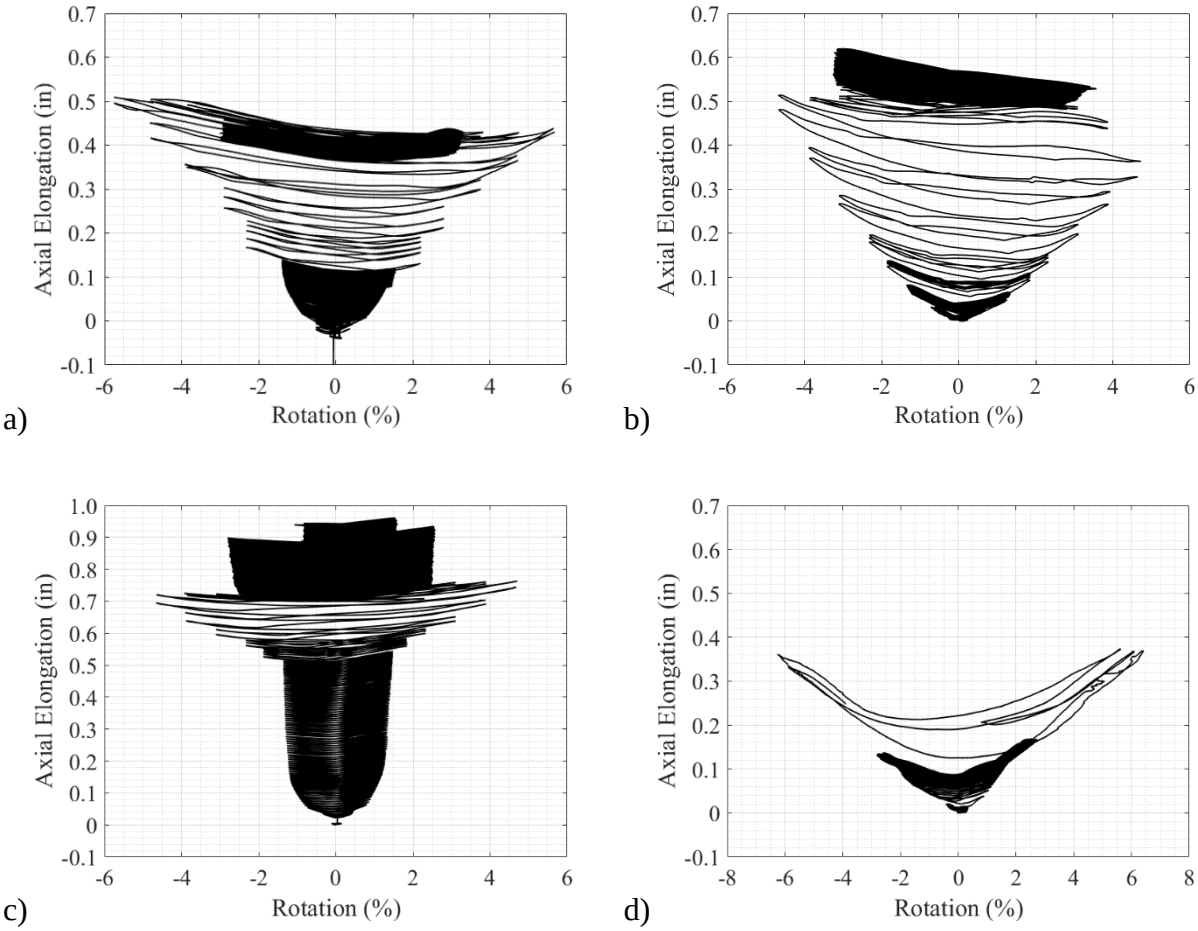

Figure 4.24. Axial Elongation versus Rotation for a) SRC-W1, b) SRC-W2, c) SRC-W3, and d) SRC-W4

4.6. Components of Beam Deformation

The components of beam deformation are provided in Figure 4.25 for SRC-W1, SRC-W2, and SRC-W3 for the first cycle of each cycle group. The slip component was taken as the rotation measured at the beam-wall interface multiplied by the 30" span length. Although the sensors at this location spanned 6", measured deformation in the beam span was minimal, as indicated by the

flexural deformation in Figure 4.25 and as described in Section 4.4, suggesting that the majority of the deformation at the beam-wall interface was due to slip. The flexural deformation was determined through integration of the curvature measured along the length of the beam, with average curvature used over the length of sensor pairs. This was achieved by multiplying the rotation from each pair of sensors located fully within the beam span by the length from the midpoint of the sensor pair to the point of load application and summing the resulting deformations. The exception was the sensor pair located closest to the point of load application, in which the rotation was multiplied by two-thirds of the sensor lengths rather than one-half of the sensor lengths. The shear deformation was determined using the procedure described by Massone and Wallace (2004), in which geometry is used to remove the measured flexural deformation from the measured values in a pair of diagonal sensors to determine the resulting shear deformation over the length of the pair of diagonal sensors. The component labeled "Other" in Figure 4.25 was determined as the difference between the beam displacement and the combined displacement from slip, flexure, and shear.

It is evident from the plots in Figure 4.25 that the majority of the beam deformation was due to slip. This is consistent with results reported by Motter et al (2017a). For SRC-W1 and SRC-W3, the slip was larger in the positive than negative loading direction, and the "Other" component was larger in the negative than the positive direction. The slip component exceeded 100% in the positive loading direction, corresponding with the "Other" component providing a negative contribution. This is consistent with the behavior observed for SRC2 reported by Motter et al (2013). This behavior may be indicative of more beam plasticity at the beam-wall interface in the positive than negative loading direction, suggesting that plasticity may be moving into the

embedment in the negative loading direction due to wall tension at the embedment region. This was associated with a reduction in the force developed in the negative loading direction relative to the positive loading direction for SRC2 but not for SRC-W1 and SRC-W3. For SRC-W2, components of deformation were more symmetric, consistent with SRC1 tested by Motter et al (2017a). The lower wall moments for SRC-W2 relative to SRC-W1 and the increased wall reinforcement for SRC-W2 relative to SRC-W3 may have contributed to this behavior.

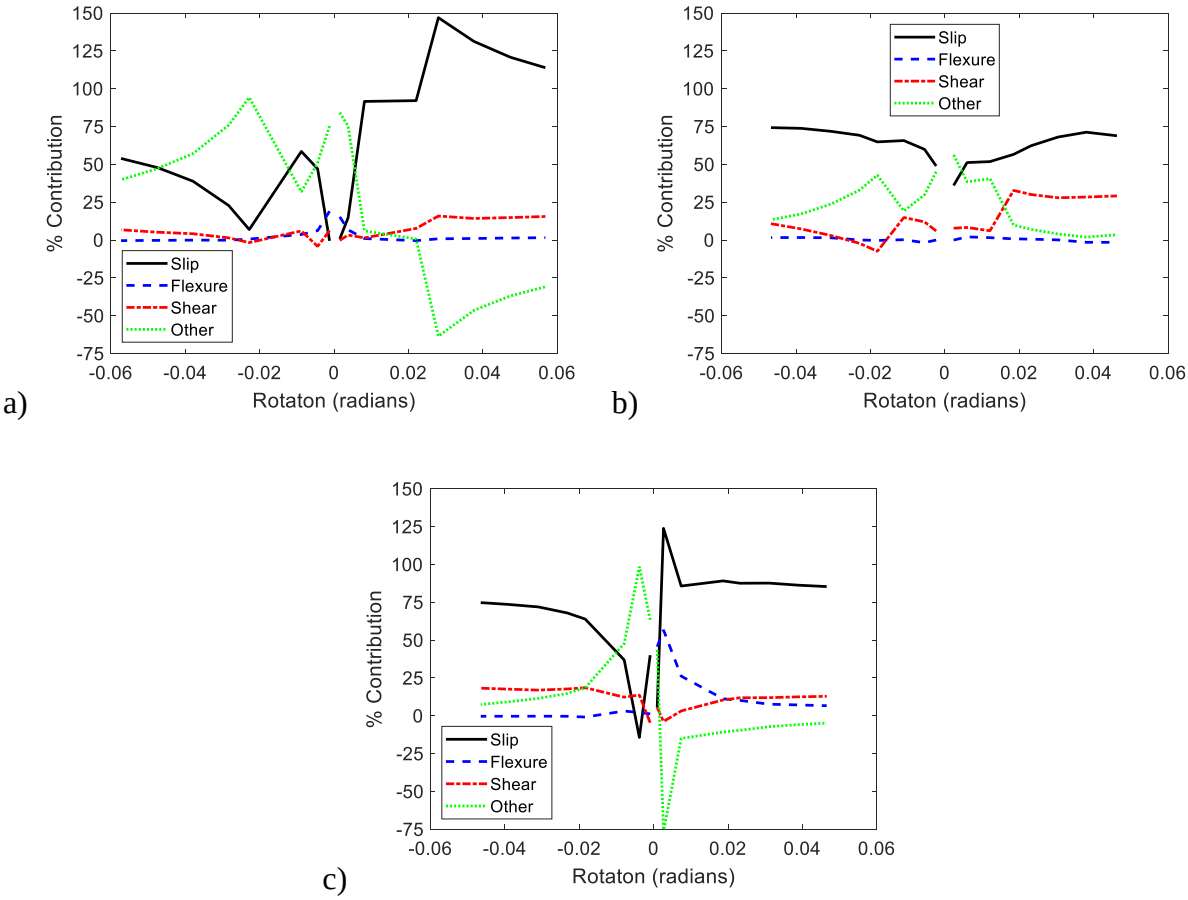

Figure 4.25. Components of Deformation for a) SRC-W1, b) SRC-W2, c) SRC-W3

4.7. Wall Load-Deformation

Plots of wall load-deformation are provided in Figure 4.26. Rotation was determined using measured data from two LVDTs, one near each edge of the wall, spanning the clear height of the wall from the top of the bottom block to the bottom of the top block. The rotation is provided in the plots as radians times 100%. It is evident from the plots that deformation in the wall was minimal relative to rotational demand in the test beams for SRC-W1, SRC-W2, and SRC-W3. For SRC-W4, the rotation in the wall was significant, reaching 0.49% during the 500 cycles at $0.4M_{pbe}$ and reaching 1.30% during the two subsequent cycles to 6.0% coupling beam chord rotation. The wall ratcheted in one direction, with tension on the side of the wall with the test beam, as the beam pried the wall at the connection. As noted in Section 3.6, a correction was made to beam rotation to account for wall rotation. Based on the measured wall rotation shown in Figure 4.26, this correction was small for SRC-W1, SRC-W2, and SRC-W3 but more significant for SRC-W4. The peak measured wall rotation for SRC-W1, SRC-W2, and SRC-W3 was less than that measured for SRC1 tested by Motter et al (2017a). The peak measured wall rotation for SRC-W4 was comparable to that for SRC-W4 tested by Motter et al (2017a). Buckling of longitudinal reinforcement in the wall was not observed for SRC-W4, suggesting that local tension demands created in the wall by the SRC coupling beam may have exceeded the compressive demands due to applied wall demand. Buckling of longitudinal reinforcement in the wall was observed for SRC4, which had larger moment applied to the wall than SRC-W4. Although ratcheting was evident in the wall load-deformation response for both tests, the difference in wall rotation for positive and negative cycles was more significant for SRC4, likely due to the larger wall demands.

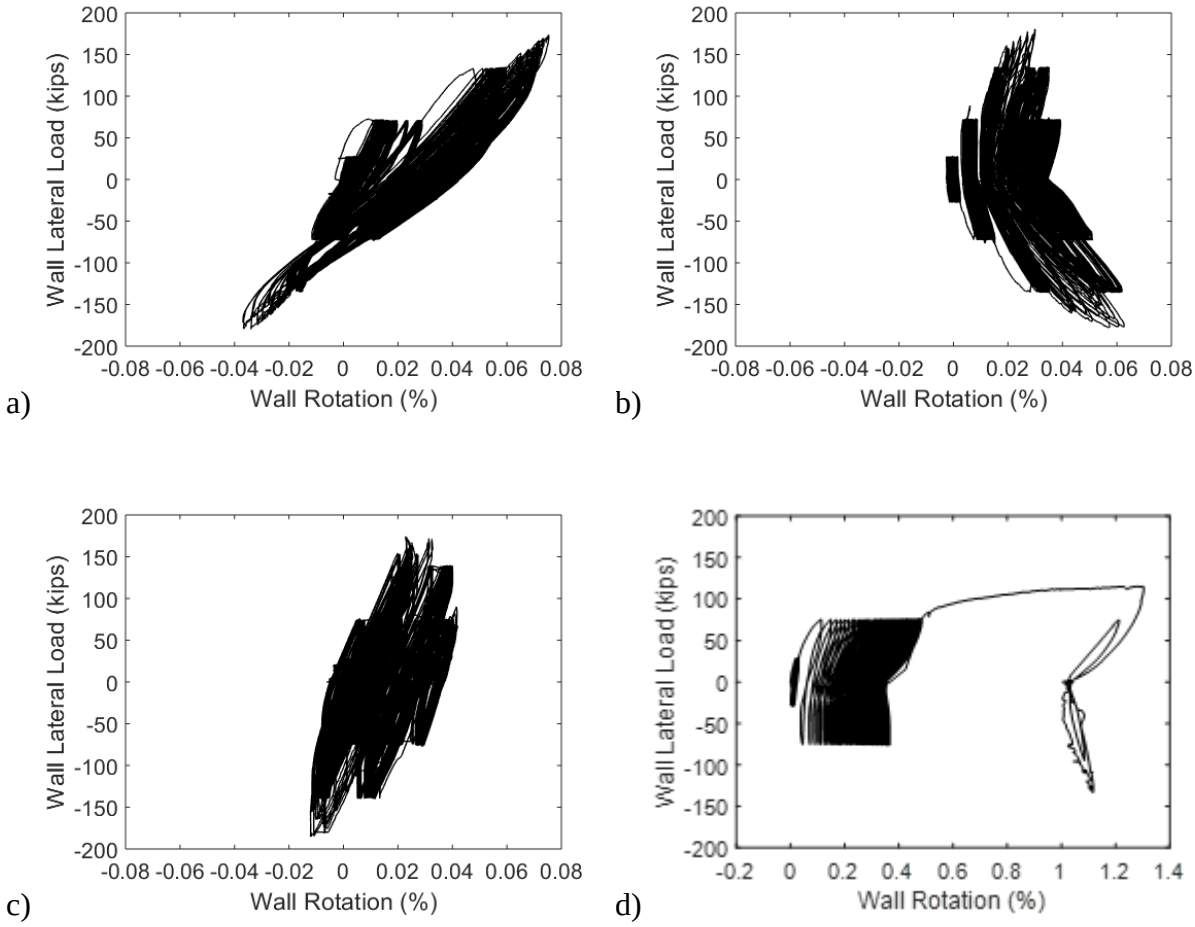

Figure 4.26. Wall Rotation for a) SRC-W1, b) SRC-W2, c) SRC-W3, and d) SRC-W4

It was shown in Section 4.2 that stiffness degradation was significant in the beams within groups of cycles prior to yielding, particularly during the 75 cycles at $0.75M_{pbe}$ for SRC-W1, SRC-W2, and SRC-W3 and during the cycles at lower levels for SRC-W4. For SRC-W1, SRC-W2, and SRC-W3, plots of secant stiffness during the first group of 75 cycles at $0.75M_{pbe}$ for both the wall and the beams are provided in Figure 4.27, with the wall secant stiffness determined from the data in Figure 4.26. The stiffness values provided in Figure 4.27 were normalized to the stiffness of the final cycle in this group of 75. It is evident from the data shown in Figure 4.27 that stiffness

degradation at this loading level was most significant in the beam for SRC-W1 and SRC-W3. The stiffness degradation for the wall was larger for SRC-W2 than SRC-W1 over the first 15 cycles in this group, with much of this difference coming from the first to second cycles. The level of stiffness degradation in the beam for SRC-W2 was comparable to that in the wall during testing of SRC-W1. The level of stiffness degradation in the wall for SRC-W3 was lower than that for SRC-W1 and SRC-W2, as degradation of stiffness in the wall did not occur for SRC-W3 over these 75 cycles.

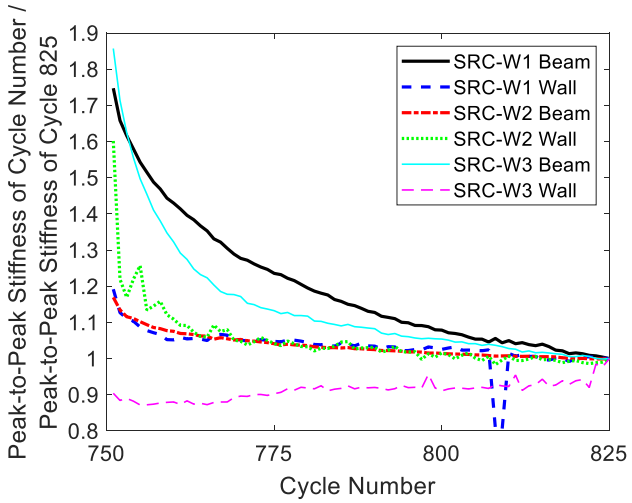

Figure 4.27. Stiffness Degradation during First Group of 75 Cycles at 0.75M_{pbe}

4.8. Wall Strain Profiles

Wall strain profiles, based on LVDT measurements, at the locations shown in Figure 3.16 are provided in Figure 4.28 through Figure 4.35. The strain profiles were formulated using strain values at the peak of each first cycle at each increment of load or displacement applied. The plots

for SRC-W2 and SRC-W4 do not include residual strain after completion of testing of SRC-W1 and SRC-W3, respectively, as some LVDT locations changed within the wall between tests to accommodate the consistent LVDT layout relative to the test beam, as shown in Figure 3.16. Plane-section behavior is often not evident in Figure 4.28 through Figure 4.31, with larger strains measured at the end of the wall with the embedded beam. For SRC-W1, SRC-W2, and SRC-W3, the measured strains were generally less than the yield strain, which was computed for each test based on the measured yield stress in the reinforcement, provided in Table 3.2, and an elastic modulus for steel of 29,000 ksi. The peak compressive strains occurred in the vicinity of the embedded steel section and approached the yield strain for the three tests. For SRC-W4, yielding was measured in compression at locations below the coupling beam, and yielding was measured in tension at locations in Row 3 through Row 8. The majority of these locations were above and below the embedded steel section, but there were also locations on the other side of the wall. The largest tensile strains for this beam were measured at Row 5, the location at which the sensors spanned across the embedded steel section, and reached peak values between 5% and 6% at locations closest to the beam-wall interface.

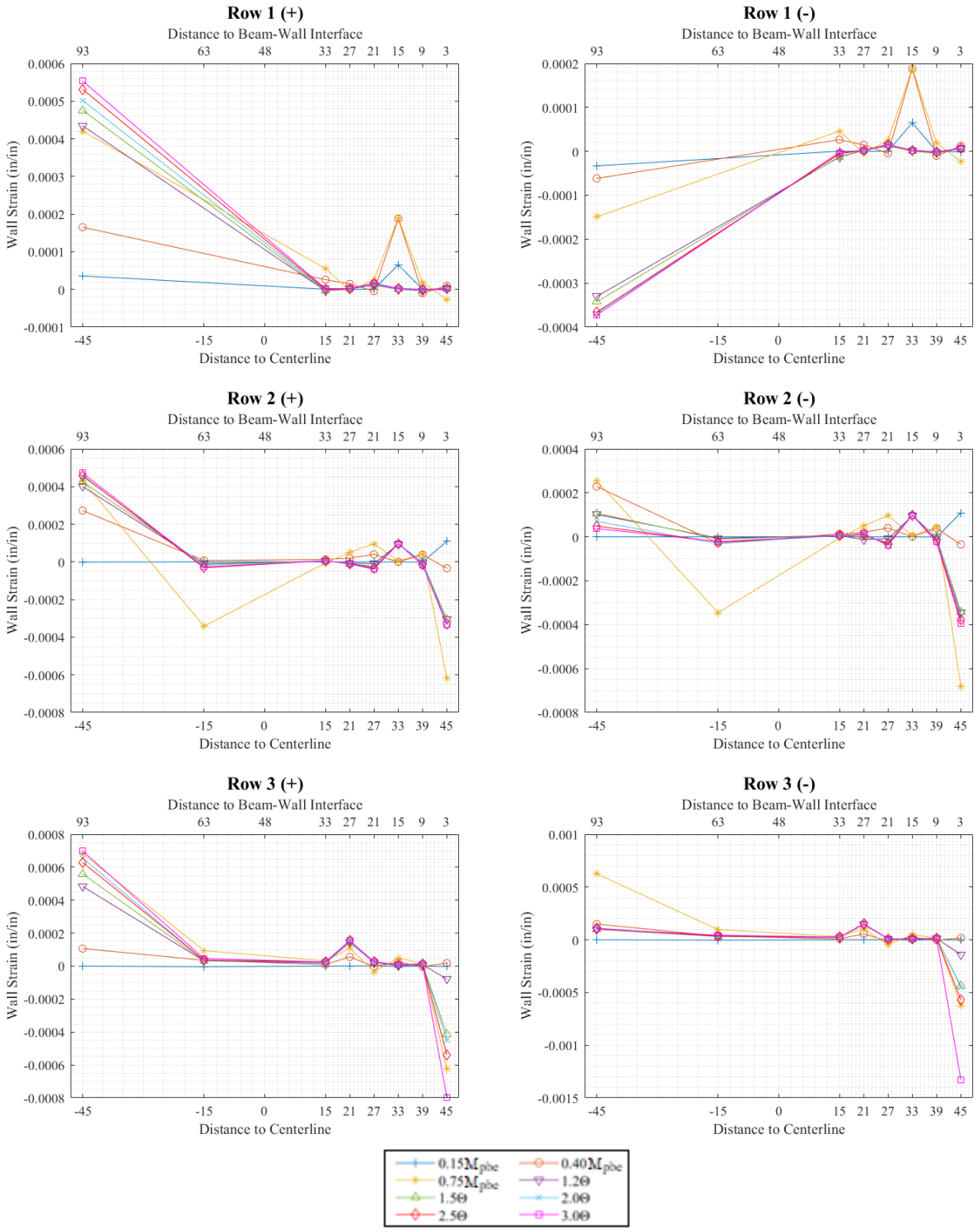

Figure 4.28. Wall Strain along Cross-Sections for SRC-W1

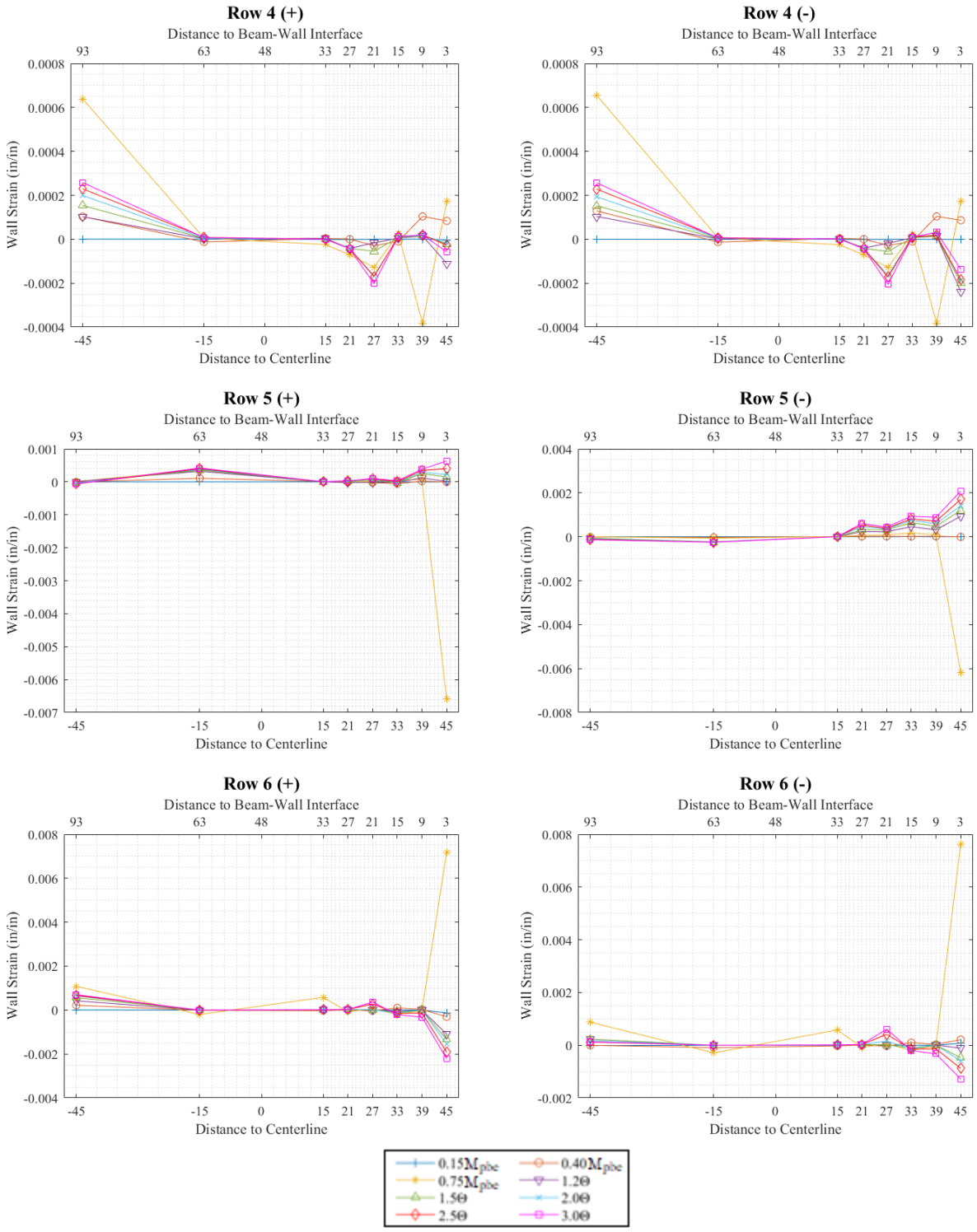

Figure 4.28. Wall Strain along Cross-Sections for SRC-W1 (continued)

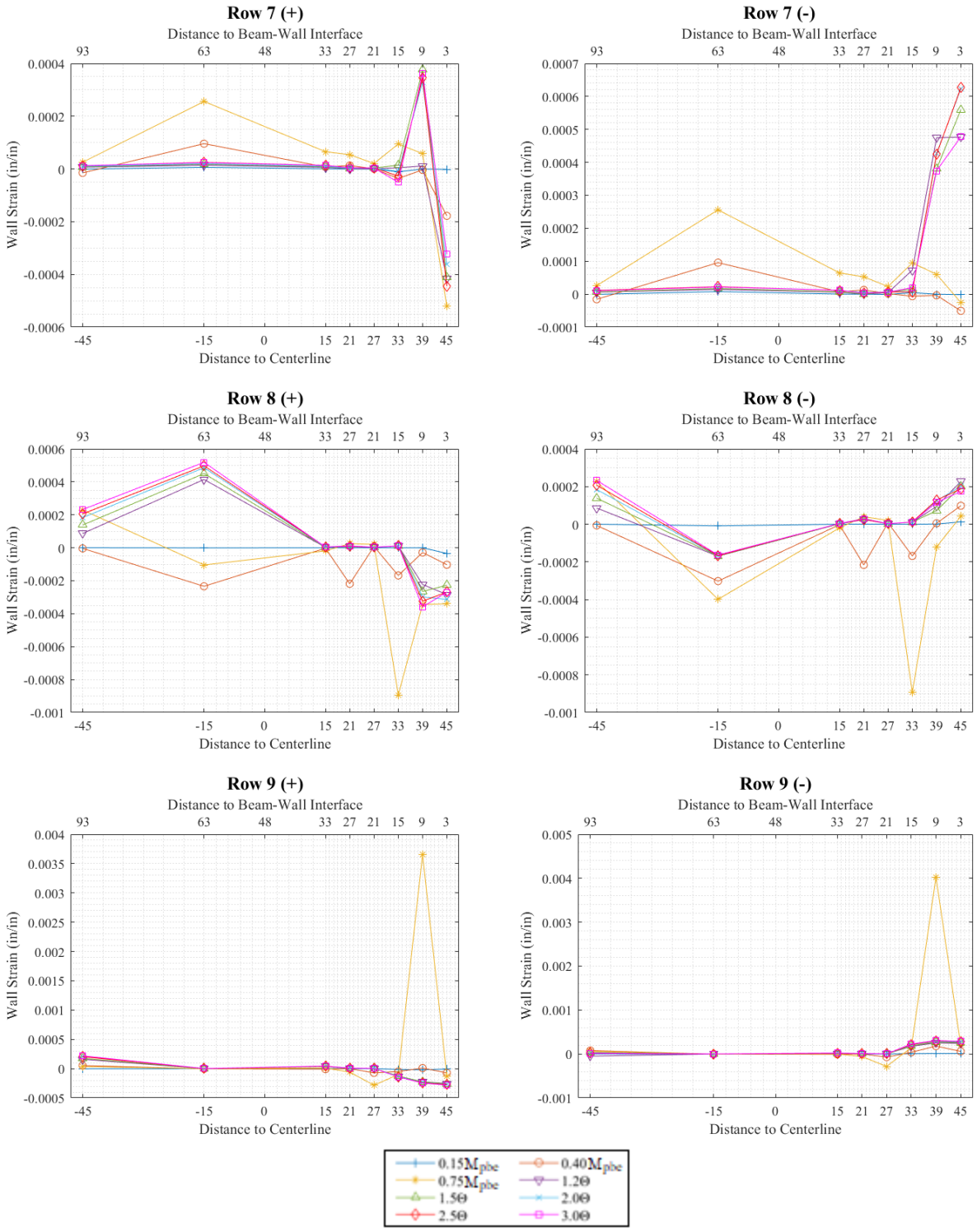

Figure 4.28. Wall Strain along Cross-Sections for SRC-W1 (continued)

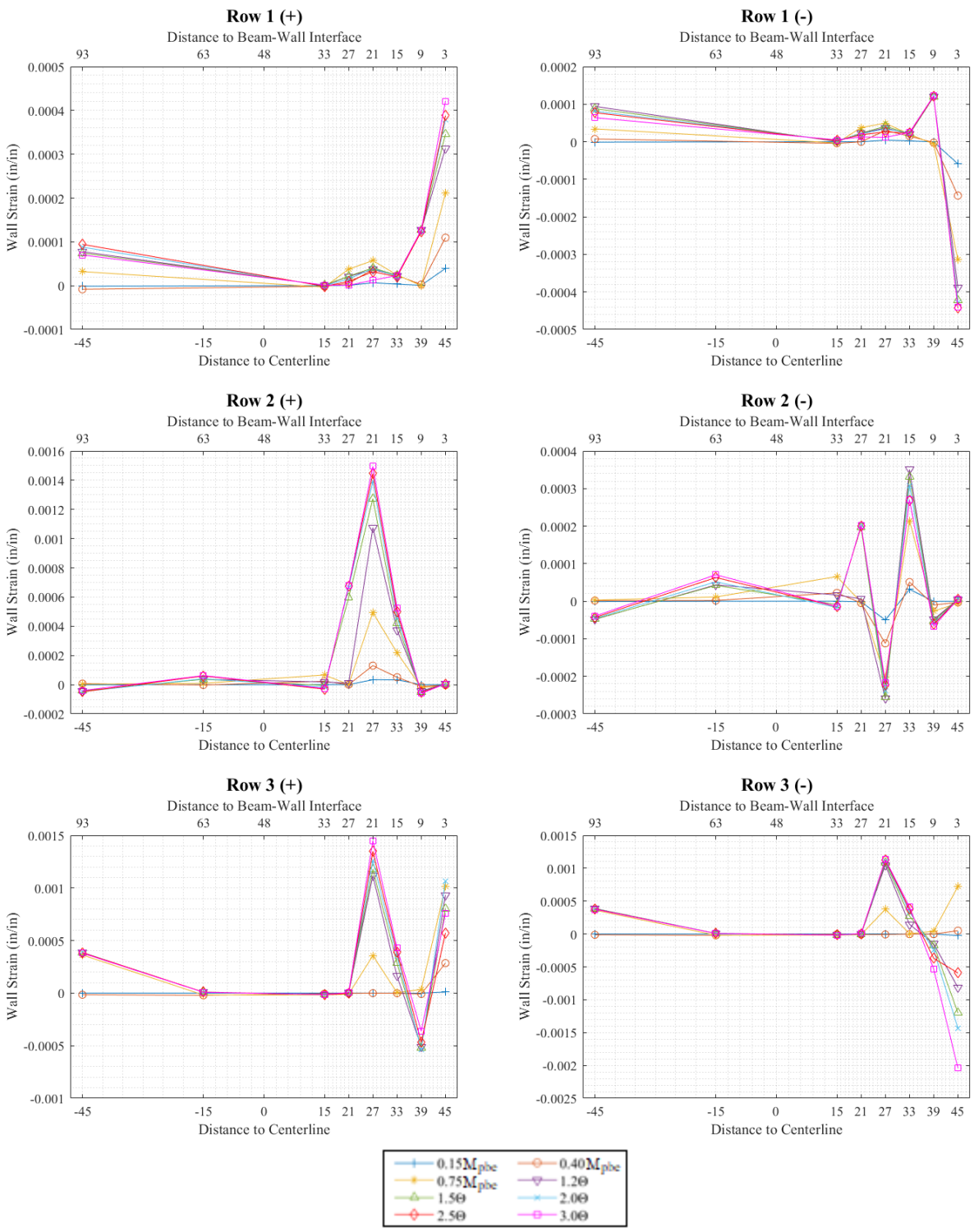

Figure 4.29. Wall Strain along Cross-Sections for SRC-W2

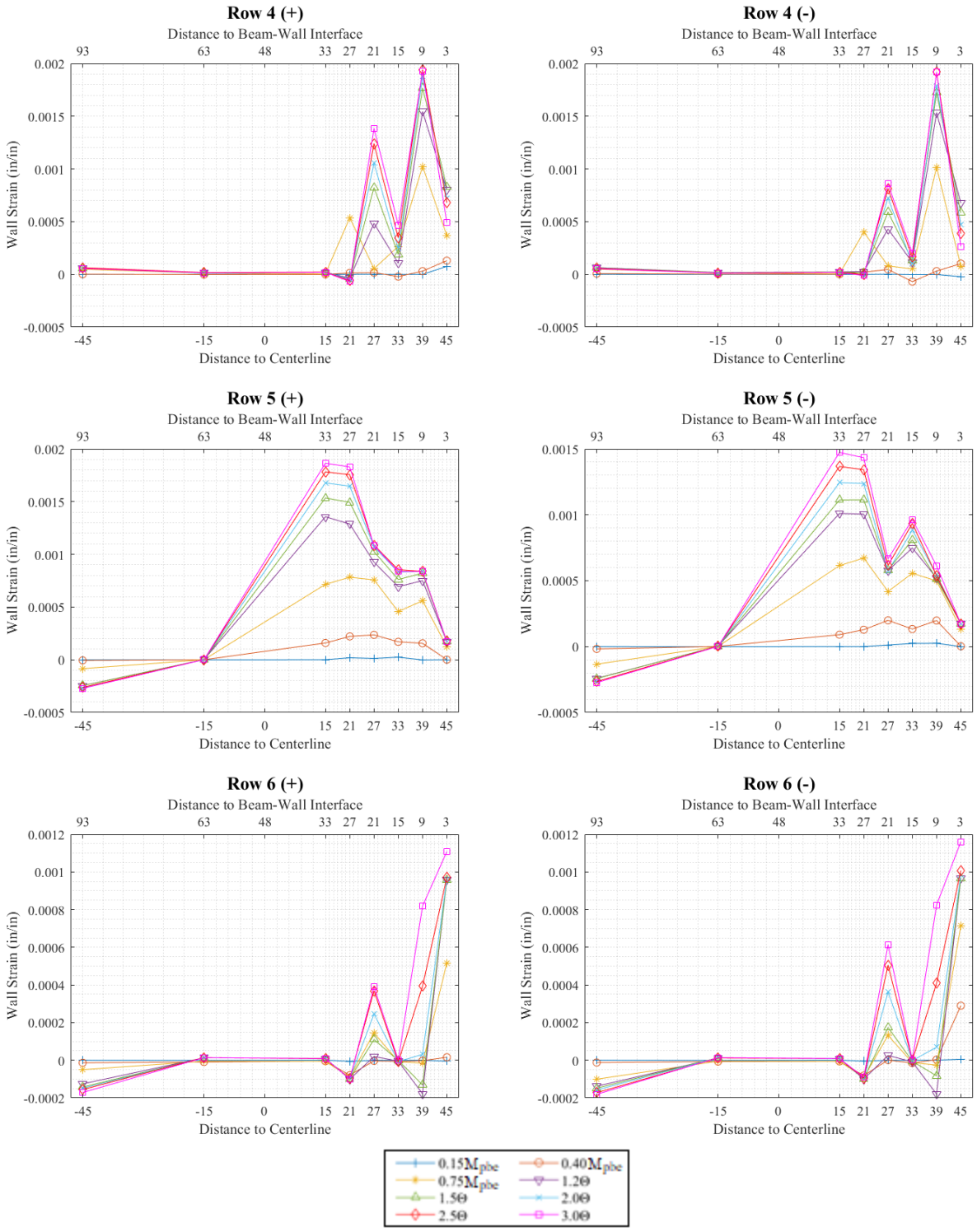

Figure 4.29. Wall Strain along Cross-Sections for SRC-W2 (continued)

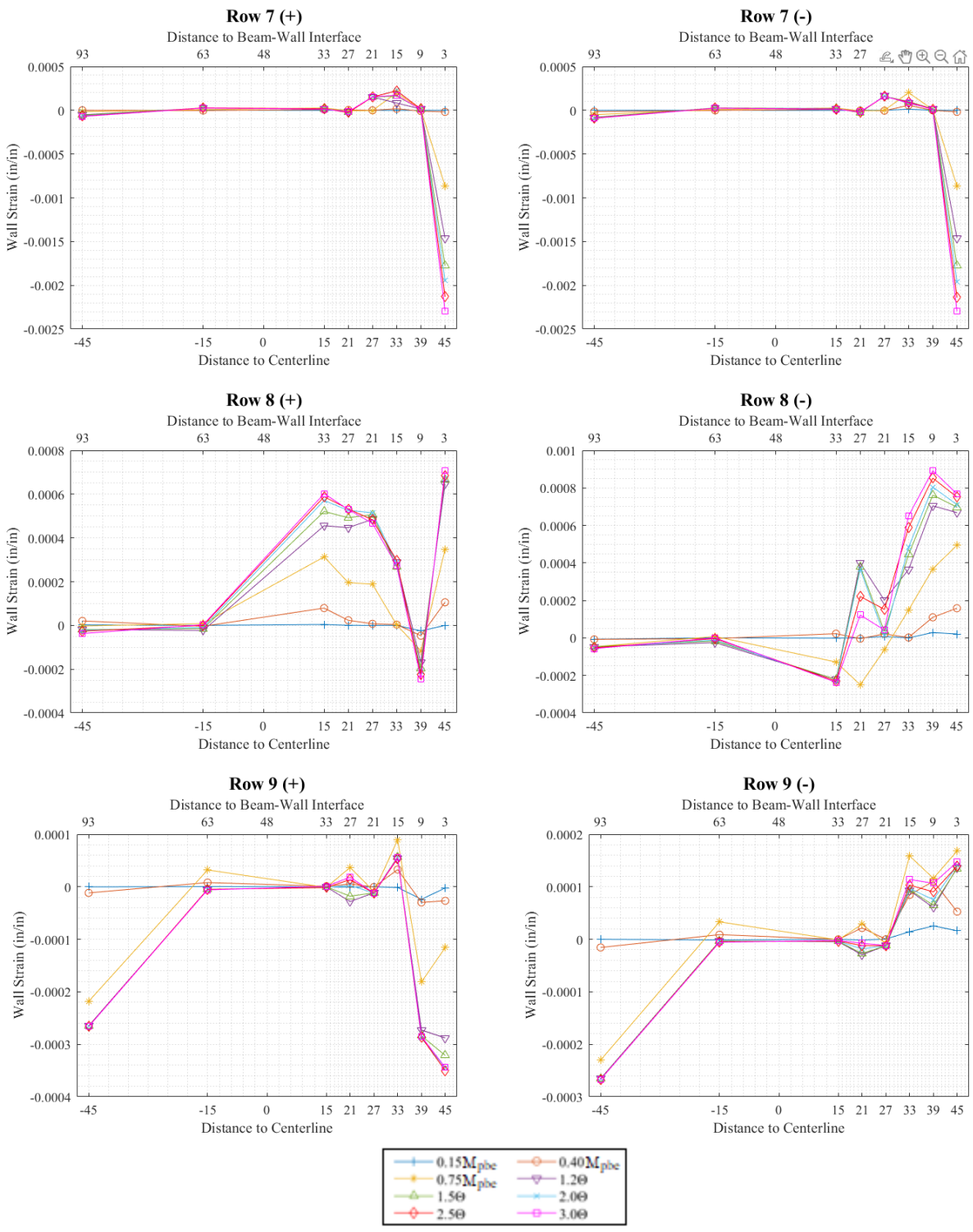

Figure 4.29. Wall Strain along Cross-Sections for SRC-W2 (continued)

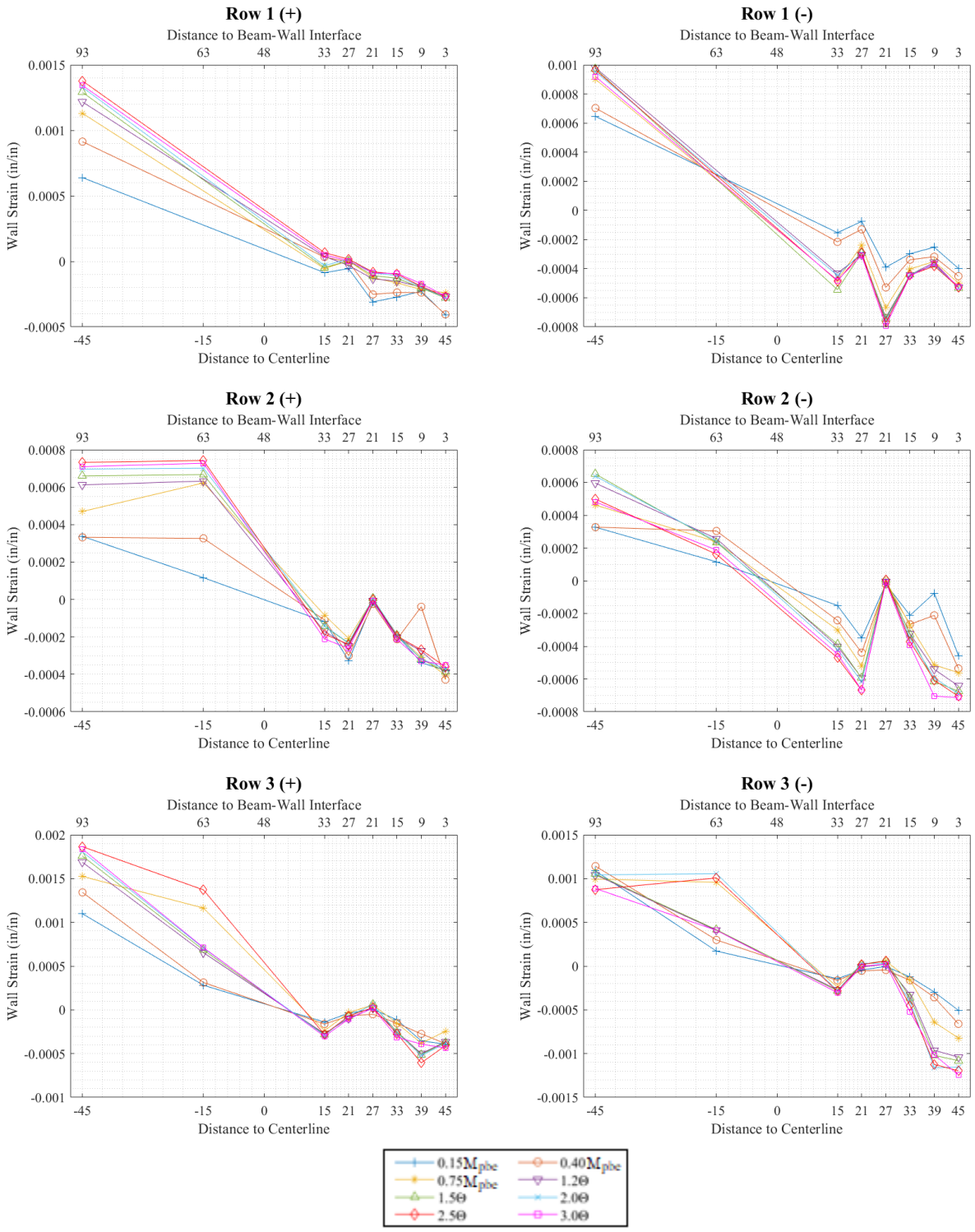

Figure 4.30. Wall Strain along Cross-Sections for SRC-W3

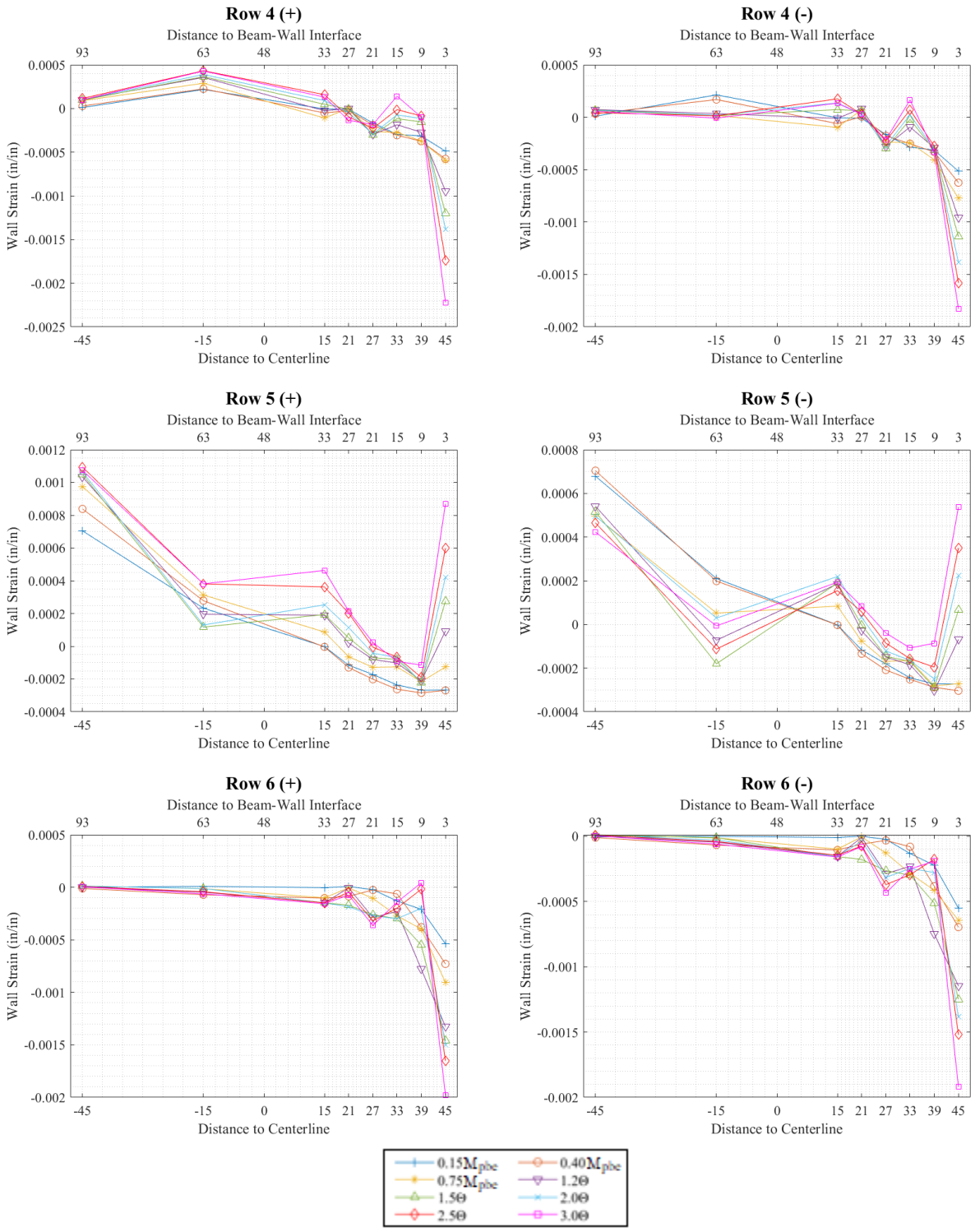

Figure 4.30. Wall Strain along Cross-Sections for SRC-W3 (continued)

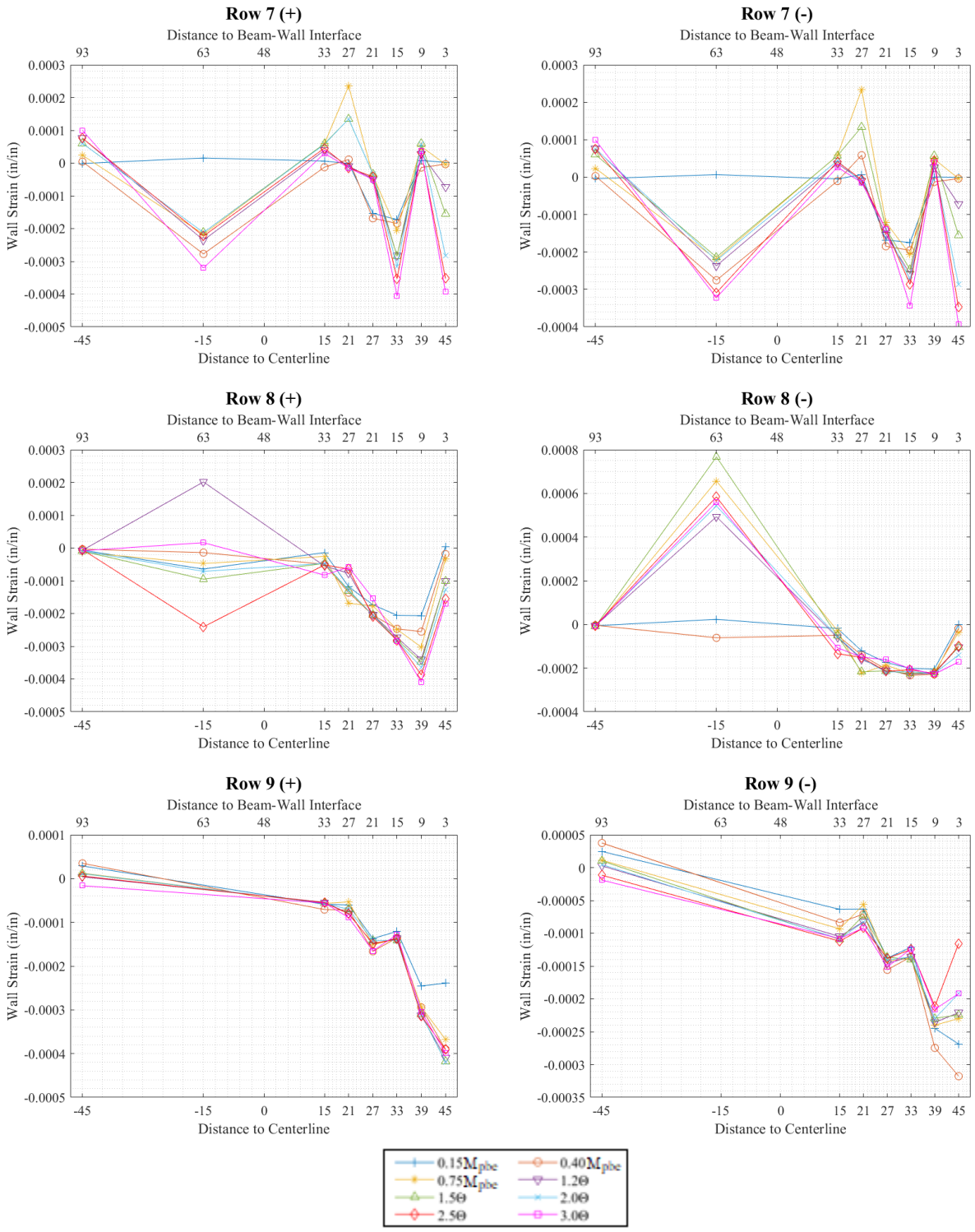

Figure 4.30. Wall Strain along Cross-Sections for SRC-W3 (continued)

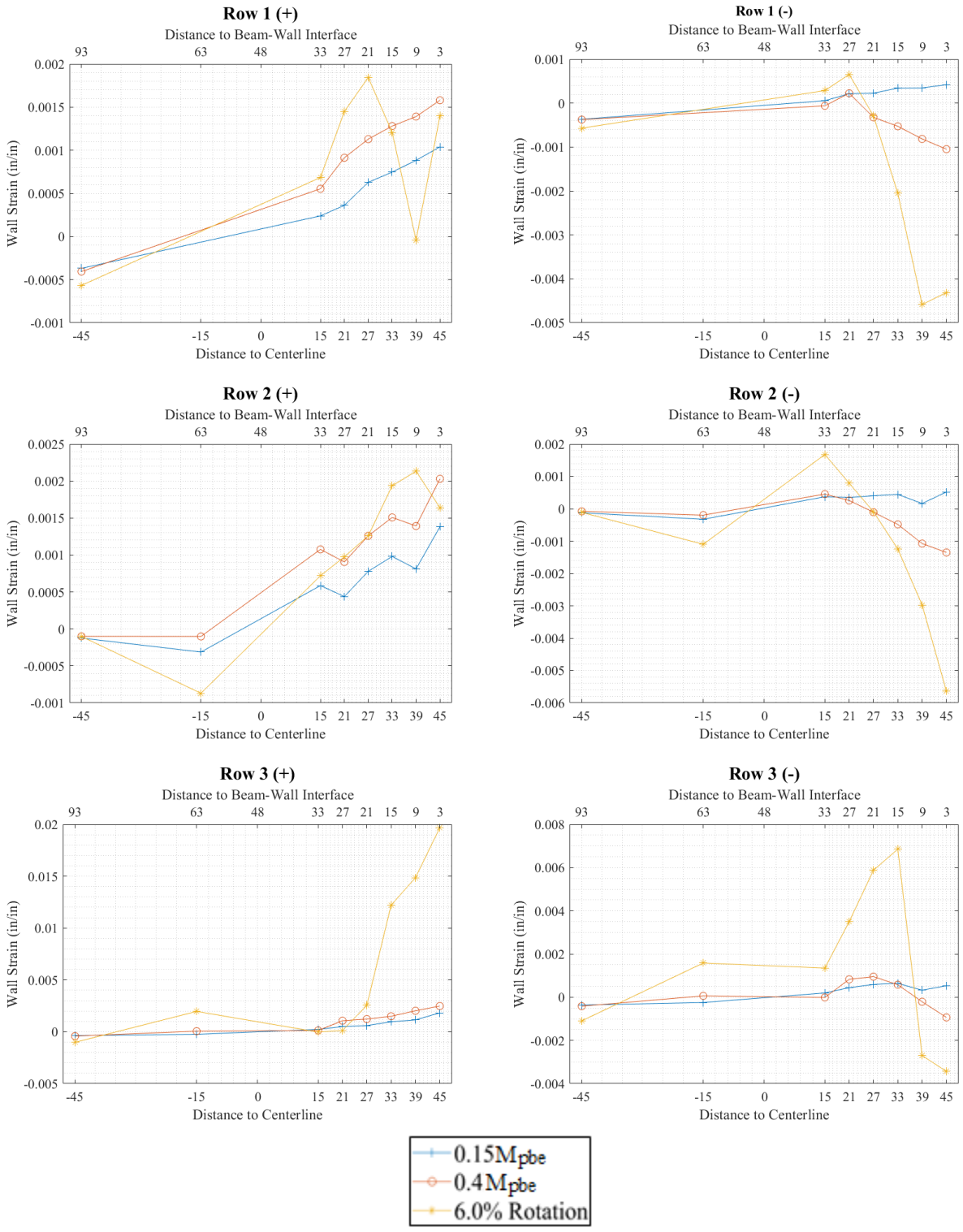

Figure 4.31. Wall Strain along Cross-Sections for SRC-W4

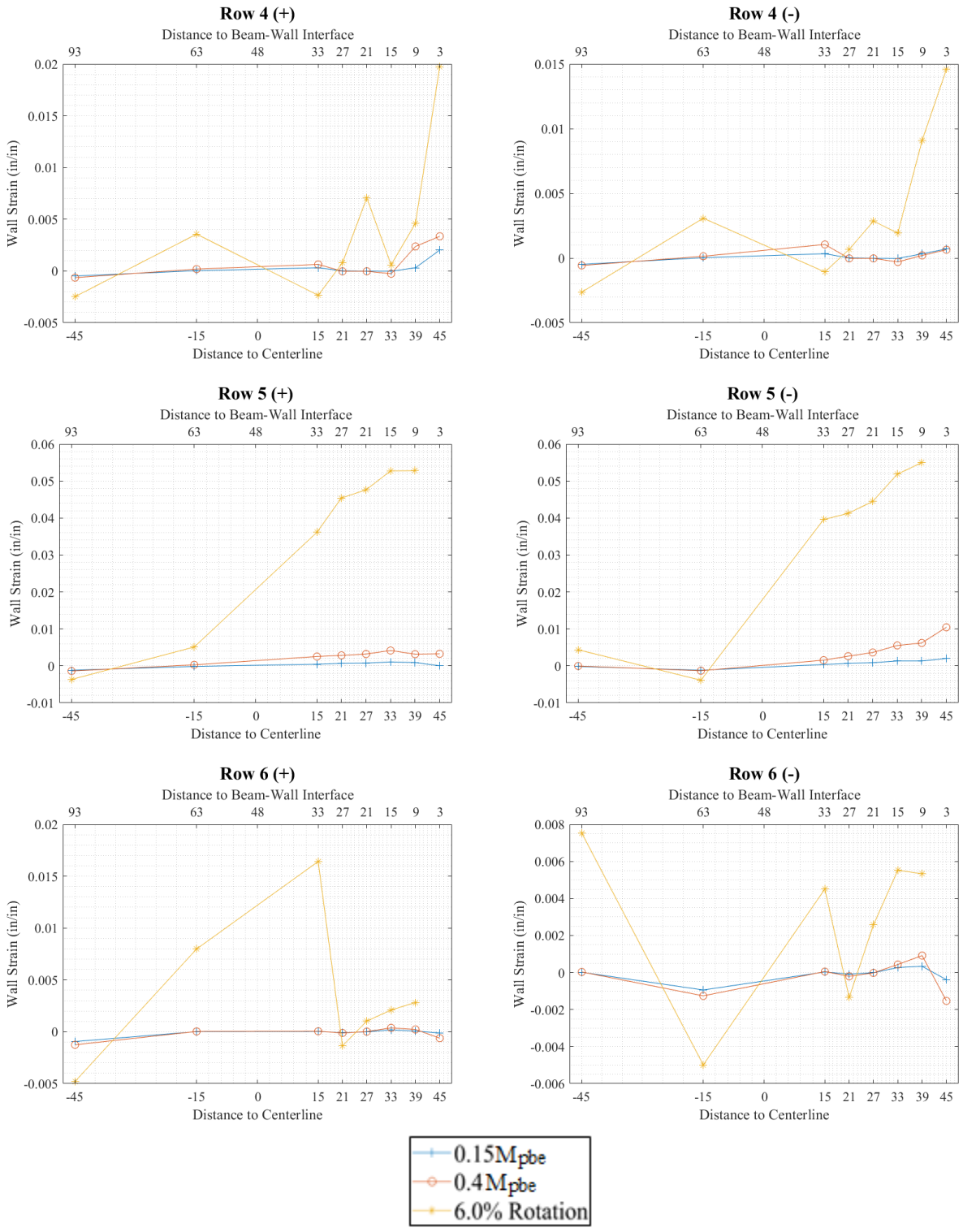

Figure 4.31. Wall Strain along Cross-Sections for SRC-W4 (continued)

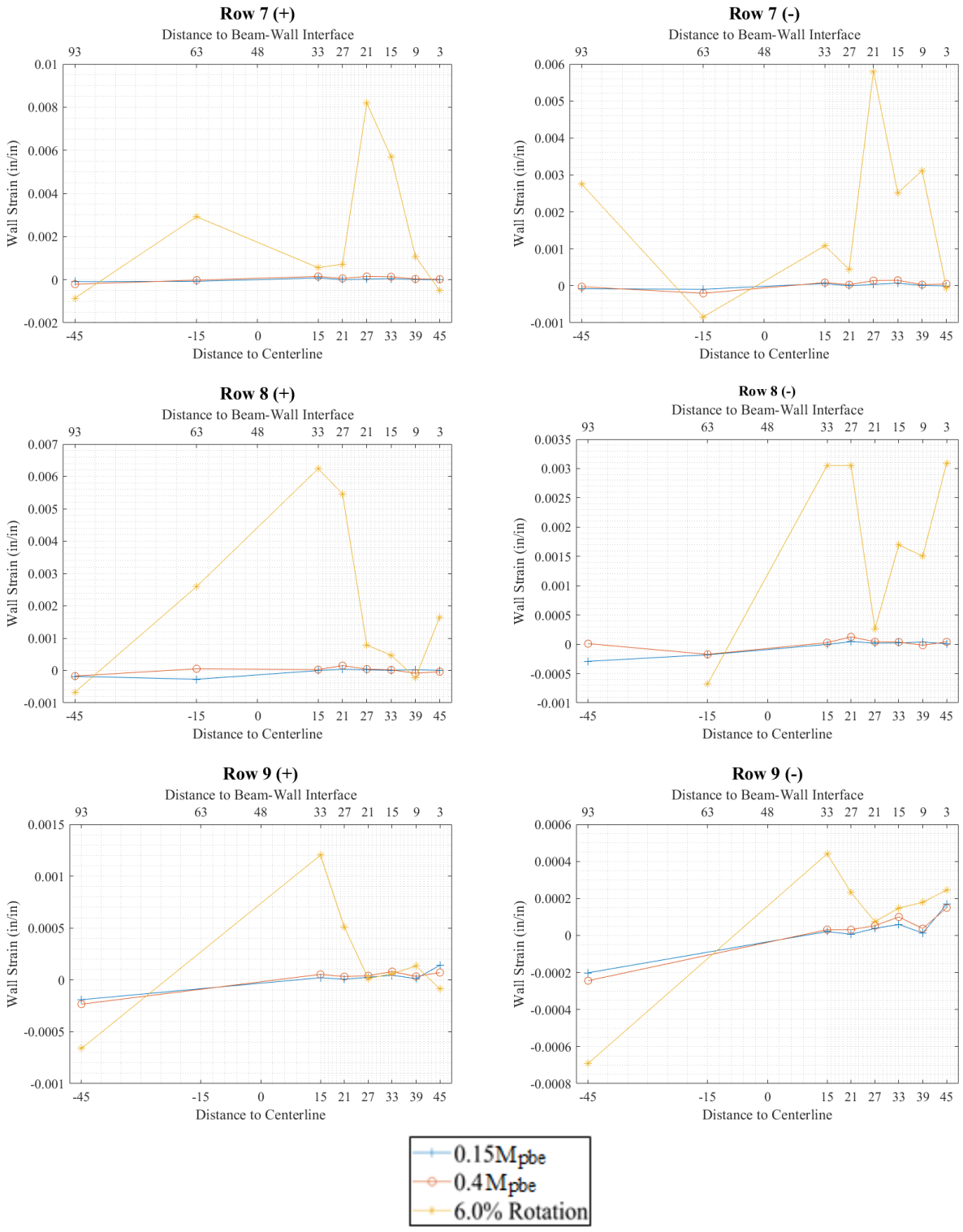

Figure 4.31 Wall Strain along Cross-Sections for SRC-W4 (continued)

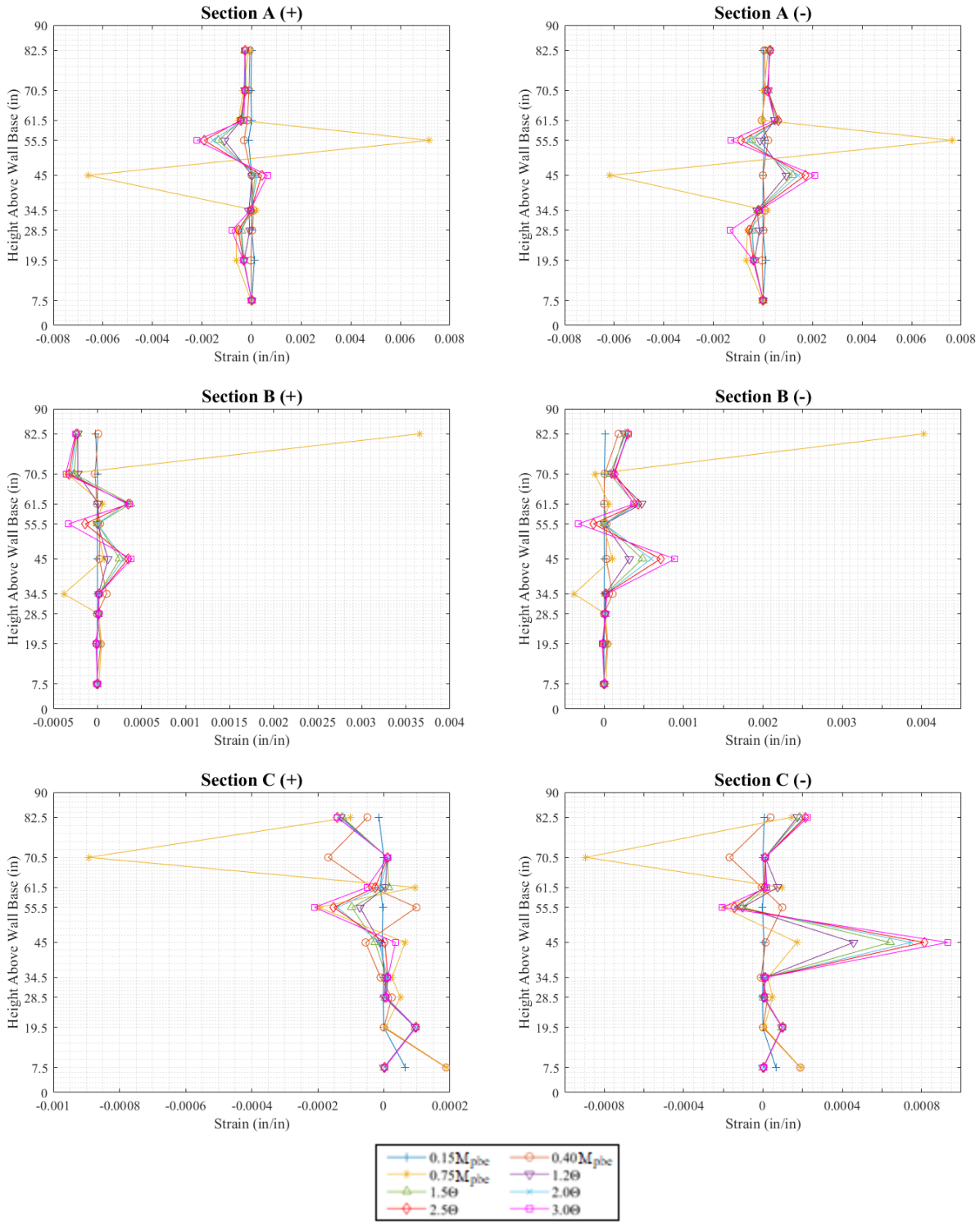

Figure 4.32. Wall Strain over Height for SRC-W1

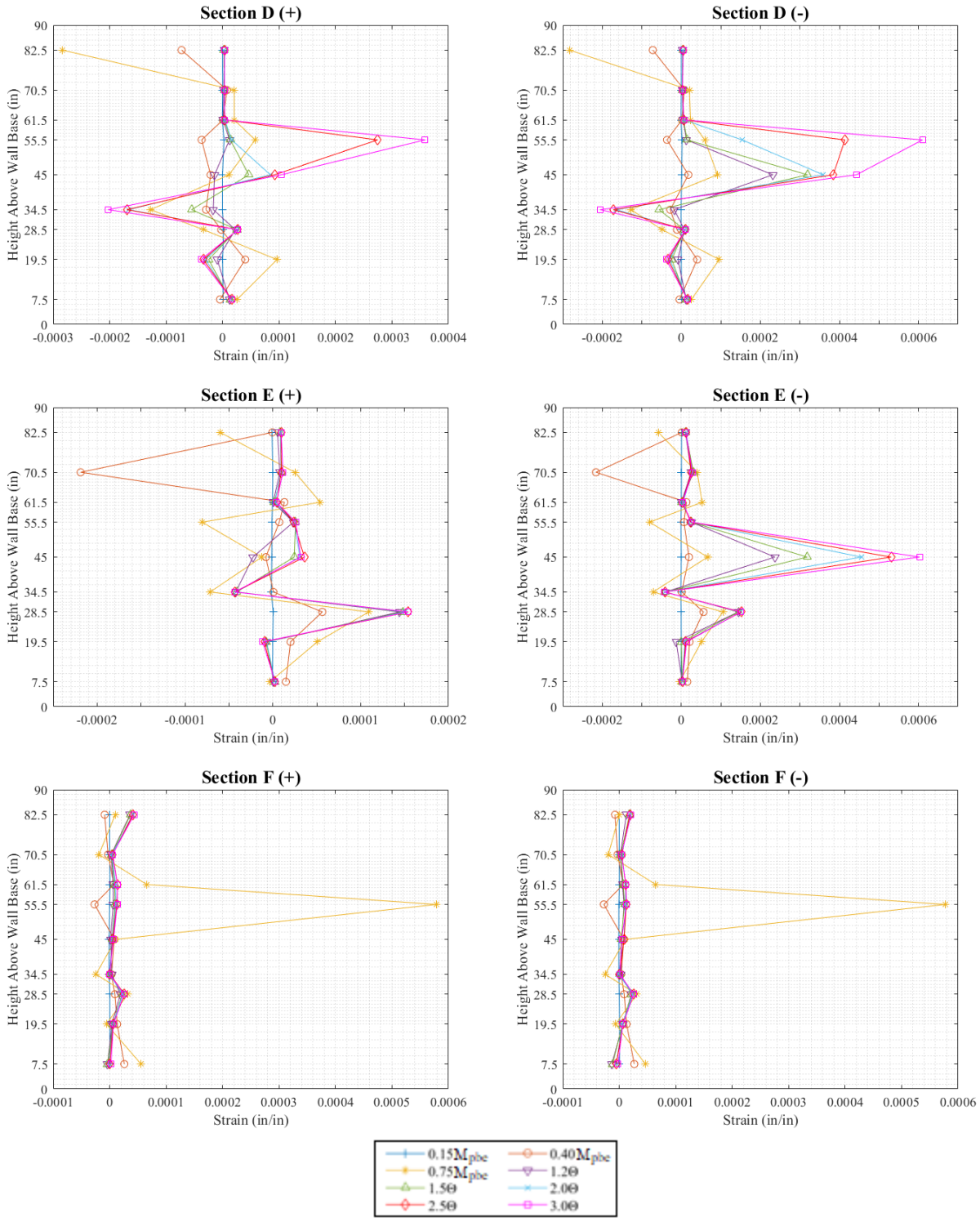

Figure 4.32. Wall Strain over Height for SRC-W1 (continued)

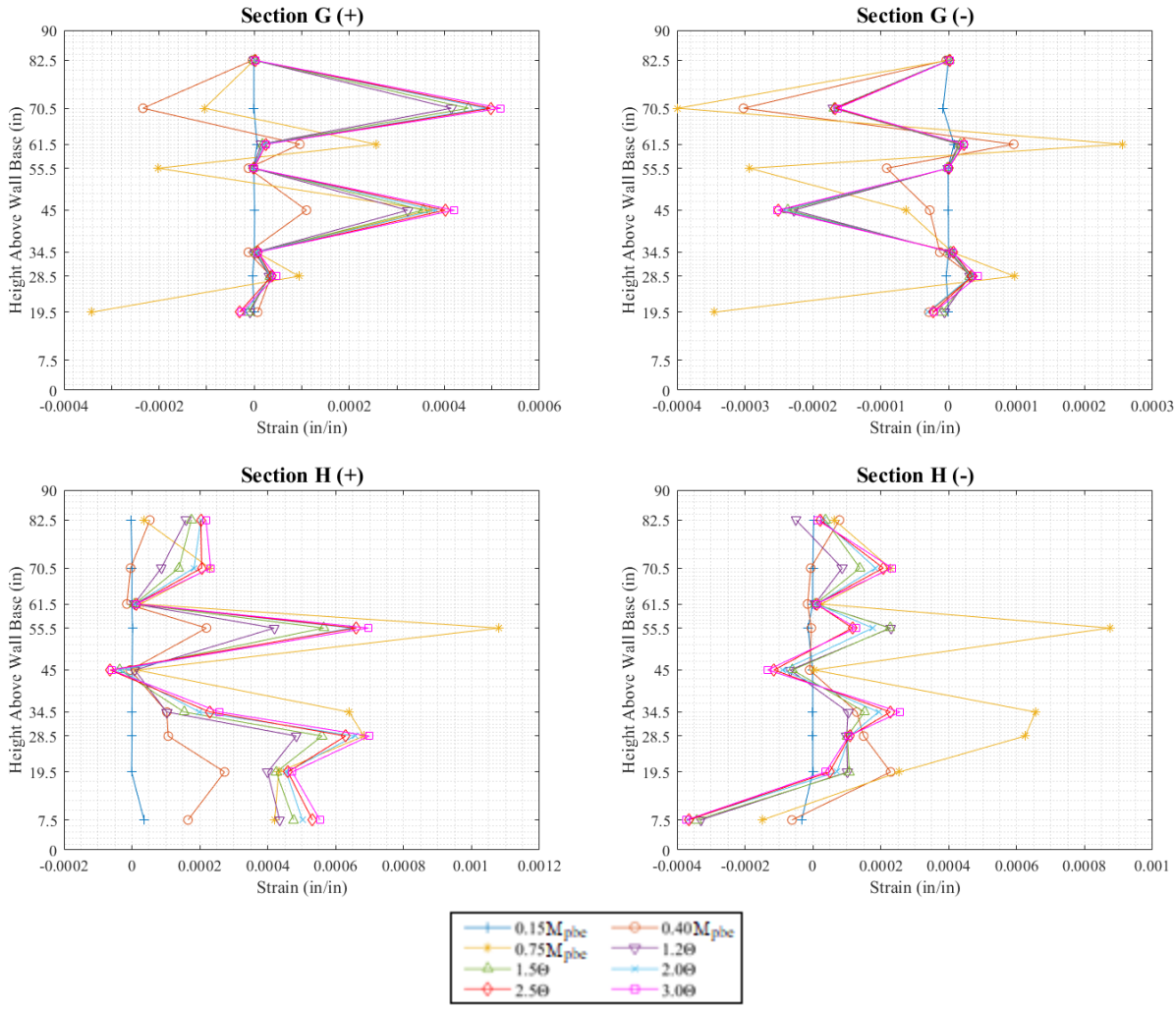

Figure 4.32. Wall Strain over Height for SRC-W1 (continued)

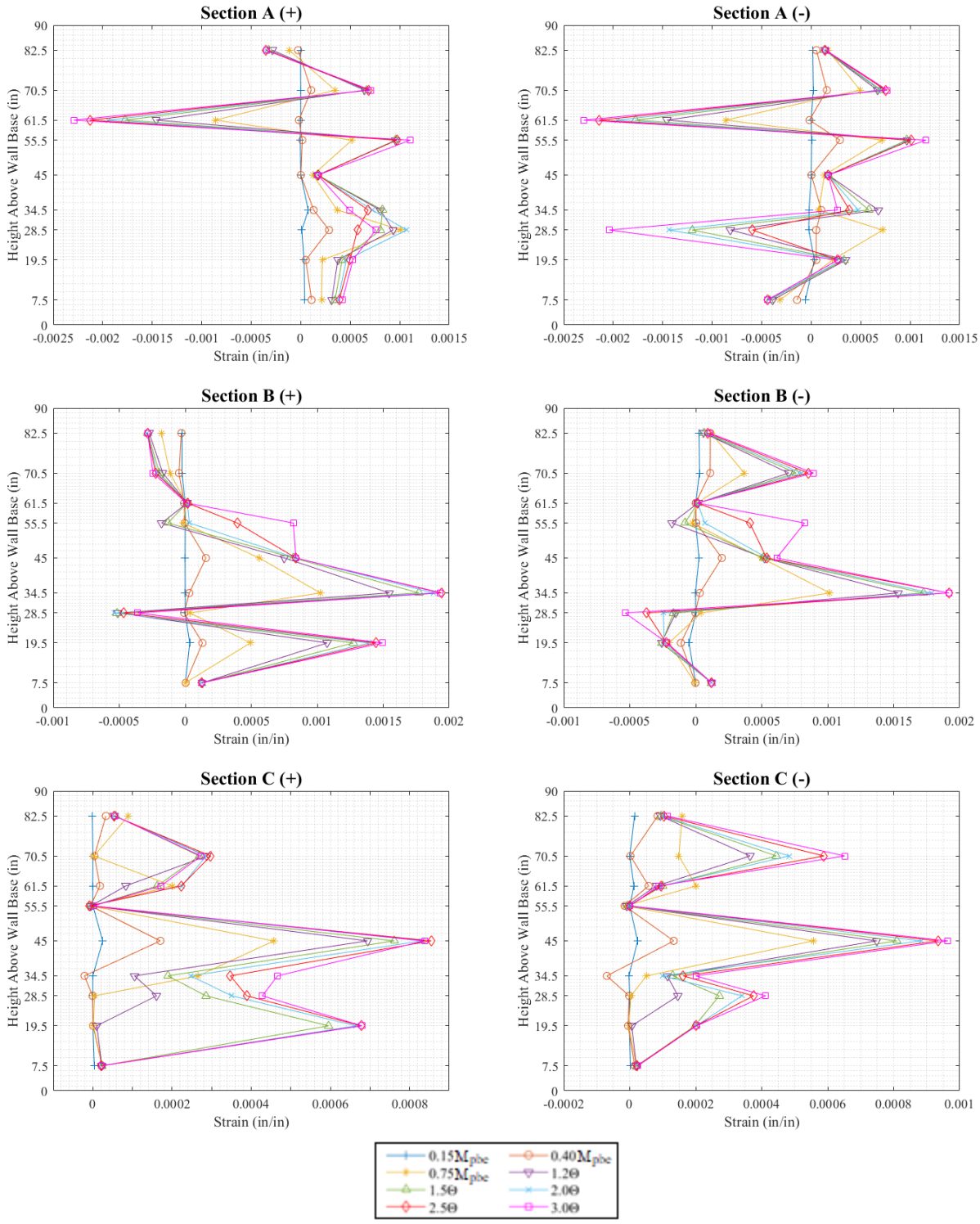

Figure 4.33. Wall Strain over Height for SRC-W2

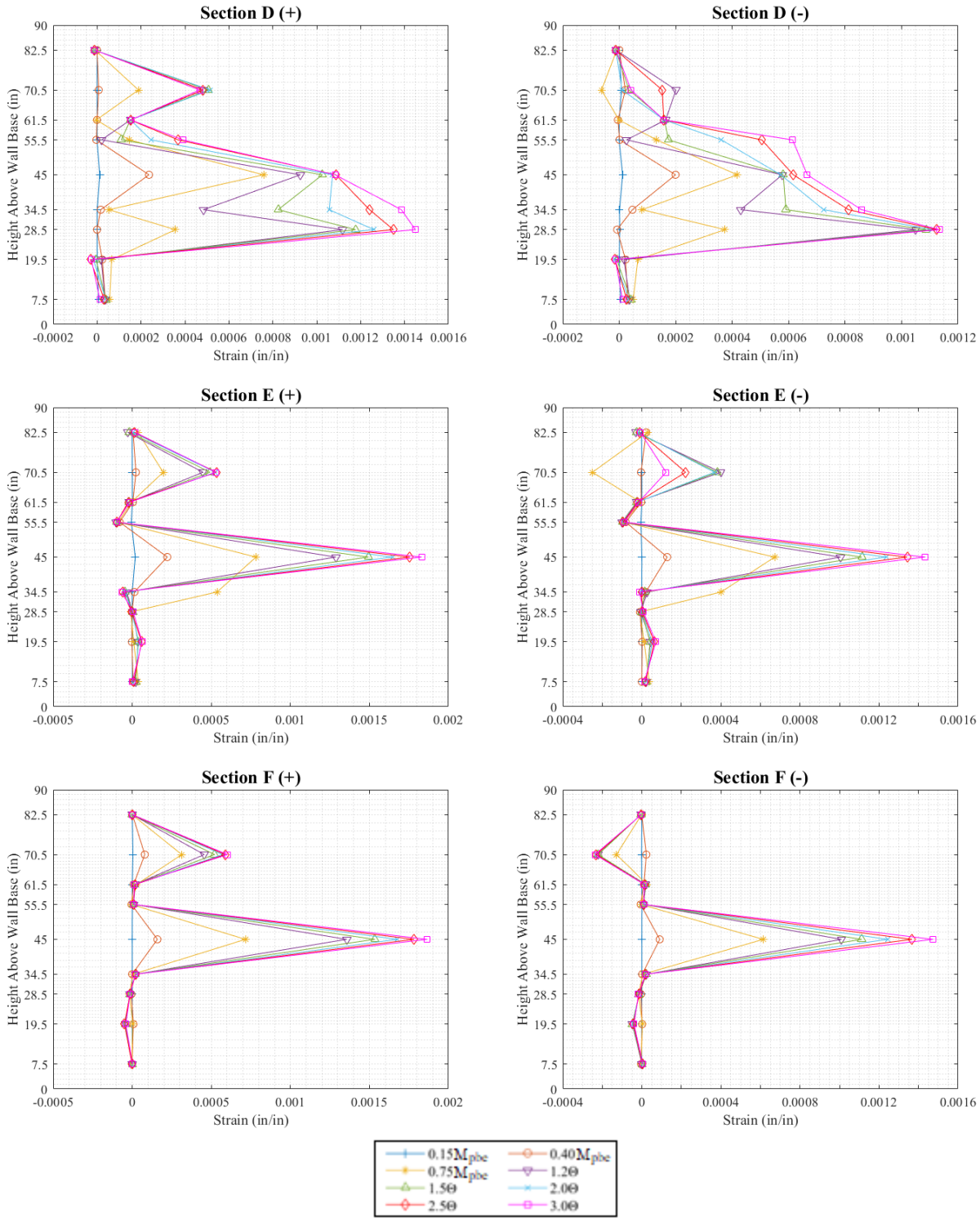

Figure 4.33. Wall Strain over Height for SRC-W2 (continued)

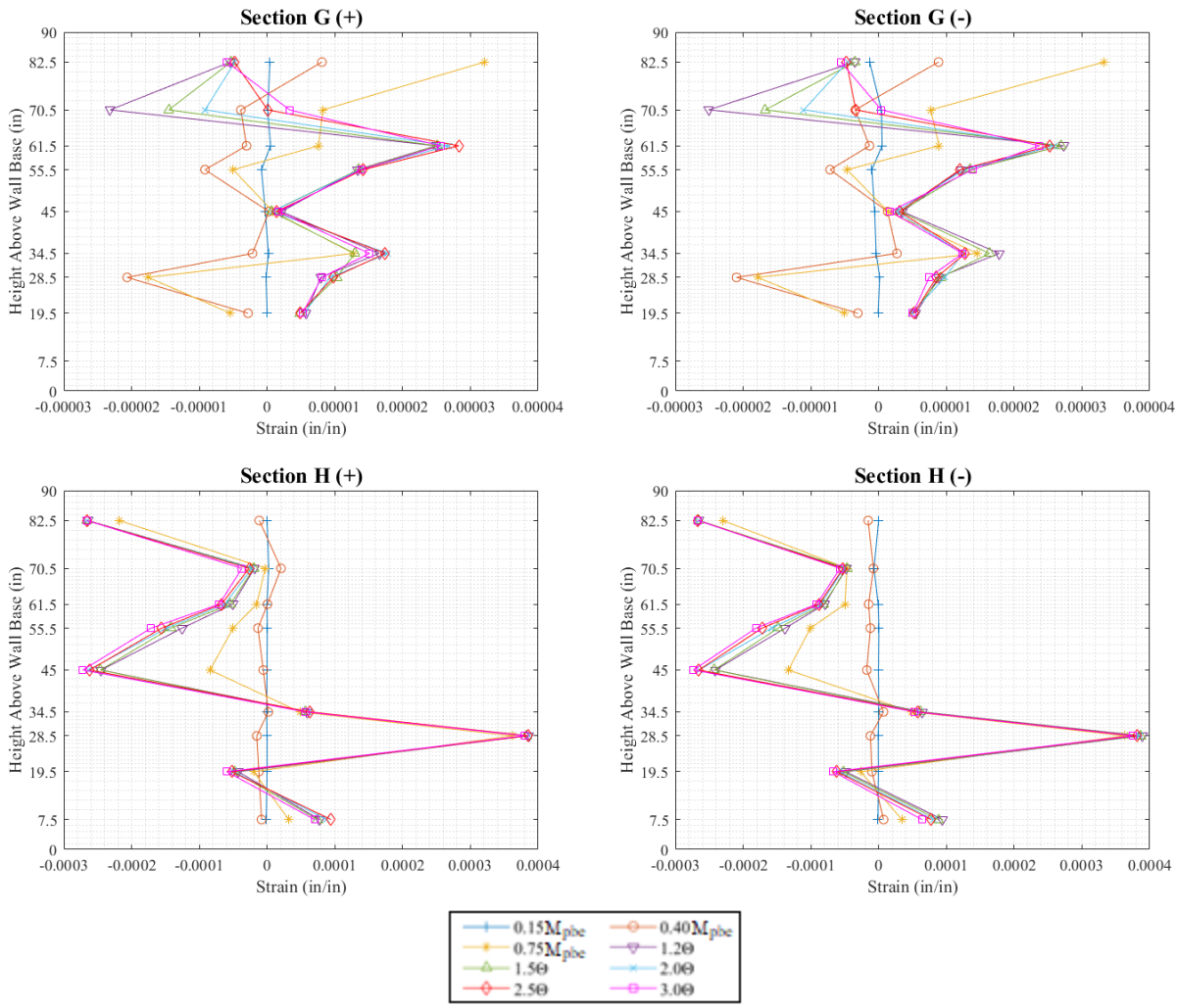

Figure 4.33. Wall Strain over Height for SRC-W2 (continued)

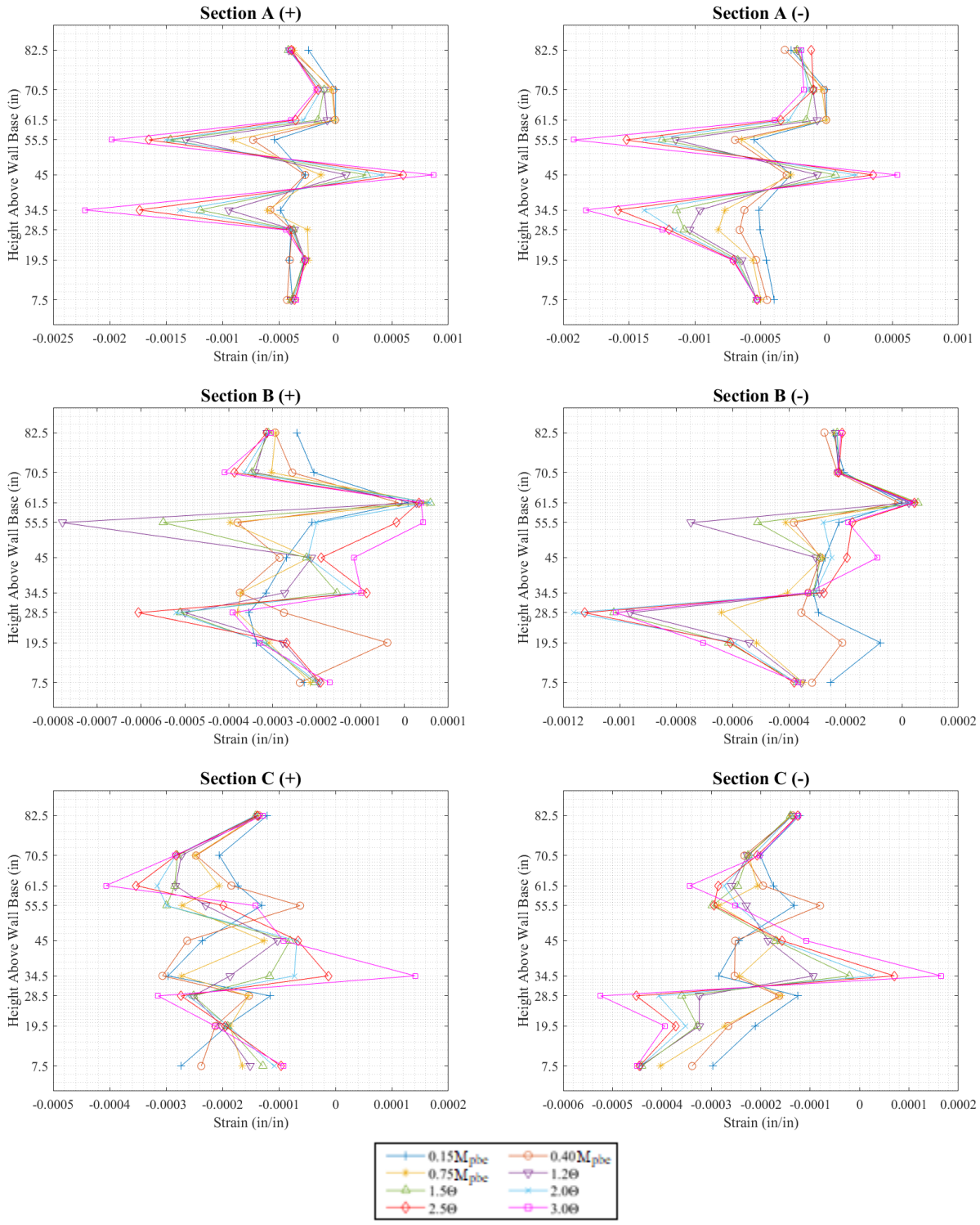

Figure 4.34. Wall Strain over Height for SRC-W3

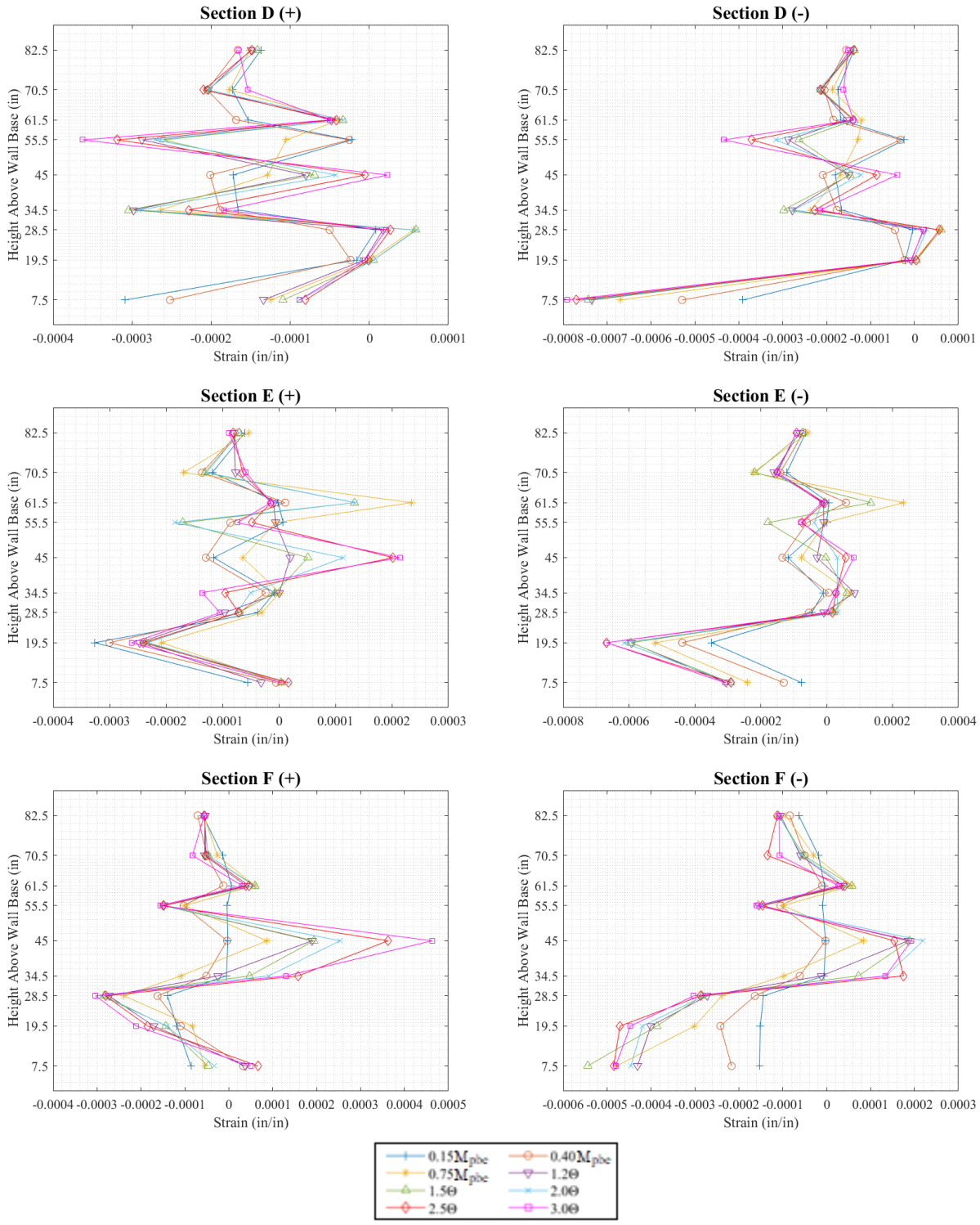

Figure 4.34. Wall Strain over Height for SRC-W3 (continued)

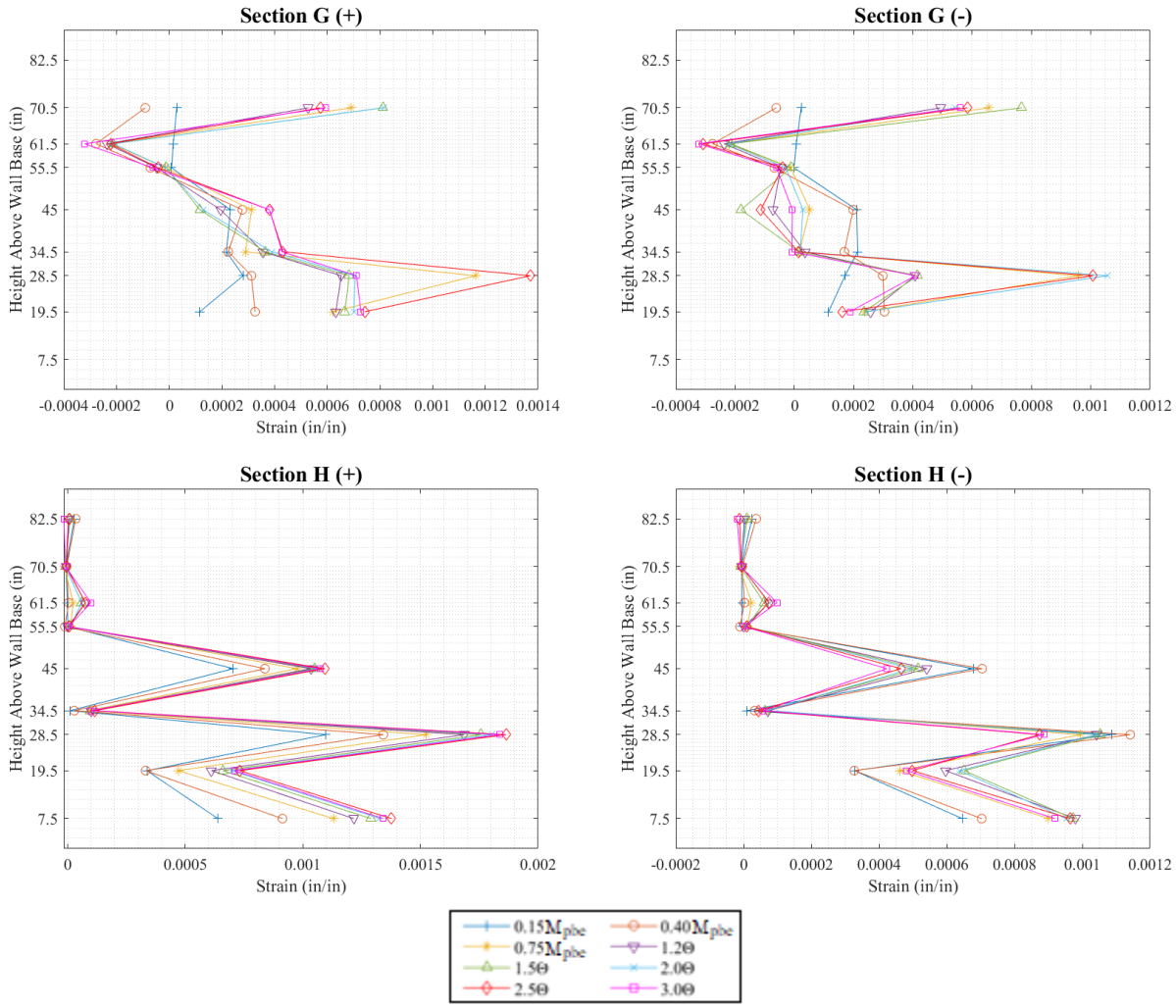

Figure 4.34. Wall Strain over Height for SRC-W3 (continued)

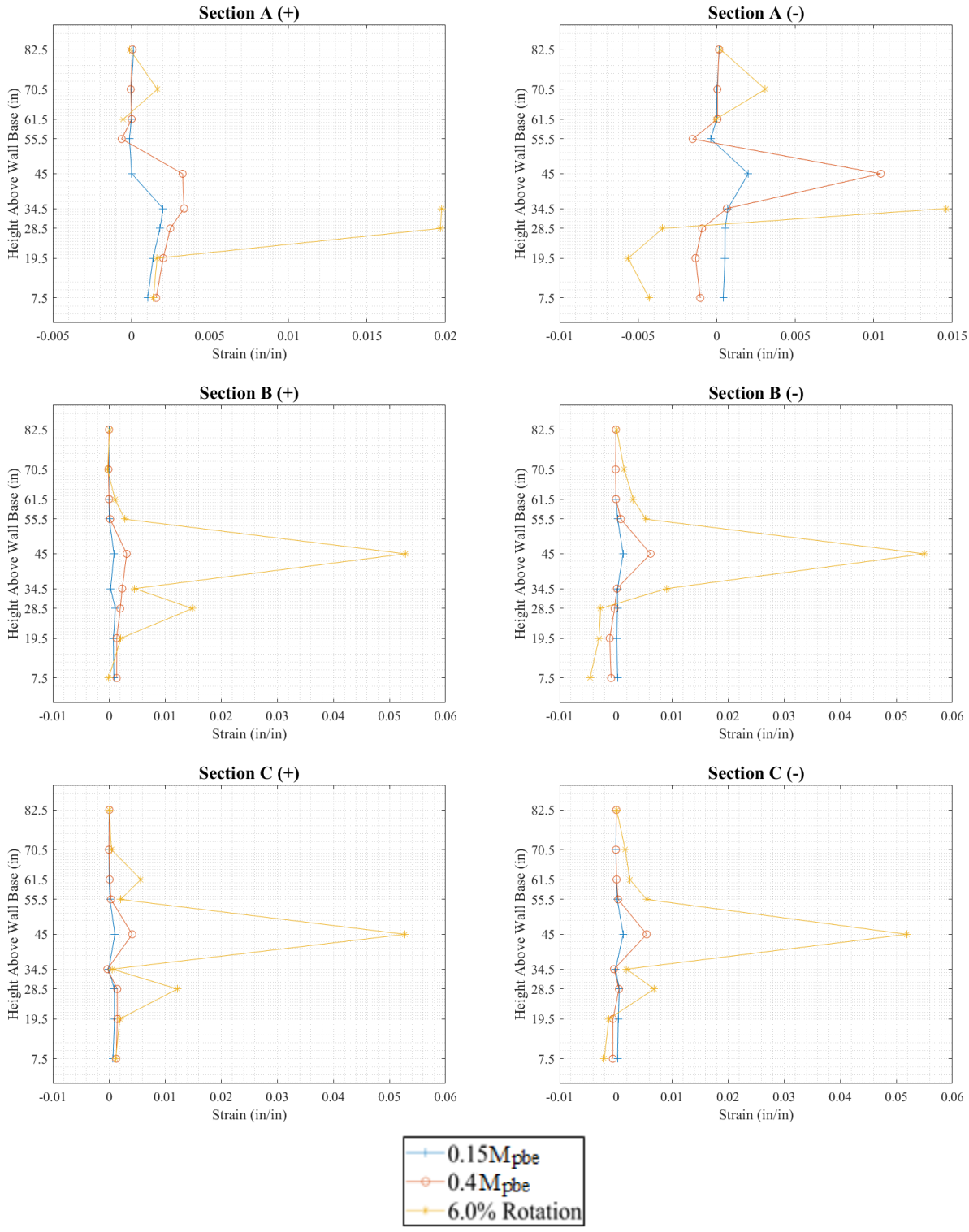

Figure 4.35. Wall Strain over Height for SRC-W4

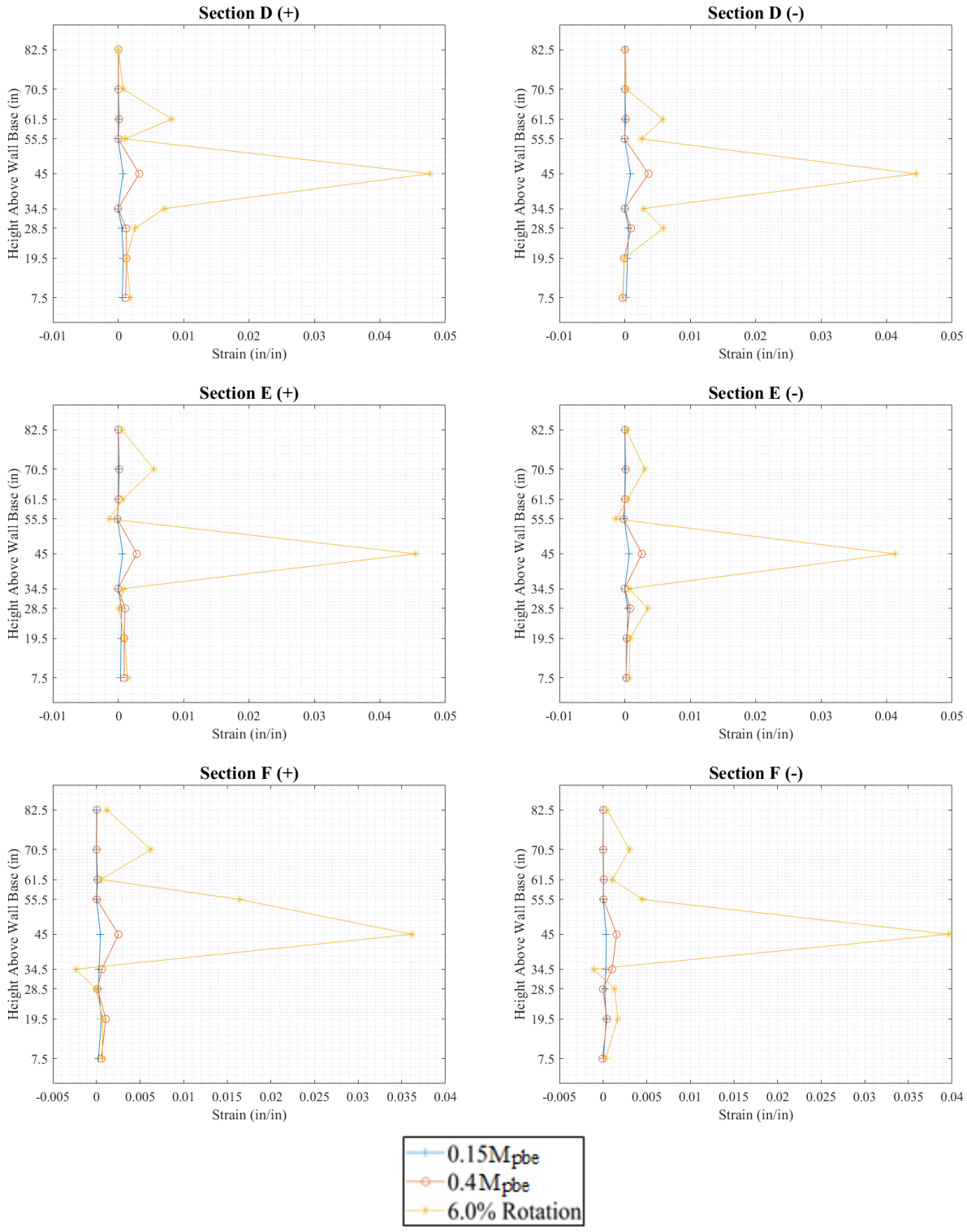

Figure 4.35. Wall Strain over Height for SRC-W4 (continued)

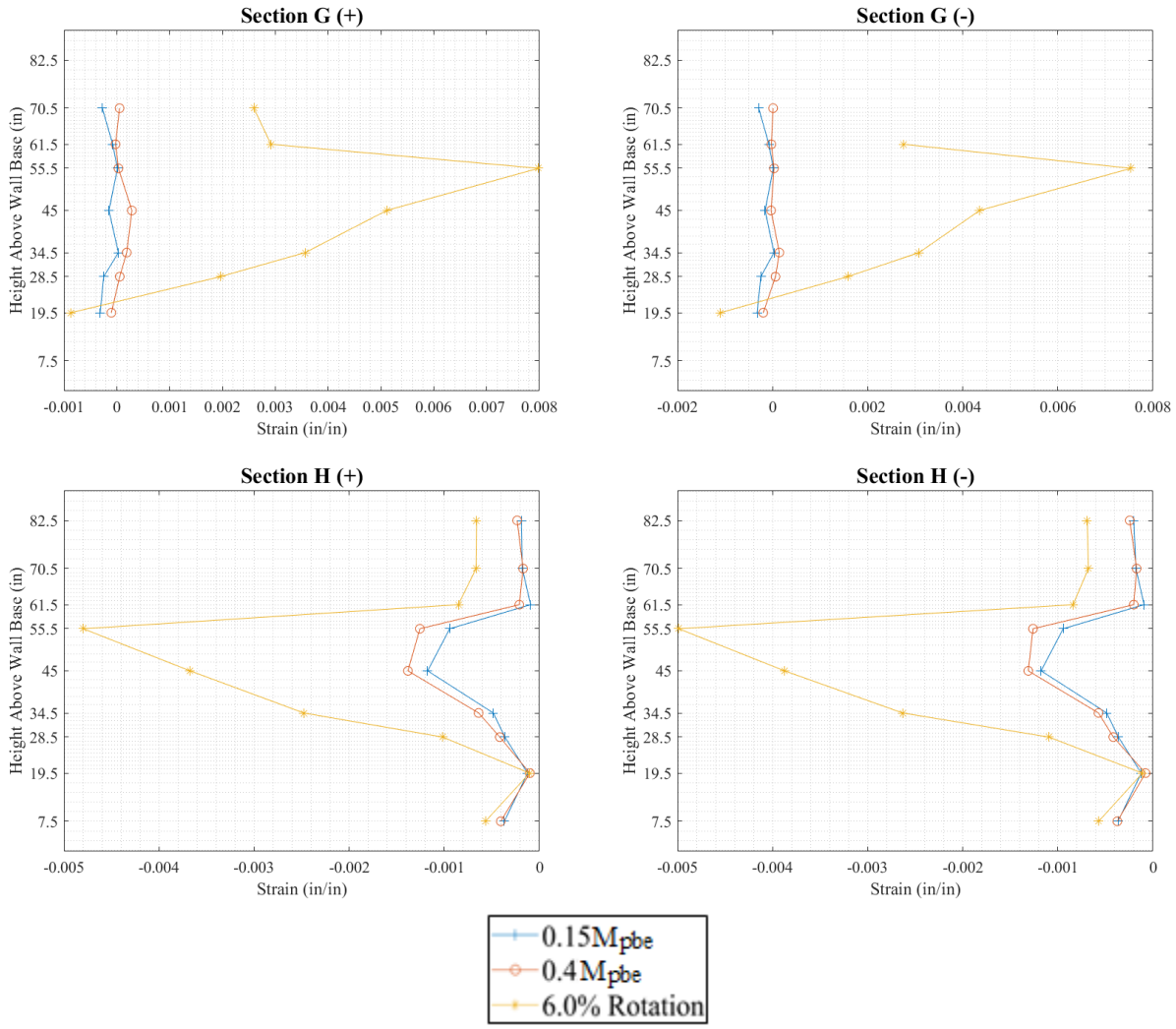

Figure 4.35. Wall Strain over Height for SRC-W4 (continued)

4.9. Wall Reinforcement Strain

For SRC-W1 and SRC-W2, which included strain gauges on wall longitudinal reinforcement, wall strain profiles at the locations shown in Figure 3.17 are provided in Figure 4.36 through Figure 4.39. The strain profiles were formulated using strain values at the peak of each first cycle at each increment of load or displacement applied. The plots for SRC-W2 include residual strain after completion of testing of SRC-W1. Plane-section behavior is not evident in Figure 4.36 through Figure 4.39.

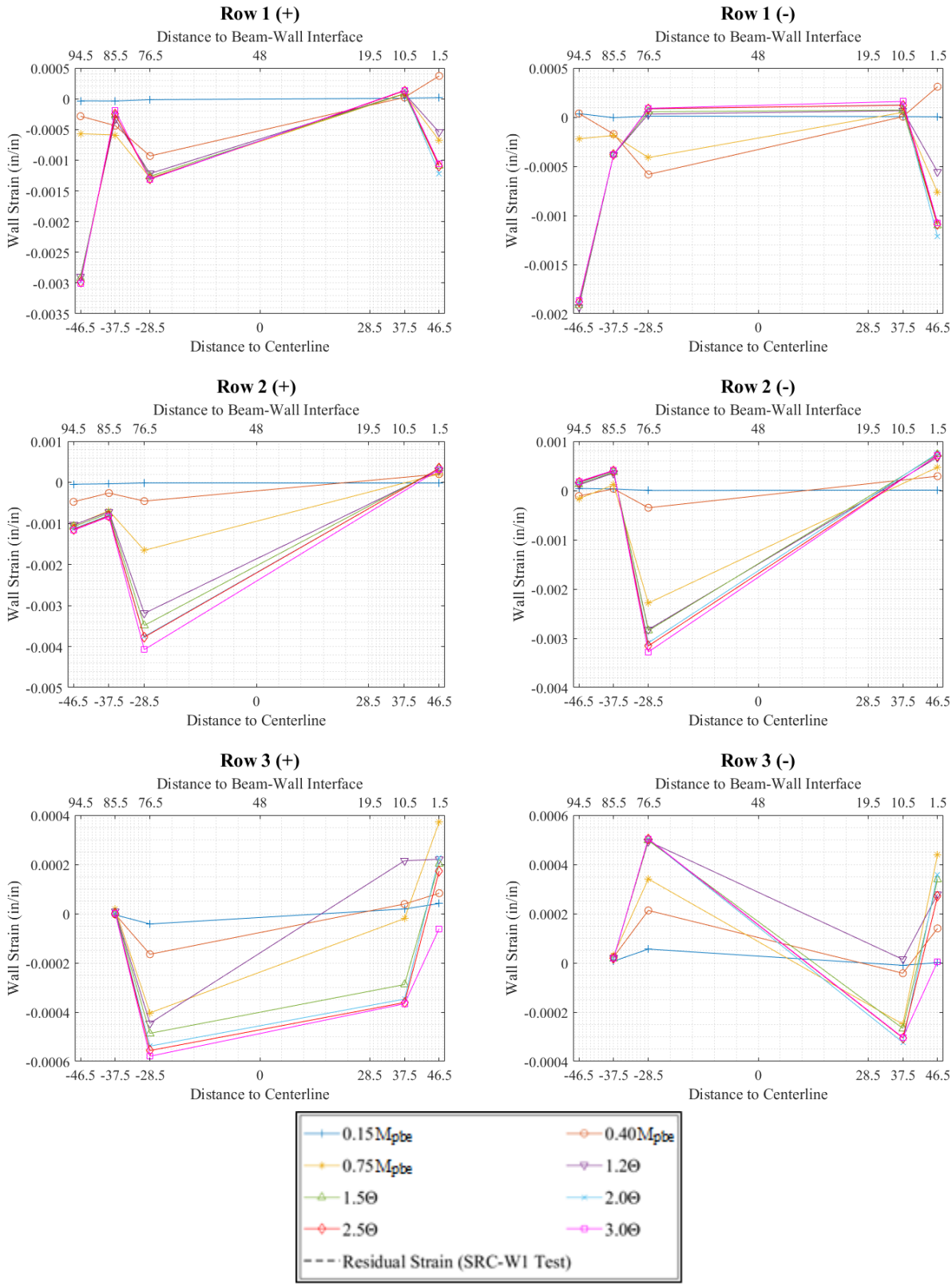

Figure 4.36. Wall Longitudinal Reinforcement Strain along Cross-Sections for SRC-W1

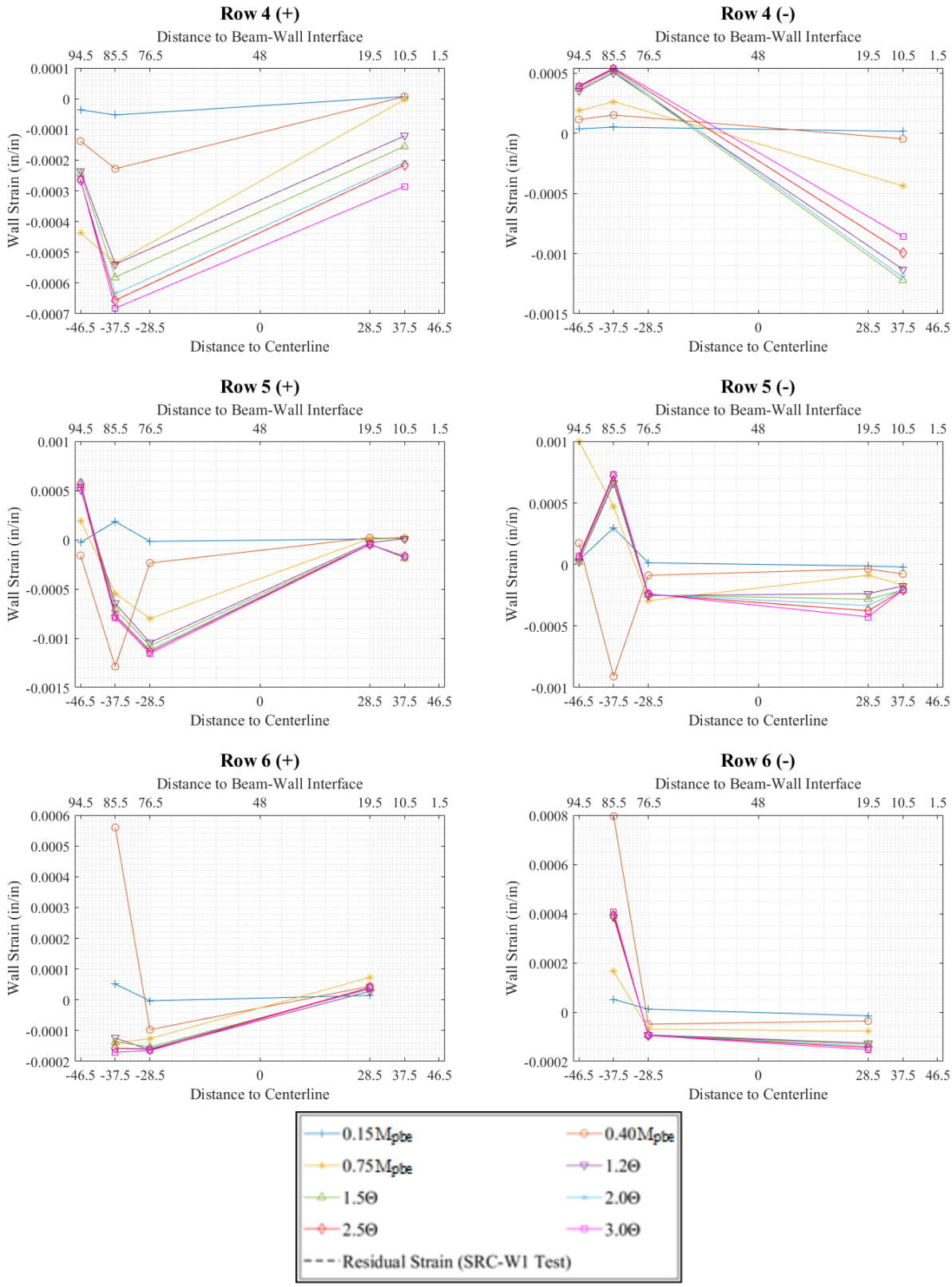

Figure 4.36. Wall Longitudinal Reinforcement Strain along Cross-Sections for SRC-W1 (cont.)

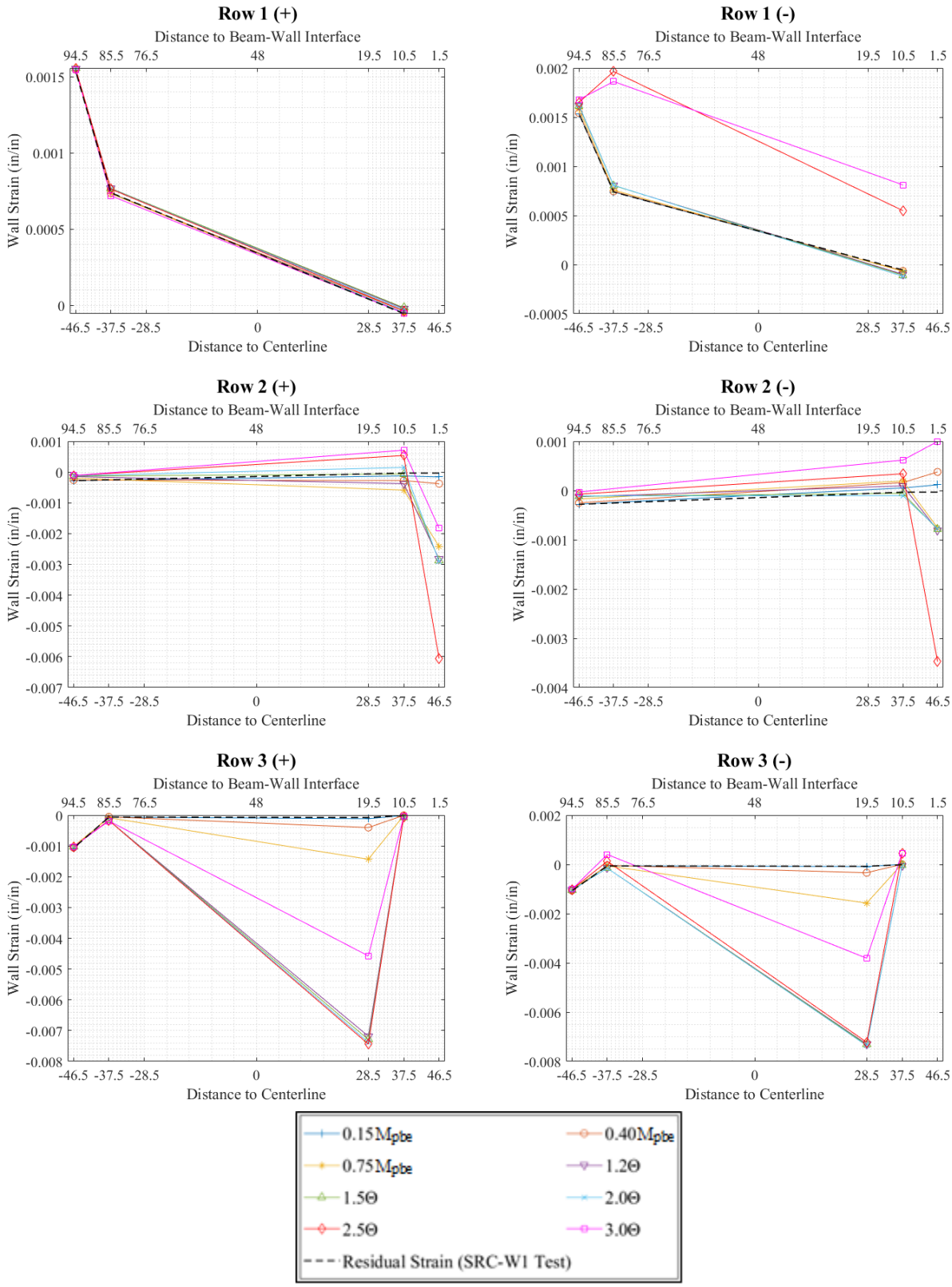

Figure 4.37. Wall Longitudinal Reinforcement Strain along Cross-Sections for SRC-W2

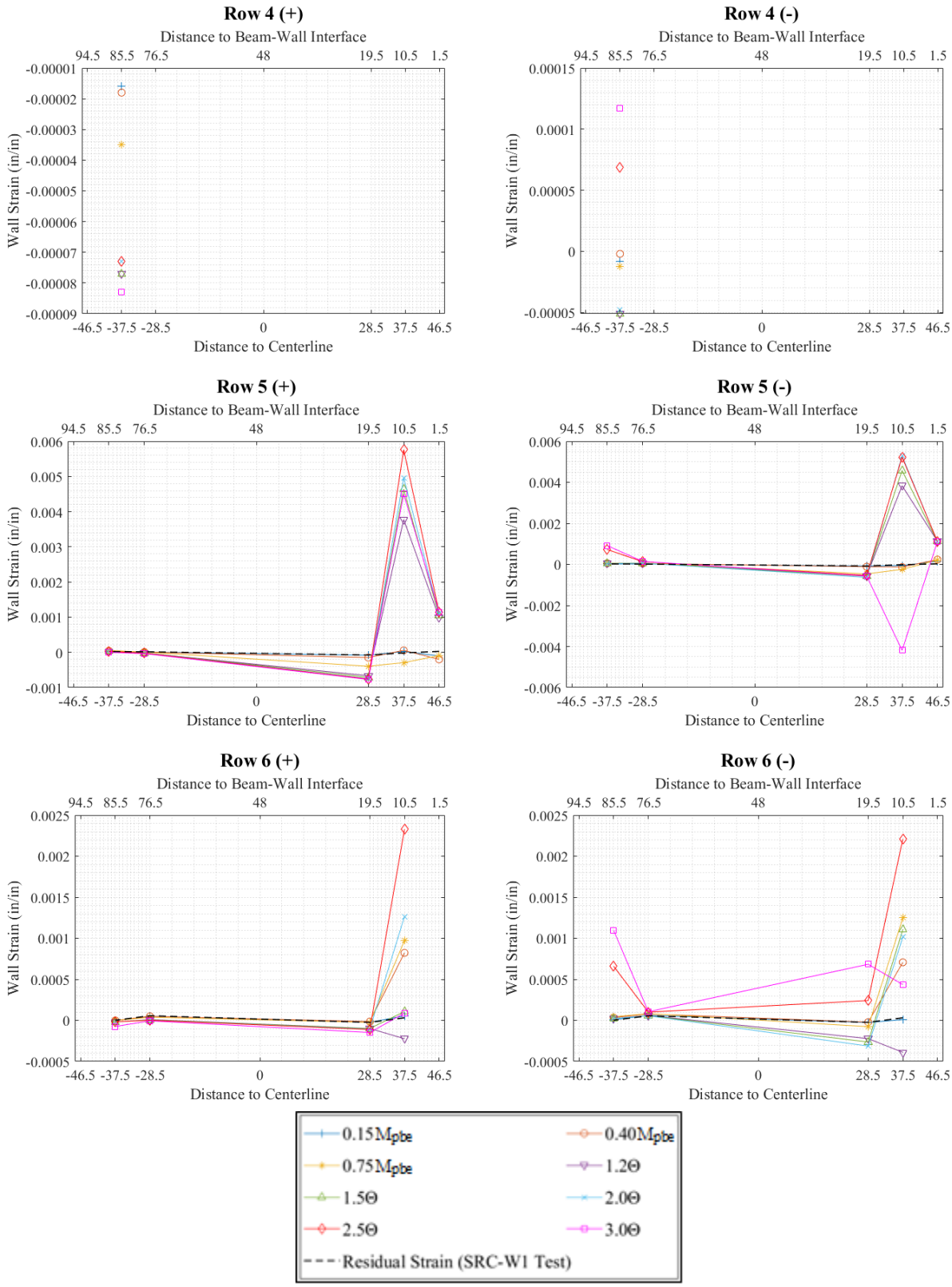

Figure 4.37. Wall Longitudinal Reinforcement Strain along Cross-Sections for SRC-W2 (cont.)

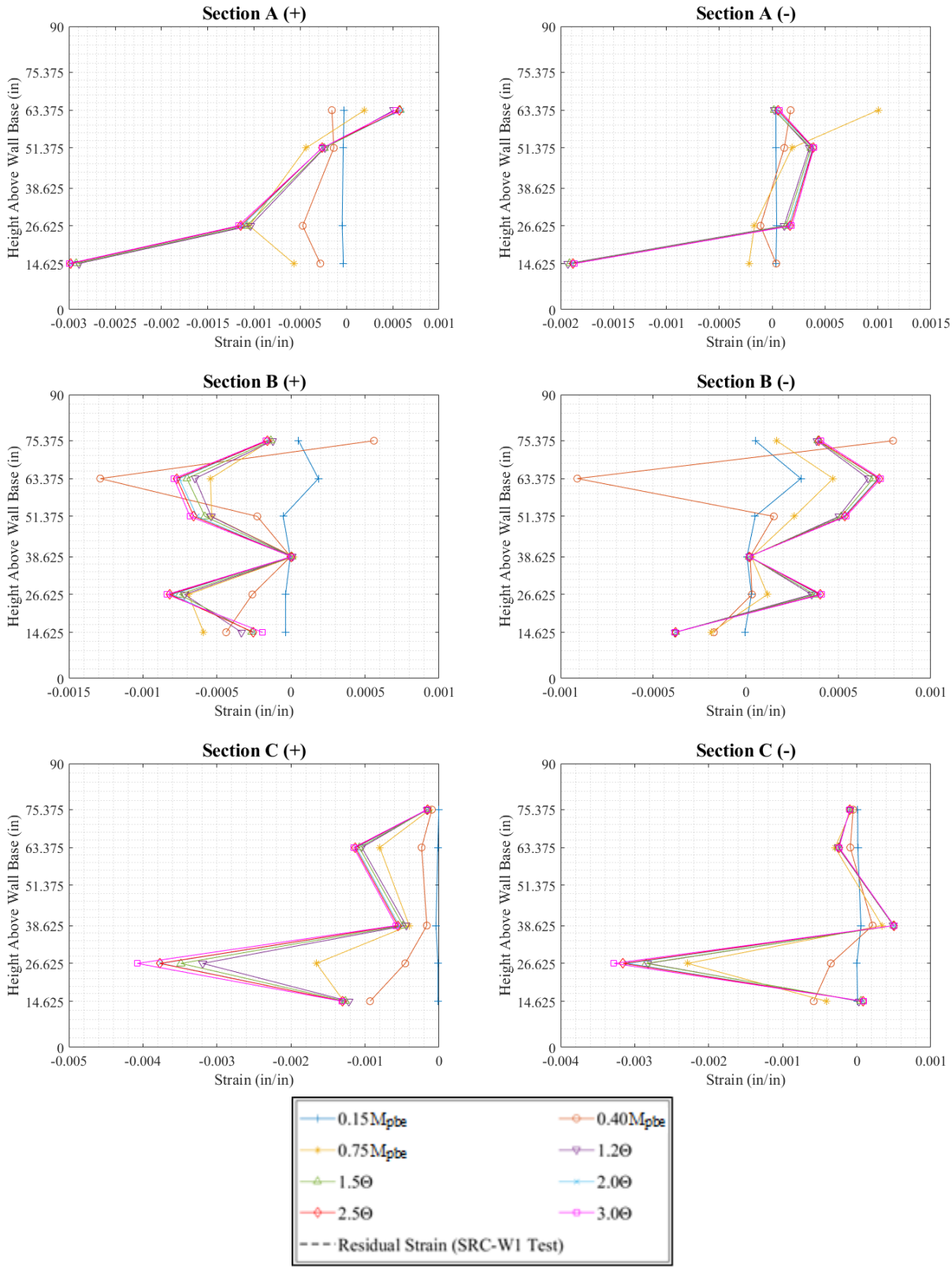

Figure 4.38. Wall Longitudinal Reinforcement Strain over Height for SRC-W1

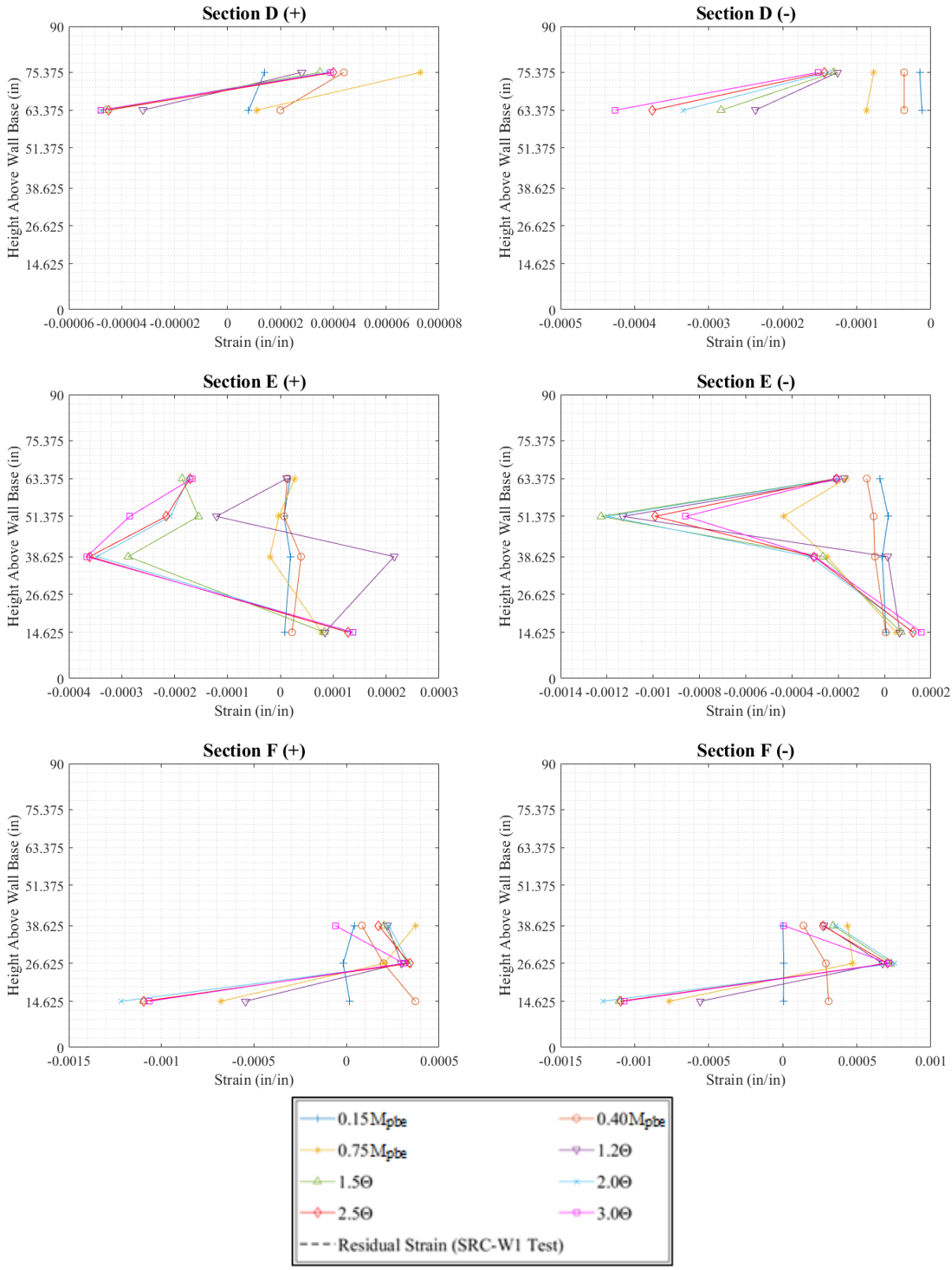

Figure 4.38. Wall Longitudinal Reinforcement Strain over Height for SRC-W1 (continued)

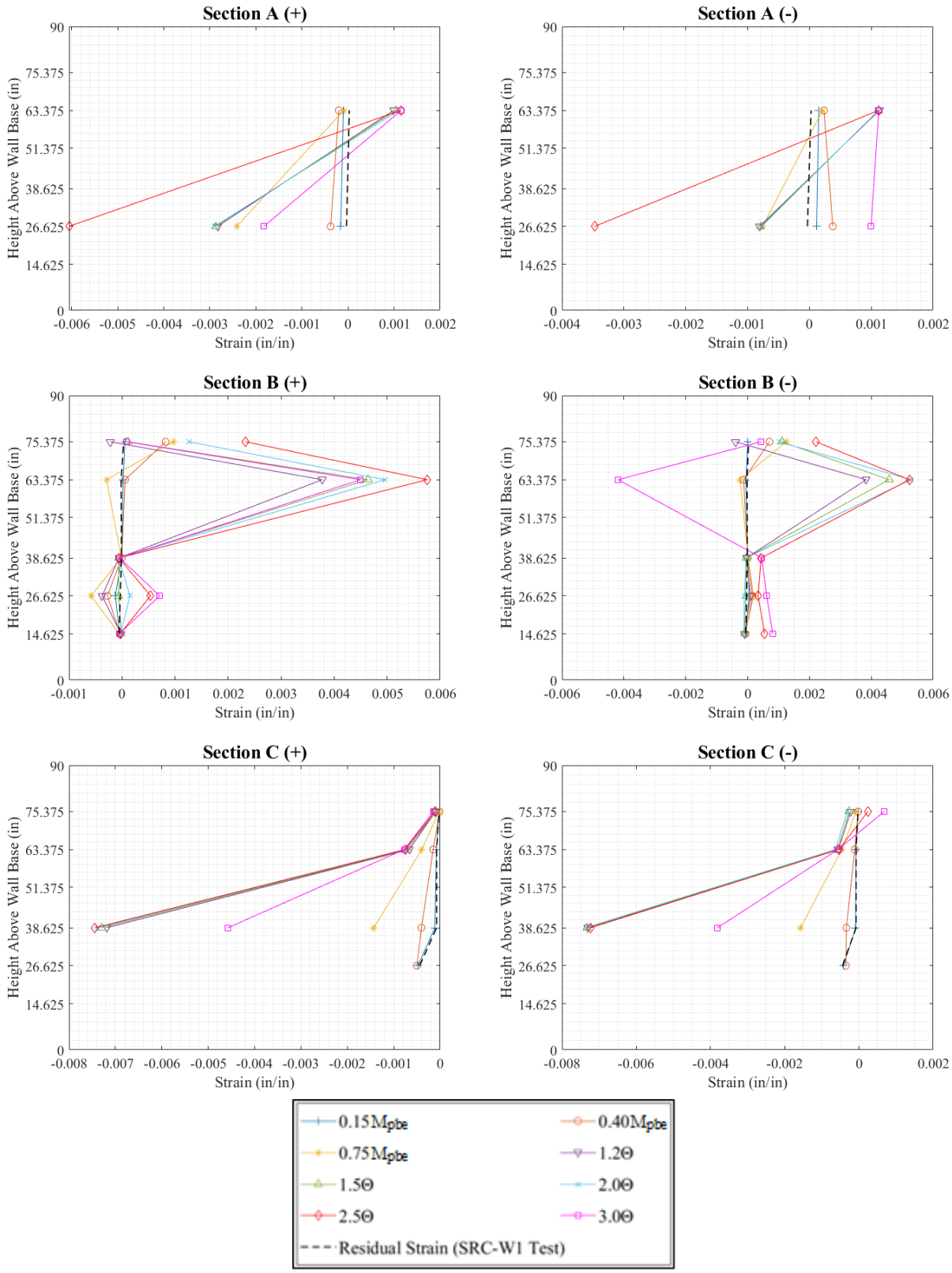

Figure 4.39. Wall Longitudinal Reinforcement Strain over Height for SRC-W2

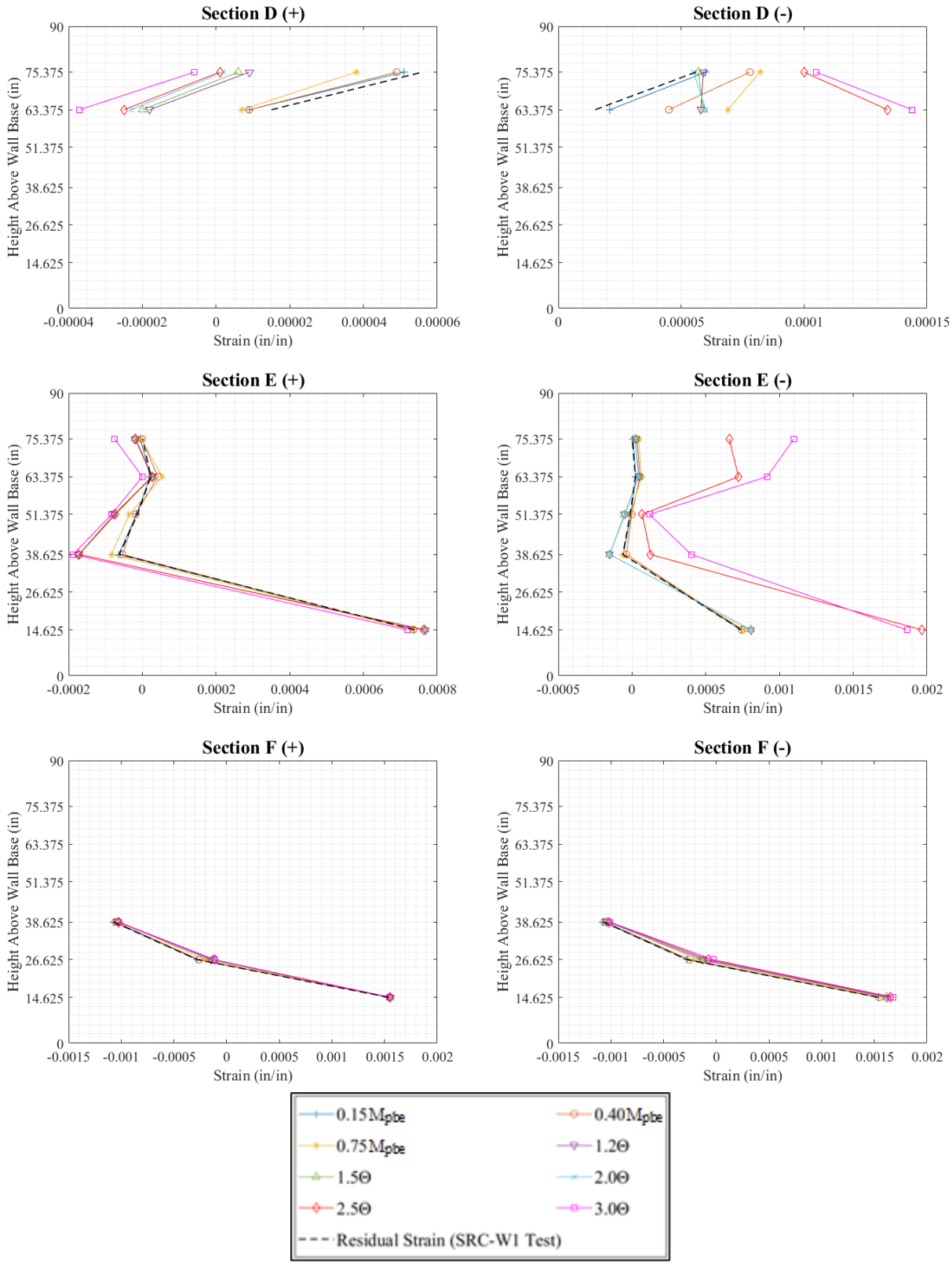

Figure 4.39. Wall Longitudinal Reinforcement Strain over Height for SRC-W2 (continued)

5. Modeling Recommendations

5.1. Effective Stiffness

It was shown in Section 4.6 and Section 4.4 that the majority of the coupling beam elastic deformation was measured at the beam-wall interface due to slip of the steel section. This was consistent with results from Motter et al (2017a) for seismic tests on SRC coupling beams. Motter et al (2017b) recommended an effective stiffness based on flexural rigidity of:

$$(EI)_{eff} = \frac{M_p L}{6\theta_y} \tag{5-1}$$

or:

$$(EI)_{eff} = 0.06\alpha E_s I_{trans} \tag{5-2}$$

where M_p is the plastic moment of the section using a Whitney stress block for concrete in compression, L is the beam length, θ_y is the yield rotation, taken as 0.0133 radians of chord rotation, α is the span-to-depth ratio of the beam, E_s is the elastic modulus of steel, and I_{trans} is the transformed moment of inertia, transforming concrete to steel. AISC 341-22, consistent with PEER TBI (2017), recommended an effective stiffness based on flexural and shear rigidity of:

$$(EI)_{eff} = 0.07\alpha (EI)_{trans} \tag{5-3}$$

$$(GA)_{eff} = 1.0 G_s A_{sw} \quad (5\text{-}4)$$

where $(EI)_{trans}$ is the flexural rigidity of the cracked transformed section, G_s is the shear modulus of steel, and A_{sw} is the area of the web of the steel section.

The predicted and measured chord rotation at $0.75M_{pbe}$ are provided in Table 5.1 for SRC-W1 and SRC-W2 tested in this study, CB6 tested by Abdullah et al (2020), and SRC1 and SRC2 tested by Motter et al (2017a). M_{pbe} was calculated here using tested material properties. SRC-W4 from this study and SRC3 and SRC4 from Motter et al (2017a) were excluded from this comparison, as the wall yielded prior to reaching $0.75M_{pbe}$, leading to significant reduction in beam stiffness at $0.75M_{pbe}$ for these tests. Although wall yielding did not occur for SRC2, $0.75M_{pbe}$ was not reached for SRC2 in the negative loading direction due to the strength reduction from wall demands reducing beam fixity. Therefore, a measured chord rotation at $0.75M_{pbe}$ for SRC2 was not provided in Table 5.1 in the negative loading direction.

Table 5.1. Measured and Predicted Chord Rotation for Test Beams at $0.75M_{pbe}$

Test Name	Reference	Predicted			Measured			
		Eq. (5-1)	Eq. (5-2)	AISC	1st +	1st -	75th +	75th -
SRC-W1	This Study	0.0100	0.0103	0.0105	0.0079	-0.0092	0.0160	-0.0135
SRC-W2	This Study	0.0100	0.0103	0.0105	0.0121	-0.0110	0.0135	-0.0135
SRC-W3	This Study	0.0100	0.0104	0.0105	0.0074	-0.0079	0.0136	-0.0148
CB6	Abdullah et al (2020)	0.0100	0.0089	0.0113	0.0055	-0.0056	0.0088	-0.0087
SRC1	Motter et al (2017a)	0.0100	0.0105	0.0107	0.0151	-0.0149	NA	NA
SRC2	Motter et al (2017a)	0.0100	0.0105	0.0107	0.0080	NA	NA	NA

The wall demands at $0.75M_{pbe}$ for each test, determined from moment-curvature analysis, are provided in Figure 5.1. The wall demands produced compression in the embedment region in the positive loading direction and tension in the negative loading direction. The demands for CB6, which are not shown, were constant compression, as this test did not include a cyclically loaded wall. The measured stiffness for this test was roughly equal in the positive and negative loading direction. For SRC-W1, the stiffness was 16% lower in the negative than the positive loading direction. In the positive loading direction, SRC1 had significantly lower stiffness than the other tests, which may have been a result of the significantly lower compressive force in the wall, as shown in Figure 5.1. Assuming linear stress-strain behavior in the embedment concrete at $0.75M_{pbe}$, the front embedment force for SRC1 was estimated as 375 kips, which was more than double the 160 kip compressive force in the wall. This was not the case for the other beams, with wall compressive forces of 405 kips for SRC2, 457 kips for SRC-W1, 344 kips for SRC-W2 and 333 kips for SRC-W3. The significantly lower wall compressive force for SRC1 likely led to the reduction in stiffness, including the reduced stiffness in the negative loading direction.

For the four beams tested under wind loading, namely SRC-W1, SRC-W2, SRC-W3, and CB6, the level of stiffness degradation differed at $0.75M_{pbe}$. The ratio of the stiffness of the 75th and final cycle to the 1st cycle was 0.63 and 0.64 for CB6, 0.49 and 0.68 for SRC-W1, 0.90 and 0.81 for SRC-W2, and 0.54 and 0.53 for SRC-W3 in the positive and negative loading directions, respectively. For the measured moment-rotation at the beam-wall interface, shown in Figure 4.21, these ratios were 0.34 and 0.80 for SRC-W1, 0.95 and 0.90 for SRC-W2, and 0.51 and 0.33 for SRC-W3 in the positive and negative loading directions, respectively. SRC-W1 had larger wall demands than SRC-W2 with the same quantity of wall longitudinal reinforcement crossing the

embedment, and SRC-W3 had the same wall demands as SRC-W2 with less wall longitudinal reinforcement crossing the embedment. A higher level of wall compression relative to the quantity of wall longitudinal reinforcement, even if cyclic compression, may be associated with a higher level of stiffness degradation, given that stiffness degradation for SRC-W2 was less than the other tests at this loading level.

For the first cycle at $0.75M_{pbe}$ for SRC-W1, SRC-W2, and SRC-W3, the average ratio of measured stiffness to predicted stiffness is 1.08 using Eq. (5-1), 1.12 using Eq. (5-2), and 1.14 using AISC 341-22 (Eq. (5-3) and Eq. (5-4)), based on the values in Table 5.1. These values were 1.80, 1.60, and 2.04, respectively, for the Abdullah et al (2020) test, which did not include a cyclically loaded wall. It is recommended that the effective stiffness used for seismic design, which is provided in AISC 341-22, be adjusted for nonlinear wind design to account for stiffness degradation. This could be achieved through the use of a stiffness degradation factor that matches the behavior shown in Figure 4.15b. However, most commercially available computer software used by practicing engineers does not have such a feature for stiffness degradation. Thus, it is recommended that an average stiffness be used. For the 75 cycles at $0.75M_{pbe}$, the average ratio of secant stiffness to initial cycle secant stiffness was 0.66 and 0.71 for SRC-W1, 0.93 and 0.85 for SRC-W2, and 0.53 and 0.65 for SRC-W3 in the positive and negative loading directions, respectively. Seismic protocols have significantly fewer cycles, with three cycles used in past tests by Motter et al (2017a) for loading at this level. For the first three cycles at $0.75M_{pbe}$, the average ratio of secant stiffness to initial cycle secant stiffness was 0.95 and 0.96 for SRC-W1, 0.98 and 0.97 for SRC-W2, and 0.95 and 1.01 SRC-W3. For the six sets of values, the average ratio of the value for 75 cycles to the value for three cycles is 0.74. Therefore, it is recommended that the effective stiffness

for nonlinear wind design be taken as 0.75 times the value determined using AISC 341-22 for seismic design.

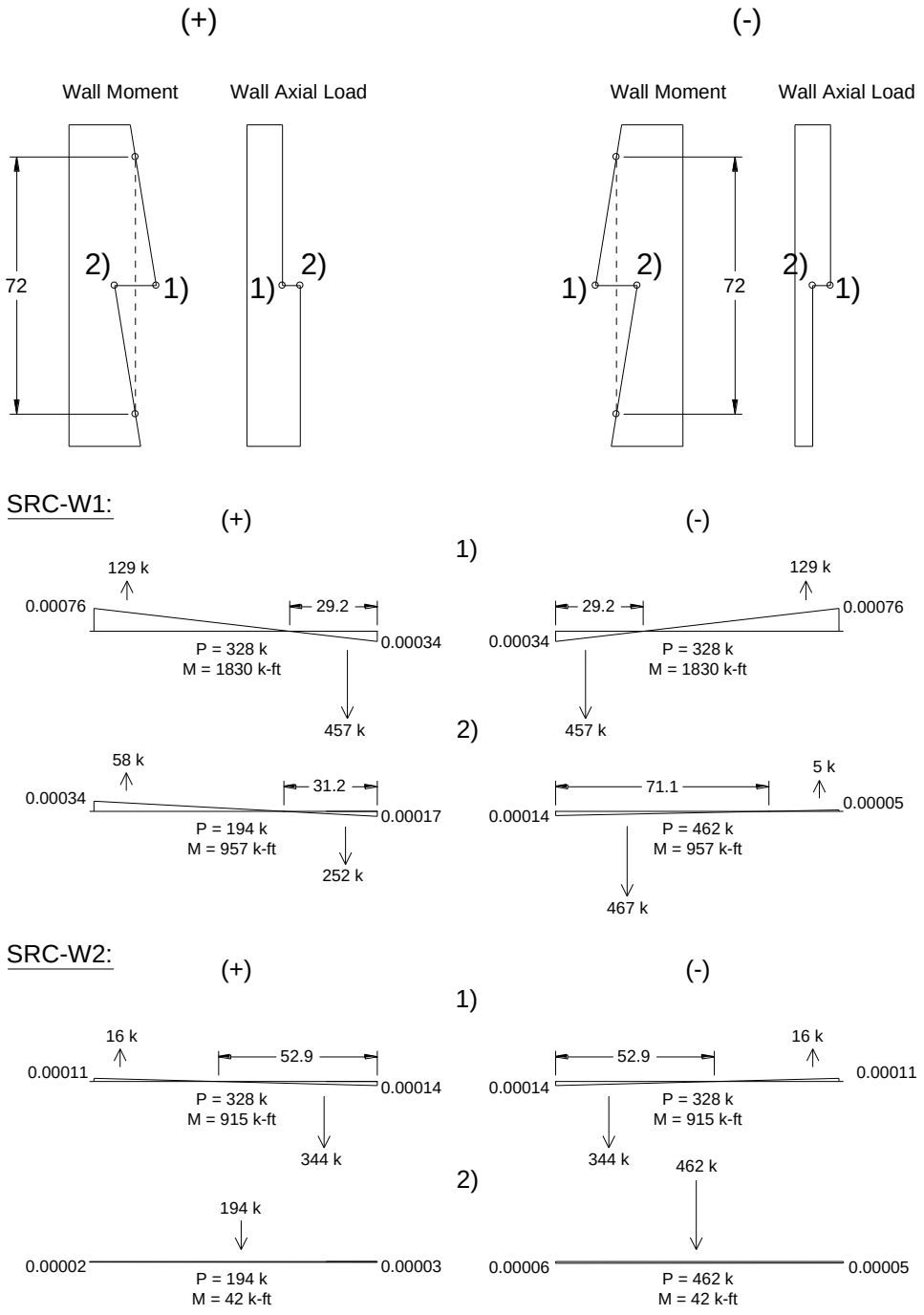

Figure 5.1. Wall Demands at 0.75M_{pbe}, Excluding Coupling Beam Demands, at Location of Coupling Beam (Coupling Beam on Right), Determined from Moment-Curvature Analysis

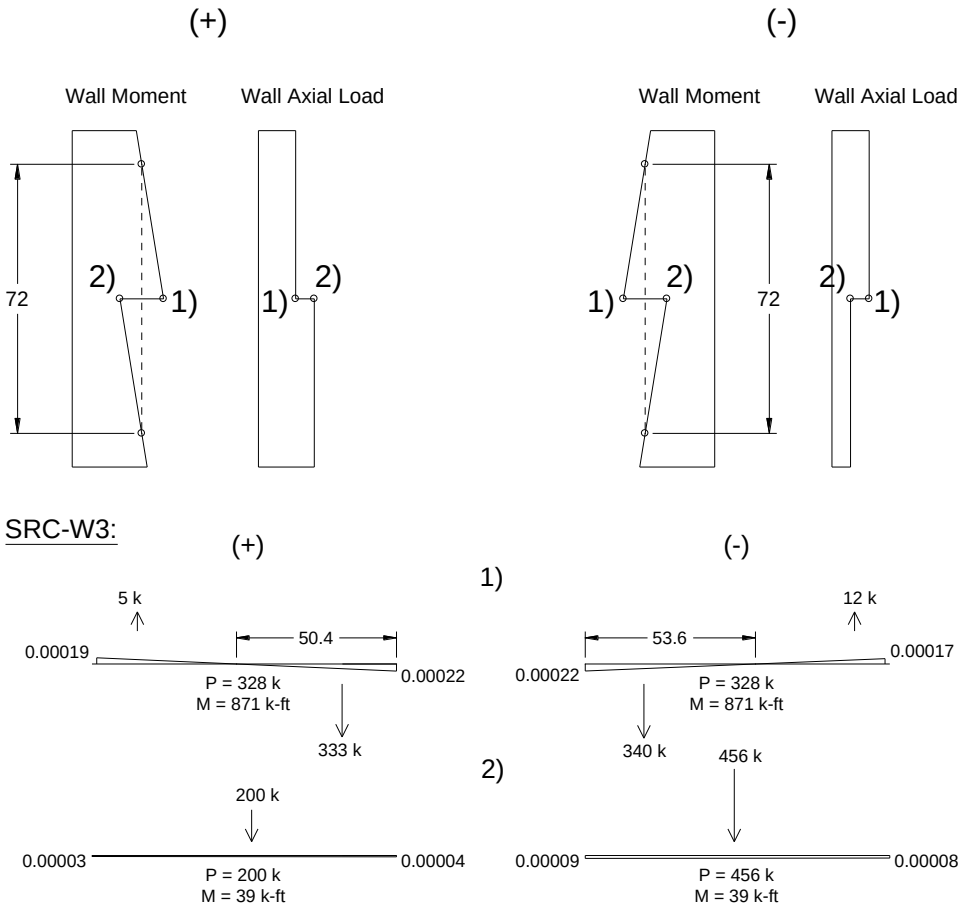

Figure 5.1. Wall Demands at 0.75M_{pbe}, Excluding Coupling Beam Demands, at Location of Coupling Beam (Coupling Beam on Right), Determined from Moment-Curvature Analysis (continued)

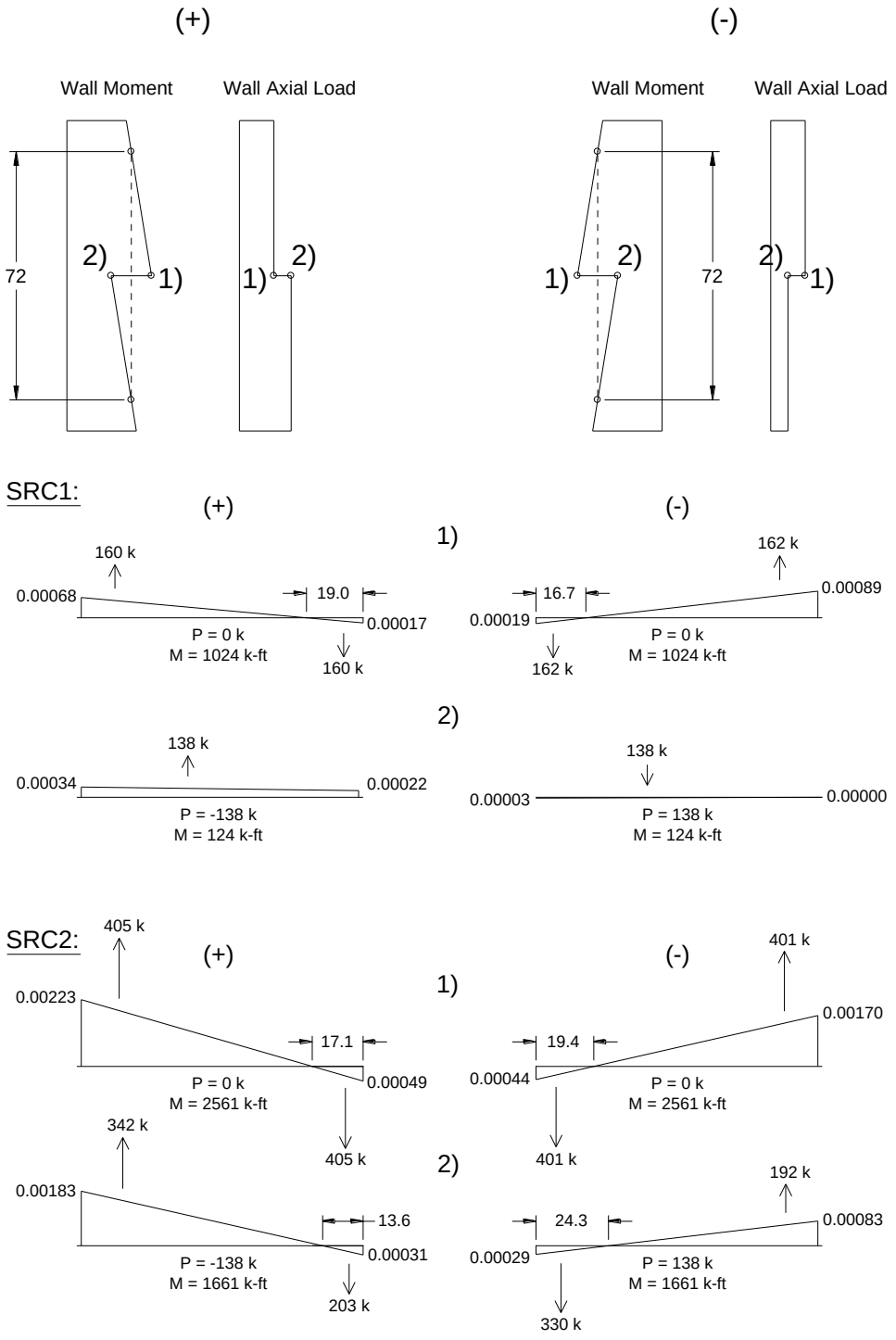

Figure 5.1. Wall Demands at 0.75M_{pbe}, Excluding Coupling Beam Demands, at Location of Coupling Beam (Coupling Beam on Right), Determined from Moment-Curvature Analysis (continued)

5.2. Backbone Models

Nonlinear backbone models are typically fit to load-deformation test data to formulate models that are suitable for implementation into commercially available computer software. This is commonplace for seismic tests, which typically have a few loading cycles at each increment, often resulting in a lack of significant stiffness degradation prior to yielding. As discussed in the previous section, stiffness degradation for repeated loading cycles at a given increment in the wind loading protocol was significant for the tests conducted in this study, particularly for cycles at $0.75M_{pbe}$. Most commercially available software used for nonlinear modeling of structural behavior with moment-rotation or shear-deformation hinges does not include a feature for degrading stiffness at repeated loading cycles to the same level. This creates debate as to how best to fit a typical backbone model to these test data. If the backbone model is fit based on test data at initial cycles, the energy under the model would be more than the test data. If the backbone model is fit based on test data at final cycles, the energy under the model would be less than the test data. It is recommended to fit the backbone model based on average values of all cycles at each increment. This would promote equal area under the curve for the backbone model and test data. Equal area is consistent with the approach for backbone modeling currently being proposed by ACI Committee 374 (ACI 374.3R-16) for performance-based seismic design.

To fit the backbone model to test data, a linearized backbone of the test data was first formulated by connecting data points at each loading increment, as shown in Figure 5.2 with resulting data provided in Table 5.2. Backbone models fit to data based on first cycles, final cycles, and average cycles are provided in Figure 5.2 and Table 5.3. In each of these cases the backbone model

considered only cyclic increments larger than previous increments, such that cycles in the loading protocol after the two cycles at $3.0\theta_y$ were excluded. The backbone model was bilinear up to the maximum shear force, V_{max}, similar to the backbone model described in ASCE/SEI 41 Section 7.4.3.2.4. The first line connected the origin to the yield force, $V_{y,test}$, and intersected the test data backbone at 0.6 of the yield force. The second line connected the yield force to the peak shear force. The yield force was determined such that the area under the test data backbone and model backbone were equal up to the peak shear force. The backbones from SRC-W1, SRC-W2, and SRC-W3 are provided on the same plot in Figure 5.3 for comparative purposes. Less difference in stiffness at yield between the initial and final cycle backbone was evident for SRC-W2 relative to SRC-W1 and SRC-W3.

For SRC-W1, SRC-W2, and SRC-W3, ratios of tested strength to predicted strength are provided in Table 5.4, with values for $V@M_y$ and $V@M_{pbe}$ consistent with the values in Section 3.6. The plastic rotation in the test, $\theta_{plastic}$, also provided in Table 5.4, was the difference between the maximum rotation and the rotation at yield. For the values in Table 5.4, the average $V_{y,test}$ / $V@M_y$ is 0.97, the average V_{max} / $V@M_{pbe}$ is 0.98, and the average $\theta_{plastic}$ is 4.05. A suggested bilinear backbone model for the SRC coupling beams for nonlinear wind design uses the effective stiffness from AISC 341-22 multiplied by 0.75, a yield strength of $V@M_y$, and a post-yield stiffness, $k_{plastic}$, in units of force per radian chord rotation, of:

$$k_{plastic} = \frac{V@M_{pbe} - V@M_y}{0.04} \quad (5\text{-}5)$$

with calculation of M_{pbe} and M_y based on expected material properties for concrete compressive strength and yield strength of the flange steel, which could differ for built-up versus rolled sections. The hysteretic behavior used in the model should be determined by modeling the tests with calibration to the energy dissipation provided in Figure 4.20 and Table 4.6. While the suggested backbone model is reflective of behavior observed in the tests, the tests did not include the influence of axial restraint from floors and walls on coupling beam behavior. Axial restraint is expected to alter the load-deformation response in the coupling beam, and it is recommended that future research examine the influence of axial restraint.

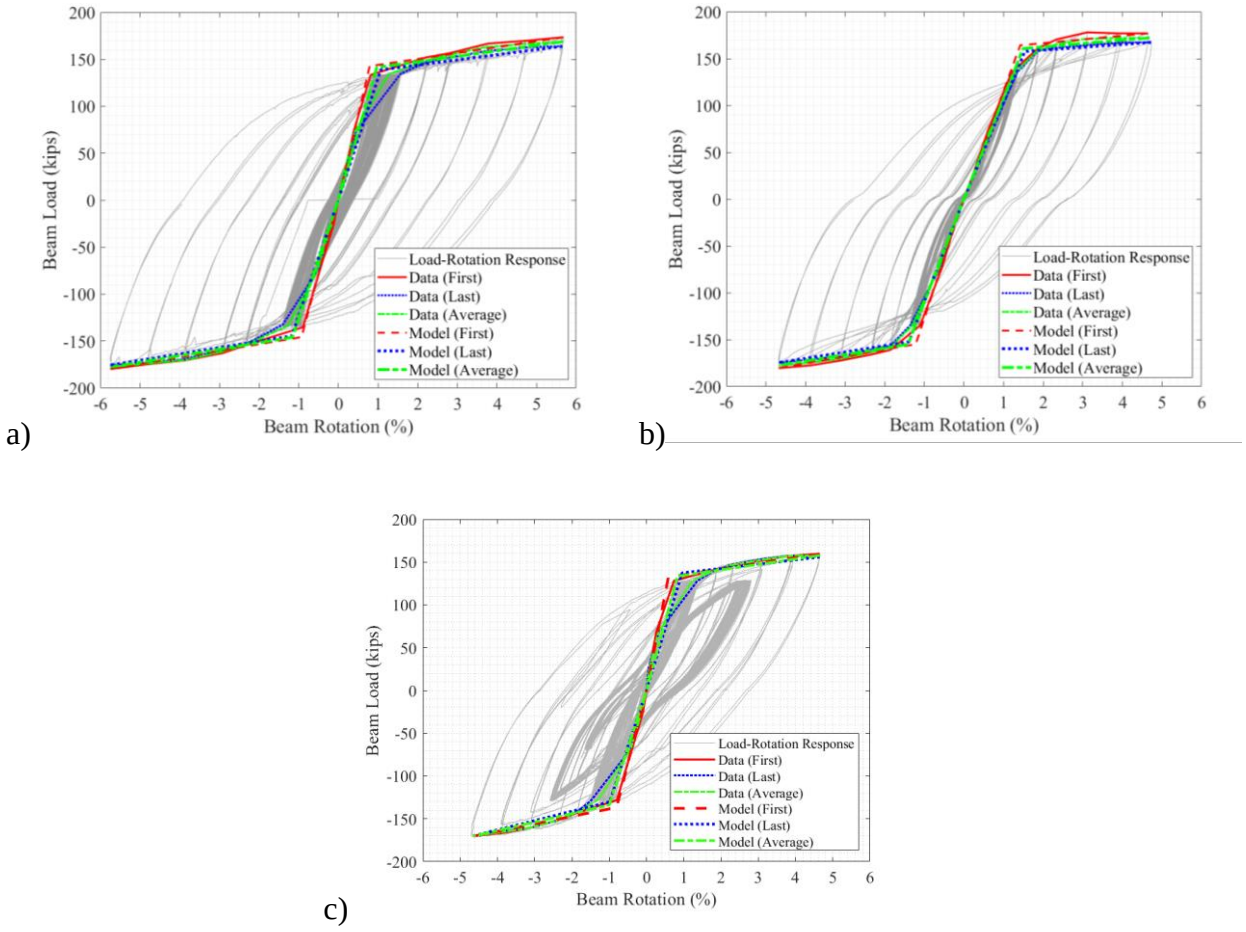

Figure 5.2. Backbone Models Fit to Test Data for a) SRC-W1, b) SRC-W2, and c) SRC-W3

Table 5.2. Load-Rotation Coordinates of Test Data Backbones

SRC-W1						SRC-W2						SRC-W3					
First		Last		Average		First		Last		Average		First		Last		Average	
Rot. (%)	Load (Kips)	Rot. (%)	Load (Kips)	Rot. (%)	Load (Kips)	Rot. (%)	Load (Kips)	Rot. (%)	Load (Kips)	Rot. (%)	Load (Kips)	Rot. (%)	Load (Kips)	Rot. (%)	Load (Kips)	Rot. (%)	Load (Kips)
5.68	173.5	5.65	164	5.67	168.8	4.65	177.0	4.73	167.4	4.69	172.2	4.65	159.7	4.65	155.8	4.65	157.7
4.74	169.8	4.71	162.7	4.67	166.2	3.89	177.0	3.94	167	3.84	172	3.88	157.5	3.88	157.5	3.88	157.5
3.77	166.7	3.76	158.9	3.7	162.8	3.12	178.0	3.11	164.4	3.07	171.2	3.10	151.9	3.10	153.3	3.10	152.6
2.8	156.6	2.81	152	2.72	154.1	2.33	170.5	2.33	161.4	2.31	164.9	2.32	146.2	2.33	147.3	2.33	146.8
2.21	152	2.21	146.7	2.19	148.4	1.86	160.5	1.87	158.6	1.85	158.2	1.86	141.5	1.86	141.0	1.86	140.9
0.82	133.4	1.57	134.6	1.27	134	1.21	135.7	1.35	135.5	1.31	135.3	0.74	128.2	1.37	128.2	1.24	128.2
0.38	72.5	0.42	71.1	0.39	70.8	0.60	72.2	0.69	72.3	0.64	72.3	0.26	68.3	0.33	68.5	0.32	68.5
0.15	27.5	0.14	27.3	0.13	27.3	0.24	27.1	0.26	27.1	0.25	27.1	0.09	25.8	0.05	25.6	0.08	25.8
0	0	0	0	0	0	0	0	0	0	0	0	0	0	0	0	0	0
-0.12	-26.7	-0.17	-26.7	-0.17	-26.7	-0.23	-27.1	-0.25	-27	-0.26	-27.1	-0.10	-25.8	-0.16	-25.6	-0.14	-25.7
-0.44	-71.3	-0.49	-72.7	-0.51	-72.5	-0.54	-72.1	-0.6	-72.2	-0.62	-72.2	-0.39	-68.3	-0.43	-68.9	-0.42	-68.5
-0.89	-135.2	-1.4	-132.4	-1.26	-133.3	-1.11	-134.8	-1.35	-134.5	-1.3	-134.6	-0.79	-128.1	-1.48	-128.5	-1.29	-127.5
-2.32	-154.2	-2.3	-152.7	-2.3	-153.6	-1.86	-161.1	-1.86	-156.6	-1.85	-158.2	-1.84	-142.8	-1.84	-141.0	-1.85	-141.9
-2.91	-162.7	-2.9	-159.5	-2.9	-160.9	-2.32	-165.7	-2.32	-160.2	-2.31	-162.9	-2.33	-151.0	-2.32	-151.2	-2.33	-151.2
-3.87	-170.5	-3.92	-169.6	-3.84	-170.1	-3.12	-172.3	-3.11	-167.8	-3.08	-170	-3.10	-160.3	-3.10	-160.2	-3.10	-160.2
-4.80	-174.7	-4.82	-172.8	-4.74	-173.7	-3.87	-177.4	-3.89	-171.3	-3.88	-174.4	-3.88	-166.6	-3.87	-164.9	-3.88	-165.4
-5.75	-179.8	-5.75	-175.6	-5.75	-177.7	-4.68	-180.4	-4.68	-174.6	-4.68	-177.5	-4.65	-170.3	-4.65	-170.0	-4.65	-170.2

Table 5.3. Load-Rotation Coordinates of Bilinear Backbone Models

	SRC-W1		**SRC-W2**		**SRC-W3**	
	Rotation (%)	**Load (Kips)**	**Rotation (%)**	**Load (Kips)**	**Rotation (%)**	**Load (Kips)**
First	5.68	173.5	4.65	177.0	4.65	159.7
	0.79	142.7	1.42	164.3	0.59	132.4
	0.00	0.0	0.00	0.0	0.00	0.0
	-0.93	-145.8	-1.22	-154.9	-0.80	-136.7
	-5.75	-179.8	-4.68	-180.4	-4.65	-170.3
Last	5.65	164.0	4.73	167.4	4.65	155.8
	1.07	138.7	1.54	157.7	0.96	137.3
	0.00	0.0	0.00	0.0	0.00	0.0
	-1.18	-144.5	-1.39	-152.2	-0.99	-130.1
	-5.75	-175.6	-4.68	-174.6	-4.65	-170.0
Average	5.67	168.8	4.69	172.2	4.65	157.7
	0.97	141.4	1.49	160.8	0.83	133.5
	0.00	0.0	0.00	0.0	0.00	0.0
	-1.16	-145.9	-1.41	-155.0	-1.00	-133.9
	-5.75	-177.7	-4.68	-177.5	-4.65	-170.2

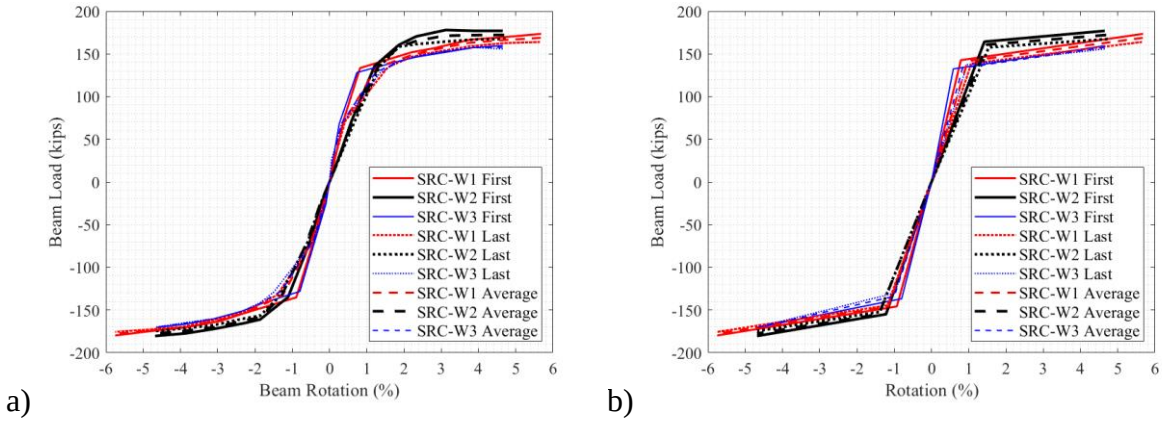

Figure 5.3. Backbone Models using a) Data at Cycle Peaks, b) Bilinear Fit

Table 5.4. Strength and Plastic Deformation of Bilinear Backbone Models

Test Name	$V_{y,test}$ / $V@M_y$		V_{max} / $V@M_{pbe}$		$\theta_{plastic}$ (%)	
	(+)	(-)	(+)	(-)	(+)	(-)
SRC-W1	0.94	0.96	0.97	1.00	4.89	4.82
SRC-W2	1.07	1.01	0.98	1.00	3.23	3.46
SRC-W3	0.91	0.94	0.94	1.00	4.06	3.85

6. Summary and Conclusions

Four steel reinforced concrete (SRC) coupling beams, SRC-W1, SRC-W2, SRC-W3, and SRC-W4 were tested quasi-statically under fully reversed cyclic wind demands. Each test specimen included two test beams and one wall, with the steel sections in the test beams embedded into opposite ends of the reinforced concrete structural wall. The beams were tested individually as cantilevers, with SRC-W1 tested prior to SRC-W2 in one wall and SRC-W3 tested prior to SRC-W4 in another wall. Passive axial compressive restraint was applied to each beam during testing. The beams and walls were designed in accordance with AISC 341-22 Section H5, with the exception of the wall longitudinal reinforcement crossing the embedment length for SRC-W3 and SRC-W4, which had 0.53 and 0.22, respectively, times the strength required, and, for SRC-W4, the lack of wall boundary transverse reinforcement at the embedment region. The walls had reinforcement detailing that was compliant with ACI 318-19 Section 18.10.6.5. The test beams were nominally identical, with the only test variable being the wall demand and quantity of wall reinforcement. During each test, the wall was subjected to constant axial gravity load and fully reversed-cyclic lateral load that was linearly proportional to the load in the test beam. The ratio of wall shear to beam shear was the same for all tests. The ratio of applied wall moment to beam shear was the same for SRC-W2, SRC-W3, and SRC-W4 and differed for SRC-W1 to produce twice the wall moment demand from wall loads at the height of the coupling beam. The loading cycles applied to SRC-W1, SRC-W2, and SRC-W3 consisted of 250 cycles at $0.15M_{pbe}$, 500 cycles at $0.40M_{pbe}$, 75 cycles at $0.75M_{pbe}$, five cycles at $1.2\theta_y$, three cycles at $1.5\theta_y$, two cycles at $2.0\theta_y$, two cycles at $2.5\theta_y$, and one cycle at $3.0\theta_y$, followed by the same sequence in reverse, where θ_y

was the yield rotation, and M_{pbe} was the expected flexural strength calculated using the plastic stress distribution or the strain compatibility method. The loading cycles applied to SRC-W4 consisted of 250 cycles at 0.15M_{pbe}, 500 cycles at 0.40M_{pbe}, and two cycles at 6.0% chord rotation, as 0.75M_{pbe} was not reached prior to reaching 6.0% chord rotation during the first excursion after 500 cycles at 0.40M_{pbe}. Data were collected during the tests using measurements from LVDTs, strain gages, and load cells, as well as crack measurements and photos of damage.

Based on analysis of measured data, as well as analysis of results from previous tests, the following conclusions were reached on SRC coupling beams:

- It is recommended that nonlinear wind design of steel reinforced concrete (SRC) coupling beams follow the seismic provisions in AISC 341-22 Section H5, with exceptions noted in subsequent points. This study did not include testing on SRC coupling beams that were designed using provisions in AISC 341-22 Section H4 and tested to peak deformation demands more consistent with ordinary walls.
- Consistent with seismic behavior, damage to AISC 341-22 Section H5 compliant beams concentrates at the beam-wall interface for wind demand, with the crack width growing as deformation demand increases. For these beams, the majority of the coupling beam deformation was measured to occur at this location, and damage in the embedment region was limited to cracking.
- A minimum area of wall longitudinal reinforcement crossing the embedment length is prescribed in AISC 341-22 for seismic design. For cases in which an insufficient quantity of wall longitudinal reinforcement is provided, wall yielding can occur, with damage at the embedded connection. The quantity of reinforcement prescribed by AISC 341-22 Section

H5 was determined to be overly conservative in some instances, based on test results for SRC-W3. For SRC-W3, the wall demands were sufficiently low that a 47% reduction in the quantity of reinforcement determined from AISC 341-22 Section H5 resulted in favorable performance that was similar to SRC-W1 and SRC-W2, which had a quantity of wall reinforcement that satisfied the AISC 341-22 Section H5 provision. However, a 78% reduction in this quantity of reinforcement in combination with a lack of wall boundary transverse reinforcement for SRC-W4 resulted in unfavorable performance, even for relatively modest levels of applied wall demand. It is recommended that the quantity of wall longitudinal reinforcement crossing the embedment length prescribed by AISC 341-22 Section H5 be reduced by 50% for cases in which wall demands do not exceed that applied for SRC-W3. The peak wall demands for SRC-W3 were $0.49M_y$ and 0.00047 tensile strain in outermost reinforcement at the coupling beam mid-height and an average of $0.24M_y$ and 0.00008 tensile strain in outermost reinforcement over one story height, taken as half a story above and below the coupling beam mid-height. These demands were determined from moment-curvature analysis for the moment and axial load, with moment and axial load diagrams determined based on transfer of coupling beam moment and shear to the wall at mid-height of the coupling beam. The M_y indicated here was based on reaching 70 ksi, the expected yield strength of A615 Grade 60 reinforcement (PEER TBI, 2017), in the outermost longitudinal reinforcement.

- Minimal axial compressive force is needed in the coupling beam to reduce outward ratcheting and alter the post-yield stiffness in the load-deformation response. The measured axial load in the test beams did not exceed $0.015A_g f'_{c,test}$, where A_g is the gross area of the beam cross-section and $f'_{c,test}$ is the tested compressive strength of concrete. At this level

of axial load, the effect of P-M interaction on beam strength was determined to be minimal. The increase in axial elongation with repeated loading cycles at a given increment was less for the tests in this study with axial restraint than for SRC1 and SRC2, tested by Motter et al (2017a), without axial restraint. The post-yield strength increase was larger for SRC-W1, SRC-W2, and SRC-W3 than for SRC1, which was the only test beam in that test program that was fully compliant with AISC 341-22 Section H5. This was likely due to improved concrete contact in compression for the case of reduced axial elongation.

- Stiffness for the first cycle at $0.75M_{pbe}$ was examined using the results from SRC-W1, SRC-W2, and SRC-W3 from this study and three beams from other studies. The difference between stiffness in the positive and negative direction was more significant for larger cyclic wall demands, with higher stiffness in the positive direction due to wall demands producing compression at the embedment region. The average of the positive and negative stiffness was larger for walls with higher compression force in the wall on the positive excursion.
- Stiffness degradation in SRC coupling beams subjected to repeating loading cycles is significant. This was particularly true for repeated loading cycles at $0.75M_{pbe}$ prior to yielding. The ratio of stiffness on the 75^{th} cycle to stiffness on the first cycle was 0.49 in the positive and 0.68 in the negative for SRC-W1, 0.90 in the positive and 0.81 in the negative for SRC-W2, and 0.54 in the positive and 0.53 in the negative for SRC-W3. Abdullah et al (2020) tested an SRC coupling beam embedded into concrete blocks subjected to constant compression, and these ratios were 0.63 and 0.64 for the two loading directions. SRC-W1 had larger wall demands than SRC-W2 with the same quantity of wall longitudinal reinforcement crossing the embedment, and SRC-W3 had the same wall

demands as SRC-W2 with less wall longitudinal reinforcement crossing the embedment. A higher level of wall compression relative to the quantity of wall longitudinal reinforcement, even if cyclic compression, may be associated with a higher level of stiffness degradation, given that stiffness degradation for SRC-W2 was less than the other tests at this loading level. Less stiffness degradation of the beam may correspond to more stiffness degradation in the wall, as the stiffness degradation in the wall at this loading level was larger for SRC-W2 than SRC-W1 and SRC-W3, with the level of stiffness degradation in the beam for SRC-W2 comparable to that in the wall during testing of SRC-W1. Additional test data are needed to further examine these items. The ratio of the average stiffness for the 75 cycles at $0.75M_{pbe}$ to the average stiffness for the first three of these cycles, which is more reflective of a seismic testing protocol, averaged 0.74 for SRC-W1, SRC-W2, and SRC-W3. It is recommended that the effective stiffness for nonlinear wind design be 75% of that prescribed in AISC 341-22 for seismic design.

- The yield rotation, θ_y, for the test beams was larger than that of previous seismic tests, although this was dependent on the definition of yield rotation. For the test beams, θ_y was determined during testing. During the first positive excursion to $1.2\theta_y$, the measured chord rotation at $0.75M_{pbe}$ was multiplied by $M_y/(0.75M_{pbe})$ to determine θ_y, where M_y was the moment at which the tension flange fully yields (i.e., the strain on the inner face of the tension flange is equal to the yield strain), computed from moment-curvature using the same material properties used for computation of M_{pbe}. For this definition of θ_y, the cyclic stiffness degradation during the first batch of 75 cycles at $0.75M_{pbe}$ significantly increased θ_y relative to previous seismic tests.

- Despite the significant stiffness degradation for repeated loading cycles at a given increment, SRC coupling beams can reach advanced levels of deformation demand under wind demands without significant strength degradation of initial cycles at new peak deformation demands or significant pinching in the load-deformation response. Peak deformation demand was 5.70% for SRC-W1 and 4.65% for SRC-W2 and SRC-W3, with favorable performance observed. Strength degradation of initial cycles at new peak deformation demands was not observed in the tests, with the peak measured load in each test attained on the first loading cycle to the peak deformation level. Similar to seismic design, a specified deformation capacity limit on the coupling beam is likely unnecessary for nonlinear wind design. However, based on the available data, the use of a deformation capacity limit of 6.0% chord rotation could be considered, based on modest extrapolation of data for SRC-W1.
- The ASCE/SEI Prestandard for Performance-Based Wind Design specifies the formulation of nonlinear models to capture structural response. Backbone models that represent load-deformation response of structural components are typically used for this purpose. For SRC coupling beams in which cyclic stiffness degradation for repeated cycles at a given increment is not explicitly modeled, it is recommended to use a backbone model based on average values of all cycles at each increment, as this would lead to equal area under the curve for the backbone model and test data. Backbone models for the four tests are provided in Section 5.2. A bilinear backbone model for nonlinear wind design was suggested that uses an effective stiffness of 75% of that prescribed in AISC 341-22, a computed yield moment from moment-curvature, a computed expected strength from AISC 341-22, and a post-yield slope based on 4.0% chord rotation from yield to expected strength.

References

Abdullah, S., Aswegan, K., Jaberansari, S., Klemencic, R., and Wallace, J. (2020). “Performance of Reinforced Concrete Coupling Beams Subjected to Simulated Wind Loading.” ACI Structural Journal, 117(3): 283-295.

ACI (American Concrete Institute). (2019). “Building code requirements for structural concrete.” ACI 318-19, Farmington Hills, MI.

ACI 374.3R-16 (2016). “Guide to Nonlinear Modeling Parameters for Earthquake-Resistant Structures”. American Concrete Institute, Farmington Hills, MI.

AISC. (2022). “Seismic provisions for structural steel buildings.” ANSI/AISC 341-22, Chicago, IL.

AISC. (2022). “Specification for structural steel buildings.” ANSI/AISC 360-22, Chicago, IL.

ASCE/SEI. (2016). “Minimum design loads for buildings and other structures.” ASCE/SEI Standard 7-16, Reston, VA.

ASCE/SEI (2019). “Prestandard for performance-based wind design.” American Society of Civil Engineers, Reston, VA.

ASTM C31/C31M-22. Standard Practice for Making and Curing Concrete Test Specimens in the Field. American Society of Testing and Materials, West Conshohocken, PA.

Barbachyn, S.M., Kurama, Y.C., and Novak, L.C. (2012). "Analytical Evaluation of Diagonally Reinforced Concrete Coupling Beams under Lateral Loads." ACI Structural Journal, 109(4): 497-507.

Gong, B. and Shahrooz, B. M. (2001a). “Concrete-steel composite coupling beams. I: Component testing.” J. Struct. Eng., 10.1061/(ASCE) 0733-9445(2001)127:6(625), 625–631.

Gong, B. and Shahrooz, B. M. (2001b). “Concrete-steel composite coupling beams. II: Subassembly testing and design verification.” J. Struct. Eng., 10.1061/(ASCE)0733-9445(2001)127:6(632), 632–638.

Harries, K.A., Mitchell, D., Cook, W.D., and Redwood, R.G. (1993). “Seismic Response of Steel Beams Coupling Concrete Walls.” Journal of Structural Engineering. 119(12), 3611-3629.

Harries, K.A., Mitchell, D., Redwood, R.G., and Cook, W.D., (1997). “Seismic Design of Coupled Walls – A Case for Mixed Construction.” Canadian Journal of Civil Engineering. 24, 448-459.

Hognestad, E. (1951). “A Study of Combined Bending and Axial Load in Reinforced Concrete Members.” Bulletin 399, University of Illinois Engineering Experiment Station, Urbana, IL.

Marcakis, K. and Mitchell, D. (1980). Precast Concrete Connections with Embedded Steel Members. Precast Concrete Institute (PCI) Journal. 25:4, 88-116.

Massone, L. M. and Wallace, J. W. (2004). "Load-Deformation Response of Slender Reinforced Concrete Walls." ACI Structural Journal, 101(1), 103–113.

Mattock, A.H. and Gaafar, G.H. (1982). Strength of Embedded Steel Sections as Brackets. ACI Journal. 79:9, 83-93.

Moehle, J., Bozorgnia, Y., Jayaram, N., Jones, P., Rahnama, M., Shome, N., Tuna, Z., Wallace, J., Yang, T., Zareian, F. (2011). Case Studies of the Seismic Performance of Tall Buildings Designed by Alternative Means. Task 12 Report for the Tall Buildings Initiative. PEER Report 2011/05, CSSC Report 11-02. Pacific Earthquake Engineering Research Center, Berkeley, CA.

Motter, C.J., Fields, D.C., Hooper, J.D., Klemencic, R., and Wallace, J.W. (2013). Design Recommendations for Steel Reinforced Concrete (SRC) Coupling Beams. UCLA SGEL Research Report 2013-06, University of California, Los Angeles.

Motter, C. J., Fields, D. C., Hooper, J. D., Klemencic, R., and Wallace, J.W. (2017a). "Steel-reinforced concrete coupling beams. I: Testing." J. Struct. Eng., 143(3): 04016191.

Motter, C. J., Fields, D. C., Hooper, J. D., Klemencic, R., and Wallace, J.W. (2017b). “Steel reinforced concrete coupling beams. Part II: Modeling.” J. Struct. Eng., 143(3): 04016192.

Paulay, T., and Binney J.R. (1974). “Diagonally Reinforced Coupling Beams of Shear Walls,” ACI Special Publication 42-46, Farmington Hills, MI.

PEER (Pacific Earthquake Engineering Research Center) TBI (Tall Buildings Initiative). (2017). “Guidelines for performance-based seismic design of tall buildings.” PEER Rep. 2017/06, Univ. of California, Berkeley, CA.

Shahrooz, B. M., Remetter, M. E., and Qin, F. (1993). “Seismic design and performance of composite coupled walls.” J. Struct. Eng., 119(11), 3291–3309.